

Ministry of Science and Higher Education of the Russian Federation
ITMO University

ISSN 2220-8054

NANOSYSTEMS:
PHYSICS, CHEMISTRY, MATHEMATICS

2024, volume 15(2)

Наносистемы: физика, химия, математика

2024, том 15, № 2



NANOSYSTEMS:

PHYSICS, CHEMISTRY, MATHEMATICS

ADVISORY BOARD MEMBERS

Chairman: V.N. Vasiliev (*St. Petersburg, Russia*),
V.M. Buznik (*Moscow, Russia*); V.M. Ievlev (*Voronezh, Russia*), P.S. Kop'ev (*St. Petersburg, Russia*), N.F. Morozov (*St. Petersburg, Russia*), V.N. Parmon (*Novosibirsk, Russia*),
A.I. Rusanov (*St. Petersburg, Russia*),

EDITORIAL BOARD

Editor-in-Chief: I.Yu. Popov (*St. Petersburg, Russia*)

Section Co-Editors:

Physics – V.M. Uzdin (*St. Petersburg, Russia*),

Material science – V.V. Gusarov (*St. Petersburg, Russia*); O.V. Al'myasheva (*St. Petersburg, Russia*);

Chemistry – V.K. Ivanov (*Moscow, Russia*),

Mathematics – I.Yu. Popov (*St. Petersburg, Russia*).

Editorial Board Members:

V.M. Adamyan (*Odessa, Ukraine*); A.P. Alodjants (*St. Petersburg, Russia*); S. Bechta (*Stockholm, Sweden*); J. Behrndt (*Graz, Austria*); A. Chatterjee (*Hyderabad, India*); A.V. Chizhov (*Dubna, Russia*); A.N. Enyashin (*Ekaterinburg, Russia*), P.P. Fedorov (*Moscow, Russia*); E.A. Gudilin (*Moscow, Russia*); H. Jónsson (*Reykjavik, Iceland*); A.A. Kiselev (*Durham, USA*); Yu.S. Kivshar (*Canberra, Australia*); S.A. Kozlov (*St. Petersburg, Russia*); P.A. Kurasov (*Stockholm, Sweden*); A.V. Lukashin (*Moscow, Russia*); I.V. Melikhov (*Moscow, Russia*); G.P. Miroshnichenko (*St. Petersburg, Russia*); I.Ya. Mittova (*Voronezh, Russia*); H. Najjar (*Monastir, Tunisia*), Nguyen Anh Tien (*Ho Chi Minh, Vietnam*); V.V. Pankov (*Minsk, Belarus*); K. Pankrashkin (*Orsay, France*); A.V. Ragulya (*Kiev, Ukraine*); V. Rajendran (*Tamil Nadu, India*); A.A. Rempel (*Ekaterinburg, Russia*); A.A. Rogachev (*Minsk, Belarus*); V.Ya. Rudyak (*Novosibirsk, Russia*); H.M. Sedighi (*Ahvaz, Iran*); D Shoikhet (*Karmiel, Israel*); M.N. Smirnova (*Moscow, Russia*); P. Stovicek (*Prague, Czech Republic*); V.M. Talanov (*Novocherkassk, Russia*); A.Ya. Vul' (*St. Petersburg, Russia*); A.V. Yakimansky (*St. Petersburg, Russia*), V.A. Zagrebnoy (*Marseille, France*).

Editors:

I.V. Blinova; A.I. Popov; A.I. Trifanov; E.S. Trifanova (*St. Petersburg, Russia*),
R. Simoneaux (*Philadelphia, Pennsylvania, USA*).

Address: ITMO University, Kronverkskiy pr., 49, St. Petersburg 197101, Russia.

Phone: +7(812)607-02-54, **Journal site:** <http://nanojournal.ifmo.ru/>,

E-mail: nanojournal.ifmo@gmail.com

AIM AND SCOPE

The scope of the journal includes all areas of nano-sciences. Papers devoted to basic problems of physics, chemistry, material science and mathematics inspired by nanosystems investigations are welcomed. Both theoretical and experimental works concerning the properties and behavior of nanosystems, problems of its creation and application, mathematical methods of nanosystem studies are considered.

The journal publishes scientific reviews (up to 30 journal pages), research papers (up to 15 pages) and letters (up to 5 pages). All manuscripts are peer-reviewed. Authors are informed about the referee opinion and the Editorial decision.

CONTENT

MATHEMATICS

A.S. Melikhova, A.I. Popov, I.V. Blinova, I.Y. Popov
Mathematical model of weakly coupled spherical resonator chains under the influence of external magnetic field 155

T.K. Yuldashev, A.K. Fayziyev
Mixed problem for a linear differential equation of parabolic type with nonlinear impulsive conditions 160

PHYSICS

Rupesh Singh, Dilip Kumar Giri
Photon antibunching in sixth harmonic generation 170

Syed Ziad Z. Aljunid, Nurul Athirah M. A. Ghafar, Bilal A. Ahmad, Retna Apsari, Sulaiman W. Harun
Q-Switched and mode-locked pulse generations with Ti_3AlC_2 absorber 184

M.N. Potkina, I.S. Lobanov
Nucleation of magnetic skyrmions at a notch 192

R.V. Shalayev, A.I. Izotov, V.V. Syrotkin
Some features of the thermoelectric properties of the “metal-carbon film” junction 201

S.V. Bulyarsky, L.N. Vostretsova, V.A. Ribenek
Tunneling recombination in GaN/InGaN LEDs with a single quantum well 204

CHEMISTRY AND MATERIAL SCIENCE

T.O. Kozlova, E.D. Sheichenko, D.N. Vasilyeva, D.A. Kozlov, I.V. Kolesnik, I.V. Tronev, M.A. Teplonogova, A.E. Baranchikov, V.K. Ivanov
Ultrasonic-assisted hydrothermal synthesis of nanoscale double ceric phosphates 215

M.N. Smirnova, G.E. Nikiforova, O.N. Kondrat'eva
Synthesis of magnesium ferrite by combustion of glycine-nitrate gel: the influence of reagents on the gel-precursor and the microstructure of nanopowders 224

K.D. Martinson, A.A. Murashkin, A.A. Lobinsky, D.D. Maltsev, K. Qi, J. Yu, O.V. Almjashaeva, V.I. Popkov
Structural, magnetic and electrochemical studies on $Zn_xMg_{1-x}Fe_2O_4$ nanoparticles prepared via solution combustion method 233

M.S. Lomakin, O.V. Proskurina, A.A. Levin, V.N. Nevedomskiy Pyrochlore phase in the $\text{Bi}_2\text{O}_3\text{--Fe}_2\text{O}_3\text{--WO}_3\text{--(H}_2\text{O)}$ system: its stability field in the low-temperature region of the phase diagram and thermal stability	240
P.A. Popov, A.V. Shchelokov, P.P. Fedorov Numerical model of temperature-dependent thermal conductivity in $M_{1-x}R_x\text{F}_{2+x}$ heterovalent solid solution nanocomposites where M stands for alkaline-earth metals and R for rare-earth metals	255
N.N. Chukavin, D.D. Kolmanovich, A.D. Filippova, M.A. Teplonogova, V.K. Ivanov, A.L. Popov Synthesis of redox-active $\text{Ce}_{0.75}\text{Bi}_{0.15}\text{Tb}_{0.1}\text{F}_3$ nanoparticles and their biocompatibility study <i>in vitro</i>	260
S.V. Kononova, G.K. Lebedeva, V.S. Kozlov, E.N. Korytkova, T.P. Maslennikova, E.V. Kruchinina, E.N. Vlasova, N.N. Saprykina, G.N. Gubanova, M.E. Vylegzhanina, V.T. Lebedev Nanocomposites of aromatic poly(amide-imide) with nanotubular Mg-Fe hydrosilicate	268
P.M. Yeletsky, N.A. Yazykov, Yu.V. Dubinin, M.M. Borodaevskiy, S.A. Selishcheva, V.A. Yakovlev Green approach to production of porous char adsorbents via oxidative carbonization in fluidized catalyst bed	285
Thanh Thi Van Nguyen A plasmonic turn-on insulin sensing platform on centimeter scale nanostructure arrays	300
Information for authors	307

Mathematical model of weakly coupled spherical resonator chains under the influence of external magnetic field

Alina S. Melikhova^{1,a}, Anton I. Popov^{1,b}, Irina V. Blinova^{1,c}, Igor Y. Popov^{1,d}

¹ITMO University, St. Petersburg, Russia

^aalina.s.melikhova@gmail.com, ^bpopov239@gmail.com, ^cirin-a@yandex.ru, ^dpopov1955@gmail.com

Corresponding author: I. Y. Popov, popov1955@gmail.com

PACS 73.22.-f,71.15.Dx,71.70.Di,81.05.Uw

ABSTRACT The Schrödinger operators with constant magnetic field in a bent chain and Y-type chain of coupled balls are considered. Coupling exists due to point-like openings at the touching points of neighbor spheres. The mathematical background of the model is the theory of self-adjoint extensions of symmetric operators. The spectral equations for the model operators in each case were derived and analyzed.

KEYWORDS spectrum; operator extensions theory; balls chain; magnetic field

ACKNOWLEDGEMENTS The work was supported by Russian Science Foundation (grant number 23-21-00096 (<https://rscf.ru/en/project/23-21-00096/>)).

FOR CITATION Melikhova A.S., Popov A.I., Blinova I.V., Popov I.Y. Mathematical model of weakly coupled spherical resonator chains under the influence of external magnetic field. *Nanosystems: Phys. Chem. Math.*, 2024, **15** (2), 155–159.

1. Introduction

Last decades various nanostructures attract attention of researches. Single-walled nanotubes (SWNTs) were first seen in 1993 as cylinders rolled from a single graphene sheet. In 1998, the first peapod was observed by B. Smith, M. Monthieux and D. Luzzi [1]. Carbon peapod is a hybrid nanomaterial consisting of spheroidal fullerenes encapsulated within a carbon nanotube. It is named due to their resemblance to the seedpod of the pea plant. There are a number of works dealing with mathematical modelling of mechanical, optical and electronic properties of nano-peapods [2–5]. Since the properties of carbon peapods differ from those of nanotubes and fullerenes, the carbon peapod can be recognized as a new type of a self-assembled graphitic structure [6]. Possible applications of nano-peapods include nanoscale lasers, single electron transistors, spin-qubit arrays for quantum computing, nanopipettes, and data storage devices thanks to the memory effects and superconductivity of nano-peapods [7–10]. Spectral problems for a chain of coupled resonator attract a special interest due to its usefulness for micro and nanoelectronics, radio physics, acoustics [3, 11, 12].

In the present paper, we suggest a solvable model of a chain of weakly coupled spheres. A presence of a magnetic field is assumed. The mathematical background of the model is given by the theory of self-adjoint extensions of symmetric operators. This approach appeared initially as a mathematical justification of zero-range potential method in atomic physics [13]. Later, it became a well-developed method of construction of solvable models for systems with singular interactions [14–16]. We consider two systems shown in Fig. 1, bent chain and Y-type chain of coupled spheres. Coupling exists due to point-like openings at the touching points of neighbor spheres. The spectral equations for the model operators in each case was derived and analyzed.

2. Model construction

At all junction points of the resonators, the presence of the so-called condition δ -connection, and it is assumed that its intensity $\alpha \in \mathbb{R}$ is the same for all junction points of the resonators. At the boundary of the resonators, which is not involved in their connection, it is placed Neumann boundary condition. It is also believed that all balls making up the chain have same radius. We consider the magnetic field to be uniform and directed along an axis perpendicular to the plane containing all the junction points of the circuit resonators.

To study the stationary states of a non-relativistic spinless particle placed in the described chain structure, it is necessary to consider the stationary Schrödinger equation:

$$H^B \psi(\mathbf{x}) = E \psi(\mathbf{x}), \quad (1)$$

where H^B is the Hamiltonian of the system under the influence of an external magnetic field \mathbf{B} , $\psi(\mathbf{x})$ is the wave function of the three-dimensional spatial coordinate \mathbf{x} , and E is the energy of the system. The main goal of the work is to describe the spectrum of the Hamiltonian of the system $\sigma(H^B)$ depending on its physical and geometric parameters.

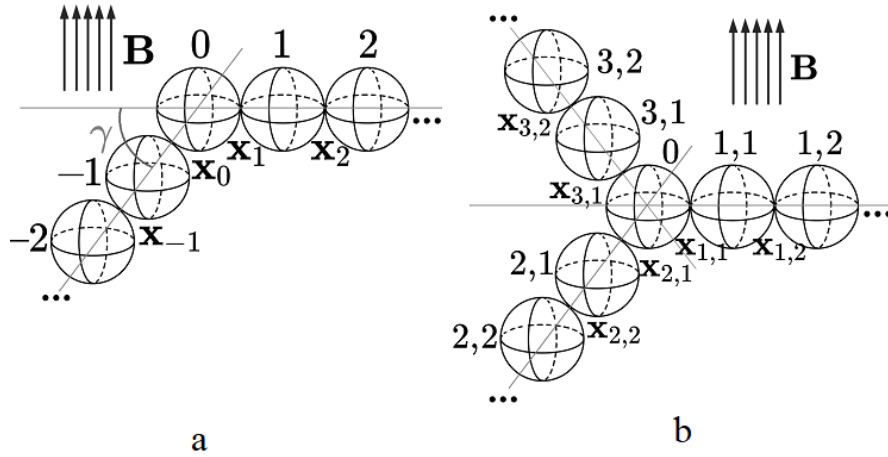


FIG. 1. Geometrical configuration of the system: a - bent chain, b- Y-type chain.

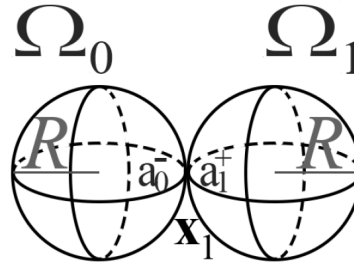


FIG. 2. Two coupled balls.

A mathematical model of interacting resonators is constructed within the framework of the theory of self-adjoint extensions of symmetric operators [17]. The scheme for constructing a model of interacting resonators under the influence of an external magnetic field is similar to that in [3].

The operator H_j^B defined for the j -th resonator in the chain ($j \in \mathbb{Z}$) takes the form:

$$H_j^B = \frac{1}{2m} \left(-i\hbar\nabla - \frac{e(\mathbf{B} \times \mathbf{r})}{2} \right)^2, \tag{2}$$

where i is the imaginary unit, \hbar is the reduced Planck constant, e is the particle charge, $\mathbf{B} = B\mathbf{k}$ is the magnetic field induction vector, \mathbf{r} is the radius vector: $\mathbf{r} = \{x, y, z\}$, and m is the particle mass. We choose the symmetric gauge for the magnetic field.

To understand the scheme for constructing a model of a chain of interacting resonators at exposure to an external magnetic field, consider the simplest chain - two coupled resonators Ω_0 and Ω_1 , having one common point x_1 (Fig. 2).

Starting with the orthogonal sum of the self-adjoint Hamiltonians for each ball, we restrict it to the set of functions vanishing at the common point of two balls and come to the symmetric operator. Its self-adjoint extension gives us a model of coupled resonators. To construct it, one can restrict the domain of the adjoint operator [13]. The corresponding limitation is that the following boundary form annihilates for elements from the domain of the adjoint operator:

$$\left((H^B)^* u, v \right) - \left(u, (H^B)^* v \right) = \int_{\Omega_0 \cup \Omega_1} \left((H^B)^* u \bar{v} - u \overline{(H^B)^* v} \right) d(\Omega_0 \cup \Omega_1), \tag{3}$$

where the bar denotes complex conjugation, and $d(\Omega_0 \cup \Omega_1)$ is the volume element $\Omega_0 \cup \Omega_1$. The function $u \in \text{dom}((H^B)^*)$ can be represented in the following form [3]:

$$u = \begin{pmatrix} u_0^0 + a_{0(u)}^- G_0^B(\mathbf{x}, \mathbf{x}_1, \lambda_0) + b_{0(u)}^- \\ u_1^0 + a_{1(u)}^+ G_1^B(\mathbf{x}, \mathbf{x}_1, \lambda_0) + b_{1(u)}^+ \end{pmatrix}, \tag{4}$$

where $G_j^B(\mathbf{x}, \mathbf{x}_1, \lambda_0)$ are Green's functions for the problem ($j = 0, 1$), are the deficiency elements of the symmetric operator $\overset{\circ}{H}^B$.

By direct calculation, one obtains the boundary form and, correspondingly, the condition of its annihilation:

$$((H^B)^*u, v) - (u, (H^B)^*) = \overline{a_{0(v)}^-} b_{0(u)}^- - a_{0(u)}^- \overline{b_{0(v)}^-} + \overline{a_{1(v)}^+} b_{1(u)}^+ - a_{1(u)}^+ \overline{b_{1(v)}^+} = 0. \quad (5)$$

Expression (5) is similar to that for the boundary form in the absence of external fields [17].

3. Results

Based on all of the above, the following theorem is valid:

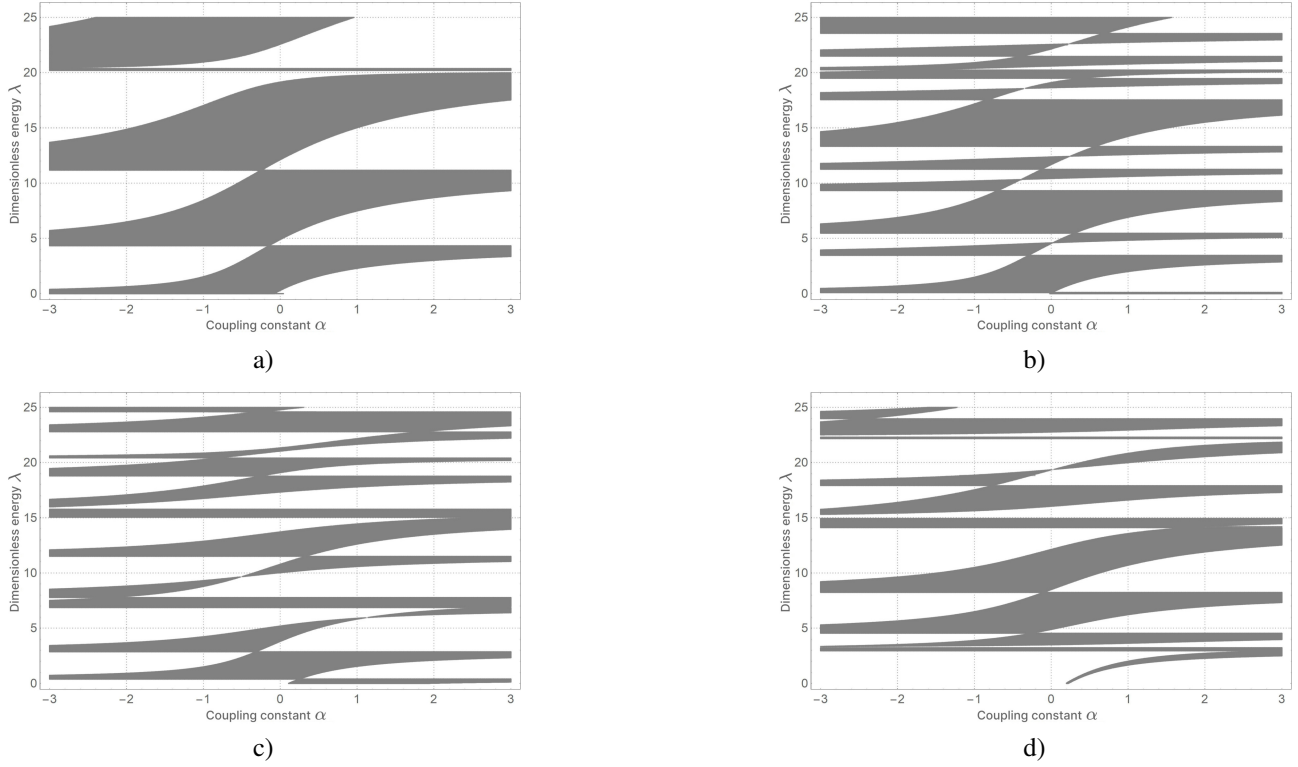


FIG. 3. Structure of the continuous spectrum of a chain with a break (or branching) depending on the connection parameter α at a fixed magnetic field: a) $B = 0$, b) $B = 0.5$, c) $B = 1$, d) $B = 3$

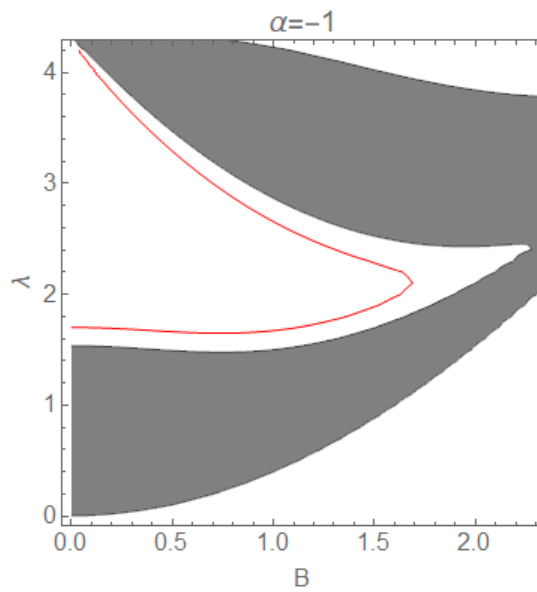


FIG. 4. Structure of the spectrum of the basic Y-branch of the chain depending on B at $\alpha = -1$ (gray areas — continuous spectrum zones; solid line — energy values belonging to the discrete spectrum)

Theorem 1. Let the chain break angle γ be such that $\gamma \in [0, \frac{2\pi}{3})$. Then the essential spectrum of the model Hamiltonian of a chain with a kink and with the condition of δ -connection at the junction points of the resonators, subject to the influence of the magnetic field \mathbf{B} , consists of eigenvalues of infinite multiplicity — the eigenvalues of the Neumann Laplacian in the ball, corresponding to the eigenfunctions equal to 0 at both junction points of the resonators (\mathbf{x}_{j-1} and \mathbf{x}_j), and continuous spectrum. The continuous spectrum of the model Hamiltonian has a band structure completely described by inequality (6)

$$|\mu_B^\pm| = 1 \Leftrightarrow \left| \frac{X_B}{2G^B} \right| \leq 1. \quad (6)$$

At $\gamma = 0$, the discrete spectrum of the model Hamiltonian is empty.

Let now the chain break angle γ be such that $\gamma \in (0, \frac{2\pi}{3})$. The discrete spectrum of the model Hamiltonian consists of all λ that resolve equation (11) and satisfy conditions (7)-(8):

$$|\mu_B^+| < 1 \Leftrightarrow \frac{X_B}{2G^B} < -1, \quad (7)$$

$$|\mu_B^-| < 1 \Leftrightarrow \frac{X_B}{2G^B} > 1, \quad (8)$$

where $X_B = \lim_{\mathbf{x} \rightarrow \mathbf{x}_j} (G^B(\mathbf{x}, \mathbf{x}_1, \lambda) - G^B(\mathbf{x}, \mathbf{x}_1, \lambda_0))$. We also present here the eigenvalues μ_B of this transfer matrix and the corresponding eigenvectors ν_B (for $j \neq 1$):

$$\mu_B = \frac{X_B}{2G^B} \pm \sqrt{\left(\frac{X_B}{2G^B}\right)^2 - 1}, \quad (9)$$

$$\nu_B = \varrho \begin{pmatrix} 1 \\ -\mu_B \end{pmatrix}, \quad (10)$$

where $G^B = G^B(\mathbf{x}_{j-1}, \mathbf{x}_j, \lambda) = G^B(\mathbf{x}_j, \mathbf{x}_{j-1}, \lambda)$ ($j \neq 1$), ϱ is some constant ($\varrho \neq 0$).

$$\frac{|Z_\gamma^B|^2 - (G^B)^2}{G^B Z_\gamma^B} = 0. \quad (11)$$

For Y-type chain of balls, the structure of the spectrum is described by the following theorem [7]:

Theorem 2. The essential spectrum of the model Hamiltonian of a Y-branched chain with the condition of δ -connection at the junction points of the resonators, subject to the influence of the magnetic field \mathbf{B} , consists of eigenvalues of infinite multiplicity - the eigenvalues of the Neumann Laplacian in the ball, corresponding to the eigenfunctions equal to 0 at both junction points of the resonators (\mathbf{x}_{j-1} and \mathbf{x}_j), and continuous spectrum. The continuous spectrum of the model Hamiltonian has a band structure completely described by inequality (6). The discrete spectrum of the model Hamiltonian consists of all λ that resolve equation (12) and satisfy conditions (7) – (8)

$$\frac{1}{(G^B)^3} ((X_B - \mu_B G^B)^3 - (X_B - \mu_B G^B) (|G_{[2,3]}|^2 + |G_{[1,2]}|^2 + |G_{[1,3]}|^2) + G_{[1,2]} G_{1,[3]} G_{[2,3]} + \overline{G_{[1,2]} G_{1,[3]} G_{[2,3]}}) = 0. \quad (12)$$

The picture of the dependence of the continuous spectrum on the magnitude of the magnetic field in the case of a Y-branched chain has the same form as in the case of a chain with a break It is shown in Fig. 4 (the gap between the first and second zones of the continuous spectrum contains energy values belonging to the discrete spectrum).

4. Conclusion

Explicitly solvable model was constructed for electron in a system of bent chain and Y-type chain of weakly coupled balls in a magnetic field. The model is based on the theory of self-adjoint extensions of symmetric operators in the Hilbert space. The spectral problems are of special interest for systems of such type (see, e.g., [18–22]). Spectral equations were derived. The continuous and the point spectra of the model operator were described.

References

- [1] Smith, Brian W., Monthioux, Marc, Luzzi, David E. Carbon nanotube encapsulated fullerenes: A unique class of hybrid materials. *Chemical Physics Letters*. 1999, **315**(1-2), P. 31–36.
- [2] Lee J.Y., Lee Ch., Osawa E., et.al. Snapshots of the Fragmentation for C70@Single-Walled Carbon Nanotube: Tight-Binding Molecular Dynamics Simulations. *International Journal of Molecular Science*, 2021, **22**(8), p. 3929.
- [3] Melikhova A.S., Popov I.Y. Spectral problem for solvable model of bent nanopeapod. *Applicable Analysis*. 2017, **96**(2), P. 215–224.
- [4] Li Y., Kaneko T. and Hatakeyama R. Photoresponse of fullerene and azafullerene peapod field effect transistors, 2009 9th IEEE Conference on Nanotechnology (IEEE-NANO), Genoa, Italy, 2009, P. 86–89.
- [5] Matsuno T., Terasaki S., Kogashi K. et al. A hybrid molecular peapod of sp²- and sp³-nanocarbons enabling ultrafast terahertz rotations. *Nat Commun* 12, 5062 (2021).
- [6] Iijima, Sumio. Carbon nanotubes: Past, present, and future. *Physica B: Condensed Matter*, 2002, **323**(1-4), P. 1–5.
- [7] Utko P., Nygerd J., Monthioux M., Noe L. Sub-Kelvin transport spectroscopy of fullerene peapod quantum dots. *Applied Physics Letters*, 2006, **89**(23), P. 233118.
- [8] Pichler T., Kuzmany H., Kataura H., Achiba Y. Metallic Polymers of C60 Inside Single-Walled Carbon Nanotubes. *Physical Review Letters*, 2001, **87**(26), P. 267401.
- [9] Enyashin A.N., Ivanovskii A.L. Nanotubular composites: modeling of capillary filling of nanotubes of disulfide of molybdenum by molecules of TiCl₄. *Nanosystems: Phys. Chem. Math.*, 2010, **1**(1) P. 63–71.
- [10] Tao X., Zhang Zh., et.al. Peapod-Like Structured B/N Co-Doped Carbon Nanotube Array Encapsulating MxPy (M = Fe, Co, and Ni) Nanoparticles for High-Rate Potassium Storage. *ACS Appl Mater Interfaces*, 2024, **16**(1), P. 772–783.
- [11] Pazynin V. Multiplet properties in the spectrum of oscillations of coupled waveguide resonators chain. *Radiofizika i Elektronika*, 2017, **22**(1), P. 3–14.
- [12] Gao Z., Gao F., Shastri K. et al. Frequency-selective propagation of localized spoof surface plasmons in a graded plasmonic resonator chain. *Sci. Rep.*, 2016, **6**, P. 25576.
- [13] Berezin F.A., Faddeev L.D. Remark on the Schrödinger equation with singular potential. *Dokl. Akad. Nauk SSSR*, 1961, **137**(5), P. 1011–1014.
- [14] Pavlov B.S. *Extensions theory and explicitly solvable models*. *Russian Math. Surveys*, 1987, **42**(6), P. 127–168.
- [15] Popov I.Y. The resonator with narrow slit and the model based on the operator extensions theory. *J. Math. Phys.*, 1992, **33**(11), P. 3794–3801.
- [16] Albeverio S., Kuracov P. *Singular Perturbations of Differential Operators: Solvable Schrödinger-type Operators (London Mathematical Society Lecture Note Series, Series Number 271)*, Cambridge, Cambridge University Press, 2000, 444 p.
- [17] Popov I.Yu. The extension theory and localization of resonances for the domain of trap type, *Matematicheskii sbornik*, 1990, **181**(10), P. 1366–1390. English: *Mathematics of the USSR-Sbornik*, 1992, **71**(1), P. 209–234.
- [18] Duclos P., Exner P., Turek O. On the spectrum of a bent chain graph. *J. Phys. A: Math. Theor.*, 2008, **41**, P. 415206.
- [19] Popov I.Yu., Smirnov P.I. Spectral problem for branching chain quantum graph. *Phys. Lett. A*, 2013, **377**(6), P. 439–442.
- [20] Popov I.Y., Skorynina A.N., Blinova I.V. On the existence of point spectrum for branching strips quantum graph. *J. Math. Phys.*, 2014, **55**, P. 033504/1-20.
- [21] Blinova I.V., Popov A.I., Bosova A.A. Spectral gaps for star-like quantum graph and for two coupled rings. *Nanosystems: Phys. Chem. Math.*, 2022, **13**(3), P. 245–249.
- [22] Borisov D.I., Pankrashkin K.V. Gap opening and split band edges in waveguides coupled by a periodic system of small windows. *Math. Notes*, 2013, **93**(5-6), P. 660–675.

Submitted 23 May 2023; accepted 27 July 2023

Information about the authors:

Alina S. Melikhova – Center of Mathematics, ITMO University, Kroverkskiy, 49, St. Petersburg, 197101, Russia; alina.s.melikhova@gmail.com

Anton I. Popov – Center of Mathematics, ITMO University, Kroverkskiy, 49, St. Petersburg, 197101, Russia; ORCID 0000-0001-7137-4067; popov239@gmail.com

Irina V. Blinova – Center of Mathematics, ITMO University, Kroverkskiy, 49, St. Petersburg, 197101, Russia; ORCID 0000-0003-2115-2479; irin-a@yandex.ru

Igor Y. Popov – Center of Mathematics, ITMO University, Kroverkskiy, 49, St. Petersburg, 197101, Russia; ORCID 0000-0002-5251-5327; popov1955@gmail.com

Conflict of interest: the authors declare no conflict of interest.

Mixed problem for a linear differential equation of parabolic type with nonlinear impulsive conditions

Tursun K. Yuldashev^{1,a}, Aziz K. Fayziyev^{1,b}

¹Tashkent State University of Economics, Tashkent, Uzbekistan

^at.yuldashev@tsue.uz, ^bfayziyev.a@inbox.ru

Corresponding author: T. K. Yuldashev, t.yuldashev@tsue.uz

ABSTRACT In this paper, we consider a linear parabolic type partial differential equation in the space of generalized functions as the equation of neutron diffusion in the presence of neutron absorption by the atomic nucleus with nonlinear impulsive effects. Spectral equation is obtained from the Dirichlet boundary value conditions and this spectral problem is studied. The Fourier method of variables separation is used. Countable system of nonlinear functional integral equations is obtained with respect to the Fourier coefficients of unknown function. Theorem on a unique solvability of the countable system of functional integral equations is proved. The method of successive approximations is used in combination with the method of contracting mapping. Criteria of uniqueness and existence of generalized solution of the impulsive mixed problem is obtained. Solution of the mixed problem is derived in the form of the Fourier series. It is shown that the Fourier series converges uniformly.

KEYWORDS Mixed problem, impulsive parabolic equation, nonlinear impulsive conditions, involution, unique solvability

FOR CITATION Yuldashev T.K., Fayziyev A.K. Mixed problem for a linear differential equation of parabolic type with nonlinear impulsive conditions. *Nanosystems: Phys. Chem. Math.*, 2024, **15** (2), 160–169.

1. Formulation of the problem statement

Differential equations of mathematical physics have direct applications in the theory of nanosystems (see, for example, [1–13], and [14]). Partial differential and integro-differential equations of parabolic type with initial and boundary conditions are investigated widely by large number of scientists and have different applications in sciences and technology (see, for example, [15–28]). Note that the differential equations of parabolic type are associated with heat and diffusion processes. Neutron diffusion plays a significant role in the operation of nuclear reactors. The diffusion equation makes it possible to calculate the neutron density inside the core of a nuclear reactor, the neutron flux from the moderator surface, and the reflection and transmission of neutrons by biological protection structures.

Differential and integro-differential equations with impulse effects have applications in sciences, ecology, biotechnology, industrial robotics, pharmacokinetics, optimal control, etc. [29–38]. A lot of publications are devoted to study differential equations with impulsive effects, describing many natural and technical processes (see, for example, [39–50]). The questions of existence and uniqueness of periodic solutions of differential and integro-differential equations were studied in [51–55]. In [56–58], the Whitham type partial differential equations of the first order with impulsive effects are studied.

To date, the impulsive systems for ordinary differential and integro-differential equations have been well studied. As for the partial differential equations of mathematical physics, the authors are not aware of any work where the differential equations of mathematical physics with impulsive influences were studied. It is necessary to solve problems associated with the use of the Fourier series, the integration of impulsive countable systems in different subdomains and the definition of the class of solutions. So, in the present paper, we study the solvability of the impulsive mixed problem for a linear differential equation with involution and nonlinear impulsive conditions in the space of generalized functions.

In the domain

$$\Omega = \{t \in (0, T), t \neq t_m, 0 < t_m < T, m = 1, 2, \dots, p, x \in (-1, 1)\},$$

we consider the following differential equation of neutron diffusion in the presence of neutron absorption by the atomic nucleus

$$U_t(t, x) - U_{xx}(t, x) - \varepsilon U_{xx}(t, -x) = a(t)U(t, x) + f(t, x) \quad (1)$$

with the Dirichlet boundary value conditions

$$U(t, -1) = U(t, 1) = 0, \quad 0 \leq t \leq T; \quad (2)$$

and initial value condition

$$U(0, x) = \varphi(x), \quad -1 \leq x \leq 1, \quad (3)$$

where T is given positive number, unknown function $U(t, x)$ characterizes the neutron density with the impulsive effects, ε is the diffusion coefficient, $0 < \varepsilon < 1$, $a(t) \in C[0; T]$ is the function characterizing the lifetime of a neutron in a medium before absorption, the function $f(t, x) \in L_2(\Omega)$ characterizes the rate of the neutron production, $\varphi(x)$ is given function on the segment $[-1, 1]$. We assume that for the initial value function $\varphi(x) \in L_2[-1, 1]$ the following conditions are fulfilled $\varphi(-1) = \varphi(1) = 0$. We also suppose that $f(t, -1) = f(t, 1) = 0$.

Since the equation (1) is impulsive and the unknown function $U(t, x)$ has some discontinuity points t_1, t_2, \dots, t_p on the interval $(0, T)$, in integration processes, we need to know the difference between the right and the left side limit values of unknown function at these discontinuity points. However, in practice, it is often impossible to determine these differences explicitly. So, we use them in the form of nonlinear functions. Therefore, we consider equation (1) with the following impulsive conditions

$$U(t_m^+, x) - U(t_m^-, x) = I_m \left(x, \int_{-1}^1 G(y)U(t_m, y)dy \right), \quad m = 1, 2, \dots, p, \tag{4}$$

where $I_m(x, \cdot)$ are continuous functions on x , $\int_{-1}^1 |G(x)| dx < \infty$, $0 < t_1 < \dots < t_p < T < \infty$, $U(t_m^+, x) = \lim_{\nu \rightarrow 0^+} U(t_m + \nu, x)$, $U(t_m^-, x) = \lim_{\nu \rightarrow 0^-} U(t_m - \nu, x)$ are the right-hand side and the left-hand side limits of function $U(t, x)$ at the points $t = t_m$, respectively.

2. Formal solution of the mixed problem

First, consider the homogeneous partial differential equation

$$U_t(t, x) - U_{xx}(t, x) - \varepsilon U_{xx}(t, -x) = 0 \tag{5}$$

with boundary value conditions of the Dirichlet type

$$U(t, -1) = U(t, 1) = 0, \quad 0 \leq t \leq T. \tag{6}$$

Problem (5), (6) will be solved by the method of separation of variables: $U(t, x) = u(t)\vartheta(x)$. After separation of variables, from (5), (6), we arrive at the following spectral problem for an ordinary differential equation

$$\vartheta''(x) + \varepsilon\vartheta''(-x) + \lambda\vartheta(x) = 0 \tag{7}$$

with boundary value conditions

$$\vartheta(-1) = 0, \quad \vartheta(1) = 0. \tag{8}$$

It is obvious that for the case of even eigenfunctions, equation (7) takes the form

$$(1 + \varepsilon)\vartheta_1''(x) + \lambda_1\vartheta_1(x) = 0. \tag{9}$$

Solving differential equation (9) with conditions (8), we find the eigenvalues

$$\lambda_{1,n} = (1 + \varepsilon)\pi^2(n + 0.5)^2 \tag{10}$$

and eigenfunctions of problem (7), (8):

$$\vartheta_{1,n}(x) = \cos \pi(n + 0.5)x, \quad n \in \mathbb{N}. \tag{11}$$

In the case of odd eigenfunctions, equation (7) takes another form

$$(1 - \varepsilon)\vartheta_2''(x) + \lambda_2\vartheta_2(x) = 0. \tag{12}$$

Solving differential equation (12) with spectral (zero) conditions (8), we find the eigenvalues and the corresponding eigenfunctions of problem (12), (8):

$$\lambda_{2,n} = (1 - \varepsilon)\pi^2 n^2, \quad 0 < \varepsilon < 1, \tag{13}$$

$$\vartheta_{2,n}(x) = \sin \pi n x, \quad n \in \mathbb{N}. \tag{14}$$

Note that the eigenfunctions $\vartheta_{i,n}(x)$ ($i = 1, 2$) determined by (11) and (14) form a complete system of orthonormal eigenfunctions in the space $L_2[-1, 1]$. Therefore, we seek desired solutions to the nonhomogeneous partial differential equation (1) in the forms $U(t, x) = U_1(t, x) + U_2(t, x)$ of the Fourier series

$$U_i(t, x) = \sum_{n=1}^{\infty} u_{i,n}(t) \vartheta_{i,n}(x), \quad i = 1, 2, \tag{15}$$

where $U_1(t, x)$ and $U_2(t, x)$ satisfy the given differential equation (1)

$$U_{it}(t, x) - U_{ixx}(t, x) - \varepsilon U_{ixx}(t, -x) = a(t)U_i(t, x) + f_i(t, x),$$

$$\begin{aligned}
 &= -u_{i,n}(0) - e^{\lambda_{i,n}t_1} [u_{i,n}(t_1^+) - u_{i,n}(t_1)] - e^{\lambda_{i,n}t_2} [u_{i,n}(t_2^+) - u_{i,n}(t_2)] - \\
 &\quad - \dots - e^{\lambda_{i,n}t_p} [u_{i,n}(t_p^+) - u_{i,n}(t_p)] + e^{\lambda_{i,n}t} u_{i,n}(t) = \\
 &= -u_{i,n}(0) - \sum_{0 < t_m < t}^p e^{\lambda_{i,n}t_m} I_{m,i,n} + e^{\lambda_{i,n}t} u_{i,n}(t).
 \end{aligned}$$

Hence, we obtain that

$$e^{\lambda_{i,n}t} u_{i,n}(t) = u_{i,n}(0) + \int_0^t e^{\lambda_{i,n}s} [a(s) u_{i,n}(s) + f_{i,n}(s)] ds + \sum_{0 < t_m < t}^p e^{\lambda_{i,n}t_m} I_{m,i,n}$$

or

$$u_{i,n}(t) = u_{i,n}(0)e^{-\lambda_{i,n}t} + \int_0^t e^{-\lambda_{i,n}(t-s)} [a(s) u_{i,n}(s) + f_{i,n}(s)] ds + \sum_{0 < t_m < t}^p e^{-\lambda_{i,n}(t-t_m)} I_{m,i,n}. \tag{23}$$

For given function $\varphi(x)$ in (3), we set $\varphi(x) = \varphi_1(x) + \varphi_2(x)$. Now, supposing that the functions $\varphi_1(x)$ and $\varphi_2(x)$ are expanded in the Fourier series and using the Fourier coefficients (16), from condition (3), we obtain

$$u_{i,n}(0) = \int_{-1}^1 U_i(0, x) \vartheta_{i,n}(x) dx = \int_{-1}^1 \varphi_i(x) \vartheta_{i,n}(x) dx = \varphi_{i,n}, \quad i = 1, 2. \tag{24}$$

To find the unknown coefficients $u_{i,n}(0)$ in the presentations (23), we use the initial value conditions (24). Then we have

$$u_{i,n}(t) = \varphi_{i,n}e^{-\lambda_{i,n}t} + \int_0^t e^{-\lambda_{i,n}(t-s)} [a(s) u_{i,n}(s) + f_{i,n}(s)] ds + \sum_{0 < t_m < t}^p e^{-\lambda_{i,n}(t-t_m)} I_{m,i,n}. \tag{25}$$

We note that representations (25) are the Fourier coefficients of the solution to problem (1)–(4) and have been considered as a countable system of nonlinear functional and integral equations. Taking into account (18) and (19), we rewrite it as

$$\begin{aligned}
 u_{i,n}(t) = A(t; u_{i,n}) &\equiv \varphi_{i,n}e^{-\lambda_{i,n}t} + \int_0^t e^{-\lambda_{i,n}(t-s)} a(s) u_{i,n}(s) ds + \\
 &+ \int_0^t e^{-\lambda_{i,n}(t-s)} \int_{-1}^1 f_i(s, x) \vartheta_{i,n}(x) dx ds + \\
 &+ \sum_{0 < t_m < t}^p e^{-\lambda_{i,n}(t-t_m)} \int_{-1}^1 I_{m,i} \left(x, \int_{-1}^1 G(y) \sum_{j=1}^{\infty} u_{i,j}(t_m) \vartheta_{i,j}(y) dy \right) \vartheta_{i,n}(x) dx.
 \end{aligned} \tag{26}$$

The representation (26) is countable system of functional equations. Substituting representation (26) into the Fourier series (15), we obtain a formal solution of the problem (1)–(4) on the domain Ω

$$\begin{aligned}
 U_i(t, x) &= \sum_{n=1}^{\infty} \vartheta_{i,n}(x) \left[\varphi_{i,n}e^{-\lambda_{i,n}t} + \int_0^t e^{-\lambda_{i,n}(t-s)} a(s) u_{i,n}(s) ds + \right. \\
 &+ \int_0^t e^{-\lambda_{i,n}(t-s)} \int_{-1}^1 f_i(s, x) \vartheta_{i,n}(x) dx ds + \\
 &+ \left. \sum_{0 < t_m < t}^p e^{-\lambda_{i,n}(t-t_m)} \int_{-1}^1 I_{m,i} \left(x, \int_{-1}^1 G(y) \sum_{j=1}^{\infty} u_{i,j}(t_m) \vartheta_{i,j}(y) dy \right) \vartheta_{i,n}(x) dx \right].
 \end{aligned} \tag{27}$$

3. Solvability of the countable system of nonlinear functional equations

Let us investigate the countable system of nonlinear functional equations (26) from the point of view of its unique solvability. Consider the following well-known Banach spaces, which will be used below: the space $B_2[0, T]$ of function sequences $\{u_n(t)\}_{n=1}^\infty$ on the segment $[0, T]$ with the norm

$$\|\vec{u}(t)\|_{B_2[0,T]} = \sqrt{\sum_{n=1}^\infty \left(\max_{t \in [0,T]} |u_n(t)|\right)^2} < \infty;$$

the Hilbert coordinate space ℓ_2 of number sequences $\{\varphi_n\}_{n=1}^\infty$ with the norm

$$\|\varphi\|_{\ell_2} = \sqrt{\sum_{n=1}^\infty |\varphi_n|^2} < \infty;$$

the space $L_2[-1, 1]$ of square-integrable functions on the interval $[-1, 1]$ with the norm

$$\|\vartheta(x)\|_{L_2[-1,1]} = \sqrt{\int_{-1}^1 |\vartheta(x)|^2 dx} < \infty;$$

the space

$$PC_{B_2}([0, T]; \mathbb{R}) = \{u_n : [0, T] \rightarrow \mathbb{R}; \vec{u}(t) \in (B_2[t_m, t_{m+1}]; \mathbb{R}), m = 0, 1, \dots, p\}$$

with the norm

$$\|\vec{u}(t)\|_{PC_{B_2}[0,T]} = \max \left\{ \|\vec{u}(t)\|_{B_2[t_m, t_{m+1}]}, m = 0, 1, 2, \dots, p \right\},$$

where $u_n(t_m^+)$ and $u_n(t_m^-)$ ($m = 0, 1, \dots, p$) exist and are bounded; $u_n(t_m^-) = u_n(t_m)$.

Theorem 1. Let the estimate $\sum_{j=1}^\infty |\varphi_j| < \infty$ be valid for the Fourier coefficients of the function $\varphi(x) \in L_2[-1, 1]$.

If the following conditions are fulfilled:

$$\begin{aligned} & \max_{m=1,p} \max_{t \in [t_m, t_{m+1}]} \sqrt{\int_{-1}^1 \left[I_{i,m} \left(x, \int_{-1}^1 G(y) \sum_{j=1}^\infty u_{i,j}^0(t) \vartheta_{i,j}(y) dy \right) \right]^2} dx \leq M_{0,i} = \text{const} < \infty, \\ & \left| I_{m,i} \left(x, \int_{-1}^1 G(y) \sum_{j=1}^\infty u_{i,j}^\tau(t_m) \vartheta_{i,j}(y) dy \right) - I_{m,i} \left(x, \int_{-1}^1 G(y) \sum_{j=1}^\infty u_{i,j}^{\tau-1}(t_m) \vartheta_{i,j}(y) dy \right) \right| \leq \\ & \leq N_{m,i}(x) \left| \int_{-1}^1 G(y) \sum_{j=1}^\infty |u_{i,j}^\tau(t_m) - u_{i,j}^{\tau-1}(t_m)| \vartheta_{i,j}(y) dy \right|, \quad 0 < N_{m,i}(x) \in L_2[-1, 1], \\ & \rho_i = C \cdot M_{2,i} [M_4 \|N_i(x)\|_{L_2[-1,1]} \|G(x)\|_{L_2[-1,1]} + M_{1,i} M_5] < 1, \quad i = 1, 2, \end{aligned} \tag{28}$$

where $C, M_{1,i}, M_4, M_5, M_{2,i}$ are some constants, then the countable system of nonlinear functional equations (26) is uniquely solvable in the space $PC_{B_2}[0, T]$. In this case, the desired solution can be found by the following iterative process:

$$\begin{cases} u_{i,n}^0(t) = \varphi_{i,n} e^{-\lambda_{i,n} t} + \int_0^t e^{-\lambda_{i,n}(t-s)} \int_{-1}^1 f_i(s, x) \vartheta_{i,n}(x) dx ds, \\ u_{i,n}^{\tau+1}(t) = A(t; u_{i,n}^\tau), \quad i = 1, 2, \quad \tau = 0, 1, 2, \dots \end{cases} \tag{29}$$

Proof. We use the method of contracting maps in combination with the method of successive approximations in the space $PC_{B_2}[0, T]$. We take into account that

$$\int_0^t e^{-\lambda_{i,n}(t-s)} ds \leq \frac{1}{\lambda_{i,n}} [1 - e^{-\lambda_{i,n} t}] \leq \frac{1}{\lambda_{i,n}} M_{1,i}.$$

Then, by virtue of conditions of the theorem and applying the Cauchy–Schwartz inequality and the Bessel inequality, we obtain from the approximations (29) that the following estimate is valid:

$$\|\vec{u}_i^0(t)\|_{PC_{B_2}[0,T]} \leq \max_{m=1,p} \sum_{n=1}^\infty \max_{t \in [t_m, t_{m+1}]} |u_{i,n}^0(t)| \leq \max_{m=1,p} \sum_{n=1}^\infty |\varphi_{i,n}| \max_{t \in [t_m, t_{m+1}]} \{e^{-\lambda_{i,n} t}\} +$$

$$\begin{aligned}
& +C \max_{m=1,p} \sum_{n=1}^{\infty} \sup_{t \in (t_m, t_{m+1})} \left| \int_0^t e^{-\lambda_{i,n}(t-s)} \int_{-1}^1 f_i(s, x) \vartheta_{i,n}(x) dx ds \right| \leq \\
& \leq \sum_{n=1}^{\infty} |\varphi_{i,n}| + C \cdot M_{1,i} \max_{m=1,p} \sum_{n=1}^{\infty} \frac{1}{\lambda_{i,n}} \max_{t \in [t_m, t_{m+1}]} \left| \int_{-1}^1 f_i(t, x) \vartheta_{i,n}(x) dx \right| \leq \\
& \leq \sum_{n=1}^{\infty} |\varphi_{i,n}| + C \cdot M_{1,i} \sqrt{\sum_{n=1}^{\infty} \frac{1}{\lambda_{i,n}^2} \max_{m=1,p} \max_{t \in [t_m, t_{m+1}]} \left[\int_{-1}^1 f_i(t, x) \vartheta_{i,n}(x) dx \right]^2} \leq \\
& \leq \sum_{n=1}^{\infty} |\varphi_{i,n}| + C \cdot M_{1,i} M_{2,i} M_{3,i} = \delta_{1,i} < \infty, \quad i = 1, 2,
\end{aligned} \tag{30}$$

where

$$\begin{aligned}
M_{2,i} &= \sqrt{\sum_{n=1}^{\infty} \frac{1}{\lambda_{i,n}^2}}, \quad M_{3,i} = \max_{m=1,p} \max_{t \in [t_m, t_{m+1}]} \|f_i(t, x)\|_{L_2[-1,1]}, \quad 0 < C = \text{const}, \\
\lambda_{1,n} &= (1 + \varepsilon) \pi^2 (n + 0.5)^2, \quad \lambda_{2,n} = (1 - \varepsilon) \pi^2 n^2, \quad |\varepsilon| < 1.
\end{aligned}$$

Taking into account estimate (30), applying the Cauchy–Schwartz inequality and the Bessel inequality, for the first difference of approximations (29), we obtain:

$$\begin{aligned}
& \|\vec{u}_i^1(t) - \vec{u}_i^0(t)\|_{PC_{B_2}[0,T]} \leq \max_{m=1,p} \sum_{n=1}^{\infty} \max_{t \in [t_m, t_{m+1}]} |u_{i,n}^1(t) - u_{i,n}^0(t)| \leq \\
& \leq C \max_{m=1,p} \sum_{n=1}^{\infty} \sup_{t \in (t_m, t_{m+1})} \left| \sum_{0 < t_m < t}^p e^{-\lambda_{i,n}(t-t_m)} \int_{-1}^1 I_{m,i} \left(x, \int_{-1}^1 G(y) \sum_{j=1}^{\infty} u_{i,j}^0(t_m) \vartheta_{i,j}(y) dy \right) \vartheta_{i,n}(x) dx \right| + \\
& \quad + C \max_{m=1,p} \sum_{n=1}^{\infty} \sup_{t \in (t_m, t_{m+1})} \left| \int_0^t e^{-\lambda_{i,n}(t-s)} a(s) u_{i,n}^0(s) ds \right| \leq \\
& \leq C \max_{m=1,p} \sum_{n=1}^{\infty} \frac{1}{\lambda_{i,n}} \sup_{t \in (t_m, t_{m+1})} \sum_{m=1}^p \frac{1}{t - t_m} \left| \int_{-1}^1 I_{m,i} \left(x, \int_{-1}^1 G(y) \sum_{j=1}^{\infty} u_{i,j}^0(t) \vartheta_{i,j}(y) dy \right) \vartheta_{i,n}(x) dx \right| + \\
& \quad + C \cdot M_{1,i} \max_{m=1,p} \max_{t \in [t_m, t_{m+1}]} |a(t)| \sum_{n=1}^{\infty} \frac{1}{\lambda_{i,n}} \max_{t \in [t_m, t_{m+1}]} |u_{i,n}^0(t)| \leq \\
& \leq C \cdot M_4 \sqrt{\sum_{n=1}^{\infty} \frac{1}{\lambda_{i,n}^2} \max_{m=1,p} \max_{t \in [t_m, t_{m+1}]} \left[\sum_{n=1}^{\infty} \left[\int_{-1}^1 I_{m,i} \left(x, \int_{-1}^1 G(y) \sum_{j=1}^{\infty} u_{i,j}^0(t) \vartheta_{i,j}(y) dy \right) \vartheta_{i,n}(x) dx \right]^2} \right.} \\
& \quad \left. + C \cdot M_{1,i} M_5 \sqrt{\sum_{n=1}^{\infty} \frac{1}{\lambda_{i,n}^2} \|\vec{u}_i^0(t)\|_{PC_{B_2}[0,T]}^2} \leq \\
& \leq C \cdot M_4 M_{2,i} \max_{m=1,p} \left\| I_{m,i} \left(x, \int_{-1}^1 G(y) \sum_{j=1}^{\infty} \delta_{1,i} \vartheta_{i,j}(y) dy \right) \right\|_{L_2[-1,1]} + C \cdot M_{1,i} M_{2,i} M_5 \delta_{1,i} \leq \\
& \leq C \cdot M_{2,i} [M_4 M_{0,i} + M_{1,i} M_5 \delta_{1,i}] < \infty,
\end{aligned} \tag{31}$$

$$M_4 = \sup_{t \in (t_m, t_{m+1})} \sum_{m=1}^p \frac{1}{t - t_m}, \quad M_5 = \max_{m=1,p} \max_{t \in [t_m, t_{m+1}]} |a(t)|.$$

Continuing this process, similarly to the estimate (31), we obtain

$$\begin{aligned}
& \|\vec{u}_i^{\tau+1}(t) - \vec{u}_i^{\tau}(t)\|_{PC_{B_2}[0,T]} \leq \max_{m=1,p} \sum_{n=1}^{\infty} \max_{t \in [t_m, t_{m+1}]} |u_{i,n}^{\tau}(t) - u_{i,n}^{\tau-1}(t)| \leq \\
& \leq C \max_{m=1,p} \left| \sum_{n=1}^{\infty} \sum_{0 < t_m < t}^p \sup_{t \in (t_m, t_{m+1})} e^{-\lambda_{i,n}(t-t_m)} \int_{-1}^1 N_{m,i}(x) \times \right.
\end{aligned}$$

$$\begin{aligned}
 & \times \left| \int_{-1}^1 G(y) \sum_{j=1}^{\infty} [u_{i,j}^{\tau}(t_m) - u_{i,j}^{\tau-1}(t_m)] \vartheta_{i,j}(y) dy \right| \vartheta_{i,n}(x) dx \Big| + \\
 & + C \max_{m=1,p} \sum_{n=1}^{\infty} \sup_{t \in (t_m, t_{m+1}]} \left| \int_0^t e^{-\lambda_{i,n}(t-s)} a(s) |u_{i,j}^{\tau}(t) - u_{i,j}^{\tau-1}(t)| ds \right| \leq \\
 \leq & C \cdot M_4 \max_{m=1,p} \sum_{n=1}^{\infty} \frac{1}{\lambda_{i,n}} \int_{-1}^1 N_{m,i}(x) \vartheta_{i,n}(x) dx \sum_{j=1}^{\infty} \max_{t \in [t_m, t_{m+1}]} |u_{i,j}^{\tau}(t) - u_{i,j}^{\tau-1}(t)| \left| \int_{-1}^1 G(y) \vartheta_{i,j}(y) dy \right| + \\
 & + C \cdot M_{1,i} \max_{m=1,p} \max_{t \in [t_m, t_{m+1}]} |a(t)| \sum_{n=1}^{\infty} \frac{1}{\lambda_{i,n}} \max_{t \in [t_m, t_{m+1}]} |u_{i,j}^{\tau}(t) - u_{i,j}^{\tau-1}(t)| \leq \\
 \leq & C \cdot M_4 M_{2,i} \|N_i(x)\|_{L_2[-1,1]} \|\vec{u}_i^{\tau}(t) - \vec{u}_i^{\tau-1}(t)\|_{PC_{B_2}[0,T]} \|G(x)\|_{L_2[-1,1]} + \\
 & + C \cdot M_{1,i} M_5 M_{2,i} \|\vec{u}_i^{\tau}(t) - \vec{u}_i^{\tau-1}(t)\|_{PC_{B_2}[0,T]} \leq \rho_i \|u_i^{\tau}(t) - u_i^{\tau-1}(t)\|_{PC_{B_2}[0,T]}, \tag{32}
 \end{aligned}$$

where

$$\begin{aligned}
 \rho_i &= C \cdot M_{2,i} [M_4 \|N_i(x)\|_{L_2[-1,1]} \|G(x)\|_{L_2[-1,1]} + M_{1,i} M_5], \\
 \|N_i(x)\|_{L_2[-1,1]} &= \max_{m=1,\dots,p} \|N_{m,i}(x)\|_{L_2[-1,1]}, \quad i = 1, 2.
 \end{aligned}$$

According to (28), $\rho_i < 1$. Consequently, it follows from estimate (32) that the operator on the right-hand side of countable system of nonlinear functional equations (26) is contracting. It follows from estimates (30)–(32) that there is the unique fixed point, which is a solution to the countable system of functional equations (26) in space $PC_{B_2}[0, T]$. Theorem 1 is proved. \square

4. Uniform convergence of the Fourier series

Theorem 2. Let the conditions of the Theorem 1 be fulfilled. Then the unknown function $U(t, x) = U_1(t, x) + U_2(t, x)$ of the mixed impulsive problem (1)–(4) is determined by the Fourier series (27). The series (27) are convergent on the domain Ω .

Proof. Let $\vec{u}_i(t) \in PC_{B_2}[0, T]$ be the unique solution of the countable system (26). As in the case of estimates (30) and (31), we obtain

$$\begin{aligned}
 |U_i(t, x)| &\leq \sum_{n=1}^{\infty} |\vartheta_{i,n}(x)| \left[\sum_{l=1}^{\infty} |\varphi_{i,n}| e^{-\lambda_{i,n}t} + \right. \\
 & \left. + \sum_{n=1}^{\infty} \left| \int_0^t e^{-\lambda_{i,n}(t-s)} \int_{-1}^1 f_i(s, x) \vartheta_{i,n}(x) dx ds \right| + \right. \\
 & \left. + \sum_{n=1}^{\infty} \max_{t \in [t_m, t_{m+1}]} \left| \sum_{0 < t_m < t} e^{-\lambda_{i,n}(t-t_m)} \int_{-1}^1 I_{m,i} \left(x, \int_{-1}^1 G(y) \sum_{j=1}^{\infty} u_{i,j}(t_m) \vartheta_{i,j}(y) dy \right) \vartheta_{i,n}(x) dx \right| + \right. \\
 & \left. + C \sum_{n=1}^{\infty} \sup_{t \in (t_m, t_{m+1}]} \left| \int_0^t e^{-\lambda_{i,n}(t-s)} a(s) u_{i,n}(s) ds \right| \right] \leq \\
 & \leq \sum_{n=1}^{\infty} |\varphi_{i,n}| + M_{1,i} \sqrt{\sum_{n=1}^{\infty} \frac{1}{\lambda_{i,n}^2} \max_{m=1,p} \max_{t \in [t_m, t_{m+1}]} \|f_i(t, x)\|_{L_2[-1,1]} +} \\
 & + M_4 \sqrt{\sum_{n=1}^{\infty} \frac{1}{\lambda_{i,n}^2} \max_{m=1,p} \max_{t \in [t_m, t_{m+1}]} \left\| I_{m,i} \left(x, \int_{-1}^1 G(y) \sum_{j=1}^{\infty} u_{i,j}(t) \vartheta_{i,j}(y) dy \right) \right\|_{L_2[-1,1]} +} \\
 & + C \cdot M_{1,i} M_5 \sqrt{\sum_{n=1}^{\infty} \frac{1}{\lambda_{i,n}^2} \|\vec{u}_i(t)\|_{PC_{B_2}[0,T]}^2} < \infty. \tag{33}
 \end{aligned}$$

Due to the estimate (33) one obtains the absolute and uniform convergence of the series (27). Theorem 2 is proved. \square

5. Conclusion

Neutron diffusion plays a significant role in the operation of nuclear reactors. The diffusion equation makes it possible to calculate the neutron density inside the core of a nuclear reactor, the neutron flux from the moderator surface, and the reflection and transmission of neutrons by biological protection structures.

In the domain $\Omega = \{t \in (0, T), t \neq t_m, 0 < t_m < T, m = 1, 2, \dots, p, x \in (-1, 1)\}$, we consider a parabolic type linear differential equation (1) of neutron diffusion in the presence of neutron absorption by the atomic nucleus with nonlinear impulsive effects and involution. The Dirichlet boundary value conditions, initial value condition and nonlinear impulsive conditions are used in solving the mixed problem.

The countable system of nonlinear functional equations (26) is obtained. Theorem 1 on unique solvability of countable system of nonlinear functional integral equations (26) is proved. The Picar iteration process is constructed. The generalized solution of the mixed problem (1)–(4) is obtained in the form of the Fourier series (27). The uniform convergence of the Fourier series (27) is proved (Theorem 2). Note that the Fourier series (27) characterizes the neutron density function with the first kind discontinuities. The results of this work will make it possible to determine the neutron density inside the core of a nuclear reactor and its change in the presence of a moderator and reflectors.

Moreover, the results obtained in this work will allow us to investigate direct and inverse problems for other kinds of partial differential equations of mathematical physics with impulsive actions. Differential equations with impulsive effects often allow one to reveal common features of phenomena in different branches of science. In [29], impulsive differential equations are used for solving boundary value problems on time scales. In [30], impulsive differential equations are used in studying pulse mass measles vaccination across age cohorts. In [38], impulsive differential equations are used in studying biological problems. Parabolic type differential equations as the heat equations or as the diffusion equations have different applications. In [14], the problem of fast forward evolution of the processes described in terms of the heat equation is considered. The matter is considered on an adiabatically expanding time-dependent box. Attention is paid to acceleration of heat transfer processes. As the physical implementation, the heat transport in harmonic crystals is considered.

References

- [1] Blinova I.V., Grishanov E.N., Popov A.I., Popov I.Y., Smolkina M.O. On spin flip for electron scattering by several delta-potentials for 1D Hamiltonian with spin-orbit interaction. *Nanosystems: Phys. Chem. Math.*, 2023, **14**(4), P. 413–417.
- [2] Deka H., Sarma J. A numerical investigation of modified Burgers' equation in dusty plasmas with non-thermal ions and trapped electrons. *Nanosystems: Phys. Chem. Math.*, 2023, **14**(1), P. 5–12.
- [3] Dweik J., Farhat H., Younis J. The Space Charge Model. A new analytical approximation solution of Poisson-Boltzmann equation: the extended homogeneous approximation. *Nanosystems: Phys. Chem. Math.*, 2023, **14**(4), P. 428–437.
- [4] Fedorov E.G., Popov I.Yu. Analysis of the limiting behavior of a biological neurons system with delay. *J. Phys.: Conf. Ser.*, 2021, **2086**, P. 012109.
- [5] Fedorov E.G., Popov I.Yu. Hopf bifurcations in a network of Fitzhugh-Nagumo biological neurons. *International Journ. Nonlinear Sciences and Numerical Simulation*, 2021.
- [6] Fedorov E.G. Properties of an oriented ring of neurons with the FitzHugh-Nagumo model. *Nanosystems: Phys. Chem. Math.*, 2021, **12**(5), P. 553–562.
- [7] Irgashev B.Yu. Boundary value problem for a degenerate equation with a Riemann-Liouville operator. *Nanosystems: Phys. Chem. Math.*, 2023, **14**(5), P. 511–517.
- [8] Kuljanov U.N. On the spectrum of the two-particle Schrödinger operator with point potential: one dimensional case. *Nanosystems: Phys. Chem. Math.*, 2023, **14**(5), P. 505–510.
- [9] Parkash C., Parke W.C., Singh P. Exact irregular solutions to radial Schrödinger equation for the case of hydrogen-like atoms. *Nanosystems: Phys. Chem. Math.*, 2023, **14**(1), P. 28–43.
- [10] Popov I.Y. A model of charged particle on the flat Möbius strip in a magnetic field. *Nanosystems: Phys. Chem. Math.*, 2023, **14**(4), P. 418–420.
- [11] Sibatov R.T., Svetukhin V.V. Subdiffusion kinetics of nanoprecipitate growth and destruction in solid solutions. *Theor. Math. Phys.*, 2015, **183**, P. 846–859.
- [12] Vatutin A.D., Miroshnichenko G.P., Trifanov A.I. Master equation for correlators of normalordered field mode operators. *Nanosystems: Phys. Chem. Math.*, 2022, **13**(6), P. 628–631.
- [13] Uchaikin V.V., Sibatov R.T. Fractional kinetics in solids: Anomalous charge transport in semiconductors, dielectrics and nanosystems. CRC Press, Boca Raton, FL, 2013.
- [14] Matrasulov J., Yusupov J.R., Saidov A.A. Fast forward evolution in heat equation: Tunable heat transport in adiabatic regime. *Nanosystems: Phys. Chem. Math.*, 2023, **14**(4), P. 421–427.
- [15] Galaktionov V.A., Mitidieri E., Pohozaev S. Global sign-changing solutions of a higher order semilinear heat equation in the subcritical Fujita range. *Advanced Nonlinear Studies*, 2012, **12**(3), P. 569–596.
- [16] Galaktionov V.A., Mitidieri E., Pohozaev S.I. Classification of global and blow-up sign-changing solutions of a semilinear heat equation in the subcritical Fujita range: second-order diffusion. *Advanced Nonlinear Studies*, 2014, **14**(1), P. 1–29.
- [17] Denk R., Kaip M. Application to parabolic differential equations. In: General Parabolic Mixed Order Systems in L_p and Applications. Operator Theory: Advances and Applications, **239**. Birkhäuser, Cham., 2013.
- [18] Van Dorsselaer H., Lubich C. Inertial manifolds of parabolic differential equations under high-order discretizations. *Journ. of Numer. Analysis*, 1999, **19**(3), P. 455–471.
- [19] Ivanchov N.I. Boundary value problems for a parabolic equation with integral conditions. *Differen. Equat.*, 2004, **40**(4), P. 591–609.
- [20] Mulla M., Gaweash A., Bakur H. Numerical solution of parabolic in partial differential equations (PDEs) in one and two space variable. *Journ. Applied Math. and Phys.*, 2022, **10**(2), P. 311–321.
- [21] Nguyen H., Reynen J. A space-time least-square finite element scheme for advection-diffusion equations. *Computer Methods in Applied Mech. and Engin.*, 1984, **42**(3), P. 331–342.

- [22] Pinkas G. Reasoning, nonmonotonicity and learning in connectionist networks that capture propositional knowledge. *Artificial Intelligence*, 1995, **77**(2), P. 203–247.
- [23] Pohozaev S.I. On the dependence of the critical exponent of the nonlinear heat equation on the initial function. *Differ. Equat.*, 2011, **47**(7), P. 955–962.
- [24] Pokhozhaev S.I. Critical nonlinearities in partial differential equations. *Russ. J. Math. Phys.*, 2013, **20** (4), P. 476–491.
- [25] Yuldashev T.K. Mixed value problem for a nonlinear differential equation of fourth order with small parameter on the parabolic operator. *Comput. Math. Math. Phys.*, 2011, **51** (9), P. 1596–1604.
- [26] Yuldashev T.K. Mixed value problem for nonlinear integro-differential equation with parabolic operator of higher power. *Comput. Math. Math. Phys.*, 2012, **52**(1), P. 105–116.
- [27] Yuldashev T.K. Nonlinear optimal control of thermal processes in a nonlinear Inverse problem. *Lobachevskii Journ. Math.*, 2020, **41**(1), P. 124–136.
- [28] Zonga Y., Heb Q., Tartakovsky A.M. Physics-informed neural network method for parabolic differential equations with sharply perturbed initial conditions. *arXiv:2208.08635[math.NA]*, 2022, P. 1–50.
- [29] Agarwal R.P., O'Regan D., Triple solutions to boundary value problems on time scales. *Applied Mathematics Letters*, 2000, **13**(4), P. 7–11.
- [30] Agur Z., Cojocar L., Mazaur G., Anderson R.M., Danon Y.L. Pulse mass measles vaccination across age cohorts. *Proceedings of the National Academy of Sciences of the USA*, 1993, **90**, P. 11698–11702.
- [31] Benchohra M., Henderson J., Ntouyas S.K. *Impulsive differential equations and inclusions. Contemporary mathematics and its application*. Hindawi Publishing Corporation, New York, 2006.
- [32] Catlla J., Schaeffer D.G., Witelski Th.P., Monson E.E., Lin A.L. On spiking models for synaptic activity and impulsive differential equations. *SIAM Review*, 2008, **50**(3), P. 553–569.
- [33] Halanay A., Veksler D. *Qualitative theory of impulsive systems*. Mir, Moscow, 1971, 309 p. (in Russian).
- [34] Lakshmikantham V., Bainov D.D., Simeonov P.S. *Theory of impulsive differential equations*. World Scientific, Singapore, 1989, 434 p.
- [35] Milman V.D., Myshkis A.D. On the stability of motion in the presence of impulses. *Sibirskiy Matemat. Zhurnal*, 1960, **1**(2), P. 233–237.
- [36] Perestyk N.A., Plotnikov V.A., Samoilenko A.M., Skripnik N.V. *Differential equations with impulse effect: multivalued right-hand sides with discontinuities*. DeGruyter Stud. 40, Math. Walter de Gruyter Co., Berlin, 2011.
- [37] Samoilenko A.M., Perestyk N.A. *Impulsive differential equations*. World Sci., Singapore, 1995.
- [38] Stamova I., Stamov G. Impulsive biological models. In: *Applied impulsive mathematical models. CMS Books in Mathematics*. Springer, Cham., 2016.
- [39] Anguraj A., Arjunan M.M. Existence and uniqueness of mild and classical solutions of impulsive evolution equations. *Elect. J. of Differen. Equat.*, 2005, **2005**(111), P. 1–8.
- [40] Antunes D., Hespanha J., Silvestre C. Stability of networked control systems with asynchronous renewal links: An impulsive systems approach. *Automatica*, 2013, **49**(2), P. 402–413.
- [41] Bai Ch., Yang D. Existence of solutions for second-order nonlinear impulsive differential equations with periodic boundary value conditions. *Boundary Value Problems (Hindawi Publishing Corporation)*, 2007, **2007**(41589), P. 1–13.
- [42] Bin L., Xinzhi L., Xiaoxin L. Robust global exponential stability of uncertain impulsive systems. *Acta Mathematica Scientia*, 2005, **25**(1), P. 161–169.
- [43] Benchohra M., Salimani B.A. Existence and uniqueness of solutions to impulsive fractional differential equations. *Elect. Journ. Differen. Equat.*, 2009, **2009**(10), P. 1–11.
- [44] Chen J., Tisdell Ch.C., Yuan R. On the solvability of periodic boundary value problems with impulse. *J. of Math. Anal. and Appl.*, 2007, **331**, P. 902–912.
- [45] Fecken M., Zhong Y., Wang J. On the concept and existence of solutions for impulsive fractional differential equations. *Communications in Non-Linear Science and numerical Simulation*, 2012, **17**(7), P. 3050–3060.
- [46] Mardanov M.J., Sharifov Ya.A., Habib M.H. Existence and uniqueness of solutions for first-order nonlinear differential equations with two-point and integral boundary conditions. *Electr. J. of Differen. Equat.*, 2014, **2014**(259), P. 1–8.
- [47] Yuldashev T.K., Fayziyev A.K. On a nonlinear impulsive system of integro-differential equations with degenerate kernel and maxima. *Nanosystems: Phys. Chem. Math.*, 2022, **13**(1), P. 36–44.
- [48] Yuldashev T.K., Fayziyev A.K. Integral condition with nonlinear kernel for an impulsive system of differential equations with maxima and redefinition vector. *Lobachevskii Journ. Math.*, 2022, **43**(8), P. 2332–2340.
- [49] Yuldashev T.K., Fayziyev A.K. Inverse problem for a second order impulsive system of integro-differential equations with two redefinition vectors and mixed maxima. *Nanosystems: Phys. Chem. Math.*, 2023, **14**(1), P. 13–21.
- [50] Gao Z., Yang L., Liu G. Existence and uniqueness of solutions to impulsive fractional integro-differential equations with nonlocal conditions. *Applied Mathematics*, 2013, **4**(6), P. 859–863.
- [51] Cooke C.H., Kroll J. The existence of periodic solutions to certain impulsive differential equations. *Computers and Mathematics with Applications*, 2002, **44**(5-6), P. 667–676.
- [52] Li X., Bohner M., Wang C.-K. Impulsive differential equations: Periodic solutions and applications. *Automatica*, 2015, **52**, P. 173–178.
- [53] Yuldashev T.K. Periodic solutions for an impulsive system of nonlinear differential equations with maxima. *Nanosystems: Phys. Chem. Math.*, 2022, **13**(2), P. 135–141.
- [54] Yuldashev T.K. Periodic solutions for an impulsive system of integro-differential equations with maxima. *Vestnik Sam. Gos. Universiteta. Seria: Fiz.-Mat. Nauki*, 2022, **26**(2), P. 368–379.
- [55] Yuldashev T.K., Sulaimonov F.U. Periodic solutions of second order impulsive system for an integro-differential equations with maxima. *Lobachevskii Journ. Math.*, 2022, **43**(12), P. 3674–3685.
- [56] Fayziyev A.K., Abdullozhonova A.N., Yuldashev T.K. Inverse problem for Whitham type multi-dimensional differential equation with impulse effects. *Lobachevskii Journ. Math.*, 2023, **44**(2), P. 570–579.
- [57] Yuldashev T.K., Fayziyev A.K. Determination of the coefficient function in a Whitham type nonlinear differential equation with impulse effects. *Nanosystems: Phys. Chem. Math.*, 2023, **14**(3), P. 312–320.
- [58] Yuldashev T.K., Ergashev T.G., Fayziyev A.K. Coefficient inverse problem for Whitham type two-dimensional differential equation with impulse effects. *Chelyab. Fiz.-Mat. Zhurn.*, 2023, **8**(2), P. 238–248.

Information about the authors:

Tursun K. Yuldashev – Tashkent State University of Economics, Karimov street, 49, TSUE, Tashkent, 100066, Uzbekistan;
ORCID 0000-0002-9346-5362; t.yuldashev@tsue.uz

Aziz K. Fayziyev – Tashkent State University of Economics, Karimov street, 49, TSUE, Tashkent, 100066, Uzbekistan;
ORCID 0000-0001-6798-3265; fayziyev.a@inbox.ru

Conflict of interest: the authors declare no conflict of interest.

Photon antibunching in sixth harmonic generation

Rupesh Singh^{1,a}, Dilip Kumar Giri^{2,b}¹Department of Physics, D.A.V. Public School, Koylanagar, Dhanbad, Jharkhand, India²University Department of Physics, Binod Bihari Mahto Koyalanchal University, Dhanbad, Jharkhand, India^arupesh.dav2021@gmail.com, ^bdilipkumargiri@gmail.com

Corresponding author: Rupesh Singh, rupesh.dav2021@gmail.com

PACS 42.50.Dv, 42.50.Lc, 42.65.Dr, 42.65.Ky

ABSTRACT We studied photon antibunching in the pump and the harmonic modes of the sixth harmonic generation process. The generalized interaction Hamiltonian is solved for several particular cases in the Heisenberg picture, and the possibility of observing photon antibunching is investigated using the short-time approximation technique. It is shown that the photon antibunching in the pump field depends on the number of pump photons, the interaction time, and the coupling of the field between the modes. With the same amount of pump photons, we deduced that third-order photon antibunching is more nonclassical than second- and first-order photon antibunching. In this process, the effect of photon antibunching is not seen in the harmonic mode over pump mode. It is shown that photon antibunching is more noticeable with shorter interaction times as the depth of nonclassicality increases and the second-order correlation function decreases. The first-order Hamiltonian interaction, which stimulates both pump and harmonic fields, is demonstrated to be more nonclassical than the second-order Hamiltonian interaction. It is clear that the coherent state, or vacuum state, of a pump field with a nonzero harmonic field creates photon clusters because the pump field causes interaction, which leads to bunching effects. It is interpreted that the degree of photon antibunching is maximum in the regions where the second correlation function is minimum. Photon antibunching has been shown to be one of the quantum properties of light.

KEYWORDS photon antibunching, higher-order antibunching, sixth harmonic generation, photon number operator, short-time approximation

ACKNOWLEDGEMENTS We would like to thank the referee for his comments and valuable suggestions.

FOR CITATION Rupesh Singh, Dilip Kumar Giri Photon antibunching in sixth harmonic generation. *Nanosystems: Phys. Chem. Math.*, 2024, **15** (2), 170–183.

1. Introduction

Photon antibunching [1–10], a nonclassical phenomenon [11–14], is currently of considerable interest in the context of quantum teleportation [15, 16], quantum computation [17–21], and quantum cryptography [22–24] by utilizing a single-photon source as unconditional security [25–28]. Single-photon sources are photon sources that emit photons as single particles or photons. This gives rise to an effective one-photon number state, which means that the chance of making one photon is higher than the chance of making two, three, four, or more photons at the same time. In the antibunched state, the rate of emitting two or more photons at the same time is lower than in the single-photon state. This means that it is more likely to find a source of a single photon than a source of two or more photons in a bunch. The second-order temporal coherence, $g^{(2)}(\tau)$, is the standard way to measure the quality of a single-photon source when the time delay is set to zero ($\tau = 0$) [26–28]. $g^{(2)}(0) = 0$ for a perfect source that never sends out more than one photon at a time. In his research, Stoler [1] introduced the concept of photon antibunching generation and outlined methods for observing it. Many authors [2–9] have previously centered their research on photon antibunching in various nonlinear optical systems. In addition, Lee created the notion of higher-order antibunching in 1990 [29, 30] when he proposed the first higher-order antibunching criterion. Ba An [31] and Pathak et al. [32] modified Lee's criterion, respectively. As stated by Gupta et al. [33] in detail, higher-order antibunching is not an unusual phenomenon; rather, it can be observed in numerous simple nonlinear optical processes, such as the six-wave mixing process, the four-wave mixing process, and the second harmonic generation. Antibunching occurs in pump modes, which lose energy, whereas bunching manifests in harmonic modes, which gain energy from the pump, and vice versa: as energy decreases, noise increases [34–36]. All the models studied here are experimentally realizable [37, 38], and the criteria for higher-order antibunching appear in terms of the factorial moment, which can be measured using homodyne photon counting experiments [37–40]. As a result, it is straightforward to experimentally validate the theoretical predictions of this study in the sixth harmonic generation process. In essence, all of the aforementioned simple physical models are readily observable and empirically realizable in any nonlinear optics laboratory. In addition, higher-order antibunching has been extensively studied and

published in several optical processes [41–45] in the past few years. Dell’Anno et al. [46] gave a study of the theoretical and experimental properties of multiphoton quantum optics. In this research, they offer a consistent generalization of multiphoton events and a Hamiltonian description of higher-order nonlinear multiphoton phenomena. Combining linear and nonlinear optical devices, according to their theory, enables the realization of multiphoton nonclassical states of the electromagnetic field in discrete or continuous variables, which have applications in quantum computation, quantum teleportation, and other quantum communication and information problems. As a result, it creates new avenues for investigating higher-order nonclassical effects.

The objective of this paper is to investigate the feasibility of photon antibunching in sixth harmonic generation. The structure of the paper is as follows: The criterion of photon antibunching is defined in Section 2. In Section 3, the degenerate sixth harmonic generation model and its Hamiltonian are described. In sections 3.1 and 3.2, respectively, we establish the analytic expression of photon antibunching in the pump mode up to first- and second-order Hamiltonian interactions in the sixth harmonic generation. Photon antibunching in the harmonic mode up to first- and second-order Hamiltonian interactions are studied in sixth harmonic generation, respectively, in Sections 3.3 and 3.4. Section 4 describes the second correlation function in terms of the number of photons. Section 5 contains the results and discussion. In Section 6, we finish and summarize the paper.

2. Definition of photon antibunching

A criterion for single-mode photon antibunching, in general, proposed by Lee [29, 30], as

$$\hat{R}(l, m) = \frac{\langle \hat{N}_x^{(l+1)} \rangle \langle \hat{N}_x^{(m-1)} \rangle - \langle \hat{N}_x^{(l)} \rangle \langle \hat{N}_x^{(m)} \rangle}{\langle \hat{N}_x^{(l)} \rangle \langle \hat{N}_x^{(m)} \rangle} < 0. \tag{1}$$

where $\langle \dots \rangle$ denotes the quantum average, x denotes modes of the field, l , and m are integers that satisfying the conditions $l \geq m \geq 1$ and \hat{N} is the photon number operator, where $\hat{N}_x^l = \prod_{j=0}^{l-1} (\hat{N}_x - j)$ is the j^{th} factorial moment of the photon number operator.

Equation (1) reduces by using $l = m = 1$, i.e. for first-order photon antibunching [31], as

$$\langle \hat{N}_x^{(2)} \rangle < \langle \hat{N}_x \rangle^2. \tag{2}$$

and the inequality yields

$$\langle (\Delta \hat{N}_x)^2 \rangle \equiv \langle \hat{N}_x^{(2)} \rangle - \langle \hat{N}_x \rangle^2 < \langle \hat{N}_x \rangle. \tag{3}$$

If $l \geq m = 1$ then equation (1) reduces for l^{th} -order photon antibunching for mode x , as

$$\langle \hat{N}_x^{(l+1)} \rangle < \langle \hat{N}_x^{(l)} \rangle \langle \hat{N}_x \rangle \tag{4}$$

Further, Pathak et al. [32] simplified equation (4) as

$$\langle \hat{N}_x^{(l+1)} \rangle < \langle \hat{N}_x^{(l)} \rangle \langle \hat{N}_x \rangle < \langle \hat{N}_x^{(l-1)} \rangle \langle \hat{N}_x \rangle^2 < \langle \hat{N}_x^{(l-2)} \rangle \langle \hat{N}_x \rangle^3 < \dots < \langle \hat{N}_x \rangle^{l+1}. \tag{5}$$

and the criterion for l^{th} -order photon antibunching becomes as

$$d(l) = [\Delta \hat{N}_x]^{l+1} = \langle \hat{N}_x^{(l+1)} \rangle - \langle \hat{N}_x \rangle^{l+1} < 0. \tag{6}$$

Criterion in equation (6) is precisely the property required of a probabilistic single photon source in quantum cryptography [41].

3. Degenerate sixth harmonic generation model and its Hamiltonian

The absorption of six pump photons of frequency ω_1 each interacts with a nonlinear medium in this model, as shown in Fig. 1, with the subsequent emission of one harmonic photon of frequency ω_2 with the atomic system to the ground state.

From Fig. 1, the corresponding interaction Hamiltonian is

$$\hat{H} = \hbar\omega_1 \hat{a}^\dagger \hat{a} + \hbar\omega_2 \hat{b}^\dagger \hat{b} + g (\hat{a}^6 \hat{b}^\dagger + \hat{a}^{\dagger 6} \hat{b}). \tag{7}$$

where $\hat{a}^\dagger(\hat{a})$ and $\hat{b}^\dagger(\hat{b})$ are the creation (annihilation) operators of the pump field (\hat{A} -mode) and harmonic field (\hat{B} -mode) respectively. In the interaction Hamiltonian, g is the interaction rate between the modes. It is assumed to be real, depicting the interaction between the two modes at a rate of 10^2 – 10^4 per second and proportional to the nonlinear susceptibility of the medium and the complex amplitude of the pump field [47, 48].

In this interaction, due to the fact that the time dependence of free modes ($g = 0$) is proportional to $\exp(i\omega_1 t)$ or $\exp(i\omega_2 t)$. The interaction between modes ($g \neq 0$) causes a slower dependence on time and therefore, the field operators

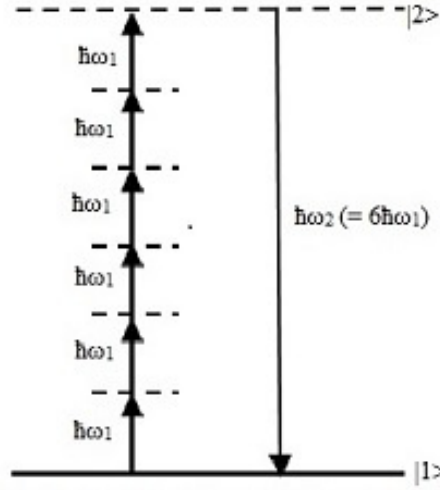


FIG. 1. Sixth harmonic generation model

may be expressed as $\hat{A} = \hat{a} \exp(i\omega_1 t)$ and $\hat{B} = \hat{b} \exp(i\omega_2 t)$ with the relation at frequency $\omega_2 = 6\omega_1$, where the operators $\hat{A}(t)$ and $\hat{B}(t)$ are vary slowly in time. Later, it will be clear that $\hat{A}(t)$ and $\hat{B}(t)$ indeed depend on a scaled time “ gt ” (rather than on t), thus satisfying their slow variation of the operators $\hat{A}(t)$ and $\hat{B}(t)$ as compared to fast variation of $\hat{a}(t)$ and $\hat{b}(t)$, since $g \ll \omega_1, \omega_2$ usually [47–49].

As operators represent observables, their time evolution directly corresponds to the changes in these observables over time. In order to study the characteristics of nonclassical states of light, like quadrature fluctuations, which are directly tied to observable quantities, utilise the complete Heisenberg picture, where all operators evolve based on the total Hamiltonian of the system. Thus, using equation (7) in Heisenberg equation of motion of slowing varying operator in the fundamental mode \hat{A} ,

$$\dot{\hat{A}} = \frac{\partial \hat{A}}{\partial t} + i [\hat{H}, \hat{A}], \quad (\hbar = 1), \quad (8)$$

we obtain

$$\dot{\hat{A}} = -6ig\hat{A}^{\dagger 5}\hat{B}. \quad (9)$$

Furthermore, we have used equation (8) to calculate the second order derivative of the pump mode, as

$$\ddot{\hat{A}} = \frac{\partial \dot{\hat{A}}}{\partial t} + i [\hat{H}, \dot{\hat{A}}]. \quad (10)$$

Using equations (8) and (9), one transforms equation (10) to the form

$$\ddot{\hat{A}} = 6|g|^2 \left[30(\hat{A}^{\dagger 4}\hat{A}^5 + 10\hat{A}^{\dagger 3}\hat{A}^4 + 40\hat{A}^{\dagger 2}\hat{A}^3 + 60\hat{A}^{\dagger}\hat{A}^2 + 24A)\hat{B}^{\dagger}\hat{B} - \hat{A}^{\dagger 5}\hat{A}^6 \right]. \quad (11)$$

We use the Taylor series in the expansion of $A(t)$ for short-time ($\approx 10^{-10}$ sec), $|gt| \ll 1$ [45, 49] and keep terms up to the second order in ‘ gt ’,

$$\hat{A}(t) = \hat{A}(0) + \dot{\hat{A}}(t) + \ddot{\hat{A}} \left(\frac{t^2}{2!} \right) + \dots \quad (12)$$

Inserting equations (9) and (11) in equation (12), we obtain

$$\hat{A}(t) = \hat{A} - 6i|gt|\hat{A}^{\dagger 5}\hat{B} + 3|gt|^2 \left[30(\hat{A}^{\dagger 4}\hat{A}^5 + 10\hat{A}^{\dagger 3}\hat{A}^4 + 40\hat{A}^{\dagger 2}\hat{A}^3 + 60\hat{A}^{\dagger}\hat{A}^2 + 24A)\hat{B}^{\dagger}\hat{B} - \hat{A}^{\dagger 5}\hat{A}^6 \right] \quad (13)$$

and in the reversal order,

$$\hat{A}^{\dagger}(t) = \hat{A}^{\dagger} + 6i|gt|\hat{A}^5\hat{B}^{\dagger} + 3|gt|^2 \left[30(\hat{A}^{\dagger 5}\hat{A}^4 + 10\hat{A}^{\dagger 4}\hat{A}^3 + 40\hat{A}^{\dagger 3}\hat{A}^2 + 60\hat{A}^{\dagger 2}\hat{A} + 24A^{\dagger})\hat{B}^{\dagger}\hat{B} - \hat{A}^{\dagger 6}\hat{A}^5 \right], \quad (14)$$

where $\hat{A}(0) = \hat{A}$ at $t = 0$.

Now, using equation (7) in Heisenberg equation of motion of the harmonic mode \hat{B} ,

$$\dot{\hat{B}} = \frac{\partial \hat{B}}{\partial t} + i [\hat{H}, \hat{B}], \quad (15)$$

we obtain

$$\dot{\hat{B}} = -ig\hat{A}^6. \quad (16)$$

For second order derivative of \hat{B} we utilize equation (16) in the Heisenberg differential equation,

$$\ddot{\hat{B}} = \frac{\partial \dot{\hat{B}}}{\partial t} + i [\hat{H}, \dot{\hat{B}}] \quad (17)$$

Then, we have,

$$\ddot{\hat{B}} = -6 |g|^2 [6\hat{A}^{\dagger 5}\hat{A}^5 + 75\hat{A}^{\dagger 4}\hat{A}^4 + 400\hat{A}^{\dagger 3}\hat{A}^3 + 900\hat{A}^{\dagger 2}\hat{A}^2 + 720\hat{A}^{\dagger}\hat{A} + 120]\hat{B} \quad (18)$$

We use the Taylor series expansion in the harmonic mode for short-time (10^{-10} sec) and maintain terms up to the second order in 'gt' ($|gt| \ll 1$) as

$$\hat{B}(t) = \hat{B}(0) + \dot{\hat{B}}(t) + \ddot{\hat{B}} \left(\frac{t^2}{2!} \right) + \dots \quad (19)$$

Using equations (16) and (18) in equation (19), we get

$$\hat{B}(t) = \hat{B} - i |gt| \hat{A}^6 - 3 |gt|^2 [6\hat{A}^{\dagger 5}\hat{A}^5 + 75\hat{A}^{\dagger 4}\hat{A}^4 + 400\hat{A}^{\dagger 3}\hat{A}^3 + 900\hat{A}^{\dagger 2}\hat{A}^2 + 720\hat{A}^{\dagger}\hat{A} + 120]\hat{B} \quad (20)$$

and its Hermitian conjugate

$$\hat{B}^{\dagger}(t) = \hat{B}^{\dagger} + i |gt| \hat{A}^{\dagger 6} - 3 |gt|^2 [6\hat{A}^{\dagger 5}\hat{A}^5 + 75\hat{A}^{\dagger 4}\hat{A}^4 + 400\hat{A}^{\dagger 3}\hat{A}^3 + 900\hat{A}^{\dagger 2}\hat{A}^2 + 720\hat{A}^{\dagger}\hat{A} + 120]\hat{B}^{\dagger} \quad (21)$$

3.1. Photon antibunching in the pump field up to first-order Hamiltonian interaction

Now, we assume an initial quantum state as a product of coherent states $|\alpha\rangle$ for the pump mode \hat{A} and $|\beta\rangle$ for the harmonic mode \hat{B} , i.e.

$$|\psi\rangle = |\alpha\rangle_A |\beta\rangle_B \quad (22)$$

Using the condition of equation (22) in equation (13) and (14), we arrive at

$$\langle \psi | \hat{A}(t) | \psi \rangle = \langle \psi | \left(\hat{A} - 6i |gt| \hat{A}^{\dagger 5} \hat{B} \right) | \psi \rangle \quad (23)$$

and

$$\langle \psi | \hat{A}^{\dagger}(t) | \psi \rangle = \langle \psi | \left(\hat{A}^{\dagger} + 6i |gt| \hat{A}^5 \hat{B}^{\dagger} \right) | \psi \rangle \quad (24)$$

Using equation (23) and (24), the expectation values of the photon number operator $\hat{N}_A(t)$ can be written as

$$\begin{aligned} \langle \psi | \hat{N}_A(t) | \psi \rangle &= \langle \psi | \hat{A}^{\dagger}(t) \hat{A}(t) | \psi \rangle = \langle \psi | \left(\hat{A}^{\dagger} \hat{A} - 6i |gt| (\hat{A}^{\dagger 6} \hat{B} - \hat{A}^6 \hat{B}^{\dagger}) \right) | \psi \rangle \\ &= |\alpha|^2 - 6i |gt| (\alpha^{*6} \beta - \alpha^6 \beta^*) \end{aligned} \quad (25)$$

where $\langle N_A \rangle = \langle \hat{A}^{\dagger} \hat{A} \rangle = |\alpha|^2$ and $\langle N_B \rangle = \langle \hat{B}^{\dagger} \hat{B} \rangle = |\beta|^2$ are the photon number operators in A and B respectively and $\alpha = |\alpha| \exp(i\theta_1)$, $\alpha^* = |\alpha^*| \exp(-i\theta_1)$, $\beta = |\beta| \exp(i\theta_2)$ and $\beta^* = |\beta^*| \exp(-i\theta_2)$; θ_1 and θ_2 are the phase angles; α^* , β^* denote the complex conjugate of α and β , respectively.

Furthermore, the expectation values of the second factorial moment and the squared of the expectation values of the photon number operator $\hat{N}_A(t)$ of equation (25) can be represented respectively, as

$$\langle \psi | \left\langle \hat{N}_A^{(2)}(t) \right\rangle | \psi \rangle = \langle \psi | \hat{A}^{\dagger 2}(t) \hat{A}^2(t) | \psi \rangle = |\alpha|^4 + 12i |gt| (\alpha^* \alpha^7 \beta^* - \alpha^{*7} \alpha \beta) + 30i |gt| (\alpha^6 \beta^* - \alpha^{*6} \beta) \quad (26)$$

and

$$\langle \psi | \left\langle \hat{N}_A(t) \right\rangle^2 | \psi \rangle = \langle \psi | \hat{A}^{\dagger}(t) \hat{A}(t) | \psi \rangle^2 = |\alpha|^4 + 12i |gt| (\alpha^* \alpha^7 \beta^* - \alpha^{*7} \alpha \beta) \quad (27)$$

Therefore, for $l = 1$, the variation of photon number operator between equations (26) and (27) is

$$\begin{aligned} d_A(1) &= \left[\langle \psi | \Delta \hat{N}_A(t) | \psi \rangle \right]^2 = \langle \psi | \hat{N}_A^{(2)}(t) | \psi \rangle - \langle \psi | \hat{N}_A(t) | \psi \rangle^2 \\ &= 30i |gt| (\alpha^6 \beta^* - \alpha^{*6} \beta) = -60 |gt| |\alpha^6 \beta| \{ \sin(6\theta_1 - \theta_2) \} \end{aligned} \quad (28)$$

For optimal photon antibunching, let us take $\theta_1 = \frac{\pi}{12}$ and $\theta_2 = 0$, then equation (28) reduces to

$$d_A(1) = -60 |gt| |\alpha^6 \beta| \quad (29)$$

The right-hand side of equation (29) is negative and satisfies the criterion (6), indicating that first-order photon antibunching exists in the pump mode of the sixth harmonic generation.

Similarly, we use the expectation values of the third factorial moment of the photon number operator $\hat{N}_A(t)$ to investigate one of the classes of higher-order antibunching as a function of time, such as second-order antibunching for $l = 2$ of the fundamental mode,

$$\begin{aligned} \langle \psi | \hat{N}_A^{(3)}(t) | \psi \rangle &= |\alpha|^6 + 18i |gt| |\alpha|^4 \alpha^6 \beta^* + 90i |gt| |\alpha|^2 \alpha^6 \beta^* + 120i |gt| \alpha^6 \beta^* \\ &\quad - 18i |gt| |\alpha|^4 \alpha^{*6} \beta - 90i |gt| |\alpha|^2 \alpha^{*6} \beta - 120i |gt| \alpha^{*6} \beta \end{aligned} \quad (30)$$

and cubed of the expectation values of the photon number operator $\hat{N}_A(t)$ is

$$\langle \psi | \hat{N}_A(t) | \psi \rangle^3 = |\alpha|^6 + 18i |gt| |\alpha|^4 \alpha^6 \beta^* - 18i |gt| |\alpha|^4 \alpha^{*6} \beta \quad (31)$$

Hence, the variance in photon number is

$$\begin{aligned} d_A(2) &= \langle \psi | \hat{N}_A^3(t) | \psi \rangle - \langle \psi | \hat{N}_A(t) | \psi \rangle^3 = 30i |gt| (\alpha^6 \beta^* - \alpha^{*6} \beta) (3|\alpha|^2 + 4) \\ &= -60 |gt| |\alpha^6 \beta| \{ \sin(6\theta_1 - \theta_2) \} (3|\alpha|^2 + 4) \end{aligned} \quad (32)$$

Using $\theta_1 = \frac{\pi}{12}$ and $\theta_2 = 0$ in equation (32) then the maximum variance in photon number is

$$d_A(2) = -60 |gt| |\alpha^6 \beta| (3|\alpha|^2 + 4) \quad (33)$$

Equation (33) satisfies equation (6) and is always negative, suggesting that the pump mode of the sixth harmonic generation exhibits second-order photon antibunching.

Subsequently, the expectation values of fourth factorial moment of the photon number operator $\hat{N}_A(t)$ is

$$\begin{aligned} \langle \psi | \hat{N}_A^4(t) | \psi \rangle &= |\alpha|^8 + 24i |gt| |\alpha|^6 \alpha^6 \beta^* + 180i |gt| |\alpha|^4 \alpha^6 \beta^* + 480i |gt| |\alpha|^2 \alpha^6 \beta^* + 360i |gt| \alpha^6 \beta^* \\ &\quad - 24i |gt| |\alpha|^6 \alpha^{*6} \beta - 180i |gt| |\alpha|^4 \alpha^{*6} \beta - 480i |gt| |\alpha|^2 \alpha^{*6} \beta - 360i |gt| \alpha^{*6} \beta \end{aligned} \quad (34)$$

and the fourth power of the expectation values of the photon number operator $\hat{N}_A(t)$ is

$$\langle \psi | \hat{N}_A(t) | \psi \rangle^4 = |\alpha|^8 + 24i |gt| |\alpha|^6 \alpha^6 \beta^* - 24i |gt| |\alpha|^6 \alpha^{*6} \beta \quad (35)$$

For $l = 3$, the variance in photon number can be calculated as,

$$\begin{aligned} d_A(3) &= \langle \psi | \hat{N}_A^4(t) | \psi \rangle - \langle \psi | \hat{N}_A(t) | \psi \rangle^4 = 60i |gt| (\alpha^6 \beta^* - \alpha^{*6} \beta) (3|\alpha|^4 + 8|\alpha|^2 + 6) \\ &= -120 |gt| |\alpha^6 \beta| \{ \sin(6\theta_1 - \theta_2) \} (3|\alpha|^4 + 8|\alpha|^2 + 6) \end{aligned} \quad (36)$$

Substituting $\theta_1 = \frac{\pi}{12}$ and $\theta_2 = 0$ for getting optimal effect of photon antibunching in equation (36) yields:

$$d_A(3) = -120 |gt| |\alpha^6 \beta| (3|\alpha|^4 + 8|\alpha|^2 + 6) \quad (37)$$

Equation (37) satisfies the requirements of equation (6) and verifies the existence of the third-order photon antibunching in the pump mode of the sixth harmonic generation.

3.2. Photon antibunching in the pump field up to second-order Hamiltonian interaction

Now, we assume an initial quantum state as a product of coherent states $|\alpha\rangle$ for the pump mode \hat{A} and $|0\rangle$ for the harmonic mode \hat{B} , i.e.

$$|\psi\rangle = |\alpha\rangle_A |0\rangle_B \quad (38)$$

Using the condition of equation (38) in equation (13) and (14), we obtain

$$\langle \psi | \hat{A}(t) | \psi \rangle = \langle \psi | \left(\hat{A} - 3|gt|^2 \hat{A}^{\dagger 5} \hat{A}^6 \right) | \psi \rangle \quad (39)$$

and

$$\langle \psi | \hat{A}^\dagger(t) | \psi \rangle = \langle \psi | \left(\hat{A}^\dagger - 3|gt|^2 \hat{A}^{\dagger 6} \hat{A}^5 \right) | \psi \rangle \quad (40)$$

Using equations (39) and (40), the expectation values of the photon number operator $\hat{N}_A(t)$ can be expressed as

$$\langle \psi | \hat{N}_A(t) | \psi \rangle = \langle \psi | \hat{A}^\dagger(t) \hat{A}(t) | \psi \rangle = \langle \psi | \left(\hat{A}^\dagger \hat{A} - 6|gt|^2 (\hat{A}^{\dagger 6} \hat{A}^6) \right) | \psi \rangle = |\alpha|^2 - 6|gt|^2 |\alpha|^{12} \quad (41)$$

Furthermore, the expectation values of the second factorial moment and the squared of the expectation values of the photon number operator $\hat{N}_A(t)$ of equation (41) can be represented respectively, as

$$\langle \psi | \left\langle \hat{N}_A^2(t) \right\rangle | \psi \rangle = \langle \psi | \hat{A}^{\dagger 2}(t) \hat{A}^2(t) | \psi \rangle = |\alpha|^4 - 12|gt|^2 |\alpha|^{14} - 30|gt|^2 |\alpha|^{12} \quad (42)$$

and

$$\langle \psi | \left\langle \hat{N}_A(t) \right\rangle^2 | \psi \rangle = \langle \psi | \hat{A}^\dagger(t) \hat{A}(t) | \psi \rangle^2 = |\alpha|^4 - 12|gt|^2 |\alpha|^{14} \quad (43)$$

Hence, the fluctuation of photon number is

$$d'_A(1) = \left[\langle \psi | \Delta \hat{N}_A(t) | \psi \rangle \right]^2 = \langle \psi | \hat{N}_A^2(t) | \psi \rangle - \langle \psi | \hat{N}_A(t) | \psi \rangle^2 = -30|gt|^2 |\alpha|^{12} \quad (44)$$

The fact that the right-hand side of equation (44) is negative and meets the condition of equation (6) indicates that first-order photon antibunching exists in the pump mode of the sixth harmonic generation.

Similarly, we use the expectation values of the third factorial moment of the photon number operator $\hat{N}_A(t)$ to analyze one of the classes of higher-order antibunching, such as second-order antibunching for $l = 2$ of the fundamental/pump mode as a function of time,

$$\langle \psi | \hat{N}_A^{(3)}(t) | \psi \rangle = |\alpha|^6 - 18 |gt|^2 |\alpha|^{16} - 90 |gt|^2 |\alpha|^{14} - 120 |gt|^2 |\alpha|^{12} \quad (45)$$

and cubed of the expectation values of the photon number operator $\hat{N}_A(t)$ is

$$\langle \psi | \hat{N}_A(t) | \psi \rangle^3 = |\alpha|^6 - 18 |gt|^2 |\alpha|^{16} \quad (46)$$

Hence, the variance in photon number is

$$d'_A(2) = \langle \psi | \hat{N}_A^{(3)}(t) | \psi \rangle - \langle \psi | \hat{N}_A(t) | \psi \rangle^3 = -30 |gt|^2 |\alpha|^{12} (3 |\alpha|^2 + 4) \quad (47)$$

Equation (47) is always negative and meets the condition of equation (6), suggesting that the second-order photon antibunching occurs in the pump mode of the sixth harmonic generation.

Subsequently, the expectation values of the fourth factorial moment of the photon number operator $\hat{N}_A(t)$ is

$$\langle \psi | \hat{N}_A^{(4)}(t) | \psi \rangle = |\alpha|^8 - 24 |gt|^2 |\alpha|^{18} - 180 |gt|^2 |\alpha|^{16} - 480 |gt|^2 |\alpha|^{14} - 360 |gt|^2 |\alpha|^{12} \quad (48)$$

and the fourth power of the expectation values of the photon number operator $\hat{N}_A(t)$ is

$$\langle \psi | \hat{N}_A(t) | \psi \rangle^4 = |\alpha|^8 - 24 |gt|^2 |\alpha|^{18} \quad (49)$$

As a result, for $l = 3$, the variance in photon number for third-order antibunching can be calculated as,

$$d'_A(3) = \langle \psi | \hat{N}_A^{(4)}(t) | \psi \rangle - \langle \psi | \hat{N}_A(t) | \psi \rangle^4 = -60 |gt|^2 |\alpha|^{12} (3 |\alpha|^4 + 8 |\alpha|^2 + 6) \quad (50)$$

The criterion of equation (6) is satisfied by equation (50), indicating the presence of the third-order photon antibunching in the pump mode of the sixth harmonic generation.

3.3. Photon antibunching in the harmonic field up to first-order Hamiltonian interaction

Now, we use the condition of equation (22) in equations (20) and (21) for the photon number in the harmonic mode as

$$\hat{N}_B(t) = \hat{B}^\dagger(t) \hat{B}(t) = (\hat{B}^\dagger + igt \hat{A}^{\dagger 6}) (\hat{B} - igt \hat{A}^6) \quad (51)$$

and

$$\langle \psi | \hat{N}_B(t) | \psi \rangle_\alpha = \langle \psi | \hat{B}^\dagger(t) \hat{B}(t) | \psi \rangle_\alpha = \langle \psi | (\hat{B}^\dagger \hat{B} + igt (\hat{A}^{\dagger 6} \hat{B} - \hat{A}^6 \hat{B}^\dagger)) | \psi \rangle_\alpha = |\beta|^2 + igt (\alpha^{*6} \beta - \alpha^6 \beta^*) \quad (52)$$

In addition, the expectation values of the second factorial moment and the squared of the expectation values of the photon number operator $\hat{N}_B(t)$ of equation (52) can be represented respectively, as

$$\langle \psi | \langle \hat{N}_B^{(2)}(t) \rangle | \psi \rangle_\alpha = \langle \psi | \hat{B}^{\dagger 2}(t) \hat{B}^2(t) | \psi \rangle_\alpha = |\beta|^4 + 2igt |\beta|^2 (\alpha^{*6} \beta - \alpha^6 \beta^*) \quad (53)$$

and

$$\langle \psi | \langle \hat{N}_B(t) \rangle^2 | \psi \rangle_\alpha = \langle \psi | \hat{B}^\dagger(t) \hat{B}(t) | \psi \rangle_\alpha^2 = |\beta|^4 + 2igt |\beta|^2 (\alpha^{*6} \beta - \alpha^6 \beta^*) \quad (54)$$

As a result of the first-order antibunching, the fluctuation of photon number in the harmonic mode over pump mode is

$$d_{B\alpha}(1) = \langle \psi | \hat{N}_B^{(2)}(t) | \psi \rangle_\alpha - \langle \psi | \hat{N}_B(t) | \psi \rangle_\alpha^2 = 0 \quad (55)$$

Similarly, the result of the second-order antibunching in the harmonic mode over pump mode is as follows

$$d_{B\alpha}(2) = \langle \psi | \hat{N}_B^{(3)}(t) | \psi \rangle_\alpha - \langle \psi | \hat{N}_B(t) | \psi \rangle_\alpha^3 = 0 \quad (56)$$

where the expectation values of the third factorial moment and cubed of the expectation values of the photon number operator in the harmonic mode $\hat{N}_B(t)$ are

$$\langle \psi | \hat{N}_B^{(3)}(t) | \psi \rangle_\alpha = |\beta|^6 + 3igt |\beta|^4 (\alpha^{*6} \beta - \alpha^6 \beta^*), \quad (57)$$

and

$$\langle \psi | \hat{N}_B(t) | \psi \rangle_\alpha^3 = |\beta|^6 + 3igt |\beta|^4 (\alpha^{*6} \beta - \alpha^6 \beta^*) \quad (58)$$

For equations (55) and (56) there are no normal and the higher-order photon antibunching in the harmonic mode over pump mode in the sixth harmonic generation up to first-order Hamiltonian interaction. In contrast, the coherent state of a pump field with a nonzero harmonic field generates photon clusters. This is due to the fact that the coherent state of the pump field causes interaction, which results in the bunching effects.

3.4. Photon antibunching in the harmonic field up to second-order Hamiltonian interaction

Now, if we assume an initial quantum state as a product of vacuum state $|0\rangle$ for the pump mode \hat{A} and $|\beta\rangle$ for the harmonic mode \hat{B} , i.e.

$$|\psi\rangle_\beta = |0\rangle_A |\beta\rangle_B \quad (59)$$

Using condition of equation (59) in equations (20) and (21) leads to the following result

$$\hat{N}_B(t) = \hat{B}^\dagger(t)\hat{B}(t) = \left(\hat{B}^\dagger - 360|gt|^2\hat{B}^\dagger\right)\left(\hat{B} - 360|gt|^2\hat{B}\right) \quad (60)$$

The expectation value of equation (60) is as follows

$$\langle\psi|\hat{N}_B(t)|\psi\rangle_\beta = \langle\psi|\hat{B}^\dagger(t)\hat{B}(t)|\psi\rangle_\beta = |\beta|^2\left(1 - 720|gt|^2\right) \quad (61)$$

In addition, the expectation values of the second factorial moment and the squared of the expectation values of the photon number operator $\hat{N}_B(t)$ of equation (61) can be represented, respectively, as

$$\langle\psi|\langle\hat{N}_B^{(2)}(t)\rangle|\psi\rangle_\beta = \langle\psi|\hat{B}^{\dagger 2}(t)\hat{B}^2(t)|\psi\rangle_\beta = |\beta|^4\left(1 - 1440|gt|^2\right) \quad (62)$$

and

$$\langle\psi|\langle\hat{N}_B(t)\rangle^2|\psi\rangle_\beta = \langle\psi|\hat{B}^\dagger(t)\hat{B}(t)|\psi\rangle_\beta^2 = |\beta|^4\left(1 - 1440|gt|^2\right) \quad (63)$$

As a result, the variance in photon number i.e. first-order antibunching in the harmonic mode over pump mode is

$$d_{B\beta}(1) = \langle\psi|\hat{N}_B^{(2)}(t)|\psi\rangle_\beta - \langle\psi|\hat{N}_B(t)|\psi\rangle_\beta^2 = 0 \quad (64)$$

Similarly, the result of the second-order antibunching in the harmonic mode over pump mode is as follows

$$d_{B\beta}(2) = \langle\psi|\hat{N}_B^{(3)}(t)|\psi\rangle_\beta - \langle\psi|\hat{N}_B(t)|\psi\rangle_\beta^3 = 0 \quad (65)$$

where the expectation values of the third factorial moment and cubed of the expectation values of the photon number operator $\hat{N}_B(t)$ are

$$\langle\psi|\hat{N}_B^{(3)}(t)|\psi\rangle_\beta = |\beta|^6\left(1 - 2160|gt|^2\right), \quad (66)$$

and

$$\langle\psi|\hat{N}_B(t)|\psi\rangle_\beta^3 = |\beta|^6\left(1 - 2160|gt|^2\right) \quad (67)$$

Equations (64) and (65) do not meet the criteria of equation (6); hence, there is no existence of normal and higher-order photon antibunching in the harmonic mode over pump mode in the sixth harmonic generation up to second-order Hamiltonian interaction. On the other hand, the vacuum state of a pump field with a nonzero harmonic field, results in the photon bunching. This is due to the fact that the vacuum state of the pump field stimulates interaction, producing bunching effects.

4. The photon number correlation $g^2(0)$

Now, consider the second-order correlation function for zero-time delay $g^2(0)$ in terms of photon number. The expression is as follows [10, 12, 27]:

$$g^2(0) = 1 + \frac{\langle(\Delta n)^2\rangle - \langle n\rangle}{\langle n\rangle^2} \quad (68)$$

Substituting the values of equations (25), (27), and (28) with $\theta_1 = \frac{\pi}{12}$ and $\theta_2 = 0$ in equation (68) yields the second-order correlation function or photon number correlation up to the first-order Hamiltonian interaction i.e., dimensionless interaction constant gt , as

$$g^2(0) = 1 + \frac{-60|gt||\alpha^6\beta| - \left(|\alpha|^2 - 12|gt||\alpha^6\beta|\right)}{|\alpha|^4 - 24|gt||\alpha|^2|\alpha^6\beta|} \quad (69)$$

Similarly, using equations (41), (43), and (44), in equation (68), we have the second-order correlation function or photon number correlation up to the second-order Hamiltonian interaction i.e., dimensionless interaction constant $|gt|^2$, as

$$g^2(0)' = 1 + \frac{-30|gt|^2|\alpha|^{12} - \left(|\alpha|^2 - 6|gt|^2|\alpha|^{12}\right)}{|\alpha|^4 - 12|gt|^2|\alpha|^{14}} \quad (70)$$

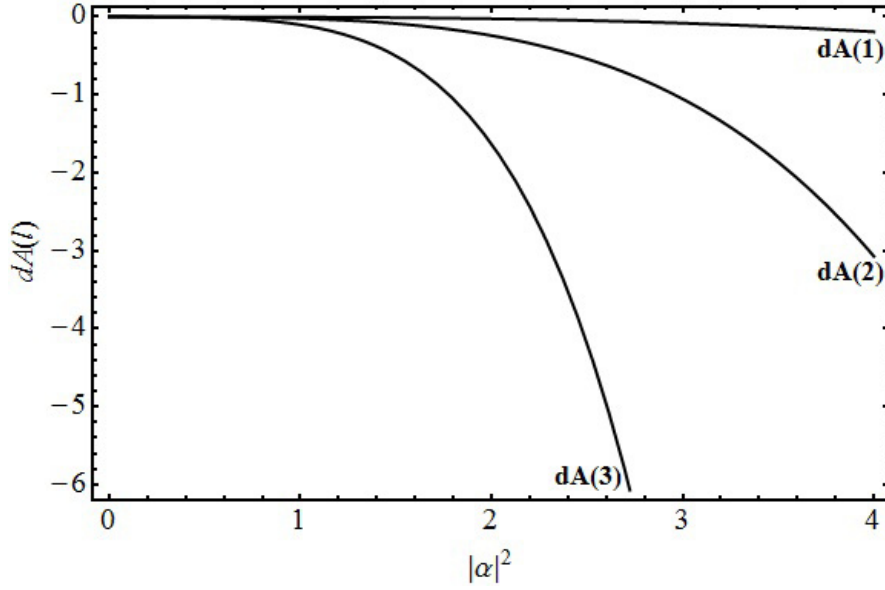


FIG. 2. Degree of photon antibunching $d_A(l)$ with $|\alpha|^2$ of the pump field up to first-order Hamiltonian interaction in sixth harmonic generation (when $|\beta| = 5$ (arbitrarily value) and $|gt| = 10^{-5}$)

5. Results and discussion

We plot a graph (Fig. 2) between the left-hand side of equations (29), (33) and (37) say $d_A(l)$ vs. $|\alpha|^2$ having $|gt| = 10^{-5}$ and $|\beta| = 5$ (any arbitrarily value).

In Fig. 2, the steady fall of the curve shows that the effect of photon antibunching increases nonlinearly with the increase in the number of pump photons $|\alpha|^2$.

This confirms that the photon antibunched states are associated with a large number of pump photons. When the plots in Fig. 2 are compared, we see that the third-order photon antibunching $d_A(3)$ is more nonclassical than the second-order $d_A(2)$ and the first-order $d_A(1)$ photon antibunching with the same number of pump photons. Hence, we inferred that higher-order (third- and second-order) photon antibunching makes it possible to achieve a significantly larger noise reduction than ordinary or the first-order photon antibunching.

Fig. 3,4,5 show the variations of $d_A(1)$, $d_A(2)$, and $d_A(3)$ with $|\alpha|^2$ of equations (29), (33) and (37), respectively, for various harmonic mode $|\beta|$ values.

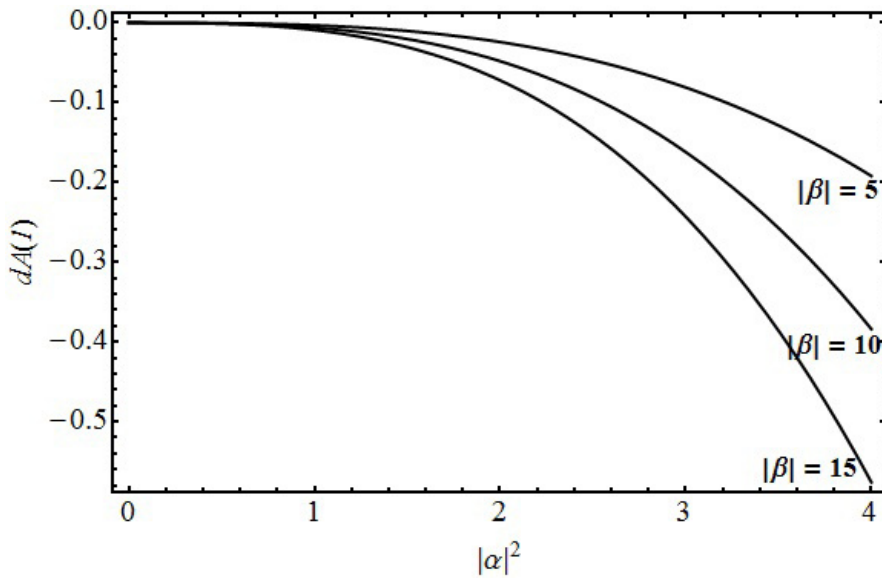


FIG. 3. First-order photon antibunching $d_A(1)$ with $|\alpha|^2$ in the pump field up to first-order Hamiltonian interaction of sixth harmonic generation (when $|\beta| = 5, 10, 15$ and $|gt| = 10^{-5}$)

The steady fall of plots in Fig. 3,4,5 show that degree of photon antibunching occurs in the sixth harmonic generation and responds nonlinearly to the number of pump photons. It demonstrates that when the photon number in pump mode $|\alpha|^2$ is increasing, the degree of photon antibunching $d_A(l)$ increases. In a comparison among Fig. 3,4,5, it is observed that higher the value of $|\beta|$, the effect of photon antibunching increases and lowers the depth of classicality of the field amplitude. It is also shown that the photon antibunching directly depends on the photon number of the fundamental mode as well as the harmonic mode.

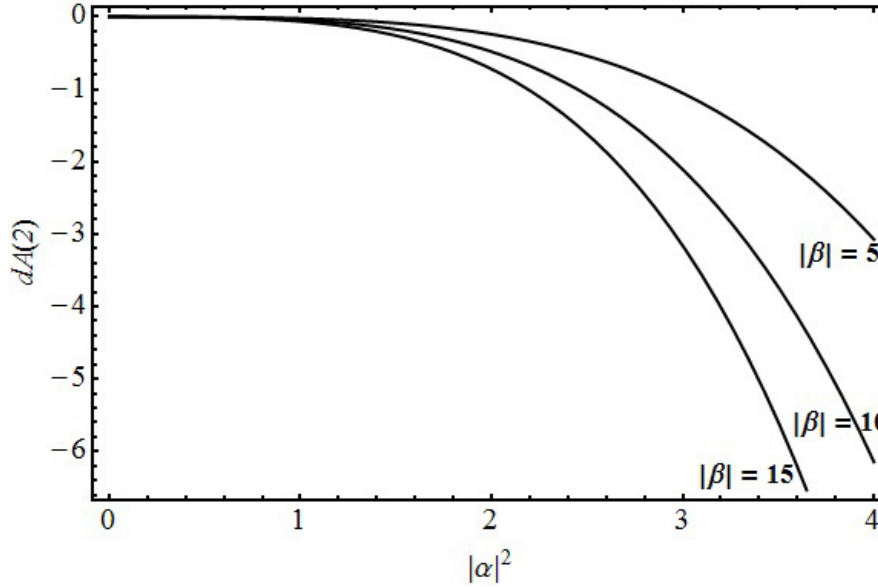


FIG. 4. Second-order photon antibunching $d_A(2)$ with $|\alpha|^2$ in the pump field up to first-order Hamiltonian interaction of sixth harmonic generation (when $|\beta| = 5, 10, 15$ and $|gt| = 10^{-5}$)

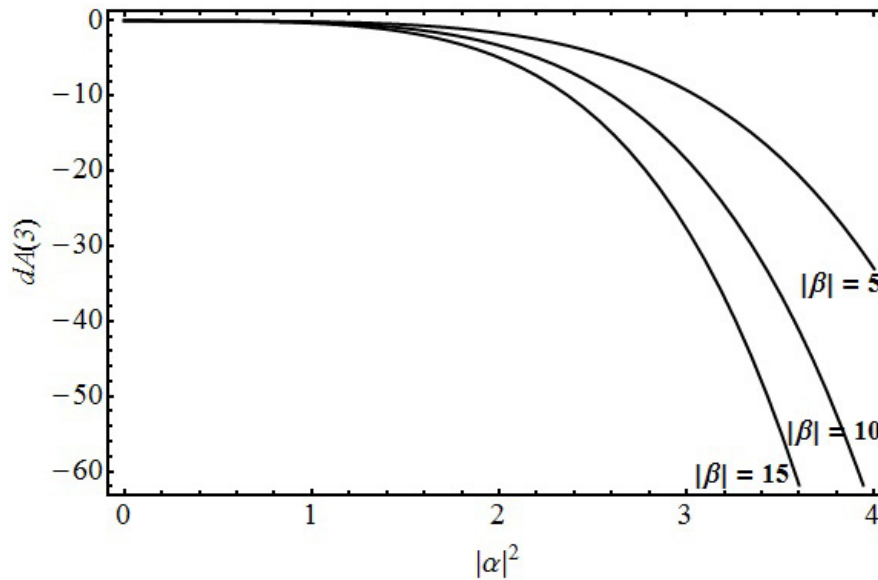


FIG. 5. Third-order photon antibunching $d_A(3)$ with $|\alpha|^2$ in the pump field up to first-order Hamiltonian interaction of sixth harmonic generation (when $|\beta| = 5, 10, 15$ and $|gt| = 10^{-5}$)

The variations of $d_A(l)$ and $|gt|$ of equations (29), (33) and (37) are shown in Fig. 6. The curves show that the degree of photon antibunching increases and directly depends upon the coupling of the field and the interaction time of the pump field. Fig. 7 depict the variation of $d_A(l)$ and $|\alpha|^2$ of equation (37) with different values of $|gt|$, demonstrating that the maximum reachable degree of antibunching is dependent on interaction time and is limited by a short interaction time. It is also worth noting that as the interaction time becomes shorter, the effect of photon antibunching increases [50–52].

We further plot a graph (Fig. 8) between the left-hand side of equations (44), (47) and (50) say $d'_A(l)$ and $|\alpha|^2$, when dimensionless interaction constant, $|gt|^2 = 10^{-10}$. The steady fall of the curves infer that the photon antibunching exists

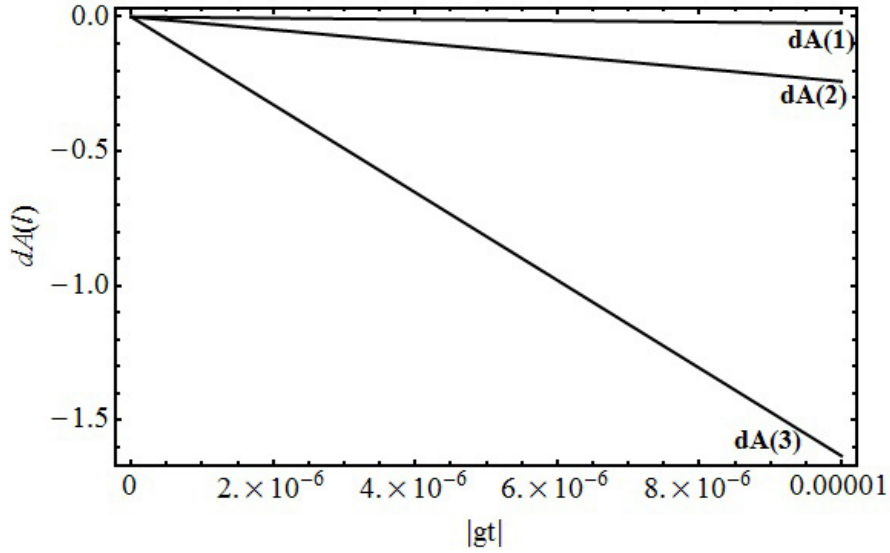


FIG. 6. Degree of photon antibunching $d_A(l)$ with $|gt|$ in the pump field up to first-order Hamiltonian interaction of sixth harmonic generation (when $|\alpha| = 2$ and $|\beta| = 5$ have arbitrarily value)

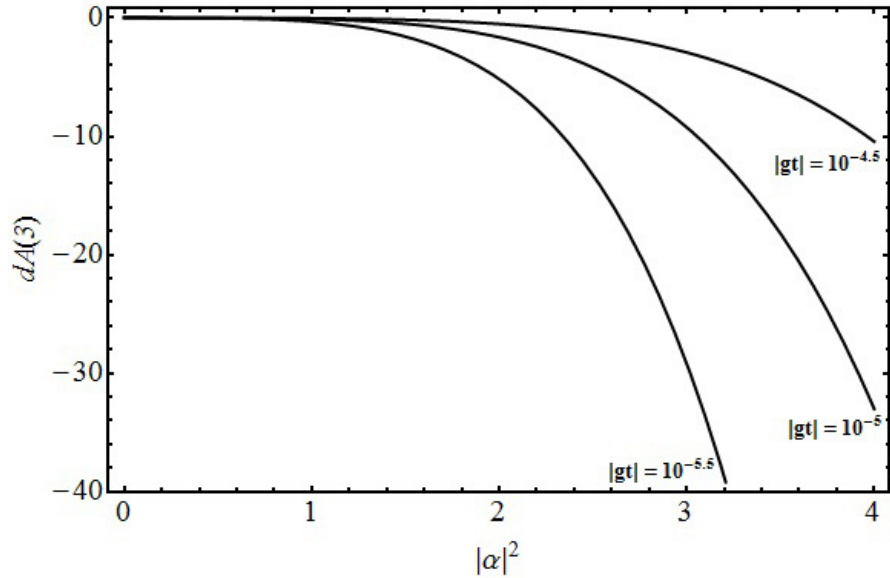


FIG. 7. Third-order photon antibunching $d_A(3)$ with $|\alpha|^2$ in the pump field up to first-order Hamiltonian interaction of sixth harmonic generation (when $|\beta| = 5$ (arbitrarily value) and $|gt| = 10^{-4.5}, 10^{-5}, 10^{-5.5}$)

in the sixth harmonic generation and responds nonlinearly to the number of pump photons. It demonstrates that when $|\alpha|^2$ is increasing the degree of photon antibunching increases. When the plots in Fig. 8 are compared, the third-order plot $d'_A(3)$ shows more photon antibunching than the second-order $d'_A(2)$ and the first-order $d'_A(1)$ plots, despite the fact that the number of photons is the same. It implies that the third-order photon antibunching is more nonclassical than the first- and the second-order photon antibunching.

The variations of $d'_A(l)$ and $|gt|^2$ of equations (44), (47) and (50) are shown in Fig. 9. The curves show that the degree of photon antibunching increases nonlinearly and directly depends upon the coupling of the field and the interaction time of the pump field. It also infers that the third-order photon antibunching is more nonclassical at shorter-time than the first- and the second-order photon antibunching.

It also shows that the maximum reachable degree of antibunching depends upon the interaction time and will be limited by short interaction time. It is worth noting that as the interaction time becomes shorter, the effect of photon antibunching increases [50–52].

Hence, it is inferred that the depth of nonclassicality is increasing with an increase of $|\alpha|^2$ and the maximum reachable degree of photon antibunching is dependent upon the interaction time.

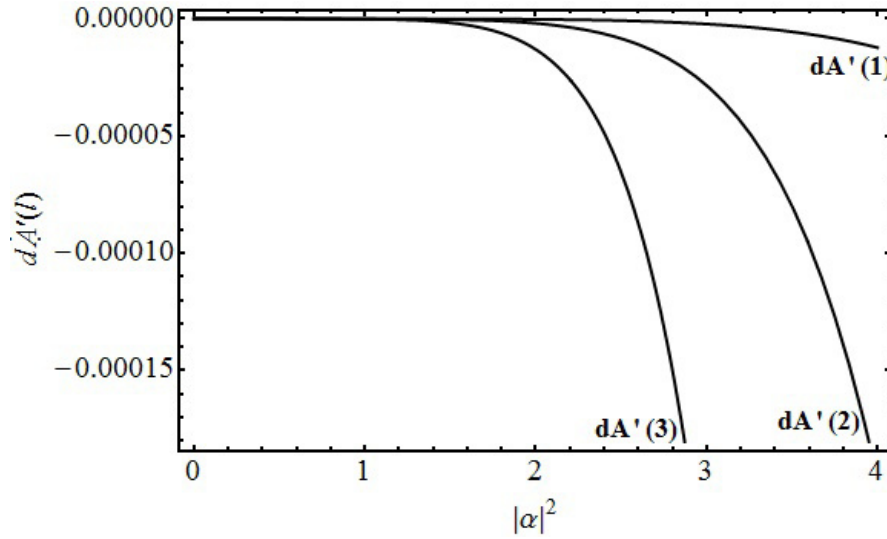


FIG. 8. Degree of photon antibunching $d'_A(l)$ with $|\alpha|^2$ in the pump field up to second-order Hamiltonian interaction of sixth harmonic generation (when $|gt|^2 = 10^{-10}$)

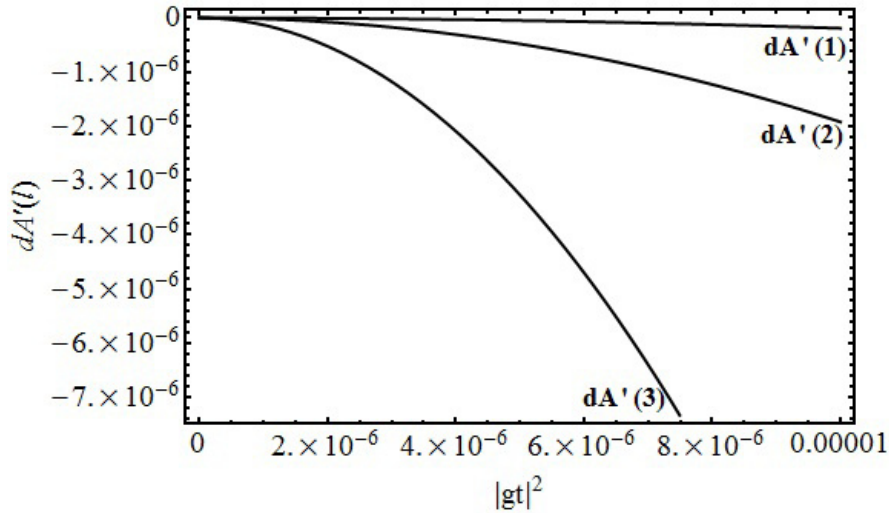


FIG. 9. Degree of photon antibunching $d'_A(l)$ with $|gt|^2$ in the pump field up to second-order Hamiltonian interaction of sixth harmonic generation (when $|\alpha|^2 = 2$ (arbitrarily value))

By comparing figures (2) and (8), it is clear that the first-order Hamiltonian interaction is more nonclassical than the second-order Hamiltonian interaction since it stimulates both pump and harmonic fields. It is observed that a powerful pump field induces a stronger interaction and is helpful for obtaining stronger photon antibunching.

It is found that, from sections 3.3 and 3.4, there is no evidence of photon antibunching in the harmonic mode over pump mode up to first- and second-order Hamiltonian interaction in the sixth harmonic generation process.

In contrast, the coherent state of a pump field with a nonzero harmonic field generates photon clusters. This is due to the fact that the coherent state of the pump field causes interaction, which results in bunching effects. On the other hand, the vacuum state of a pump field with a nonzero harmonic field, results in photon bunching. This is due to the fact that the vacuum state of the pump field stimulates interaction, producing bunching effects.

In order to discuss the depth of nonclassicality, we consider equations (69) and (70) in terms of pump photon number and plot a graph (Fig. 10) between $g^2(0)$ and $g^2(0)'$ versus $|\alpha|^2$ having when $|\beta| = 5$ (any arbitrarily constant value) and $|gt| = 10^{-5}$.

Fig. 10 shows that the condition of antibunching $g^2(0) < 1$ exists [10, 12, 27] and is, thus, a conclusive signature of the quantum nature of light. We also infer that the fall of plots of the second-order correlation function for zero time delay or the photon number correlation decreases, i.e., the depth of nonclassicality increases with the increase of photons in the sixth harmonic generation.

Fig. 10 between $(g^2(0))'$ and $|\alpha|^2$ of the pump field up to the second-order Hamiltonian interaction in sixth harmonic generation (when $|gt|^2 = 10^{-10}$) reveals that the second-order correlation function for zero time delay or the photon number correlation decreases, i.e., the depth of nonclassicality increases, and hence it is more nonclassical in a shorter interaction time. We see that the second correlation function is minimum in regions where the degree of photon antibunching is maximum.

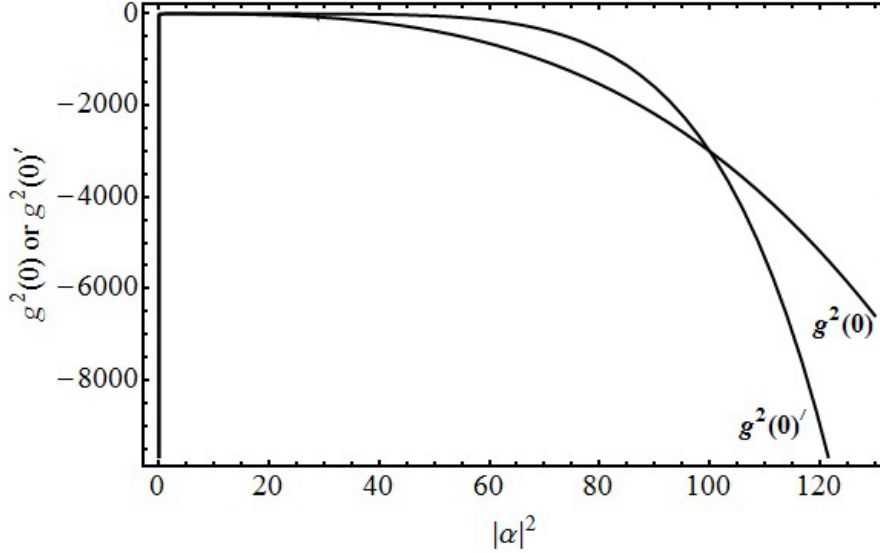


FIG. 10. Second-order correlation function $g^2(0)$ or $g^2(0)'$ versus $|\alpha|^2$ in the pump field up to first-order or second-order Hamiltonian interaction of sixth harmonic generation respectively (when $|\beta| = 5$ (arbitrarily value) and $|gt|^2 = 10^{-10}$)

It is evident that, in general, higher-order antibunching is a phenomenon that reduces the probability of detecting multiple photons simultaneously compared to a classical light source. This effect extends the concept of antibunching beyond pairs of photons to encompass higher-order correlations. Mathematically, the depth of non-classicality in higher-order antibunching can be defined using correlation functions, or $g^2(n)$ functions, where n represents the order of the correlation. These functions measure the probability of detecting n photons simultaneously at different times. The depth of non-classicality provides a quantitative measure of the extent to which the observed higher-order photon correlations deviate from classical predictions, indicating the degree of non-classical behaviour exhibited by the light source beyond first-order (normal) antibunching effects.

6. Summary and conclusions

The present manuscript investigates photon antibunching in the sixth harmonic generation. We demonstrate that the number of pump photons, the field coupling between the modes, and the interaction time closely influence the first-, second-, and third-order photon antibunching. Therefore, the interaction time, limited by short interaction times, governs the highest degree of antibunching achievable. It is worth noting that as the interaction time becomes shorter, the effect of photon antibunching increases.

The number of photons present in pump mode appears to be a good way to regulate the depth of nonclassicality. We conclude that the photon-antibunched states are associated with a large number of pump photons. We also demonstrate that the photon numbers of the fundamental mode and the harmonic mode directly influence the photon antibunching. We found that the third-order antibunching, with the same number of pump photons, has the most nonclassical features, followed by the second- and the first-order antibunching. We observe that the higher-order antibunching (second and third-order) achieves nonclassicality depth more effectively than ordinary (normal) antibunching.

We found that the first-order Hamiltonian interaction, which stimulates both pump and harmonic fields, is more nonclassical than the second-order Hamiltonian interaction. A powerful pump field creates a stronger interaction and is useful for achieving stronger photon antibunching.

It was found that there is no evidence of photon antibunching in the harmonic mode over pump mode up to the first- and second-order Hamiltonian interactions in the sixth harmonic generation process. In contrast, the coherent state of a pump field with a nonzero harmonic field generates photon clusters. This is due to the fact that the coherent state of the pump field causes interaction, resulting in bunching effects. On the other hand, the vacuum state of a pump field with a nonzero harmonic field results in photon bunching. This is due to the fact that the vacuum state of the pump field stimulates interaction, producing bunching effects.

We observe that in the sixth harmonic generation, as the number of photons in the pump mode increases, the second-order correlation function with zero time delay, or photon number correlation, declines, and the depth of nonclassicality increases. Consequently, we argued that the second correlation function becomes minimal in locations where photon antibunching is at its highest. We revealed photon antibunching as conclusive evidence of the quantum character of light. Overall, higher-order antibunching is a phenomenon that diminishes the likelihood of concurrently detecting multiple particles in comparison with the standard light source. This phenomenon broadens the definition of antibunching to include higher-order correlations as well as pairs of particles. Beyond normal antibunching effects, the depth of nonclassicality quantifies the degree to which observed higher-order photon correlations deviate from classical predictions, thereby indicating the light source's degree of non-classical behaviour.

The results of this paper are simple and easy to reproduce in most physical systems labs. This opens the door for the experimental observation of higher-order antibunching and the development of probabilistic single-photon sources for quantum teleportation and quantum cryptography. More than these basic and abstract ideas, making larger and better nonclassical multiphoton states possible could help in creation of new devices like quantum dots, nanolasers, and on-chip integrated photonic circuits. These devices leverage the quantum properties of light and enable advancements in areas like on-chip quantum information processing and quantum communication.

References

- [1] Stoler D. Photon antibunching and possible ways to observe it. *Phys. Rev. Lett.*, 1974, **33**(23), P. 1397–1400.
- [2] Tanas R. On nonlinear optical activity and photon statistics. *Optik*, 1974, **40**, P. 109.
- [3] Loudon R. Photon bunching and antibunching. *Phys. Bull.*, 1976, **27**(1), P. 21–23.
- [4] Kimble H.J., et al. Photon antibunching in resonance fluorescence. *Phys. Rev. Lett.*, 1977, **39**(11), P. 691–695.
- [5] Paul H. Photon antibunching. *Rev. Mod. Phys.*, 1982, **54**(4), P. 1061–1102.
- [6] Mandel L. Squeezing and photon antibunching in harmonic generation. *Opt. Commun.*, 1982, **42**(6), P. 437–439.
- [7] Kielich S., et al. Photon antibunching and squeezing- Two non-trivial effects of the nonlinear interaction of laser photon with matter. *Optica Acta*, 1985, **32**, P. 1023.
- [8] Zou X.T., Mandel L. Photon-antibunching and sub-Poissonian photon statistics. *Phys. Rev. A*, 1990, **41**(1), P. 475–476.
- [9] Pathak A., Mandal S. Photon-bunching, photon-antibunching and nonclassical photon statistics of coherent photon coupled to a cubic nonlinear medium. *Mod. Phys. Lett. B*, 2003, **17**(5-6), P. 225–233.
- [10] Fox M. *Quantum Optics: An Introduction*, Chapter 6. New York: Oxford University Press, 2006.
- [11] Kozierowski M., R. Tanaś. Quantum fluctuations in second-harmonic photon generation. *Opt. Commun.*, 1977, **21**(2), P. 229–231.
- [12] Loudon R., Knight P.L. Squeezed light. *J. Mod. Opt.*, 1987, **34**(6-7), P. 709–759.
- [13] Meystre P., Sargent M. III. *Elements of Quantum Optics*, 4th ed. Berlin: Springer-Verlag, 1991.
- [14] Dodonov V.V. Nonclassical states in quantum optics: A squeezed review of the first 75 years. *J. Opt. B: Quantum Semiclass. Opt.*, 2002, **4**(1), P. R1-R33.
- [15] Bennett C.H. et al. Teleporting an unknown quantum state via dual classical and Einstein-Podolsky-Rosen channels. *Phys. Rev. Lett.*, 1993, **70**(13), P. 1895–1899.
- [16] Furusawa A. et al., Unconditional quantum teleportation. *Science*, 1998, **282**(5389), P. 706–709.
- [17] Gottesman D., Chuang I.L. Demonstrating the viability of universal quantum computation using teleportation and single-qubit operations. *Nature*, 1999, **402**(6760), P. 390–393.
- [18] Benioff P. The computer as a physical system: A microscopic quantum mechanical Hamiltonian model of computers as represented by Turing machines. *J. Stat. Phys.*, 1980, **22**(5), P. 563–591.
- [19] Feynman R.P. Simulating physics with computers. *Int. J. Theor. Phys.*, 1982, **21**(6-7), P. 467–488.
- [20] Deutsch D. Quantum theory, The Church–Turing principle and the universal quantum computer. *Proc. R. Soc. Lond. A*, 1985, **400**(1818), P. 97–117.
- [21] Raginsky M., Kumar P. Generation and manipulation of squeezed states of photon in optical networks for quantum communication and computation. *J. Opt. B: Quantum Semiclass. Opt.*, 2001, **3**(4), P. L1-L4.
- [22] Bennett C.H., Brassard G. Quantum public key distribution system. *IBM Tech. Discl. Bull.*, 1985, **28**, P. 3153.
- [23] Ekert A.K. Quantum cryptography based on Bell's theorem. *Phys. Rev. Lett.*, 1991, **67**(6), P. 661–663.
- [24] Hillery M. Quantum cryptography with squeezed states. *Phys. Rev. A*, 2000, **61**(2), P. 022309.
- [25] Matsuoka M., Hirano T. Quantum key distribution with a single photon from a squeezed coherent state. *Phys. Rev. A*, 2003, **67**(4), P. 042307.
- [26] Eisaman M.D. et al. Invited review article: Single-photon sources and detectors. *Rev. Sci. Instrum.*, 2011, **82**(7), P. 071101.
- [27] Stevens M.J. et al. Third-order antibunching from an imperfect single-photon source. *Opt. Exp.*, 2014, **22**(3), P. 3244–3260.
- [28] Meyer-Scott E. et al. Single-photon sources: Approaching the ideal through multiplexing. *Rev. Sci. Instrum.*, 2020, **91**(4), P. 041101.
- [29] Lee C.T. Higher-order criteria for nonclassical effects in photon statistics. *Phys. Rev. A*, 1990, **41**(3), P. 1721–1723.
- [30] Lee C.T. Many-photon antibunching in generalized pair coherent states. *Phys. Rev. A*, 1990, **41**(3), P. 1569–1575.
- [31] An N.B. Multimode higher-order antibunching and squeezing in trio coherent states. *J. Opt. B: Quantum Semiclass. Opt.*, 2002, **4**(3), P. 222–227.
- [32] Pathak A., Garcia M.E. Control of higher order antibunching. *Appl. Phys. B*, 2006, **84**(3), P. 479–484.
- [33] Gupta P. et al., Higher order antibunching is not a rare phenomenon. *J. Phys. B: At. Mol. Opt. Phys.*, 2006, **39**(5), P. 1137–1143.
- [34] Grosse N.B. et al., Measuring photon anti-bunching from continuous variable side band squeezing. *Phys. Rev. Lett.*, 2007, **98**(15), P. 153603.
- [35] Mandal S. et al., Antibunching of photons in a coherent radiation field coupled to a non-degenerate parametric oscillator beyond rotating wave approximation. *Pramana J. Phys.*, 2021, **95**(2), P. 82.
- [36] Inui Y., Yamamoto Y. Entanglement and photon anti-bunching in coupled non-degenerate parametric oscillators. *Entropy (Basel)*, 2021, **23**(5), P. 624.
- [37] Bachor H.-A. *A Guide to Experiments in Quantum Optics*, 2nd ed. Weinheim: Wiley-VCH, 1998, Chapters 8 and 10.
- [38] Vogel W. et al., Chapter 6, *Quantum Optics: An Introduction*, 2nd ed. Berlin: Wiley-VCH, 2001.
- [39] Erenso D. et al., Higher-order sub-Poissonian photon statistics in terms of factorial moments. *J. Opt. Soc. Am. B*, 2002, **19**(6), P. 1471.
- [40] Vyas R. and Singh S. Photon-counting statistics of the degenerate optical parametric oscillator. *Phys. Rev. A Gen. Phys.*, 1989, **40**(9), P. 5147–5159.
- [41] Verma A. et al., Higher order antibunching in intermediate states. *Phys. Lett. A*, 2008, **372**(34), P. 5542–5551.

- [42] Sen B. et al., Squeezing and photon antibunching in second harmonic generation: An analytical approach. *J. Mod. Opt.*, 2012, **59**(6), P. 555–564.
- [43] Truong D.M. et al., Sum squeezing, difference squeezing, higher-order antibunching and entanglement of two-mode photon-added displaced squeezed states. *Int. J. Theor. Phys.*, 2014, **53**(3), P. 899–910.
- [44] Mukhopadhyay A. et al., Squeezing and antibunching in three-mode atom-molecule Bose-Einstein condensates. *J. Physiol. Sci.*, 2017, **22**, P. 151.
- [45] Nitu Sahu et al., Higher-order antibunching of light in seven-photon interaction process. *J. Russ. Laser Res.*, 2022, **43**(3), P. 290–306.
- [46] Dell'Anno F., De Siena S., Fabrizio Illuminati. Multiphoton Quantum Optics and Quantum State Engineering. *Phys. Rep.*, 2006, **428**, P. 53–168.
- [47] Tanas R. Squeezing from an anharmonic oscillator model: $(a^+)^2 a^2$ versus $(a^+ a)^2$ interaction Hamiltonians. *Physics Letters A*, 1989, **141**, P. 217.
- [48] Tanas R. et al., Squeezing and its graphical representations in the anharmonic oscillator model. *Phys. Rev. A*, 1991, **43**(7), P. 4014–4021.
- [49] Perina J. Quantum Statistics of Linear and Nonlinear Optical Phenomena, 2nd ed. Dordrecht, The Netherlands: Kluwer, 1991, Chapters 9 and 10.
- [50] Gerry C.C., Rodrigues S. Time evolution of squeezing and antibunching in an optically bistable two-photon medium. *Phys. Rev. A Gen. Phys.*, 1987, **36**(11), P. 5444–5447.
- [51] Giri D.K., Gupta P.S. Short-time fourth-order squeezing effects in spontaneous and stimulated four- and six-wave mixing processes. *J. Opt. B: Quantum Semiclass. Opt.*, 2003, **5**(2), P. 158–163.
- [52] Latha G.M. et al., Generation of nonclassical photon by unsaturated two-photon absorption. *Opt. Photonics J.*, 2017, **7**, P. 139–150.

Submitted 14 December 2023; revised 25 March 2024; accepted 30 March 2024

Information about the authors:

Rupesh Singh – Department of Physics, D.A.V. Public School, Koylanagar, Dhanbad, Jharkhand, India; ORCID 0009-0009-3184-3274; rupesh.dav2021@gmail.com

Dilip Kumar Giri – University Department of Physics, Binod Bihari Mahto Koyalanchal University, Dhanbad, Jharkhand, India; ORCID 0000-0003-2721-5055; dilipkumargiri@gmail.com

Conflict of interest: the authors declare no conflict of interest.

Q-switched and mode-locked pulse generations with Ti_3AlC_2 absorber

Syed Ziad Z. Aljunid¹, Nurul Athirah M. A. Ghafar¹, Bilal A. Ahmad², Retna Apsari³, Sulaiman W. Harun^{1,3}

¹Department of Electrical Engineering, Faculty of Engineering, University of Malaya, Kuala Lumpur 50603, Malaysia

²Department of Communication Engineering, Al-Ma'moon University College, Al-Washash, 700921 Baghdad, Iraq

³Department of Physics, Faculty of Science and Technology, Airlangga University, Surabaya 60115 Indonesia

Corresponding author: Sulaiman W. Harun, swharun@um.edu.my

ABSTRACT Exploring advanced saturable absorber (SA) materials that exhibit exceptional performance for achieving Q-switching and mode-locking operations remains a vibrant area of research in the field of fiber lasers. The remarkable optical nonlinearity, coupled with high thermal and chemical stability of MAX phase materials, positions them as promising candidates for high-performance SAs. In this study, we demonstrated the potential of Ti_3AlC_2 MAX phase as an effective material for Q-switched and mode-locked fiber laser applications. The Ti_3AlC_2 film was synthesized through a straightforward and cost-effective casting method employing polyvinyl alcohol (PVA) as a host material. The SA was cleverly constructed from the film, utilizing a sandwich-structured fiber-ferrule platform, and seamlessly integrated into an Erbium-doped fiber laser (EDFL) ring cavity. Initially, a stable Q-switched laser was realized at a center wavelength of 1531 nm. The repetition rate exhibited a commendable increase from 35.0 to 50.8 kHz, and the pulse width reduced from 6.58 to 3.40 μs as the pump power was adjusted within the range of 25.98 to 58.29 mW. Notably, the maximum output power of 2.49 mW and a pulse energy of 49.02 nJ were recorded at a pump power of 58.29 mW. Subsequently, an additional 200 m long single-mode fiber was added into a similar laser cavity, leading to the generation of a stable mode-locked laser at a threshold pump power of 81.37 mW, operating at a central wavelength of 1558.96 nm. The observed stable repetition rate of 969.3 kHz, coupled with a pulse duration of 300 ns, demonstrated robust performance as the pump power increased from 81.37 to 113.68 mW. These findings highlight the exceptional performance of Ti_3AlC_2 SA for both Q-switching and mode-locking applications. The versatility of these lasers makes them valuable for diverse applications, including micromachining of materials, frequency comb generation, and remote sensing.

KEYWORDS Ti_3AlC_2 , max phase material, Q-switching, mode-locking, saturable absorber, erbium-doped fiber laser

FOR CITATION Aljunid S.Z.Z., Ghafar N.A.M.A., Ahmad B.A., Apsari R., Harun S.W. Q-switched and mode-locked pulse generations with Ti_3AlC_2 absorber. *Nanosystems: Phys. Chem. Math.*, 2024, **15** (2), 184–191.

1. Introduction

Fiber lasers, as exemplary representatives of third-generation laser technology, have emerged as highly promising tools across numerous scientific and industrial domains, commanding a substantial share of the commercial laser market [1]. These versatile lasers can be categorized into two primary operational modes: continuous and pulsed. Pulsed fiber lasers, characterized by high pulse energy and short pulse widths, have significantly broadened their applications in fiber optic communication, automotive manufacturing, laser cutting, medical devices, and various other sectors [2]. Pulsed lasers can be achieved through two main techniques: Q-switching and mode-locking, with options for both active and passive implementation. In recent years, passive techniques have garnered increased attention due to their inherent advantages in terms of simplicity, flexibility, compactness, and cost-effectiveness. Unlike their active counterparts, passive pulsed lasers do not rely on unwieldy and intricate optical modulators or complex electronic drivers. Instead, they can generate laser pulses by merely incorporating a saturable absorber (SA) within the resonant cavity. The SA, a pivotal component in passive Q-switched and mode-locked lasers, assumes a crucial role in shaping the laser output [3].

The evolution of passive pulsed lasers is intrinsically tied to advancements in SA materials. To date, several emerging nanomaterials have displayed promising saturable absorption properties suitable for practical saturable absorbers (SAs) [4]. Despite the prevalent use of III–V compound semiconductors in commercially available ultrafast lasers [5], intensive investigations have been conducted on a diverse range of nanomaterials to assess their saturable absorption potential. These materials encompass carbon nanotubes (CNTs) [6], graphene [7], topological semimetals [8], topological

insulators (TIs) [9], black phosphorus (BPs) [10], transition metal dichalcogenides (TMDCs) [11], gold nanoparticles [12], and MXenes [13].

Among the nano-materials mentioned, MXenes stand out as a new family of 2D materials. Their exceptional electronic and photonic properties [14] have thrust them into the limelight within the realms of materials science and engineering. MXenes are characterized by the general formula $M_{n+1}X_nT_x$ (where n ranges from 1 to 3, M represents an early transition metal, X signifies carbon and/or nitrogen, and T denotes surface terminations). These remarkable materials are derived from their ternary MAX phase precursors through a process of chemical etching [15]. Despite their extensive applicability in diverse fields, such as electrochemical capacitors, water purification, chemical catalysts, and biosensors [16, 17], the use of a chemical etching method involving hydrofluoric (HF) acid presents a significant hurdle to their large-scale production due to the severe toxicity associated with HF acid.

As a result, there has been a significant surge in technical interest in precursor materials known as MAX phases. These MAX phases still exhibit notable photonic and electronic properties that are comparable to those of MXenes, further fueling research in this area [18]. MAX phases constitute a category of ductile ceramic materials with the chemical formula $M_{n+1}AX_n$ (where $n = 1, 2, 3 \dots$), with M representing an early transition metal, A corresponding to the IIIA or IVA group element, and X signifying either nitrogen or carbon. These MAX phases are renowned for their resilience and find application in fields such as nuclear engineering, high-temperature applications, and aerospace due to their robust nature [15, 19]. In this work, we propose a novel Q-switched and mode-locked fiber laser by incorporating Ti_3AlC_2 PVA film in the Erbium-doped fiber laser (EDFL) cavity. The SA film was fabricated by using embedding Ti_3AlC_2 powder in PVA as a host polymer to form a absorb film. The SA film has saturable absorption and saturation intensity of 2 % and 1000 MW/cm^2 , respectively.

2. Fabrication and characterization of Ti_3AlC_2 /PVA-based SA

Ti_3AlC_2 powder, characterized by its 99.9 % purity and sourced from Carbon-Ukraine Ltd, was used in this work to fabricate a composite thin film through integration into a polyvinyl alcohol (PVA) solution. The PVA solution preparation involved dissolving 1 g of the compound in 120 ml of distilled water. This mixture underwent stirring in a vessel for approximately 24 hours at a speed of 300 rpm and a temperature of 200°C , ensuring complete dissolution of the material. Subsequently, 40 ml of the prepared PVA solution was transferred to a separate beaker, where it served as the base for the composite solution. Here, 10 mg of Ti_3AlC_2 powder was added, initiating a stirring process lasting 24 hours. Following this, the solution underwent sonication in an ultrasonic bath for an additional 3 hours, resulting in the formation of a homogeneous composite Ti_3AlC_2 PVA solution. To complete the fabrication process, a small quantity of the solution was directly poured onto a petri dish, allowing it to spread naturally. The solution-laden petri dish was left undisturbed for approximately 48 hours, enabling the formation and drying of the composite film. Subsequently, the film was delicately peeled off and strategically positioned between two FC/PC fiber ferrules via a fiber adaptor. This meticulous arrangement yielded a saturable absorber (SA) device with an insertion loss measuring approximately 2.4 dB. A comprehensive visualization of the step-by-step procedure for fabricating the SA thin film is illustrated in Fig. 1.



FIG. 1. Illustration of Ti_3AlC_2 PVA film preparation

The material characteristics of the Ti_3AlC_2 film were thoroughly investigated through field-emission scanning electron microscopy (FESEM) and energy-dispersive X-ray spectroscopy (EDX). Fig. 2(a) presents the FESEM image, revealing an even dispersion of Ti_3AlC_2 particles within the PVA matrix. Subsequently, the EDX spectrum of the Ti_3AlC_2 film, illustrated in Fig. 2(b), exhibits prominent peaks corresponding to titanium (Ti), aluminum (Al), carbon (C), and oxygen (O). Quantitative analysis confirms the presence of 72.8 wt.% Ti, 10.4 wt.% Al, 9.5 wt.% C, and 7 wt.% O in the composite. Moving forward, the nonlinear transmission curve of the Ti_3AlC_2 PVA thin film was determined using a twin-balance detection method. A home-built mode-locked Erbium-doped fiber laser (EDFL) operating at 1558 nm, with a temporal width of 3.62 ps and a repetition rate of 1.9 MHz, served as the input light source. Fig. 2(c) depicts the

measured nonlinear transmission output intensity plotted against the peak intensity of the incident light, accompanied by a fitted curve described by the equation [20]:

$$T(I) = 1 - \Delta T \cdot \exp\left(\frac{-I}{I_{sat}}\right) - T_{ns}$$

Here (I) represents the transmitted intensity, ΔT is the saturable absorption, I is the input pulse intensity, T_{ns} is the non-saturable absorption, and I_{sat} is the saturation intensity. The measured saturable absorption, non-saturable absorption, and saturation intensity were found to be approximately 2 %, 59 %, and 1000 MW/cm², respectively.

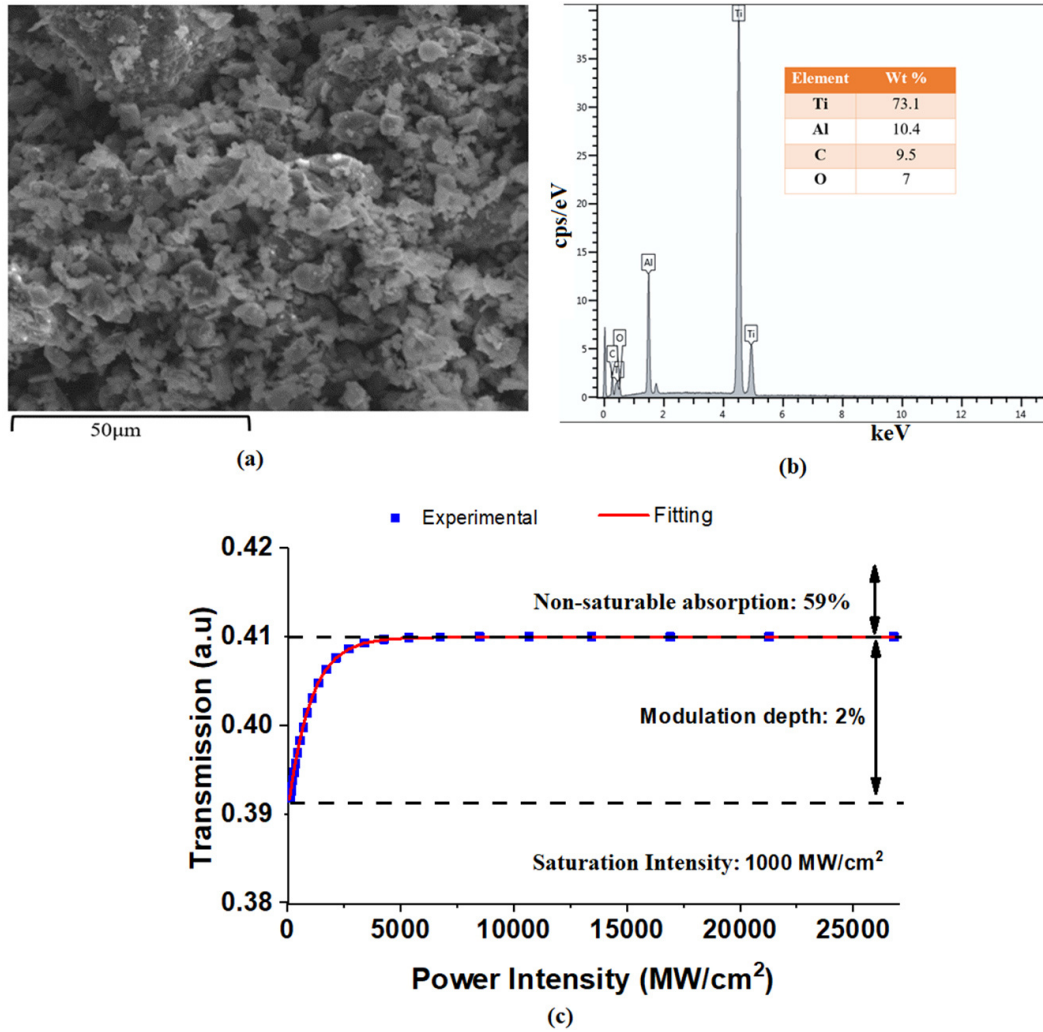


FIG. 2. The Ti_3AlC_2 PVA film characteristics (a) FESEM image (b) EDX analysis result (c) nonlinear transmission curve

3. Laser configuration

The Q-switched laser setup was firstly constructed, leveraging an all-fiber EDFL ring structure, as depicted in Fig. 3. In this configuration, an Erbium-doped fiber (EDF) served as the active medium, while the previously fabricated Ti_3AlC_2 -PVA thin film functioned as the SA. The inset figure provides an actual image of the fabricated Ti_3AlC_2 -PVA thin film, featuring a thickness of approximately 50 μm . The EDF used has a length of 1.8 m, a numerical aperture (NA) of 0.23, and core/cladding diameters of 4 μm /125 μm , with a peak absorption of 23 dB/m at the pumping wavelength. A 980 nm laser diode, facilitated by a 980/1550 nm wavelength-division multiplexer (WDM), co-pumped the EDF. To ensure unidirectional propagation, a polarization-insensitive optical isolator was incorporated into the cavity resonator. For both temporal and spectral diagnostics, a 20/80 fused-fiber coupler was employed to tap out the output laser.

The Ti_3AlC_2 SA played a key role in modulating the intra-cavity loss to produce a Q-switched pulse train. It also facilitates the phase-locking of longitudinal modes within the EDFL ring cavity to produce mode-locked pulses. The fused-fiber coupler allocated 20 % of the oscillating laser for output, while retaining the remaining 80 % within the cavity for sustained operation. To investigate the laser performance, a comprehensive measurement setup was implemented. A

digital oscilloscope and a radio frequency spectrum analyzer (RFSAs) were utilized for assessing optical parameters in the time and frequency domains, respectively. These measurements were conducted in tandem with a fast photodiode (PD). Simultaneously, an optical spectrum analyzer (OSA) with a high resolution of 0.02 nm was deployed to examine the laser's spectral characteristics. Additionally, the average output power was precisely gauged using an optical power meter coupled with an InGaAs detector.

The laser cavity underwent a strategic modification to allow mode-locked pulse generation by introducing a 200 m long single-mode fiber (SMF) between the SA device and the output coupler. This additional SMF served the dual purpose of managing the dispersion regime and enhancing nonlinearity within the system. Consequently, the total length of the mode-locked laser cavity extended to approximately ~ 206 m. The modified cavity comprised a 1.8 m long EDF, a 0.7 m long WDM fiber, and the newly incorporated 203.5 m long SMF. Each segment possessed distinct group velocity dispersion (GVD) values: approximately $27.6 \text{ ps}^2/\text{km}$ for the EDF, $-48.5 \text{ ps}^2/\text{km}$ for the WDM fiber, and $-21.7 \text{ ps}^2/\text{km}$ for the SMF. The summation of these dispersion values resulted in an estimated total cavity dispersion of approximately -4.4 ps^2 . This modification strategically managed the dispersion characteristics of the laser cavity, contributing to the optimization of mode-locked pulse generation.

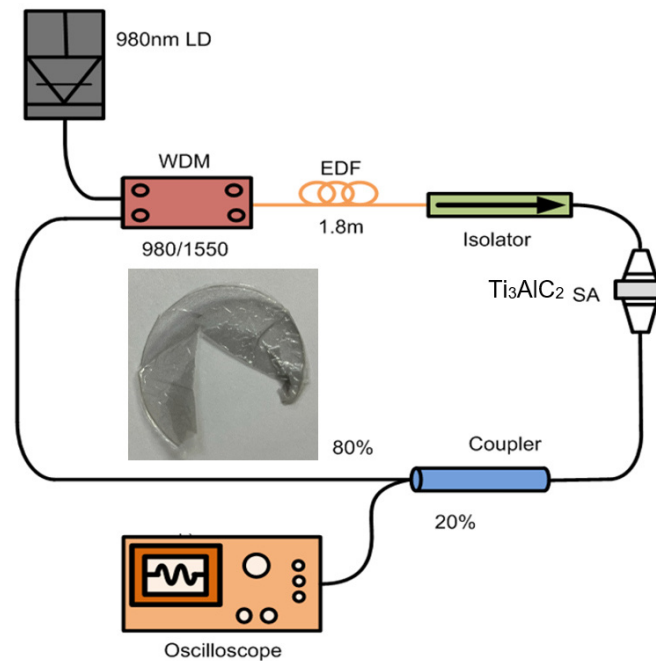


FIG. 3. Configuration of the proposed EDFL with Ti_3AlC_2 SA. Inset shows a real image of the Ti_3AlC_2 PVA film. The mode-locking was realized by adding 200 m long SMF in between the SA and output coupler.

4. Result and discussion

To eliminate the possibility of self-Q-switching or self-mode-locking operations in the EDFL without the Ti_3AlC_2 SA, initial experiments were conducted without inserting the SA into the laser cavity. During this phase, only continuous-wave (CW) operation was observed while adjusting the pump power. However, upon the introduction of the Ti_3AlC_2 SA into the laser cavity, self-started passively Q-switched pulse trains were observed when the pump power exceeded 26.0 mW. Fig. 4(a) provides a comparison of the output spectrum of the laser in CW and Q-switched operations, obtained without and with the SA at the threshold pump power of 26.0 mW. Notably, the peak laser wavelength experienced a blue shift, transitioning from 1567 to 1531 nm after the integration of the Ti_3AlC_2 SA into the cavity. This blue-shifted wavelength is a result of increased loss within the cavity, prompting the laser to emit at shorter wavelength region to achieve higher amplification gain and compensate for additional losses. The Q-switched laser exhibited a 3 dB spectral bandwidth of 2.5 nm, notably broader than the CW laser, which had a bandwidth of 0.5 nm. This spectral broadening can be attributed to the self-phase modulation effect within the laser cavity. The Q-switching operation was sustained up to a pump power of 58.3 mW, showing the effectiveness and stability of the Ti_3AlC_2 SA in inducing and maintaining Q-switched pulses.

The oscilloscope trace of the Q-switched pulse train under maximum pump power is illustrated in Fig. 4(b), revealing a highly consistent Q-switching operation. Inset of Fig. 4(b) depicts the temporal profile of two adjacent pulses, demonstrates a pulse width of $3.4 \mu\text{s}$ and a pulse interval of $19.4 \mu\text{s}$ between the Q-switched pulses. This pulse interval

corresponds to a pulse repetition rate of 50.80 kHz. The stability of the pulsing is then assessed through the measurement of the radio frequency (RF) spectrum, as depicted in Fig. 4(c). The RF spectrum of the Q-switched pulse exhibits excellent stability, with a signal-to-noise ratio (SNR) of approximately 71.4 dB achieved at the fundamental frequency of 50.80 kHz. It is noteworthy that the characteristics of the pulse trains and the optical spectrum remain largely unchanged when varying the polarization state in the cavity. This observation indicates that the Q-switching operation of the fiber laser is polarization insensitive, further enhancing its practical utility and stability.

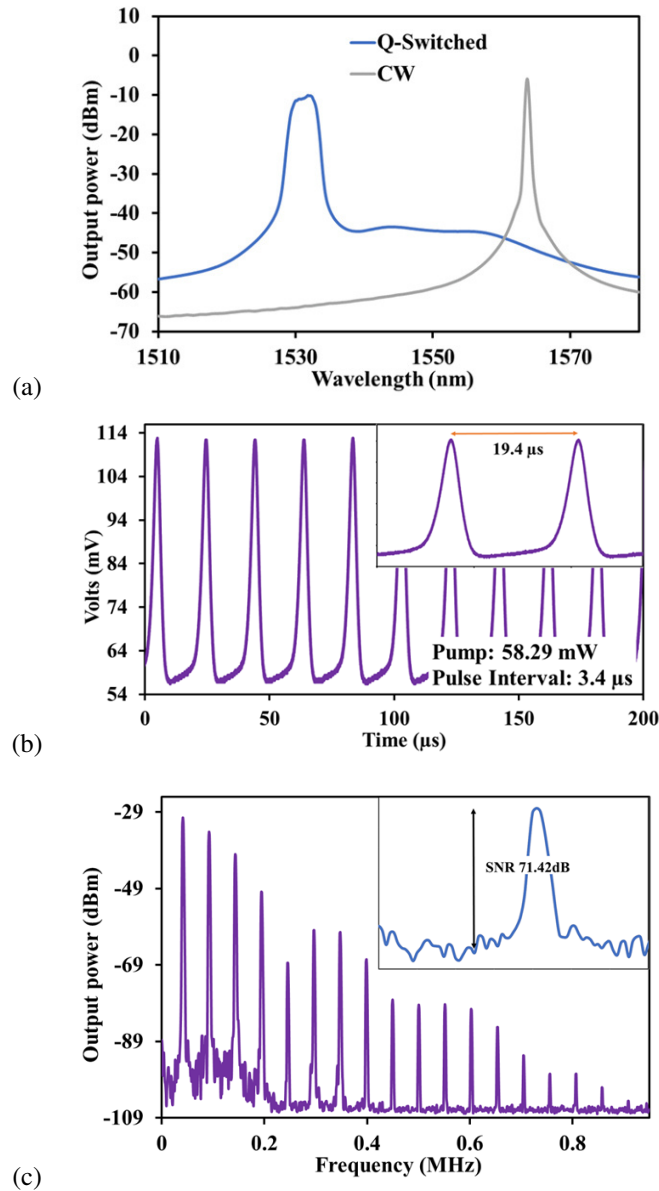


FIG. 4. Q-switching performances (a) Output spectrum of the EDFL with and without Ti_3AlC_2 SA at 26.0 mW pump, (b) typical oscilloscope pulse train at 58.3 mW. Inset shows the temporal profile of two adjacent pulses, and (c) RF spectrum at the pump power of 58.3 mW.

The characteristics of the laser pulses in relation to pump power are illustrated in Fig. 5. Fig. 5(a) presents the dependence of the pulse repetition rate and pulse width on the pump power. Unlike mode-locking operations, the generation of Q-switched pulses relies on the saturation of the SA, causing the repetition rate to be influenced by pump power rather than cavity length. As the pump power increased from 26.0 to 58.3 mW, the repetition rate displayed an almost linear growth, ranging from 35.0 to 50.8 kHz. This behavior stems from the faster saturation of the SA with increasing pump power, leading to a corresponding increase in the repetition rate. Simultaneously, the pulse width decreased from 6.58 to 3.40 μs with the escalating pump power. Both the trends in repetition rate and pulse width align with the typical characteristics of Q-switched fiber lasers. In Fig. 5(b), the average output power and pulse energy characteristics are plotted against pump power. With pump power increasing from 26.0 to 58.3 mW, the average output power exhibited nearly linear growth,

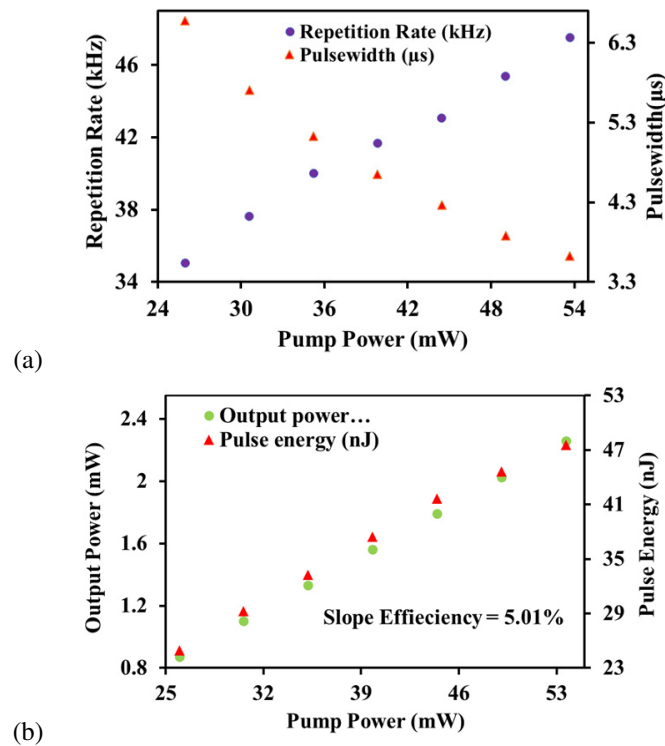


FIG. 5. The variation of (a) repetition rate and pulse width (b) output power and pulse energy as the pump power increases

ranging from 0.87 to 2.49 mW. The slope efficiency, calculated from this relationship, is approximately 5.0 %. The single pulse energy reached up to 49.0 nJ, highlighting the effectiveness of the SA in generating Q-switched pulses.

Subsequently, the introduction of an additional 200 m length of SMF into the existing cavity aimed to balance the dispersion and nonlinearity, facilitating the initiation of self-started mode-locked pulses. The EDFL initiated the generation of mode-locked pulses at a threshold pump power of 81.37 mW. The mode-locking operation continued as the pump power was further increased, sustaining up to 113.68 mW. This indicates that the use of the Ti_3AlC_2 SA was effectively facilitating pulse shaping and stabilizing the mode-locked generation within the EDFL cavity. Fig. 6(a) illustrates the output spectrum of the mode-locked EDFL at a pump power of 81.37 mW. The laser operated at a wavelength of 1558.96 nm, a shift from the previous Q-switched laser's wavelength due to the significantly higher pumping power employed in the mode-locked operation.

In Fig. 6(b), a typical oscilloscope trace of the mode-locked pulse train at a pump power of 113.68 mW is presented, showing highly stable pulses with a uniform distribution of peak intensity. The inset of Fig. 6(b) displays the corresponding two-pulse envelopes with a time interval of 1.03 ns, aligning well with the round-trip time of the cavity. Notably, no pulse shivering was observed in the oscilloscope trace. The mode-locked laser operates at a pulse rate of 969.3 kHz and a pulse duration of 300 ns. Fig. 6(c) illustrates the radio frequency (RF) spectrum with a bandwidth of 15 MHz, providing a visual representation of the stability of the mode-locked laser with a fundamental repetition rate of 969.3 kHz. The signal-to-noise ratio (SNR) of the fundamental frequency was measured at 75.16 dB, further attesting to the stability of the mode-locked pulses.

In Fig. 6(d), the graph of output power and pulse energy as a function of pump power is presented, revealing a linear relationship between both parameters and pump power. The maximum average output power reached 3.19 mW, corresponding to a pulse energy of 3.29 nJ under a pump power of 113.68 mW. A continuous 4-hour observation of the oscilloscope traces and optical spectra of the mode-locked pulses verified the long-term stability of the fiber laser. The pulse train and the central wavelength of the spectrum remained consistently stable throughout the observation period. Additionally, after a 24-hour pause in laser operation followed by restarting the pump, the mode-locked pulses continued to output stably, and the laser center wavelength remained stable at 1558.96 nm, highlighting the long-term stability of the laser system.

In addition to its applications in Q-switching and mode-locking, Ti_3AlC_2 material shows promising potential in random lasing applications [21]. By leveraging its unique properties, Ti_3AlC_2 can be utilized to create disordered structures, exploiting phenomena like multiple light scattering to facilitate the development of the innovative low threshold random lasers [22].

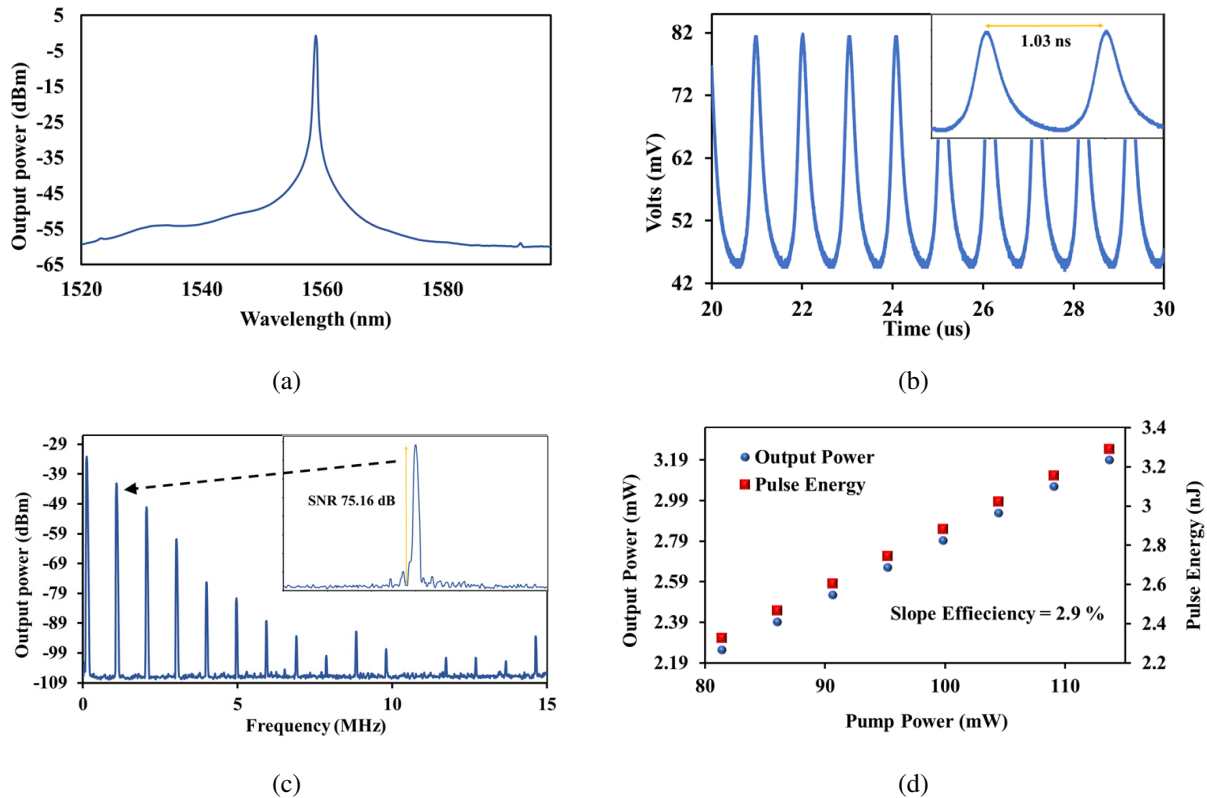


FIG. 6. Mode-locking performance: (a) output spectrum (b) Oscilloscope trace. Inset shows the two-pulse envelop (c) RF spectrum. Inset shows the enlarged fundamental mode (d). Output power and pulse energy versus pump power.

5. Conclusion

The successful demonstration of both Q-switched and mode-locked EDFLs operating in the $1.55 \mu\text{m}$ regime, utilizing the newly developed Ti_3AlC_2 as a SA, marks a significant achievement in fiber laser technology. Initially, the Ti_3AlC_2 thin film was introduced into the laser cavity, sandwiched between two fiber ferrules, to generate a passively Q-switched EDFL. The resulting stable Q-switched pulse train operated at a center wavelength of 1531 nm. As the pump power increased from 25.98 to 58.29 mW, the repetition rate rose from 35.0 to 50.8 kHz, while the pulse width decreased from 6.58 to $3.40 \mu\text{s}$. At a pump power of 58.29 mW, the system achieved a maximum output power of 2.49 mW and a pulse energy of 49.02 nJ. The Q-switched EDFL exhibited a high SNR of 71.42 dB, indicating stable pulse generation. The introduction of a 200 m SMF into the laser cavity allowed for the transition to a mode-locking regime, resulting in a laser with a central wavelength of 1558.96 nm. In this mode-locked laser configuration, the repetition rate reached 969.3 kHz, and the pulse width measured 300 ns within the pump power range of 81.37 to 113.68 mW. These results indicate the potential of the Ti_3AlC_2 -based SA as a promising candidate for both Q-switching and mode-locking applications in EDFLs.

References

- [1] Dong L., Samson B. *Fiber Lasers: Basics, Technology, and Applications*. CRC press, New York, 2016.
- [2] Shi W., et al. Fiber lasers and their applications. *Applied optics*, 2014, **53** (28), P. 6554–6568.
- [3] Sun S., et al. Demonstration of passively Q-switched and mode-locked operations through dispersion control in Er-doped fiber lasers with a cylindrite-based saturable absorber. *J. of Luminescence*, 2022, **250**, 119064.
- [4] Liu W., et al. 2D Materials for Fiber Lasers: Recent Advances of 2D Materials in Nonlinear Photonics and Fiber Lasers. *Advanced Optical Materials*, 2020, **8** (8), 2070031.
- [5] Zhang Y., et al. Study of the influence of SESAM parameters on the evolution of mode-locked pulses at different repetition rates. *Applied Physics B*, 2021, **127** (8), P. 1–10.
- [6] Nishizawa N., et al. Dynamics of a dispersion-managed passively mode-locked Er-doped fiber laser using single wall carbon nanotubes. *Photonics*, 2015, **2** (3), P. 808–824.
- [7] Haris H., et al. Generation of Vector Soliton Pulses with Graphene Oxide Film in Mode-locked Erbium-doped Fiber Laser Cavity. *Nonlinear Optics Quantum Optics-Concepts in Modern Optics*, 2020, **52** (1–2), P. 111–118.
- [8] Hu J.-W., et al. Passively mode-locked Er-doped fiber laser based on a semi-metallic InBi saturable absorber. *J. of Physics D: Applied Physics*, 2021, **55** (10), 105104.
- [9] Haris H., et al. Mode-Locked YDFL Using Topological Insulator Bismuth Selenide Nanosheets as the Saturable Absorber. *Crystals*, 2022, **12** (4), 489.

- [10] Ismail E., et al. Black phosphorus crystal as a saturable absorber for both a Q-switched and mode-locked erbium-doped fiber laser. *RSC Advances*, 2016, **6** (76), P. 72692–72697.
- [11] Tiu Z., et al. Application of transition metal dichalcogenide in pulsed fiber laser system. *Materials Research Express*, 2019, **6** (8), 082004.
- [12] Rosol A.H.A., et al. Nanosecond pulses generation with rose gold nanoparticles saturable absorber. *Indian J. of Physics*, 2020, **94** (7), P. 1079–1083.
- [13] Jafry A.A.A., et al. MXene $Ti_3C_2T_x$ as a passive Q-switcher for erbium-doped fiber laser. *Optical Fiber Technology*, 2020, **58**, 102289.
- [14] Fu B., et al. MXenes: Synthesis, optical properties, and applications in ultrafast photonics. *Small*, 2021, **17** (11), 2006054.
- [15] Gonzalez-Julian J. Processing of MAX phases: From synthesis to applications. *J. of the American Ceramic Society*, 2021, **104** (2), P. 659–690.
- [16] Khazaei M., et al. Recent advances in MXenes: From fundamentals to applications. *Current Opinion in Solid State and Materials Science*, 2019, **23** (3), P. 164–178.
- [17] Gogotsi Y., Anasori B. The rise of MXenes. *ACS Nano*, 2019, **13** (8), P. 8491–8494.
- [18] Zhang Z., et al. On the formation mechanisms and properties of MAX phases: A review. *J. of the European Ceramic Society*, 2021, **41** (7), P. 3851–3878.
- [19] Sun Z. Progress in research and development on MAX phases: a family of layered ternary compounds. *Int. Materials Reviews*, 2011, **56** (3), P. 143–166.
- [20] Wu K., et al. High-performance mode-locked and Q-switched fiber lasers based on novel 2D materials of topological insulators, transition metal dichalcogenides and black phosphorus: review and perspective. *Optics Communications*, 2018, **406**, P. 214–229.
- [21] Bazhenov A.Y., et al. Random Laser Based on Materials in the Form of Complex Network Structures. *JETP Letters*, 2023, **117** (11), P. 814–820.
- [22] Wiersma D.S. Disordered photonics. *Nature Photonics*, 2013, **7** (3), P. 188–196.

Submitted 6 January 2024; revised 25 March 2024; accepted 26 March 2024

Information about the authors:

Syed Ziad Z. Aljunid – Department of Electrical Engineering, Faculty of Engineering, University of Malaya, Kuala Lumpur 50603, Malaysia; ORCID 0009-0003-9890-6926; 22064743@siswa.um.edu.my

Nurul Athirah M. A. Ghafar – Department of Electrical Engineering, Faculty of Engineering, University of Malaya, Kuala Lumpur 50603, Malaysia; ORCID 0000-0003-4557-5695; athirahghafar97@gmail.com

Bilal A. Ahmad – Department of Communication Engineering, Al-Ma'moon University College, Al-Washash, 700921 Baghdad, Iraq; belalanwer@yahoo.com

Retna Apsari – Department of Physics, Faculty of Science and Technology, Airlangga University, Surabaya (60115) Indonesia; ORCID 0000-0002-3597-5938; retna-a@fst.unair.ac.id

Sulaiman W. Harun – Department of Electrical Engineering, Faculty of Engineering, University of Malaya, Kuala Lumpur 50603, Malaysia; Department of Physics, Faculty of Science and Technology, Airlangga University, Surabaya (60115) Indonesia; ORCID 0000-0003-4879-5853; swharun@um.edu.my

Conflict of interest: the authors declare no conflict of interest.

Nucleation of magnetic skyrmions at a notch

Maria N. Potkina^{1,b}, Igor S. Lobanov^{2,b}¹Infochemistry Scientific Center, ITMO University, St. Petersburg, Russia²Faculty of Physics, ITMO University, St. Petersburg, Russia^apotkina.maria@yandex.ru, ^blobanov.igor@gmail.com

Corresponding author: M. N. Potkina, potkina.maria@yandex.ru

PACS 82.20.Pm, 34.10.+x, 75.40.Mg

ABSTRACT Magnetic skyrmions are considered promising candidates for coding bits of information in racetrack memory devices. Information recording in such devices is assumed to occur by creating skyrmions. This work is devoted to finding solutions to make this process as energy-efficient as possible. One of the factors influencing the creation of skyrmions is the geometry of the track on which recording takes place. We study the influence of the shape and size of track boundary notches on the energy barriers of skyrmion nucleation. We show that skyrmions generation is facilitated by the presence of irregularities at the track boundary and the best solution is a deep narrow notch. On the other hand the skyrmion nucleation rate is smaller for smooth boundaries and skyrmions generation can be suppressed by their interaction with the track boundary, if notch size is smaller than the skyrmion radius. These results can be used in development of future memory devices based on skyrmions.

KEYWORDS transition state theory, topological magnetic solitons, nucleation, collapse, lifetime.

ACKNOWLEDGEMENTS MNP thank Y.M. Beltukov for useful discussions. The study was supported by the Russian Science Foundation grant No. 22-72-00059, <https://rscf.ru/en/project/22-72-00059/>. Priority 2030 is acknowledged for infrastructure support.

FOR CITATION Potkina M.N., Lobanov I.S. Nucleation of magnetic skyrmions at a notch. *Nanosystems: Phys. Chem. Math.*, 2024, **15** (2), 192–200.

1. Introduction

Magnetic racetrack memory is a perspective device for data storage proposed in 2008 by Parkin [1]. Currently large companies such as IBM are close to practical implementation of the devices, which requires to overcome some technical problems [2, 3]. Initial racetrack device was supposed to use domain wall (DW) as information carrier [1], but further research suggests that magnetic skyrmion (Sk) can be a better information carrier [3, 4]. In particular, Sk has smaller chances to pin to impurities than DW, hence energy consumption of Sk based devices is smaller [5–7], moreover Sk velocity can even increase due to interaction with impurities [8]. Function of Sk racetrack memory device consists of creation of Sk on the track (writing bit), moving Sk along the track (register shift), detection of Sk (reading) and annihilation of Sk (erasing). The material that the track is made of should both provide lifetime of Sk of decades at room temperature to be a reliable data storage, and Sk creation and annihilation should be energy efficient. Skyrmions stable at room temperature was found in ultrathin Pt/Co/MgO nanostructures [9]. Stability of Sk in Fe monolayer on an Ir(111) substrate was demonstrated in [10], and is theoretically predicted in [11, 12]. Creation of Sk can be achieved by several means, among which local heating using laser irradiation [13], applying local magnetic field [14] or by injection of current [15, 16]. The Sk generation can be facilitated by geometry of the system [17]. In particular, Sk tends to easier appear on the impurities [7, 18–21] as a result certain impurities can be used for Sk generation provided means to remove Sk from such an impurity, e.g. spin-polarized current can be applied. In the article we focus on creation of Sk by employing a notch, which represents the nonmagnetic impurity located at the track boundary. In [22] we have demonstrated that Sk generation rate due to thermal perturbations is much smaller at the boundary than inside the track. Below we show that the Sk generation at a side of the track can be significantly improved by creating a notch. This situation turns out to be more complicated for analysis, than the case of isolated impurity, because the interaction of Sk occurs not only with the impurity, but also with the boundary of the track.

An efficient generator of Sk should have the following properties: it should not create Sk in waiting mode and create Sk in robust manner under applied control. Nucleation of magnetic Sk on the track with a notch was investigated experimentally [23–26] and theoretically [27–32]. Despite the fact that the works [23–32] studied systems with different magnetic characteristics, geometries and external conditions, it was shown in all cases that notches may serve as a generator of skyrmions. However, these studies considered only one or several notches with fixed geometry, which is not enough for revealing the effect of notch design on Sk nucleation. In this work we systematically investigate this question

by making calculations of minimum energy pathes (MEPs) and energy barriers for skyrmion nucleation at notches of various geometry.

The notches can also be used to solve another problem with positioning of Sk on the track. While Sk can be moved by spin-polarized current [16, 33], electric current [34], or by voltage [35], small variation in the material parameters or in local current can lead to unexpected position of Sk and failure of the read operation. The problem can be solved by creating potentials wells, where Sk will slide to, when the spin transfer current is off. One way to create the well is to make a set of notches on the track [30, 36, 37]. Except for this purpose, at the same time, the notches can undesirably create and destroy Sk, therefore it is important to have design of the notches that resists to these processes. This issue will be analyzed in this work.

In this article we study skyrmion nucleation energy barrier on the notch in a magnetic track. For a fixed film parameters we study round and triangle notches for wide range of angles and radii. We show that Sk generation activation barrier depends on small size features such as single-atom steps on the boundary shape, medium size features such as notch curvature and on the distance from the notch to the global track boundary. Below we provide estimates for all the contributions.

2. Simulated system

We model a track for the movement of skyrmions in the racetrack memory [3]. The system is described by the atomistic generalized Heisenberg model with the energy

$$E = -J \sum_{\langle i,j \rangle} \mathbf{S}_i \cdot \mathbf{S}_j - \sum_{\langle i,j \rangle} \mathbf{D}_{ij} \cdot (\mathbf{S}_i \times \mathbf{S}_j) - \mu \sum_i \mathbf{B} \cdot \mathbf{S}_i - K \sum_i (S_i^z)^2, \quad (1)$$

where \mathbf{S}_i is a three-dimensional vector of unit length in the direction of the magnetic moment of a spin i of a two-dimensional crystal lattice. The first term describes the Heisenberg exchange with the parameter J for the magnetic moments of the nearest neighbors, the second term takes into account the Dzyaloshinskii-Moriya interaction (DMI) with the vector \mathbf{D}_{ij} lying in the plane of the track perpendicular to the vector connecting the spins i and j . The third and fourth terms correspond to the interaction with the external magnetic field and to the contribution of magnetic anisotropy with an easy axis along the z-axis perpendicular to the track plane. The spins magnetic moment μ , external field \mathbf{B} and anisotropy parameters K are assumed to be the same for all atoms. The summation $\langle i, j \rangle$ in (1) runs over all pairs of nearest neighbor atoms.

We studied Neel-type skyrmions on triangular lattice with the lattice constant $a = 2.7 \text{ \AA}$ and parameters $K = 0.49 \text{ meV}$, $|\mathbf{D}_{ij}| = 2.24 \text{ meV}$, $J = 7 \text{ meV}$, $\mu = 3\mu_B$, which corresponds to the Pd/Fe bilayer on the Ir(111) substrate [12]. This system maintains skyrmions of radius $3.95a$, defined as distance from skyrmion center to the ring $S^z = 0$. All calculations were carried out with the magnetic field value $|\mathbf{B}| = 3.75 \text{ T}$. Ground state for the selected parameters is ferromagnetic homogeneous everywhere except for boundary of the track where magnetic moments are twisted due to uncompensated DMI. For the considered parameters skyrmions are metastable states with energy 43.81 meV above ferromagnetic state. We are considering a part of the track, with the x-axis oriented along the track, and the y-axis oriented across it. Periodic boundary conditions are set along the track and the free boundary conditions are imposed on the track boundary. We simulated lattice of size $N_l \times N_w$ spins, with the first lattice vector coinciding with x-axis, that is we simulate track of length $N_l a$ and width $N_w b$, where $b = \sqrt{3}a/2$. We take the width N_w as $60 \div 90$ atomic rows, which was chosen large enough to make influence of boundaries negligible for isolated Sk at the central part of the simulated domain. N_l was chosen equal to N_w . Below we fix the coordinate system in such a way that spin (i, j) has the coordinates:

$$\frac{x}{a} = i + j \cos \frac{\pi}{3} + \frac{1 - N_l}{2}, \quad \frac{y}{a} = j \sin \frac{\pi}{3} + (1 - N_w) \sin \frac{\pi}{3}.$$

In the article we focus on generation of skyrmions due to boundary effects. The geometry of the magnetic film is taken into account by excluding spins belonging to the notch from the sums in (1). Due to discrete nature of the lattice, small variations in the geometry may lead to significant change in the number of spins belonging to the film, which, as will be shown below, affects Sk generation energy barrier. The notch is created by removing some spins from the track near its upper boundary. We consider two types of notches. The *round notch* is created by removing spins belonging to a circle:

$$x^2 + (y - Db)^2 \leq (Ra)^2,$$

where Ra is radius of curvature of the notch and Db is the distance from the circle center to the upper track side. We also remove the strip connecting the track boundary and the circle, see Fig. 2:

$$|x| < Ra \quad \text{and} \quad y > -Db.$$

Total penetration depth of the notch is $Ra + Db$. Large values of D are used to separate effect of interaction with the track boundary and with interaction with the notch.

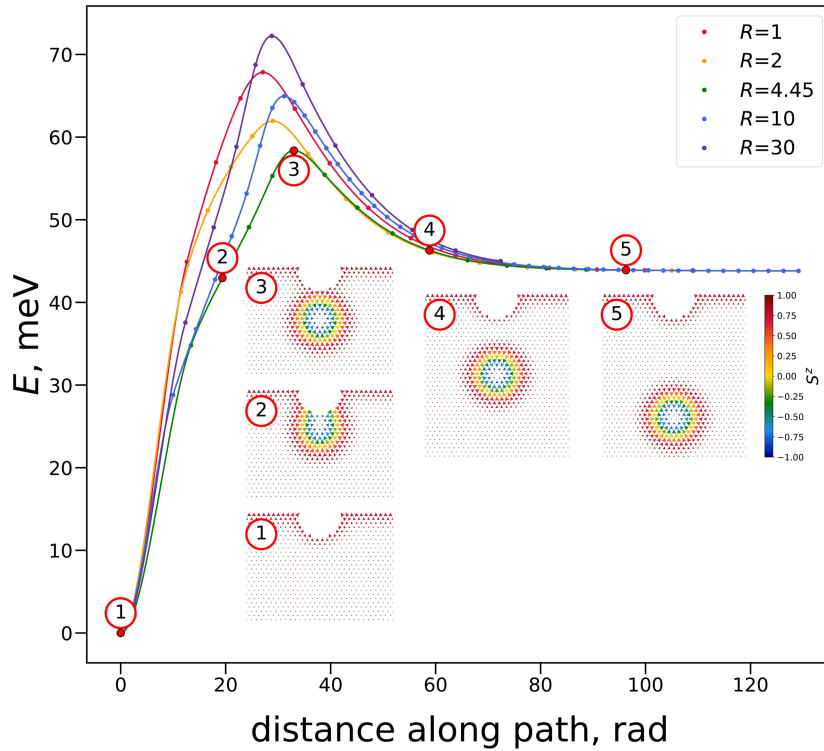


FIG. 1. MEPs for the nucleation of a skyrmion at round notch of various radius. The insets show magnetic configurations along the MEPs for $R = 4.45$. States 1 and 5 correspond to minima, state 3 corresponds to saddle point. The color in insets indicates the value of the out-of-plane component of the magnetic moments.

We also study *triangular notch*, where inner part of an angle is removed:

$$\left| \frac{x}{y+D} \right| < \tan \frac{\alpha}{2} \quad \text{and} \quad y > -Db,$$

see Fig. 6. The penetration depth in this case is D . Both notches are symmetric with respect to the line $x = 0$.

To estimate activation barriers for skyrmion nucleation we computed MEP, that is a continuous line in the phase space connecting initial and final state of magnetic texture such that each point of the line corresponds to the minimum of energy in the hyperplane orthogonal to the path at the point. In practice MEP is approximated by its discretization defined by several states of magnetization vectors (called images) computed numerically. In our computations we take $15 \div 50$ images along every path and employed string method for numerical optimization of MEP [38]. For all the paths the initial state was ferromagnetic and final state corresponds to the relaxed isolated skyrmion completely separated from the track boundary. To obtain MEP for skyrmion creation on the boundary, a reasonable initial approximation should be taken. In our study every image of the initial path contains a single copy of the equilibrium skyrmion with the center at $x = 0$ and $y = -30bl$, where l is the coordinate of reaction, $0 \leq l \leq 1$. The copy of Sk in the first image is centered at $(0, 0)$ and therefore extends beyond the track. The image is relaxed to the FM state during the MEP optimization.

3. Results

Round notch. We first studied the nucleation of skyrmions on the track with a semicircular notch centered on its boundary, see the notch shape in the insets of Fig. 1. Calculations of minimum energy paths were carried out for various radii of the notches, Fig. 1 shows the paths for the radii $R = 1, 2, 4.45, 10, 30$. As can be seen, the energy of the saddle point relative to the initial state without a skyrmion, that is, the barrier to nucleation, has a non-monotonic dependence on the notch radius. The insets in Fig. 1 show the magnetic configurations along the MEP for skyrmion nucleation at a notch radius of $R = 4.45$. Initial state 1 corresponds to the ground state having no skyrmions. Then the spins at the bottom of the notch begin to rotate so that a skyrmion is formed attached to the notch (inset 2). The maximum energy along the path corresponds to the state when the skyrmion core is fully formed and the boundaries of the skyrmion and the notch are in contact (inset 3). After passing the transition state the SK separates from the notch and moves away from it (insets 4 and 5).

We carried out calculations of the MEP for radii in the range from 1 to 30 with a step of 0.05 and obtained the dependence of the nucleation barriers on the radii of the notches, shown in Fig. 2 in blue. The energy barrier as the function of the notch radius oscillates with the period close to the lattice constant due to the discrete nature of the crystal lattice. The oscillations in most cases are associated with the appearance of a new series of vacancies with increasing notch size. The correlation between the number of removing atoms in the bottom row of the notch and the jumps in the barrier may be observed in Fig. 3a, which shows part of the dependence for the radius in Fig. 2a in the range from 13 to 14. Local maxima of the $\Delta E(R)$ dependence correspond to the maximum number of vacancies in the bottom row of notch, for example nine vacancies at $R = 13.85$, Fig. 3b, and local minima correspond to the appearance of a new row of vacancies with increasing radius, as for example in this case of $R = 13.9$ a new lower row of two atoms appeared (Fig. 3c).

When the radius of the notch tends to infinity, its boundary near the site of skyrmion nucleation tends to a straight boundary. Therefore, the barrier for skyrmion formation at the notch asymptotically tends to a constant value equal to the barrier for formation through the straight track boundary, $E_0 = 75.62$ meV, shown by green dashed line in Fig. 2a. Similar behavior is observed for the lower envelope, but in this case the notch boundary becomes similar to a flat boundary with the presence of one vacancy on it. The extreme point on the left on the blue graph corresponds to the situation of one vacancy on a straight boundary. The barrier in this case, according to our calculations, is $E_1 = 72.67$ meV, shown by purple dashed line.

To approximate the envelopes of the dependence of the barrier on the radius for $R > 16$, we used functions of the form $E_0 - p_0/R$ and $E_1 - p_1/R$ with parameters p_0 and p_1 , assuming the notch curvature is a perturbation parameter for

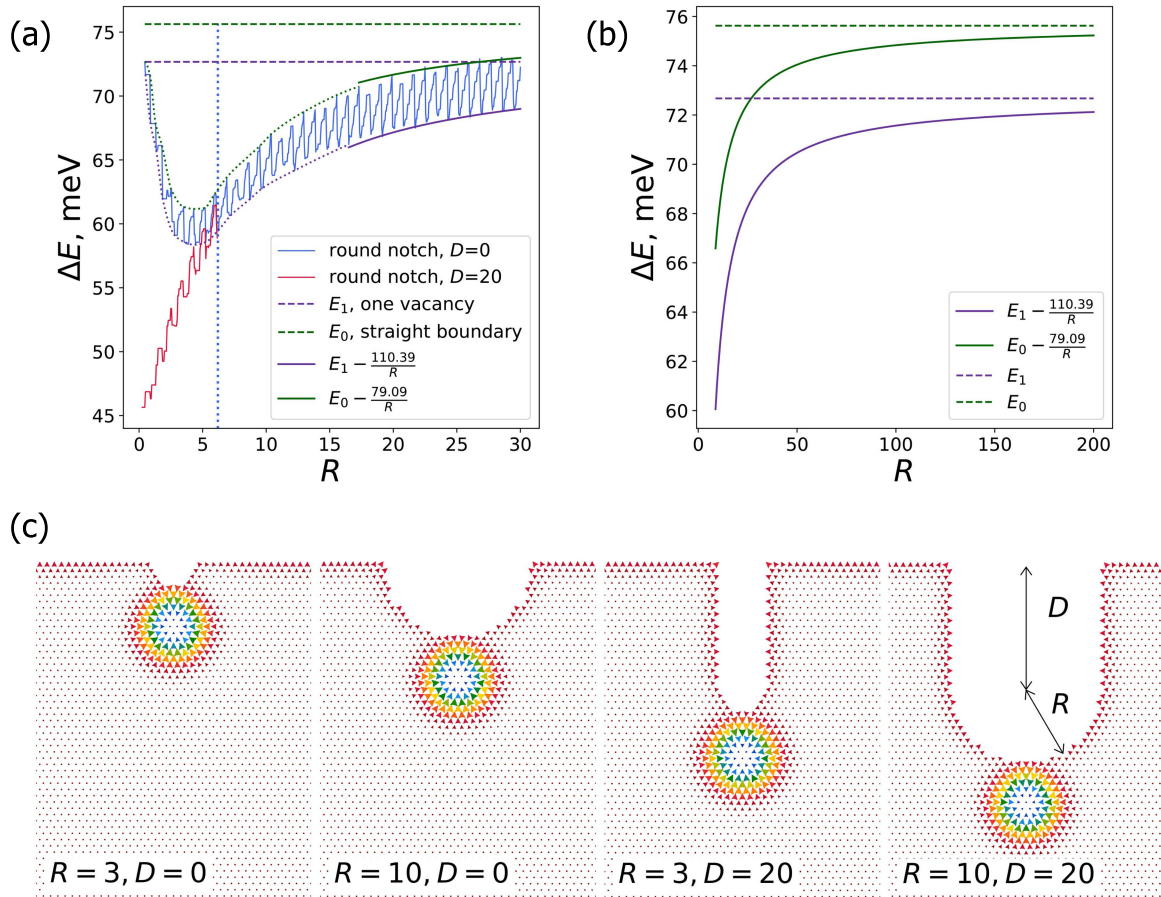


FIG. 2. (a) Energy barrier for skyrmion nucleation at the semicircular notch and round notch with depth $D = 20$ as a function of radius of notch. The vertical dotted line shows the radius value above which the barrier for nucleation at the semicircular notch and at the deep notch differ by less than 1%. Solid lines show approximations of envelopes of function of energy barrier for highest radii. Dashed lines shows asymptotics for upper and lower envelopes. (b) Approximations of envelopes and their asymptotics shown at larger interval of radius. (c) Transition state configurations for skyrmion nucleation at the boundary round notch with radius $R = 3$ and $R = 10$, and at deep round notch with depth $D = 20$ and radius $R = 3$ and $R = 10$.

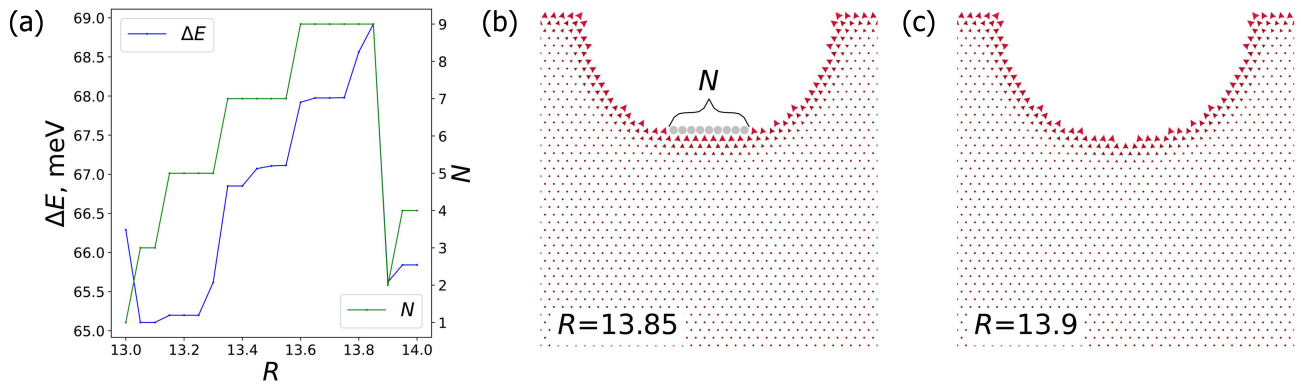


FIG. 3. (a) Energy barrier for skyrmion nucleation at the round notch and number of vacancies in the bottom row of notch as a function of radius of notch for $13 \leq R \leq 14$. Configuration of notch for radius $R = 13.85$ with exclusion of 9 atoms (b) and for radius $R = 13.9$ with exclusion of 2 atoms in the bottom row of the notch (c).

energy barrier of Sk creation on the flat boundary. Our fitting predicts the following interval of activation energy values for large R :

$$E_1 - 110 \text{ meV} \cdot R^{-1} \leq \Delta E \leq E_0 - 79 \text{ meV} \cdot R^{-1}.$$

The graph in Fig. 2b shows the envelopes and their asymptotic behavior over a larger range of radii. It allows to predict the approximate range of the barrier of skyrmion nucleation for specific value of notch radius.

As the radius decreases, the distance from the partially instantiated Sk at the transition state to the straight boundary decreases and it begins to influence the barrier. To decouple this effect from the influence of the curvature of the notch, we calculated the dependence of the barrier on the depth of the notch for the smallest Sk radius, Fig. 4a, that is the notch in the case is a chain of vacancies of one atom thick. We will further call a notch of this shape a needle. Fig. 4b and c show the saddle points for skyrmion nucleation for depths of 5 and 19. Note that the configurations differ: in the first case it has the shape of a drop, and in the second it has the shape of circle. This is because, as can be seen from Fig. 5, with an increase in D , an intermediate minimum (inset 3) and a second maximum (inset 4) appear on the MEP, which becomes dominant. This process is similar to the process of nucleation of Sk on impurities, which we studied earlier [7]. It also occurred in two stages, first the creation of a skyrmion attached to the impurity, then its separation from the impurity. As it is seen in Fig. 4a, the proximity of a flat boundary increases the barrier. This effect disappears with increasing D , and at $D > 10$ the variation of the barrier is less than 2%. Thus, considering a sufficiently deep notch makes it possible to practically avoid the influence of the boundary when studying the influence of the shape and size of the notch on the nucleation barrier. Therefore, we further calculated the nucleation barriers at a fixed notch depth $D = 20$ depending on the radius, which is shown by red in Fig. 2a. The blue dotted line in Fig. 2a shows the radius value above which the barriers of nucleation at a deep notch and at a semicircular notch with the same radius differ by less than 1%. Fig. 2c shows the spin configurations

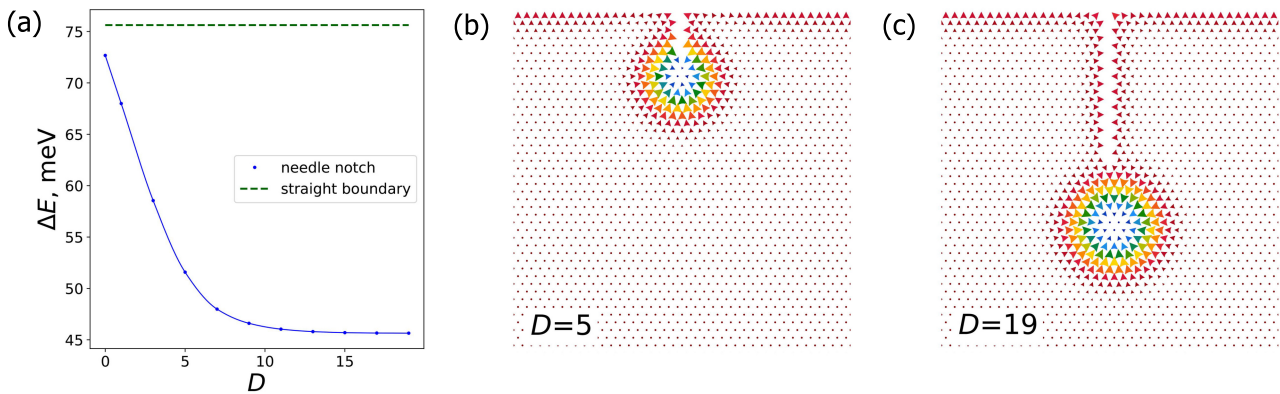


FIG. 4. Energy barrier for skyrmion nucleation at 1-atomic chain notch as a function of notch depth D . Transition states for skyrmion nucleation at the notches with depth $D = 5$ and $D = 19$.

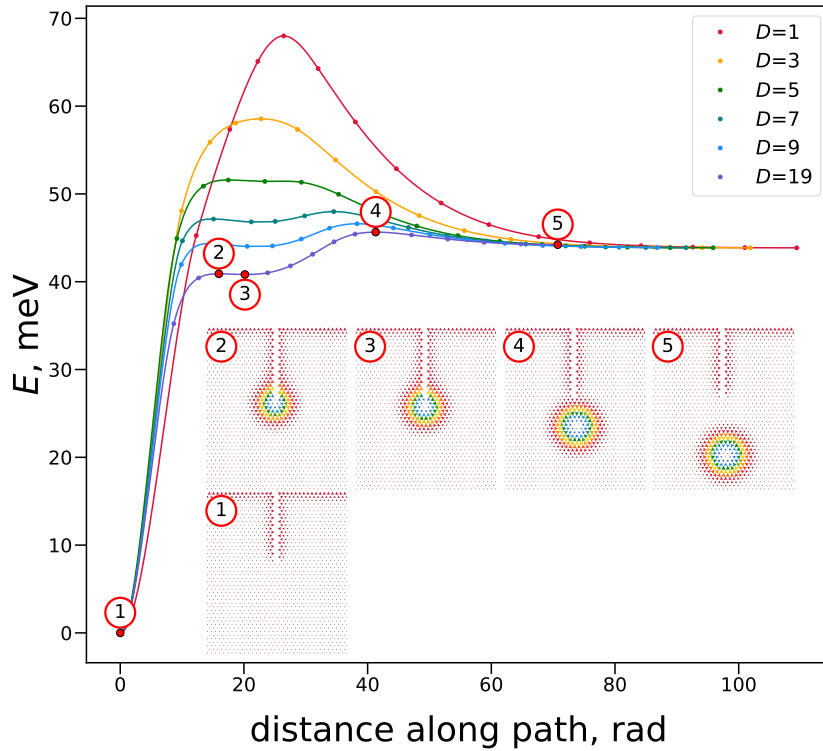


FIG. 5. MEPs for the nucleation of a skyrmion at needle notch of various depth. The insets show magnetic configurations along the MEP for notch depth $D = 19$. States 1, 3, 5 correspond to minima, states 2 and 4 correspond to saddle points.

of saddle points for nucleation on semicircular notches with radii $R = 3$ and 10 , and on notches with depth $D = 20$ and radii $R = 3$ and 10 , and the parameters D and R are indicated. We found that the barrier for nucleation at deep notch decreases down to the narrowest notches. Note that the drop in the barrier when new vacancies appear in the bottom row, discussed above, is qualitatively consistent with this result, since the notch becomes also sharper in that case.

As we have seen, the proximity of the flat boundary and the narrowness of the notch have opposite effects on the barrier of nucleation. The play of these two factors leads to the emergence of a minimum in the region of $R = 4$ for the envelopes shown by dotted curves in Fig. 2a. A minimum of the energy barrier, 58.36 meV, is reached when the notch radius is 4.45 , which is approximately equal to the Sk radius. Qualitatively the same result was obtained in [27]. There, the a skyrmion has been created on a notch by applying an electric current and it was found that skyrmions were born when the curvature radius is comparable to the size of the skyrmion.

Our calculations showed that the smallest barrier in a system with a circular notch is 45.65 meV and is achieved for the narrowest deep notch (smallest R for the red line in Fig. 2a), which corresponds to the needle notch shown in Fig. 4c. To reveal the reason of this result, we plotted the contributions to the energy of the transition state as a function of the notch radius, Fig. 6a, and density of total energy at the transition state, Fig. 6b. The smaller the notch radius, the smaller part of the skyrmion is excluded. As can be seen from Fig. 6b, the notch is located in a region with a negative total energy density. Therefore a narrower notch will lead to a decrease in the energy of the transition state. Fig. 6a shows that all contributions except for DMI one increase as curvature of notch decreases. Therefore the small activation barrier for the sharpest notch is attributed solely to DMI.

Triangular notch. Another basic situation that we studied was nucleation on a triangular shaped notch, Fig. 7b and c show the spin configurations for angles of 30° and 90° . To avoid the influence of a flat boundary, we chose a notch with a depth of $D = 20$, which in this case sets the height of the triangular notch. Fig. 7a shows the calculated dependence of the nucleation barriers on the notch angle. We see that the barrier decreases monotonically with decreasing angle, and the lowest value is achieved at zero angle, which again corresponds to the situation of the needle notch.

In both cases of triangular and round notches, Sk generation is easier for sharper notches. For all studied MEPs transition state (TS) is very similar to the equilibrium Sk touching the tip of the notch. The energy of TS is mainly affected by spins belonging both to the boundary of the track and to the TS. The number of the spins is determined by the “exit length”, to which a measure of effective angle can be attributed, that is, the angle of the triangular notch at which the same barrier value is obtained. Having the dependencies of the energy barrier on the radius of a deep circular notch

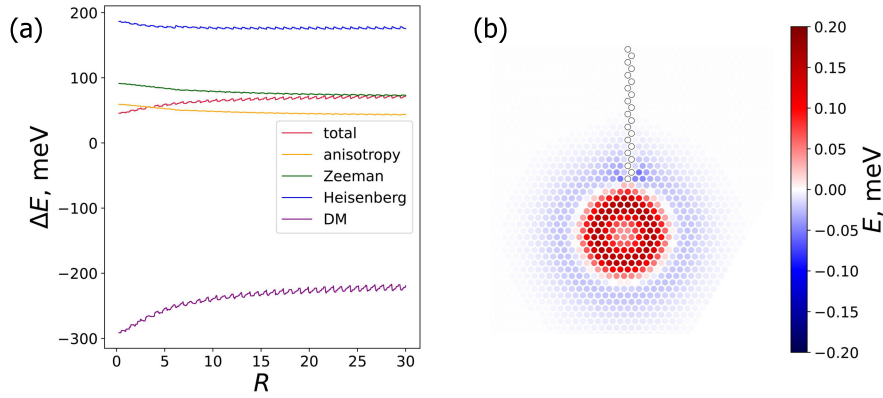


FIG. 6. (a) Contributions of Heisenberg exchange, DMI, anisotropy and Zeeman term to energy of the transition state as function of the round notch radius R for depth $D = 20$. (b) Density of total energy at transition state calculated relatively energy of state without skyrmion.

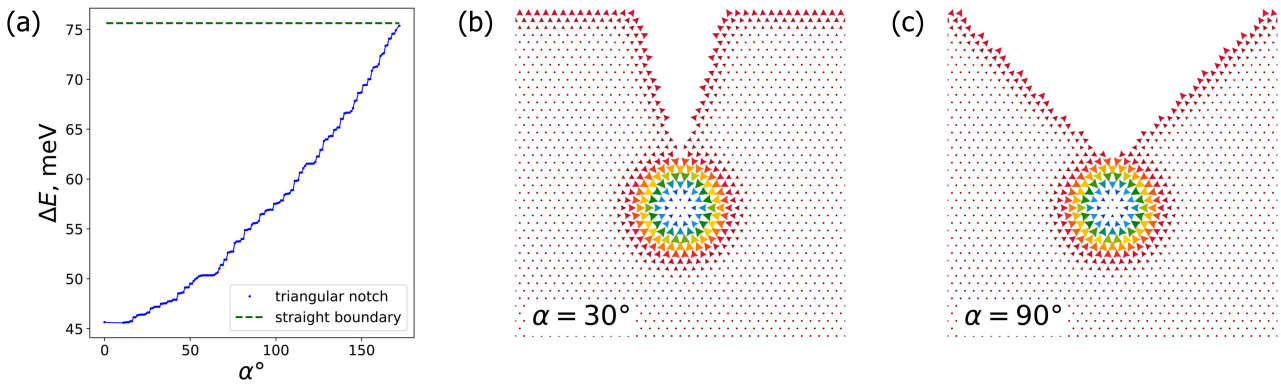


FIG. 7. (a) Energy barrier for skyrmion nucleation at triangular notch as a function of the angle of notch. Transition states for skyrmion nucleation at the notches with angle $\alpha = 30^\circ$ (b) and $\alpha = 90^\circ$ (c).

and on the angle for a triangular notch, we mapped the angle to the radius corresponding the same energy, which gives the effective angle as a function of the radius, Fig. 8. Due to discrete nature of the lattice, precise value of the angle is not strictly defined, thus an interval of angles corresponds to every notch radius. For small radii the effective angle is proportional to the radius:

$$\alpha_{eff} \sim R.$$

For large radii the effective angle dependence on the notch radius is less than variation of the angle due to discreteness of the boundary.

The obtained above results for round and triangular notches allow to estimate activation energy of Sk creation on arbitrary shaped notch. Indeed, an arbitrary boundary can be decomposed to a number of smooth curves connected at non zero angles. The activation barrier for every corner can be estimated by the barrier of the triangular notch having the same angle. The smooth curves are defined by their curvature. As we have seen above, the smallest energy barrier corresponds to the lowest radius of curvature. Hence the activation barrier for a curve can be estimated by the barrier for round notch with the radius equals to the minimum radius of curvature of the curve. The minimal of the barriers of the curves and the corners gives an approximation for the barrier of the corresponding notch.

4. Discussion.

We studied the nucleation of skyrmions on a semicircular notch with the center located at boundary of track, which was previously considered in [27]. It was found that skyrmions are best produced when the notch has a radius that matches the radius of the skyrmion, which is consistent with the results of the work [27]. The barrier depends not only on the radius, but also on the distance to the flat boundary. If we remove the influence of the boundary, the barrier will be determined entirely by the narrowness of the notch. However, if the notch tip is close to the boundary, the energy barrier is larger. So, two factors contribute to the barrier: the value of the radius of the notch, and the proximity to the flat boundary.

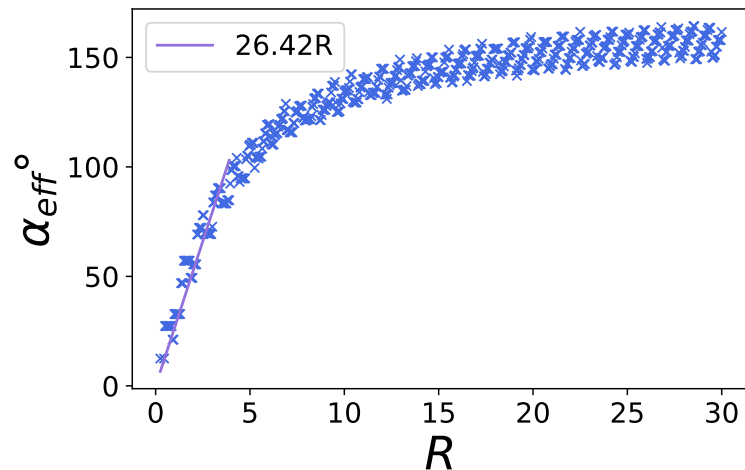


FIG. 8. Correspondence of the radius of a round notch with depth $D = 20$ to the effective angle of triangular notch giving the same nucleation barrier.

Their sum gives the minimum of barrier, or in other words, the most effective Sk generation, that was also observed in the article [27].

For rectangular notch the authors of [27] found that the angle of notch corner 90° is most suitable for the Sk creation, which in contrast to our finding that the best case for creation is the sharpest angle. The reason for that disagreement may be the following. Our calculations showed that the most energetically favorable direction of skyrmion motion during nucleation is along the bisector of notch angle. In the work [27], the direction of movement was different due to the action of the current and perhaps this led to the increase of current density in case of sharpest notches. The current add energy to the system and it can thereby overcome the energy barrier for nucleation, and eventually a skyrmion will appear. We estimated the magnitude of the barrier from which one can obtain an estimate for the minimum current required for nucleation. However, the orientation of the angle notch relative to the direction of the current constrains possible variations of the magnetic moments, therefore the actual magnitude of the current required for nucleation can be higher, which is not taken into account in our approach.

In this work, we did not consider the issue of skyrmion annihilation at the notch. The barrier for annihilation can be found as the difference between the nucleation barrier and the free skyrmion energy calculated relative to the ferromagnetic state. The latest does not depend on the geometry of the sample. Therefore, the behavior of the dependencies of annihilation barriers on geometry qualitatively coincides with the behavior of nucleation barriers presented in this work. The mechanism of skyrmion annihilation on a circular notch of two different radii was considered in the work [30]. It was found that a smaller barrier was obtained with a smaller notch radius, under condition the size of the notch exceeded the size of the skyrmion, which qualitatively coincides with our results.

Previous studies of skyrmion nucleation on a track [20] allow us to compare the results for a track with a straight boundary and with a notch. The barriers for nucleation inside the track and at its boundary were 85.07 meV and 75.62 meV, respectively, while the minimum barrier at the semicircular notch is 58.37 meV, and the barrier at the needle-type notch is 45.65 meV. Thus, for this system, the use of a notch allows one to reduce the barrier of nucleation by up to 50% compared to a track with straight boundaries. Thus, using track notches to create skyrmions could make the process of recording information in memory devices more energy efficient.

Our results allow us to make recommendation for notch design in systems where they are used for positioning Sk. Since energy barriers increase with increasing radius or angle of the notch, for these purposes it is better to use the notch with the largest radii or angles to avoid unwanted creation or destruction of Sk.

In this work, we showed that the Sk nucleation barrier depends both on the local characteristics at the tip of the notch and on the sharpness (radius or angle) of the notch. Also, if the notch is shallow, the barrier will increase due to the proximity of the straight border on either side of the notch. Our calculations provide guidance for creating skyrmions in racetrack memory, namely to use a notch as narrow as possible and with sufficient depth to avoid the influence of flat boundaries.

References

- [1] Parkin S. S. P., Hayashi M., Thomas L. Magnetic domain-wall racetrack memory. *Science*, 2008, **320**, P. 190–194.
- [2] Parkin S. S. P., Yang S.-H. Memory on the racetrack. *Nat. Nanotechnol.*, 2015, **10**, P. 195–198.
- [3] Tomasello R., Martinez E., Zivieri R., et al. A strategy for the design of skyrmion racetrack memories. *Sci. Rep.*, 2014, **4**, 6784.
- [4] Kang W., Huang Y., Zhang X., et al. Skyrmion-electronics: an overview and outlook. *Proceedings of the IEEE*, 2016, **104**(10), P. 2040–2061.

- [5] Stier M., Strobel R., Krause S., et al. Role of impurity clusters for the current-driven motion of magnetic skyrmions. *Phys. Rev. B*, 2021, **103**, P. 054420.
- [6] Zhu H., Xiang G., Feng Y., et al. Dynamics of elliptical magnetic skyrmion in defective racetrack. *Nanomater.*, 2024, **14**(3), P. 312.
- [7] Potkina M.N., Lobanov I.S., Uzdin V.M. Nonmagnetic impurities in skyrmion racetrack memory. *Nanosystems: phys., chem., math.*, 2020, **11** (6), P. 628–635.
- [8] Reichhardt C., Reichhardt C. J. O., Milosevic M. V. Statics and dynamics of skyrmions interacting with disorder and nanostructures. *Rev. Mod. Phys.*, 2022, **94**, P. 035005.
- [9] Boulle O., Vogel J., Yang H., et al. Room-temperature chiral magnetic skyrmions in ultrathin magnetic nanostructures. *Nat. Nanotechnol.*, 2016, **11**, P. 449–454.
- [10] Heinze S., von Bergmann K., Menzel M., et al. Spontaneous atomic-scale magnetic skyrmion lattice in two dimensions. *Nat. Phys.*, 2011, **7**, P. 713–718.
- [11] Bessarab P. F., Müller G. P., Lobanov I. S., et al. Lifetime of racetrack skyrmions. *Sci. Rep.*, 2018, **8**, P. 3433.
- [12] Hagemeyer J., Romming N., Bergmann K. V., Vedmedenko E. Y., Wiesendanger R. Stability of single skyrmionic bits. *Nat. Commun.*, 2015, **6**, P. 8455.
- [13] Koshibae W., Nagaosa N. Creation of skyrmions and antiskyrmions by local heating. *Nat. Commun.*, 2014, **8**, P. 5148.
- [14] Zhou Y., Iacocca E., Awad A. A., et al. Dynamically stabilized magnetic skyrmions. *Nat. Commun.*, 2015, **6**, 8193.
- [15] Romming N., Hanneken C., Menzel M., et al. Writing and deleting single magnetic skyrmions. *Science*, 2013, **341**, P. 636–639.
- [16] Sampaio J., Cros V., Rohart S., Thiaville A., Fert A. Nucleation, stability and current-induced motion of isolated magnetic skyrmions in nanostructures. *Nat. Nanotechnol.*, 2013, **8**, P. 839–844.
- [17] Jiang W., Upadhyaya P., Zhang W., et al. Blowing magnetic skyrmion bubbles. *Science*, 2015, **349**, P. 283–286.
- [18] Uzdin V.M., Potkina M.N., Lobanov I.S., Bessarab P.F., Jónsson H. The effect of confinement and defects on the thermal stability of skyrmions. *Physica B: Condensed Matter*, 2018, **549**, P. 6–9.
- [19] Potkina M.N., Lobanov I.S., Uzdin V.M. Fine energy structure of a magnetic skyrmion localized on a nonmagnetic impurity in an external magnetic field. *Physics of Complex Systems*, 2020, **1** (4), P. 165–168.
- [20] Uzdin V.M., Potkina M.N., Lobanov I.S., Bessarab P.F., Jónsson H. Energy surface and lifetime of magnetic skyrmions. *J. Magn. Magn. Mater.*, 2018, **459**, P. 236–240.
- [21] Hanneken C., Kubetzka A., von Bergmann K., Wiesendanger R. Pinning and movement of individual nanoscale magnetic skyrmions via defects. *New J. Phys.*, 2016, **18**(5), P. 055009.
- [22] Potkina M. N., Lobanov I. S., Uzdin V. M. Nucleation and collapse of magnetic topological solitons in external magnetic field. *Nanosystems: Phys. Chem. Math.*, 2023, **14** (2), P. 216.
- [23] Wang W., Song D., Wei W., et al. Electrical manipulation of skyrmions in a chiral magnet. *Nat. Commun.*, 2022, **13**, 1593.
- [24] Yu X. Z., Morikawa D., Nakajima K., Shibata K., Kanazawa N., Arima T., Nagaosa N., Tokura Y. Motion tracking of 80-nm-size skyrmions upon directional current injections. *Sci. Adv.*, 2020, **6**, eaa9744.
- [25] Twitchett-Harrison A. C., Loudon J. C., Pepper R. A., Birch M. T., Fangohr H., Midgley P. A., Balakrishnan G., Hatton P. D. Confinement of skyrmions in nanoscale FeGe device-like structures. *ACS Appl. Electron. Mater.*, 2022, **4** (9), P. 4427–4437.
- [26] Büttner F., Lemesh I., Schneider M., et al. Field-free deterministic ultrafast creation of magnetic skyrmions by spin–orbit torques. *Nature Nanotech.* 2017, **12**, P. 1040–1044.
- [27] Iwasaki J., Mochizuki M., Nagaosa N. Current-induced skyrmion dynamics in constricted geometries. *Nature Nanotech.*, 2013, **8**, P. 742–747.
- [28] Koshibae W., Kaneko Y., Iwasaki J., Kawasaki M., Tokura Y., Nagaosa N. Memory functions of magnetic skyrmions. *Jpn J. Appl. Phys.*, 2015, **54**, P. 053001.
- [29] Behera A. K., Murapaka C., Mallick S., Singh B. B., Bedanta S. Skyrmion racetrack memory with an antidot. *J. Phys. D: Appl. Phys.*, 2021, **54**, P. 025001.
- [30] Suess D., Vogler C., Bruckner F., Heistracher P., Slanovc F., Abert C. Spin torque efficiency and analytic error rate estimates of skyrmion. *Sci. Rep.*, 2019, **9**, P. 4827.
- [31] Dutta S., Nikonov D. E., Bourianoff G., Manipatruni S., Young I. A., Naeemi A. Skyrmion nucleation via localized spin current injection in confined nanowire geometry in low chirality magnetic materials. 2018. arXiv: 10.48550/arXiv.1801.10525.
- [32] Xu M., Zhang J., Meng D., Zhang Z., Jiang G. The influence of introducing holes on the generation of skyrmions in nanofilms. *Phys. Lett. A.*, 2022, **433**, P. 128034.
- [33] Fert A., Cros V., Sampaio J. Skyrmions on the track. *Nat. Nanotechnol.*, 2013, **8** (3), 152.
- [34] Jiang W., Zhang W.; Yu G., et al. Mobile Néel skyrmions at room temperature: status and future. *AIP Advances*, 2016, **6**, P. 055602.
- [35] Kang W., Huang Y., Zheng C. et al. Voltage controlled magnetic skyrmion motion for racetrack memory. *Sci Rep*, 2016, **6**, 23164. <https://doi.org/10.1038/srep23164>
- [36] Morshed M. G., Vakili H., Ghosh A. W. Positional stability of skyrmions in a racetrack memory with notched geometry. *Phys. Rev. Applied*, 2022, **17**, P. 064019.
- [37] Belrhazi H., El Hafidi M. Nucleation and manipulation of single skyrmions using spin-polarized currents in antiferromagnetic skyrmion-based racetrack memories. *Sci. Rep.*, 2022, **12**, 15225.
- [38] Weinan E., Ren W., Vanden-Eijnden E. String method for the study of rare events. *Phys. Rev. B*, 2002, **66**, P. 052301.

Submitted 25 February 2024; revised 13 April 2024; accepted 14 April 2024

Information about the authors:

Maria N. Potkina – Infochemistry Scientific Center, ITMO University, 197101 St. Petersburg, Russia; ORCID 0000-0002-1380-2454; potkina.maria@yandex.ru

Igor S. Lobanov – Faculty of Physics, ITMO University, 197101 St. Petersburg, Russia; ORCID 0000-0001-8789-3267; lobanov.igor@gmail.com

Conflict of interest: the authors declare no conflict of interest.

Some features of the thermoelectric properties of the “metal-carbon film” junction

Rostyslav V. Shalayev^{1,a}, Anatoliy I. Izotov^{1,b}, Vladimir V. Syrotkin^{1,c}

¹Galkin Donetsk Institute for Physics and Engineering, Donetsk, Russia

^asharos@donfti.ru, ^bizotov.anatoli@gmail.com, ^cvladir.52@mail.ru

Corresponding author: R. V. Shalayev, sharos@donfti.ru

PACS 81.15.Gh; 84.37.+q; 85.30.Hi

ABSTRACT Carbon films were obtained by magnetron sputtering of graphite in an argon atmosphere on various metal substrates. As a result, a “metal-semiconductor” junction is formed due to the fact that the temperature dependence of the film resistance is of a semiconductor nature. The current-voltage characteristics of the junction were studied at various ambient temperatures, and the degradation of its electrical properties over time was discovered.

KEYWORDS carbon films, metal-semiconductor contact, thermoelectric properties

FOR CITATION Shalayev R.V., Izotov A.I., Syrotkin V.V. Some features of the thermoelectric properties of the “metal-carbon film” junction. *Nanosystems: Phys. Chem. Math.*, 2024, **15** (2), 201–203.

1. Introduction

The development of electronics is accompanied by creation of new technologies and semiconductor materials that can increase the efficiency and reliability of electronic devices. Recently, semiconductor carbon materials have been actively studied [1–4], which often have more outstanding properties than classical semiconductors and are of interest as materials for micro- and nanoelectronic products. Although silicon and gallium arsenide still remain the dominant semiconductor materials, the traditional silicon platform no longer meets many modern requirements, and increasingly, researchers are citing carbon as a potential replacement in certain niches. Due to the huge variety of allotropic forms (for example, graphene and similar structures), this material has considerable potential of applications in many fields, but it is of particular interest for electronics due to the higher mobility and, consequently, high speed, of charge carriers. Allotropic modifications differ by the structure of their crystal lattices, which affect the conductive properties of the material. For example, sp^2 -hybridized carbon conducts electricity well, but sp^3 -hybridized carbon does not. Therefore, depending on the ratio of carbon atoms with different types of hybridization, electrical properties can vary from semi-metallic (like graphite) to dielectric (like diamond). Thus, under certain conditions, carbon combines dielectric, conductor and semiconductor properties. It makes this material unique. Many researchers predict the possibility of implementing the idea of all-carbon high-speed nanoelectronics in the future [4, 5].

It is known that the oldest practical semiconductor device is a metal-semiconductor contact. Such contact junctions are widely used in electronics and have the unique properties that allow one to create efficient devices and instruments. However, the mechanisms of current transfer in such structures remain incompletely studied, and, for example, it is not clear due to which reason, the Schottky barrier irreversibly transforms into an ohmic contact [6]. In connection with the above, a rather urgent task is to study the metal-carbon transition (where carbon exhibits semiconductor properties), which can demonstrate interesting contact phenomena.

This work examines some of the electrical properties of such a contact junction depending on the ambient temperature, as well as changes in such properties over time.

2. Experimental technique

Samples for the research were obtained by magnetron sputtering of graphite in an argon atmosphere. Carbon films were deposited on substrates made of dielectric (cover glass) and various metals (titanium, steel, niobium, etc.) [7]. Plasma was created using a planar DC magnetron with a flat cathode and an annular anode. The conditions for deposition of samples on all types of substrates were the same: the gas pressure in the chamber was 150 mTorr, the film growth time was 40 min, the substrate temperature was 350°C, and the magnetron current was 40 mA.

The electrical properties of the obtained samples were studied using the resistometric method in a heat chamber in the range from $\sim 20^\circ\text{C}$ to 150°C . To eliminate the influence of a highly conductive metal substrate the transverse conductivity was measured using a two-probe method in films deposited on a glass substrate. Longitudinal conductivity (along the direction of the film growth) was measured at the contact junction in the “metal substrate–carbon film–measuring contact” structure. The temperature dependences of the carbon films resistance and the current-voltage characteristics (CVC) of the “metal-carbon film” contact transition at different temperatures were studied. To study the processes of temporary

degradation of the contact junction, the current-voltage characteristics of the samples were remeasured 15–20 months after the samples were obtained, in order to evaluate changes in the characteristics.

3. Main results and discussion

As shown in [7], the temperature dependence of film resistance has classical semiconductor character - the resistance decreases with the temperature increasing. Thus, it is obvious that as a result of the work, the “metal-semiconductor” contact junction was obtained (where the semiconductor is the carbon film), which is the subject of this study. Let us consider some features of such contacts at different temperatures.

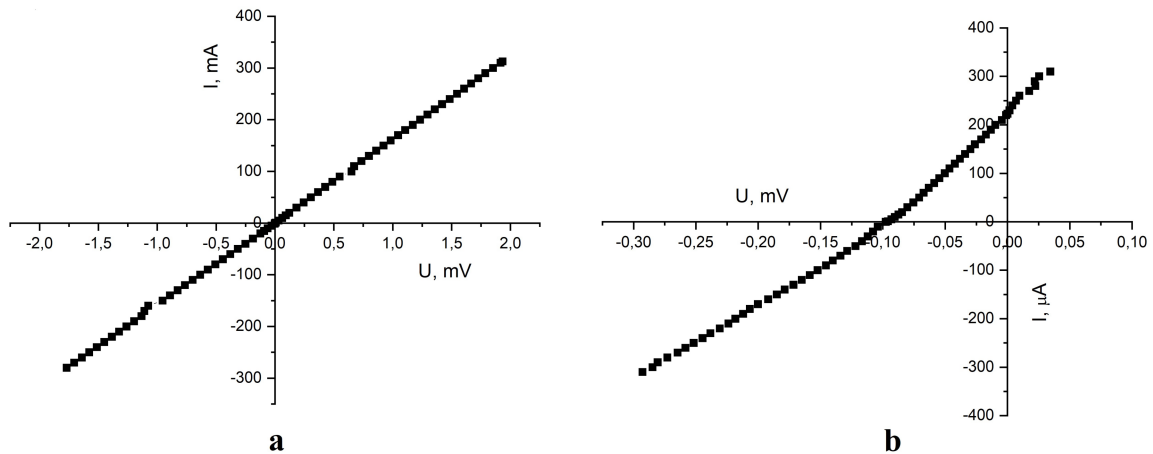


FIG. 1. Current-voltage characteristics of the “niobium-carbon” contact at room temperature (a) and when heated to 100°C (b)

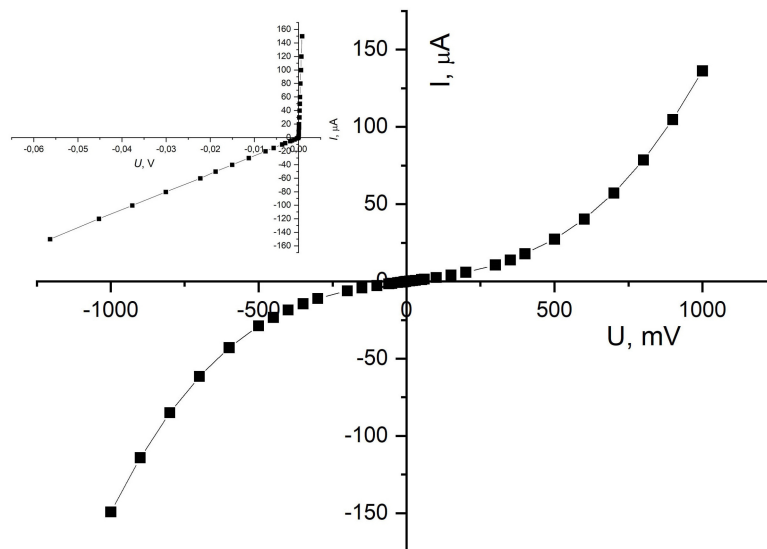


FIG. 2. Current-voltage characteristics of the titanium-carbon contact after 18 months from the moment the sample was obtained (the inset shows the original sample CVC)

Fig. 1 shows the current-voltage characteristics of the “niobium-carbon” contact at room temperature and under heating. It can be seen that the current-voltage characteristics have a symmetrical linear dependence, characteristic for ohmic contact. It is known that in such contacts, there are electric fields caused by the contact potential difference between the materials (which differ by the value of the work function) that make up the junction. The potential distribution in the semiconductor material of the “metal-semiconductor” contact can influence significantly on the current-voltage characteristics and current flow mechanisms of such junctions. In particular, in Fig. 1(b), a small contact potential difference is observed when the junction is heated to 100°C . This property may be interesting in some applied fields, correspondingly, further researches in this direction are perspective.

The current-voltage characteristics of titanium-carbon contact junction obtained some time ago (more than a year) were also re-examined. The initial contact transition, as shown in [7], demonstrated an asymmetrical nonlinear current-voltage characteristics (see inset in Fig. 2) and had the rectifying properties of a “metal-semiconductor” junction with a potential Schottky barrier, which goes into the open state at very low voltage values (about tens of microvolts). From Fig. 2, it is clear that the current-voltage characteristics of the same junction, approximately 18 months after the initial measurements, is noticeably different and has a symmetrical nonlinear dependence (also characteristic for ohmic contact). Thus, certain degradation processes have been detected in the material over time (probably due to the adsorption of atmospheric gases into the carbon film structure). As a result, the structure with a rectifying Schottky barrier undergoes irreversible changes and goes into ohmic contact (see also [6, 8]).

4. Conclusion

Studies of the thermoelectric properties of metal-carbon film junctions demonstrate a dependence characteristic for ohmic contact and the presence of a contact potential difference when the junction is heated. It is also shown that over time, the electrical characteristics and parameters of such contacts can change: the junction with the Schottky barrier degrades and the rectifying properties observed earlier disappear.

References

- [1] Kalinin Yu.E., Kashirin M.A., Makagonov V.A. et al. Electrical properties of thin films of amorphous carbon obtained by ion-beam sputtering. *ZTF*, 2017, **87**(11), P. 1722–1728.
- [2] Sorokin P.B., Chernozatonskii L.A. Graphene-based semiconductor nanostructures. *Phys. Usp.*, 2013, **183**(2), P. 113–132.
- [3] Vinogradov A.Ya., Grudinkin S.A., Besedina N.A. et al. Structure and properties of thin graphite-like films fabricated by magnetron sputtering. *Fizika i tekhnika poluprovodnikov*, 2018, **52**(7), P. 775–781.
- [4] Gubin S.P. All-carbon nanoelectronics. *Radioelectronics. Nanosystems. Information Technologies*, 2011, **3**(1), P. 47–54.
- [5] Bianco A., Chen Y., Frackowiak E., Holzinger M., Koratkar N. et al. Carbon science perspective in 2020: Current research and future challenges. *Carbon*, 2020, **161**, P. 373–391.
- [6] Blank T.V., Goldberg Yu.A. Ultraviolet semiconductor photoelectroconvertors. *Semiconductors*, 2003, **37**(9), P. 1025–1055.
- [7] Shalayev R.V., Izotov A.I., Syrotkin V.V. Electrical properties of “metal-carbon film” contact. *Nanosystems: Phys. Chem. Math.*, 2023, **14**(1), P. 86–88.
- [8] Bozhkov V.G. *Metal-Semiconductor Contacts: Physics and Models*. Tomsk: Publishing House of Tomsk State University, 2016, 528 p.

Submitted 20 March 2024; revised 22 March 2024; accepted 24 March 2024

Information about the authors:

Rostyslav V. Shalayev – Galkin Donetsk Institute for Physics and Engineering, R. Luxembourg str. 72, 283048, Donetsk, Russia; ORCID 0000-0003-1258-2434; sharos@donfti.ru

Anatoliy I. Izotov – Galkin Donetsk Institute for Physics and Engineering, R. Luxembourg str. 72, 283048, Donetsk, Russia; izotov.anatoli@gmail.com

Vladimir V. Syrotkin – Galkin Donetsk Institute for Physics and Engineering, R. Luxembourg str. 72, 283048, Donetsk, Russia; vladir.52@mail.ru

Conflict of interest: the authors declare no conflict of interest.

Tunneling recombination in GaN/InGaN LEDs with a single quantum well

Sergey V. Bulyarsky¹, Liubov N. Vostretsova², Valeriya A. Ribenek²

¹Institute of Nanotechnology of Microelectronics of the Russian Academy of Sciences (INME RAS), Moscow, Russia

²Ulyanovsk State University, Ulyanovsk, Russia

Corresponding author: Liubov N. Vostretsova, kapiton04@yandex.ru

ABSTRACT The paper proposes an analytical model of tunneling-recombination processes with forward and reverse displacements in InGaN/GaN-based structures containing a quantum well, assuming that the processes of generation and recombination are complex, while one of the stages of the transition of the charge carrier to the center is tunneling. Comparing the model with the experiment allowed us to determine the energies of the recombination centers of 0.22 and 0.45 eV. These energies may correspond to centers formed by defect complexes along filamentous dislocations, such as divacancies (V_{Ga} V_N), and a point isolated defect observed in n-type GaN layers grown by various methods, respectively.

KEYWORDS quantum well, nanoscale heterostructures, tunneling recombination, current transfer, nonradiative recombination levels

FOR CITATION Bulyarsky S.V., Vostretsova L.N., Ribenek V.A. Tunneling recombination in GaN/InGaN LEDs with a single quantum well. *Nanosystems: Phys. Chem. Math.*, 2024, **15** (2), 204–214.

1. Introduction

Structures based on InGaN/GaN currently occupy an important place in modern optoelectronics. Light-emitting devices are created based on such structures, operating in the spectral range from green light to near ultraviolet [1]. We can mention displays based on blue and green microLEDs [2–4], as well as communication systems for organizing optical data transmission at a rate of more than 1 Gbit/s [5,6]. LEDs based on III-nitride have many advantages, including high brightness, low power consumption, and long service life [7]. A wide spectral range of radiation has driven the development of microLEDs for displays of mobile devices, such as smart watches, virtual reality devices, and mobile phones [8–10]. The rapid development of the InGaN/GaN technology makes it possible to achieve the required parameters, with high radiation efficiency, reaching up to 90 % [11]. Nevertheless, these LEDs, despite their high efficiency, have high concentrations of defects, both extended and point, and the achieved high material quality enables a more reliable determination of current transfer mechanisms, including those involving defects.

Despite active research on InGaN-based LED structures, the question of the nature of the mechanisms that cause a drop in radiation efficiency during long-term operation remains unsolved. It is believed that the primary cause of the gradual decrease in the emission efficiency of LEDs based on nanoheterostructures is the formation of additional non-radiative recombination centers in the active region [12]. The degradation of SD was explained by the action of macroscopic defects [13], which could lead to the formation of tunneling channels [14] or an increase in contact resistance [15]. In other studies, changes in the characteristics of LED structures during aging are associated with the formation of non-radiative recombination centers in the active region during prolonged current flow. The influence of defects on the degradation characteristics of InGaN/GaN photodetectors with several quantum wells subjected to direct current was investigated [16]. The degradation of electrical and optical characteristics is largely explained by the activation of initially inactive defects, primarily defects associated with Mg–H, C-, and V_{Ga} , in the studied devices, followed by deterioration of their characteristics. These defects stimulate tunnel-recombination transfer of charge carriers with the participation of defects in quantum wells [17, 18], although analytical characteristics describing these processes are currently lacking. Analytical dependences of the current-voltage characteristics of diodes are essential for a deeper understanding of the processes occurring during the transfer of charge carriers and, in some cases, make it possible to determine the parameters of traps in the space charge region of the device [19–21] by using the current-voltage characteristics of the devices for diagnostic purposes. This is facilitated by the models developed [19, 20], which allow one to obtain the parameters of defects involved in tunneling-recombination processes using the analysis of current-voltage characteristics.

Volt-ampere characteristics are suitable for express diagnostics of recombination centers as they contain complete and important information about defects [20–22], however, it is essential to correctly extract this information from the experiments. The theory of generation and recombination in semiconductor diodes [23, 24] is often underutilized, lacking a thorough understanding of their depth. Several studies analyze generation-recombination processes in p-n junctions [25–28] and develop important methods for analyzing these processes. However, a simplified Shockley model is often used,

when the cross sections for the capture of electrons and holes to the recombination center are assumed to be the same. This approach is not correct. The injection of electrons and holes changes the occupation of recombination centers with deep levels in the band gap of the semiconductor. Features of the behavior of current-voltage characteristics reflect these processes, revealing the features of the parameters of defects. The influence of the defect parameters enables the discovery of new algorithms for processing current-voltage characteristics (CVCs) [19–23].

The analysis of p-n junction currents under reverse bias is also not well-established and not all available information is extracted from these studies. The diffusion theory of reverse current in p-n junction predicts an absence of dependence on the applied voltage and the activation energy of temperature dependence of diffusion current equal to the band gap of the semiconductor [24]. However, experimental studies show that this is not the case and the energy is less than the band width [21, 29]. This indicates the leading role of current generation involving defects [20, 21]. To determine the processes governing reverse current, one can examine temperature dependencies. If the experimental value of the activation energy of the current is lower than the energy of the band gap, but greater than half of it, then reverse current is determined by the process of generating electrons and holes through the levels of deep centers. This current is independent of voltage. If voltage dependence occurs, but the activation energy is greater than half of the band, then this is due to the Poole-Frenkel effect [30, 31]. The Poole-Frenkel coefficient has a numerical theoretical value. If the experimental value of this coefficient is greater than the theoretical one, then there is an electron-phonon interaction [21, 32]. If the activation energy of the reverse current is less than half the band gap, then tunneling takes part in the formation of the current.

Tunnel processes and generation-recombination processes can occur simultaneously. Therefore, it is necessary to develop diagnostic methods for determining the parameters of the deep centers involved in both processes. The aim of this study is to obtain analytical expressions for the current-voltage characteristics in the case when tunneling and generation-recombination processes simultaneously exist and to use these methods to determine defect parameters in the quantum well of InGaN/GaN LEDs.

2. Samples for research and measurement methods

Commercial shell-less blue-glow LEDs (Taiwan Oasis Technology Co., Ltd) ($\hbar\omega_{\max} = 2.66$ eV, $\lambda_{\max} = 468$ nm at room temperature) with a quantum well (QW) based on InGaN/GaN solid solution were studied.

To achieve this goal, direct volt-ampere (VAC) and volt-capacitive Faraday (VAC) characteristics were measured by an automated measuring system. The measurement of the forward and reverse branches of the HF was carried out in one measuring cycle using a generator-type capacitance meter. The LED under study is switched on in parallel to the LC circuit, the parameters of which are such that in the absence of a sample, the generated frequency is 1 MHz. This measurement scheme makes it possible to achieve an accuracy of measuring the capacitance of ± 0.5 pF.

The measurement of forward and reverse VAC was carried out on an automated measuring complex, which provides for the measurement of low currents using the Picoammeter Keithley 6485. The test sample was fixed to a heating element next to a thermocouple-based temperature sensor. The temperature was maintained with an accuracy of ± 0.5 K.

3. Experimental results

The concentration profile of the dopant (Fig. 1) was determined from the capacitive-voltage characteristic measured at room temperature. The impurity concentration in the space charge region (SCR) was determined as [30]:

$$N = \frac{2}{qS^2\varepsilon\varepsilon_0} \left[-\frac{1}{\frac{d(1/C^2)}{dU}} \right], \quad (1)$$

where e is the electron charge, S is the area of the structure (cm^2), ε is the dielectric permittivity of GaN, ε_0 is the dielectric constant (V/cm), q is the electron charge, C is the capacitance of the structure, and U is the voltage across the sample.

Current-voltage characteristics at forward bias, measured under various temperatures, are presented in Fig. 2.

To determine the mechanism of current transfer in the studied structures, the dependence at $I = f\left(\frac{1}{T}\right)$ a fixed forward voltage on the sample was used [19, 21] (Fig. 3).

Figure 4 shows the dependence of the activation energy on the forward bias voltage. As seen from Fig. 4, the activation energy E_a at a forward bias voltage below the forward bias $(E_g - qU)/2$ over the entire range of forward bias voltages is less than 2 V, therefore, tunneling current predominates in this voltage range [19, 21]. The activation energy determined from the slope of the curves in Fig. 2, ranges from 0.2 to 0.4 eV depending on the bias voltage, which is significantly lower than half the potential barrier, which is determined by $(E_g - qU)/2$ (Fig. 4). This value is much less than $0.5A_g$, but greater than zero. Such a change in energy is typical for tunnel-recombination processes.

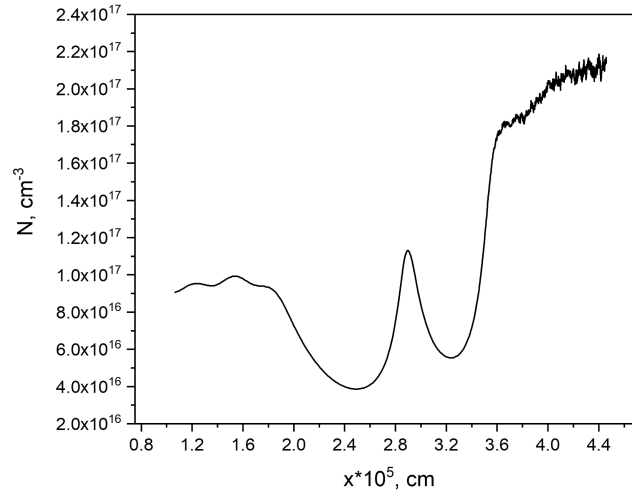


FIG. 1. Dopant distribution profile in the studied structure (1). Calculation of the concentration profile based on the results of capacitance-voltage measurements indicates the presence of a single quantum well with a width of approximately 40 nm.

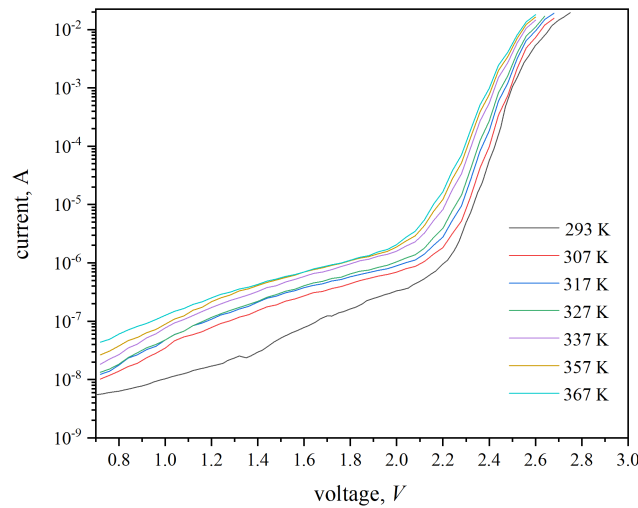


FIG. 2. Forward-biased current-voltage characteristics of InGaN/GaN LEDs, measured in the temperature range of 293 – 367 K. The change in the current value with temperature occurs quite weakly, indicating the influence of tunneling processes on charge transport.

4. Analysis of tunnel-recombination processes

Tunnel-recombination processes have been analyzed in [19, 20], where expressions for the recombination rate and various approximations of current-voltage characteristics were obtained. In this study, we propose a simpler and more convenient approach for analysis. We will adhere to the model that electrons from the conduction band tunnel into the well, and holes are injected from the p-region and are captured within it. Recombination occurs in the quantum well (QW). The transition model is shown in Fig. 5. It is important to note that this model is only valid in the initial part of the current-voltage characteristic, as long as the number of electrons injected from the conduction band is less than the number of electrons tunneling from it into the QW. In our case, this is the CVC region (Fig. 1) at voltages less than 2 V.

Taking into account that the level is closer to the conduction band and there is no emission from the center in the well to the valence band, we conclude that the hole recombination rate is equal to:

$$\frac{dp}{dt} = -c_p p n_t, \quad (2)$$

where c_p is the coefficient of hole capture by recombination centers in the QW; n_t is the electron concentration at the recombination centers in the QW.

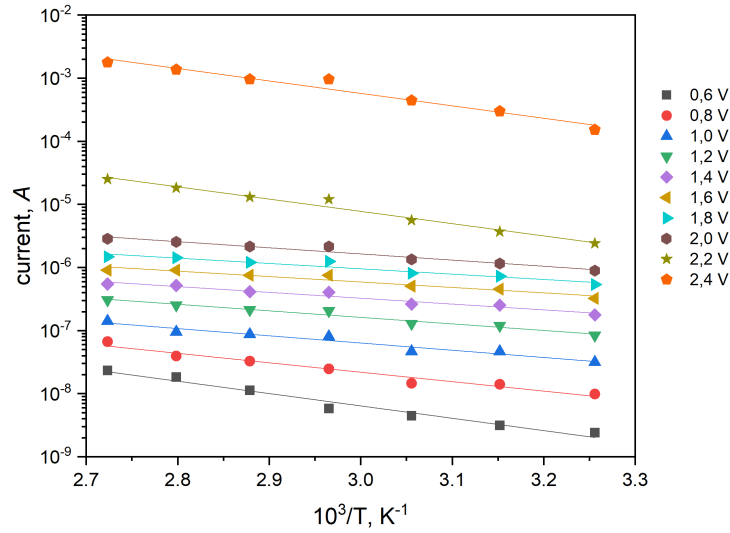


FIG. 3. Temperature dependences of the direct current at a voltage across the sample in the range of 0.6 – 2.4 V (with a step of 0.2 V). By dependence $I = f(1/T)$ the activation energy of current transfer was determined as $E_a = k \cdot \tan \alpha$, where k is the Boltzmann constant.

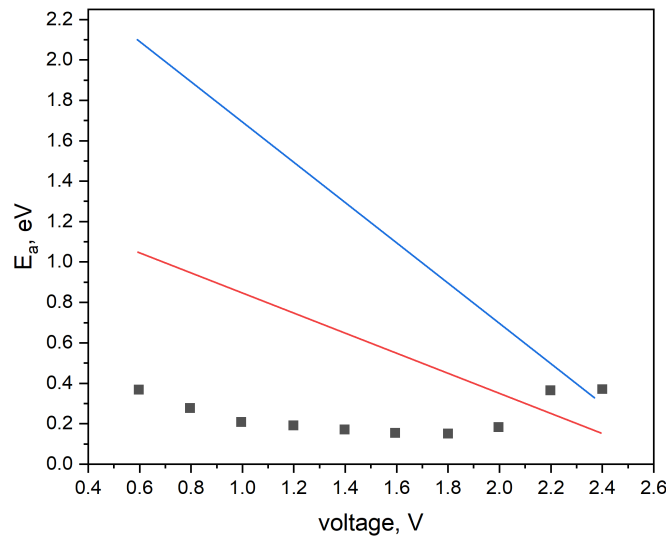


FIG. 4. Dependence of current activation energy on forward bias voltage: 1 – experimental value $E_a = f(U)$; 2 – $\frac{E_g - qU}{2}$; 3 – $E_g - qU$ (E_g – band gap, q – electron charge). The activation energy varies in the range from 0.2 to 0.4 eV, depending on the bias voltage. This value is much less than half the width of the InGaN band gap, but greater than zero, which is typical for tunnel recombination processes.

Electron tunneling rate:

$$\frac{dn}{dt} = -w_t n (N_t - n_t), \quad (3)$$

where w_t is the probability of electron tunneling from the conduction band to recombination centers in the QW; N_t is the concentration of recombination centers in the QW.

We equate these rates and obtain the probability of filling the traps and the rate of recombination with their participation:

$$\begin{aligned} \frac{dn_t}{N_t} &= \frac{w_t n}{c_p p + w_t n}, \\ R &= \frac{dp}{dt} = -\frac{c_p p w_t n}{c_p p + w_t n} N_t. \end{aligned} \quad (4)$$

The recombination current density is found as

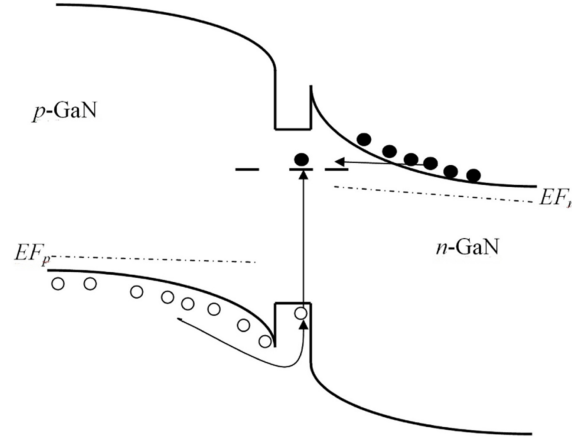


FIG. 5. Tunneling recombination model InGaN/GaN at forward bias. Electrons from the conduction band tunnel into the quantum well, and holes are injected from the p-region and trapped in the quantum well region.

$$j = e \int_{x_p}^{x_n} R(x) dx, \quad (5)$$

where x_n , x_p are the boundaries of the space charge region (SCR).

The coordinate dependence of the recombination rate is a bell-shaped function with almost exponential wings [19]. The current value is determined by the maximum recombination rate. Integral (4) is calculated assuming that the recombination rate is the same at all points of the SCR and is equal to the maximum, then

$$j = q \int_{x_p}^{x_n} R(x) dx = q \int_{x_p}^{x_n} R_{\max} dx = q R_{\max} \int_{x_p}^{x_n} dx = e R_{\max} (x_n - x_p) = q R_{\max} d, \quad (6)$$

where d is the SCR width, which can be calculated from the capacitance-voltage characteristics.

The value of the tunnel-recombination current can be obtained taking into account (6), (4). It is equal to

$$j = q d R_{\max} = q d \frac{c_p p w_t n}{c_p p + w_t n} N_t. \quad (7)$$

The probability of tunneling through a triangular barrier is given by the Fowler–Norheim formulas

$$w_t = \frac{I}{q d n S} = \frac{K F^2}{q d n S} \exp\left(-\frac{b(E_t - E_f - qU)^{3/2}}{F}\right), \quad (8)$$

where S is the area of p-n junction; F is the electric field strength; E_t is the activation energy of the level of recombination centers, measured from the conduction band; E_f is the Fermi energy,

$$a = \frac{q^3}{8\pi h} = 1.541 \cdot 10^{-6} S \text{ [eV/V}^2\text{]},$$

$$b = \frac{8\pi}{3(2m^*)^{0.5}/qh} = 6.831 \cdot 10^9 \text{ [eV}^{-3/2}\text{V/m]}.$$

The probability of tunneling for one electron is determined from formula (8):

$$w_t n = \frac{I}{q d S} = \frac{K F^2}{q d S} \exp\left(-\frac{b(E_t - E_f - qU)^{3/2}}{F}\right). \quad (9)$$

Then the current is as follows

$$j = q d R_{\max} = q d \frac{c_p p w_t n}{c_p p + w_t n} N_t = \frac{c_p p \frac{K F^2}{S} \exp\left(-\frac{b(E_t - E_f - qU)^{3/2}}{F}\right)}{c_p p + \frac{K F^2}{q d S} \exp\left(-\frac{b(E_t - E_f - qU)^{3/2}}{F}\right)} N_t. \quad (10)$$

Holes overcome the potential barrier $E_p = \frac{(V_d - qU)}{2}$, where V_d is the diffusion potential, in our case 2.7 eV.

Then,

$$j = qdR_{\max} = qd \frac{c_p p w_t n}{c_p p + w_t n} N_t = \frac{c_p p_p \exp\left(-\frac{V_d - qU}{2kT}\right) \frac{KF^2}{S} \exp\left(-\frac{b(E_t - E_f - qU)^{3/2}}{F}\right)}{c_p p_p \exp\left(-\frac{V_d - qU}{2kT}\right) + \frac{KF^2}{qdS} \exp\left(-\frac{b(E_t - E_f - qU)^{3/2}}{F}\right)} N_t. \quad (11)$$

When modeling using expression (11), the fitting parameters are the constant K , the hole capture coefficient c_p and $E_t - E_f$. The magnitude of the electric field F and the width of the SPV d were determined from capacitance-voltage characteristics. The concentration of holes in the p-region, p_p , assumed equal to the concentration of a fine impurity determined from the impurity distribution profile (Fig. 1). The energies in (11) are measured from the bottom of the conduction band in n-GaN. The position of the Fermi level in n-GaN was taken 0.7 ± 0.1 eV [33].

The simulation results are shown in Fig. 6. Comparison of calculations with the experiment made it possible to determine the activation energies of the recombination centers 0.22 ± 0.05 eV and 0.45 ± 0.05 eV.

The level with the energy of 0.22 eV in the conduction band was interpreted as defect complexes along filamentary dislocations, such as divacancies ($V_{Ga} V_N$) [34]. The level with the energy of 0.45 eV is treated as a point isolated defect, which is observed in GaN layers n-type grown by different methods [35].

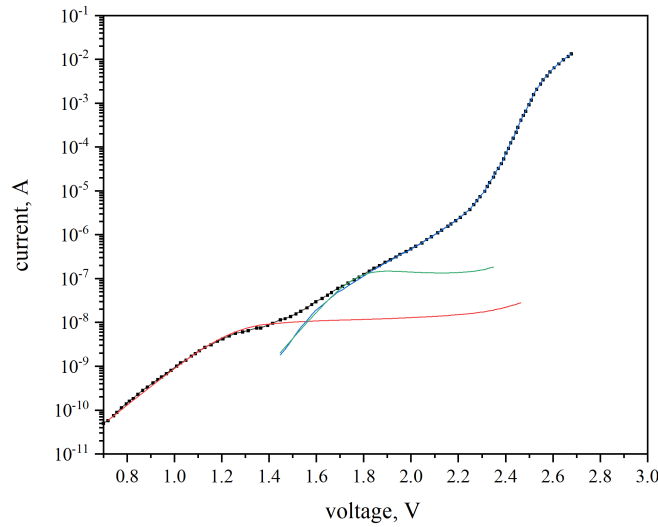


FIG. 6. Simulation of tunnel-recombination currents of InGaN/GaN LEDs under forward bias. The simulation of (11) made it possible to determine the activation energies of the recombination centers of 0.22 ± 0.05 eV (purple line) and 0.45 ± 0.05 eV (green line).

It is believed that the mechanism of the flow of direct current can be estimated by the differential indicator of the slope of the CVC (ideality factor)

$$\beta = \frac{qI}{kT} \left(\frac{dI}{dU} \right)^{-1} = \frac{q}{kT} \left(\frac{d \ln I}{dU} \right)^{-1}. \quad (12)$$

Figure 7 shows the results of calculating this parameter from equation (10) and the same parameter calculated from the experimental I-V characteristics. These values reach their maximum at the same voltage. The value of this exponent significantly exceeds the value of 2, which follows from the theory of Shockley, Noyce, and Saa [24]. This result shows that the theoretical CVC (11), obtained on the basis of the model in Fig. 6 describes the experimental results quite well, and the value of $\beta > 2$ indicates the participation of tunneling mechanism in the formation of the forward current of the LEDs.

5. Current-voltage characteristics with reverse bias

The activation energies of the reverse current were calculated for various electric field strengths. These results are shown in Fig. 8 ($E = f(F^{1/2})$):

The straight line in Fig. 8 is an approximation of the experimental data by the expression:

$$E = E_t - \beta_{\text{exp}} \sqrt{F} = 0.47 - 3.6 \cdot 10^{-4} \sqrt{F}. \quad (13)$$

Thus, the energy of the energy level of defects through which generation occurs is 0.47 eV, and the experimental value of the Poole-Frenkel coefficient $\beta_{\text{exp}} = 3.6 \cdot 10^{-4}$ eV/(B/cm). The activation energy is less than half the band gap. This fact allows us to assume the following reverse current flow model, namely: holes tunnel from a trap that forms an energy level from which electrons are generated into the conduction band (Fig. 9). In this case, the generation energy is less than half of the band gap.

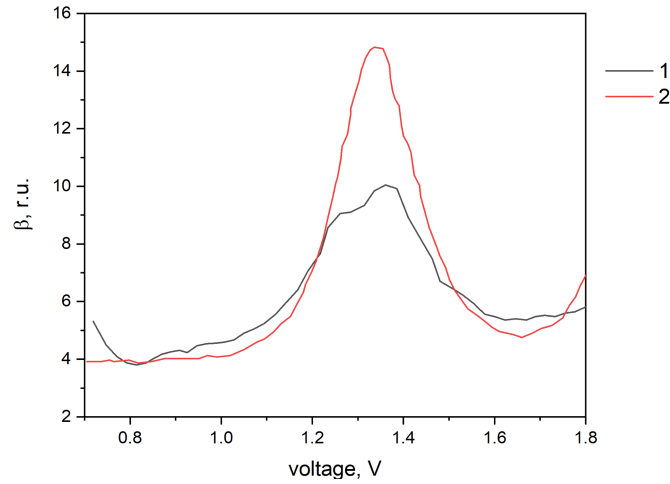


FIG. 7. Addition $\beta = f(U)$ for the structure under study at room temperature: 1 – experimental dependence (12); 2 – calculation taking into account (11). The value $\beta > 2$ indicates the involvement of the tunneling mechanism in the formation of direct current of LEDs.

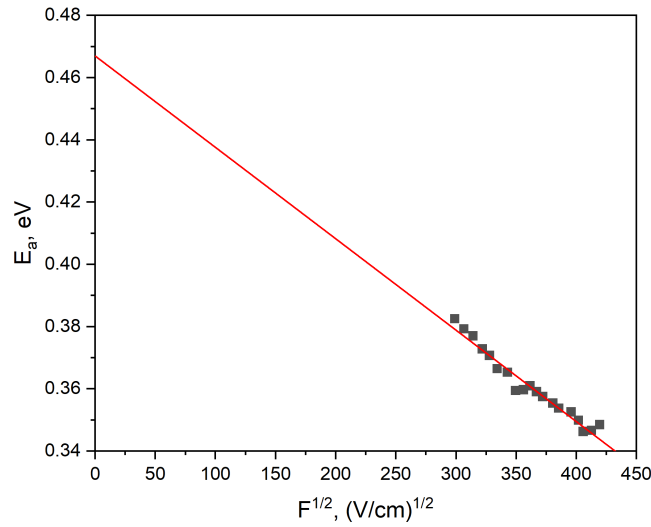


FIG. 8. Dependence of the activation energy of the inverse current-voltage characteristics on the electric field strength in the space charge region. Inverse current-voltage characteristics plotted in coordinates $\ln(I) = f(F^{1/2})$ are linear. This is the characteristics of the Poole-Frenkel effect, which reduces the generation barrier height proportionally to the root of the electric field strength [21].

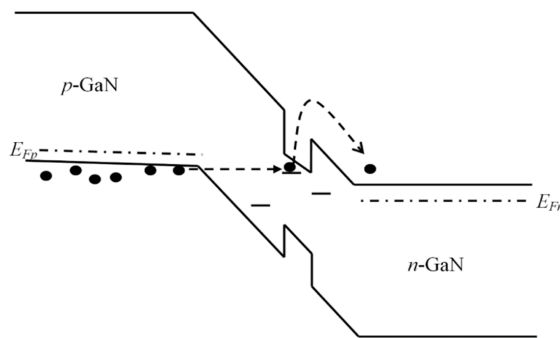


FIG. 9. Tunneling recombination model InGaN/GaN under reverse bias. The holes tunnel out of the trap, forming an energy level from which electrons are generated into the conduction band.

At a reverse voltage, the space-charge region of the p-n junction (SCR) is depleted of free charge carriers, and the equilibrium between recombination and generation is shifted towards generation. The reverse current, as well as the direct current, is determined by expression (5).

Let's consider the recombination rate in the case when one transition is the tunneling of a hole from the valence band to a level, and the second transition is the generation of electrons in the conduction band. Let the processes occur under reverse bias. In this case, the space-charge region is depleted of electrons and holes, and there are no captures of charge carriers at recombination centers. Under this condition, this velocity can be found from the system of kinetic equations:

$$\begin{aligned} R_n &= \frac{dn}{dt} = -c_n n (N_t - n_t) + e_n^t n_t, \\ R_p &= \frac{dp}{dt} = -c_p p n_t + w_p (N_t - n_t), \end{aligned} \quad (14)$$

where N_t is the concentration of deep centers, n_t is the concentration of electrons at them; e_n^t is the speed of electron emission from a deep level; w_p is the probability of hole tunneling from the valence band to a deep level.

The equilibrium condition takes place $R = R_n = R_p$ for stationary current. The recombination rate is found from (13) under the condition $n = 0$ and $p = 0$ fair with a reverse bias, we obtain:

$$I_{rev} = qA \int_0^w \frac{e_n^t(x) w_p(x) N_t(x)}{e_n^t(x) + w_p(x)} dx, \quad (15)$$

where $e_n^t = \gamma_n c_n N_c \exp\left(-\frac{(E_c - E_t)}{kT}\right)$, γ_n is the degeneracy factor of the level of the deep center for electrons and holes. These factors vary from 0.5 to 2.

In our case, the following facts take place: firstly, there is a significant temperature dependence of the current, and secondly, the activation energy is less than half of the band gap. Taking these experimental facts into account, we can assume that the tunneling probability $w_p \gg e_n^t$ is much higher than the recombination rate, and the level of the deep center is located closer to the conduction band

$$I_{rev} = qAw(U)N_t e_n^t. \quad (16)$$

From the conclusions made above and from formula (15), the expression for the current-voltage characteristics of the p-n junction with reverse bias is calculated:

$$I_{rev} = qAe_{n0}^t \int_0^w N_t(x) \exp\left(\frac{\Delta E_t(x)}{kT}\right) dx = qAe_{n0}^t \int_0^w N_t(x) \exp\left(\frac{\beta_F \sqrt{F(x)}}{kT}\right) dx, \quad (17)$$

where e_{n0}^t is the speed of electron emission without taking into account the influence of the electric field. Fig. 10 shows the inverse volt-ampere characteristic in coordinates $I = f(F^{1/2})$.

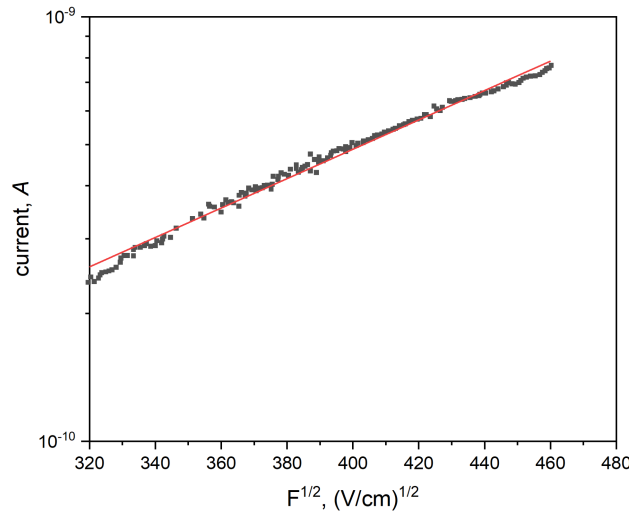


FIG. 10. Dependence of the reverse current on $F^{1/2}$ for the structure under study at room temperature. The dependence of the reverse current on $F^{1/2}$ on a logarithmic scale is close to linear, which confirms the validity of the expression used in the work [16].

The theoretical value of the Frenkel-Pool constant ($\beta_F = q^{3/2}/\sqrt{\pi\epsilon\epsilon_0}$) is equal to $2.3 \text{ eV}\cdot 10^{-4} \text{ cm}^{1/2}/\text{V}^{1/2}$. The reason for the discrepancy between this value and the value determined experimentally is the electron-phonon interaction. In the work of S. F. Timashev showed that [32]:

$$\beta_{Fex} = \beta_F \left(1 + \frac{E_0 - S\hbar\omega}{2S\hbar\omega} \right), \quad (18)$$

where $S\hbar\omega$ is a value equal to half of the heat release that accompanies the electron-phonon interaction; E_0 is the energy of a purely electronic transition, S is the Huang and Ries factor, $\hbar\omega$ is the energy of the characteristic phonon in the one-coordinate model.

The model of electron-phonon interaction, which takes into account interactions with a single phonon, gives the value for the thermal transition energy of charge carrier generation [20,21]:

$$E_t = \frac{(E_0 + S\hbar\omega)^2}{4S\hbar\omega}. \quad (19)$$

The numerical values of the activation energy and the experimental Poole-Frenkel constant are known. Parameters of the electron-phonon interaction $S\hbar\omega$ and E_0 are determined by jointly solving equations (17) and (18). They are equal to $E_0 = 0.40 \text{ eV}$, and $S\hbar\omega = 0.19 \text{ eV}$. These parameters determine the potentials of the configuration-coordinate diagram:

$$U_g = \frac{\hbar\omega Q^2}{2}; \quad U_u = \frac{\hbar\omega (Q - Q_0)^2}{2} + E_0, \quad (20)$$

where $Q_0 = \sqrt{2S}$, and Q is the current coordinate of the x-axis. Using the obtained parameters, we build a configuration-coordinate diagram of the generation center (Fig. 11).

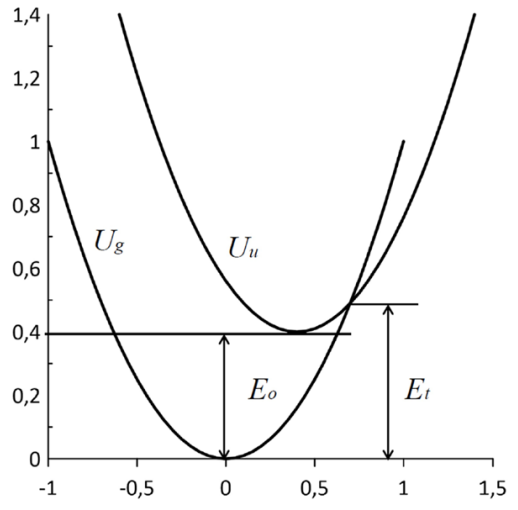


FIG. 11. Configuration-coordinate diagram of the center from which electrons are generated into the conduction band

6. Conclusion

This work proposes an analytical model of tunneling-recombination processes under forward and reverse biases, assuming that the processes of generation and recombination have a complex nature, with one of the stages of transition of the charge carrier to the center being tunneling. Under forward bias, an electron from the conduction band tunnels to the recombination center in the QW through a triangular barrier, and holes are injected from the p-region and are captured by the recombination center in the QW. This model is valid when the flux of tunneling electrons exceeds the flux of injected electrons from the conduction band. Comparison of the model with experiment made it possible to determine the energies of recombination centers in QWs, 0.22 and 0.45 eV. These energies can correspond to the centers formed by defect complexes along filamentary dislocations, such as divacancies ((VGa VN)), and a point isolated defect, which is observed in n-type GaN layers grown by various methods, respectively.

In case of reverse displacement, the following current transfer model is proposed: a hole tunnels from a trap forming an energy level in the band gap into the valence band, while an electron is generated into the conduction band. By solving kinetic equations (13) corresponding to the proposed model, an expression for the inverse characteristics of the studied structures (16) is obtained. According to (16), the reverse current exponentially depends on F (F is the electric field strength), which is confirmed experimentally (Fig. 10).

References

- [1] DenBaars S.P. Development of gallium-nitride-based light-emitting diodes (LEDs) and laser diodes for energy-efficient lighting and displays. *Acta Materialia*, 2013, **61**, P. 945–951.
- [2] Huang Y., Hsiang E.-L., Deng M.-Y., Wu S.-T. Mini-LED, Micro-LED and OLED displays: present status and future perspectives. *Light: Science & Applications*, 2020, **9**, 105.
- [3] Parbrook P.J., Corbett B., Han J., Seong T.-Y., Amano H. Micro-Light Emitting Diode: From Chips to Applications. *Laser & Photonics Reviews*, 2021, **15**, 2000133.
- [4] Lee S.-L., Cheng C.-C., Liu C.-J., Yeh C.-N., Lin Y.-C. 9.4-inch 228-ppi flexible micro-LED display. *J. of Society for Information Display*, 2021, **29**, P. 360–369.
- [5] Shi J.W., Chi K.L., Wun J.M., Bowers J.E., Sheu J.K. GaN based Cyan light-emitting diodes with GHz bandwidth. *IEEE Photonics Conf. IPC, IEEE*, Piscataway, NJ, 2016, P. 623–624.
- [6] Pepe A., Chen C.-J., Fu H.Y., Chen K.-C., Wang L., Wang L., Zhang L., Wu M.-C., Liu X., Luo Y., Dong Y., Wei Z., Wang L., Luo Y., Fu H.Y. 2 Gbps/3 m air–underwater optical wireless communication based on a single-layer quantum dot blue micro-LED. *Optics Letters*, 2020, **45**, P. 2616–2619.
- [7] Kou J., Shen Ch.-Ch., Shao H. Impact of the surface recombination on InGaN/GaN-based blue micro-light emitting diodes. *Optics Express*, 2019, **27** (12), A643–A653.
- [8] Wu T., Sher C.-W., Lin Y., Lee C.-F., Liang S., Lu Y., Huang Chen S.-W., Guo W., Kuo H.-C., Chen Z. Mini-LED and Micro-LED: Promising Candidates for the Next Generation Display Technology. *Applied Sciences*, 2018, **8** (9), 1557.
- [9] Zhang K., Peng D., Chong W.C., Lau K.M., Liu Z. Investigation of Photon-Generated Leakage Current for High-Performance Active Matrix Micro-LED Displays. *IEEE Transactions on Electron Devices*, 2016, **63** (12), P. 4832–4838.
- [10] Liu Z., Chong W.C., Wong K.M., Lau K.M. GaN-based LED micro-displays for wearable applications. *Microelectronic Engineering*, 2015, **148**, P. 98–103.
- [11] David A., Young N.G., Lund C., Craven M.D. Review—The Physics of Recombinations in III-Nitride Emitters. *ECS J. of Solid State Science and Technology*, 2020, **9** (1), 016021.
- [12] Seong T.-Y., Han J., Amano H., Morkoç H. *III-Nitride Based Light Emitting Diodes and Applications*. Springer Nature Singapore Pte Ltd XI, 2017, **495**.
- [13] Gong Z., Gaevski M., Adivarahan V., Sun W., Shatalov M., Asif Khan M. Optical power degradation mechanisms in AlGaIn-based 280 nm deep ultraviolet light-emitting diodes on sapphire. *Applied Physics Letters*, 2006, **88**, 121106.
- [14] Pinos A., Marcinkevicius S., Shur M.S. High current-induced degradation of AlGaIn ultraviolet light emitting diodes. *J. Appl. Phys.*, 2011, **109**, 103108.
- [15] Meneghini M., Barbisan D., Bilenko Y., Shatalov M., Yang J., Gaska R., Meneghesso G., Zanoni E. Defect-related degradation of Deep-UV-LEDs. *Microelectronics Reliability*, 2010, **50**, 1538.
- [16] Dalapati P., Yamamoto K., Egawa T., Miyoshi M. Impact of current-induced degradation process on the electro-optical characteristics of InGaN/GaN multiple-quantum-well photodetectors fabricated on sapphire substrate. *Applied Physics Letters*, 2021, **118**, 021101.
- [17] Bochkareva N.I., Shreter Y.G. Effect of Deep Centers on Charge-Carrier Confinement in InGaN/GaN Quantum Wells and on LED Efficiency. *Semiconductors*, 2018, **52** (7), P. 934–941.
- [18] Bochkareva N.I., Rebane Y.T., Shreter Y.G. Efficiency Droop in GaN LEDs at High Current Densities: Tunneling Leakage Currents and Incomplete Lateral Carrier Localization in InGaN/GaN Quantum Wells. *Semiconductors*, 2014, **48** (8), P. 1079–1087.
- [19] Bulyarskiy S.V., Rud' Yu.V., Vostretsova L.N., Kagarmenov A.S., Trifonov O.Yu. Tunneling recombination in semiconductor structures with nanodisordering. *Semiconductors*, 2009, **43** (4), P. 440–446.
- [20] Bulyarskiy S.V. Generation and Recombination Processes in Disordered Semiconductor Structures with Deep Centers. *Global J. of Science Frontier Research: A Physics and Space Science*, 2020, **20** (13).
- [21] Bulyarskiy S.V. The effect of electron-phonon interaction on the formation of reverse currents of pn-junctions of silicon-based power semiconductor devices. *Solid State Electronics*, 2019, **160**, 107624.
- [22] Bulyarskiy S.V., Lakalin A.V., Abanin I.E., Amelichev V.V., Svetuhin V.V. Optimization of the parameters of power sources excited by β -radiation. *Semiconductors*, 2017, **51** (1), P. 66–72.
- [23] Shockley W. The theory of pn-Junctions in semiconductors and pn-Junction transistors. *Bell System Technical J.*, 1949, **28** (3), P. 435–489.
- [24] Sah C.T., Noyce R.N., Shockley W. Carrier Generation and Recombination in PN Junctions and PN Junction Characteristics. *Proceedings of the IRE*, 1957, **45** (9), P. 1228–1243.
- [25] Rein S., Rehr T., Warta W., Glunz S.W. Lifetime spectroscopy for defect characterization: Systematic analysis of the possibilities and restrictions. *J. of Applied Physics*, 2002, **91**, P. 2059–2070.
- [26] Simoen E., Claeys C., Vanhellefont J. Defect Analysis in Semiconductor Materials Based on pn Junction Diode Characteristics. *Defect and Diffusion Forum*, 2007, **261–262**, P. 1–24.
- [27] Simoen E., Claeys C. On the impact of the capture rates on the generation/recombination lifetime ratio of a single deep level. *IEEE Transactions on Electron Devices*, 1999, **46**, P. 1487–1488.
- [28] Macdonald D., Cuevas A. Validity of simplified Shockley-Read-Hall statistics for modeling carrier lifetimes in crystalline silicon. *Physical Review B*, 2003, **67**, 075203.
- [29] Al Abdullah K., Al Alloush F., Jaafar A., Salame C. Study of the effects related to the electric reverse stress currents on the Mono-Si solar cell electrical parameters. *Energy Procedia*, 2013, **36**, P. 104–113.
- [30] Shan Q., Meynard D.S., Dai Q., Cho J., Fred Schubert E., Kon Son J., Sone C. Transport-mechanism analysis of the reverse leakage current in GaInN light-emitting diodes. *Applied Physics Letters*, 2011, **99**, 253506.
- [31] Musolino M., van Treeck D., Tahraoui A., Scarparo L., De Santi C., Meneghini M., Zanoni E., Geelhaar L., Riechert H. A physical model for the reverse leakage current in (In,Ga)N/GaN light-emitting diodes based on nanowires. *J. of Applied Physics*, 2016, **119** (4), 044502.
- [32] Timashev S.F. On the Frenkel effect during thermofield ionization of deep centers in the space charge layer in semiconductors. *Phys Solid State*, 1974, **16**, P. 804–811.
- [33] Rickert K.A., Ellis A.B., Kim J.K., Lee J.-L., Himpel F.J., Dwikusuma F., Kuech T.F. X-ray photoemission determination of the Schottky barrier height of metal contacts to n-GaN and p-GaN. *J. of Applied Physics*, 2002, **92** (11), 6671.

- [34] Narita T., Tokuda Y. Deep levels in GaN. in T. Narita, T. Kachi, (eds.), *Characterization of Defects and Deep Levels for GaN Power Devices*, Melville, New York: AIP Publishing, 2020, P. 3-1–3-36.
- [35] Krtschil A., Witte H., Lisker M., Christen J., Krost A., Birkle U., Einfeldt S., Hommel D., Scholz F., Off J., Stutzmann M. Photoelectric properties of the 0.44 eV deep level-to-band transition in gallium nitride investigate by optical admittance spectroscopy. *Applied Physics Letters*, 2000, **77** (4), 546.

Submitted 25 January 2024; revised 10 March 2024; accepted 11 March 2024

Information about the authors:

Sergey V. Bulyarsky – Institute of Nanotechnology of Microelectronics of the Russian Academy of Sciences (INME RAS), Leninskiy prospect, 32A, Moscow 119991, Russia; ORCID 0000-0002-9777-746X; dimka97@mail.ru

Liubov N. Vostretsova – Ulyanovsk State University, Tolstoy street, 42, Ulyanovsk 432097, Russia; ORCID 0000-0001-9602-0812; kapiton04@yandex.ru

Valeriya A. Ribenek – Ulyanovsk State University, Tolstoy street, 42, Ulyanovsk 432097, Russia; ORCID 0000-0002-9233-5339; ribl98@mail.ru

Conflict of interest: the authors declare no conflict of interest.

Ultrasonic-assisted hydrothermal synthesis of nanoscale double ceric phosphates

Taisiya O. Kozlova^{1,a}, Ekaterina D. Sheichenko^{1,2,b}, Darya N. Vasilyeva^{1,2,c}, Daniil A. Kozlov^{1,d}, Irina V. Kolesnik^{1,3,e}, Ilya V. Tronev^{1,2,f}, Maria A. Teplonogova^{1,g}, Alexander E. Baranchikov^{1,h}, Vladimir K. Ivanov^{1,i}

¹Kurnakov Institute of General and Inorganic Chemistry of the Russian Academy of Sciences, Moscow, Russia

²National Research University Higher School of Economics, Moscow, Russia

³Lomonosov Moscow State University, Moscow, Russia

^ataisia.shekunova@yandex.ru, ^bkseterina@yandex.ru, ^cdnavasileva_1@edu.hse.ru,

^dkozlov@inorg.chem.msu.ru, ^ekolesnik.iv@gmail.com, ^fivtronev@edu.hse.ru, ^gm.teplonogova@gmail.com,

^ha.baranchikov@yandex.ru, ⁱvan@igic.ras.ru

Corresponding author: Taisiya O. Kozlova, taisia.shekunova@yandex.ru

PACS 61.66.Fn, 43.35.Zc, 78.20.-e

ABSTRACT The combination of ultrasonic exposure on ceric phosphate gels with subsequent hydrothermal-microwave treatment resulted in the formation of nanoscale $\text{NH}_4\text{Ce}_2(\text{PO}_4)_3$ or $\text{KCe}_2(\text{PO}_4)_3$ phases. The sun protection factor (SPF) and protection factor against UV-A radiation (UVAPF) values for double ceric phosphates with the smallest crystallite sizes exceeded 4 and 3.5, respectively, which is much higher than the values for samples consisting of larger particles. These results are superior to previously published values for similar ceric compounds, and thus show promise for their application in sunscreens.

KEYWORDS cerium, ultrasonic exposure, microwave, particle size, UV shielding

ACKNOWLEDGEMENTS This work was supported by Russian Science Foundation (Grant no. 23-73-10088, <https://rscf.ru/en/project/23-73-10088/>) using the equipment of the JRC PMR IGIC RAS.

FOR CITATION Kozlova T.O., Sheichenko E.D., Vasilyeva D.N., Kozlov D.A., Kolesnik I.V., Tronev I.V., Teplonogova M.A., Baranchikov A.E., Ivanov V.K. Ultrasonic-assisted hydrothermal synthesis of nanoscale double ceric phosphates. *Nanosystems: Phys. Chem. Math.*, 2024, **15** (2), 215–223.

1. Introduction

Modern sunscreens are cosmetic preparations containing organic or inorganic UV filters as active ingredients. The use of organic UV filters in sunscreens is less preferred due to their potential to penetrate the skin barrier and to exhibit systemic effects in the body, their relatively low photostability, and ability to generate reactive oxygen species under irradiation [1,2]. The latter drawback is also characteristic of commercial metal oxide UV filters, such as TiO_2 or ZnO [3–5]. Phosphate compounds are considered as alternative inorganic UV filters because of their biocompatibility, high chemical and thermal stability of the phosphate matrix [6–8]. Recently, crystalline cerium(IV) phosphates were reported to be promising sunscreen candidates [9–12]. The primary method for synthesizing these compounds is through hydrothermal treatment, which typically results in the formation of micron or submicron particles [13–19]. However, the size of the inorganic components is a crucial parameter that can impact photoprotective properties, distribution uniformity over the skin, and overall appearance of cosmetic compositions [20–22]. In this regard, an important task is to develop methods for producing inorganic UV filter particles with a specific mean particle size and narrow size distribution. Previously, we demonstrated the use of the hydrothermal-microwave method, instead of conventional hydrothermal treatment, to produce particles of ammonium-cerium(IV) phosphates ($\text{NH}_4\text{Ce}_2(\text{PO}_4)_3$, $(\text{NH}_4)_2\text{Ce}(\text{PO}_4)_2 \cdot \text{H}_2\text{O}$) in a wide size range by varying the duration of synthesis and temperature [23]. It is also well known that ultrasonic treatment of the reaction mixtures can reduce the particle size of products and promote their uniform distribution [24–26]. At the same time, the number of papers is still limited which report on the influence of ultrasonic pre-treatment of heterogeneous precursors, such as gels, on the products of hydrothermal synthesis.

This study investigates the effect of ultrasonication of ceric phosphate gels on their crystallization upon hydrothermal or hydrothermal-microwave treatment, resulting in the formation of $\text{NH}_4\text{Ce}_2(\text{PO}_4)_3$ or $\text{KCe}_2(\text{PO}_4)_3$ samples. The influence of mean particle size and particle size distribution of the resulting samples on their UV shielding properties is also studied.

© Kozlova T.O., Sheichenko E.D., Vasilyeva D.N., Kozlov D.A., Kolesnik I.V., Tronev I.V., Teplonogova M.A., Baranchikov A.E., Ivanov V.K., 2024

2. Experimental section

The following materials were used as received, without further purification: $\text{Ce}(\text{NO}_3)_3 \cdot 6\text{H}_2\text{O}$ (pure grade, Lanhit Russia), potassium hydroxide (pure grade, Sigma Aldrich), phosphoric acid (85 wt.% aq, $\rho = 1.689 \text{ g/cm}^3$, extra-pure grade, Komponent-Reaktiv Russia), aqueous ammonia (25 wt.%, extra-pure grade, Khimmed Russia), isopropanol (extra-pure grade, Khimmed Russia), glycerol (Sigma-Aldrich, 99.5 %), sodium dodecyl sulfate (99 %, Sigma-Aldrich), distilled water.

First, ceric phosphate solution was synthesized according to the procedure reported earlier [27]. Briefly, nanocrystalline (4 – 5 nm) cerium dioxide (0.100 g) obtained by precipitation from $\text{Ce}(\text{NO}_3)_3 \cdot 6\text{H}_2\text{O}$ aqueous solution [28] was dissolved in concentrated phosphoric acid (5 ml) at 80°C . The calculated molar ratio of Ce:P in the solution was 1:126. The cooled solution was placed into an ultrasonic bath Bandelin Sonorex Longlife RK 1050 for 30 min, then 35 ml of 0.5 M aqueous ammonia solution or 1 M potassium hydroxide aqueous solution was added to the reaction mixture. The obtained gels ($\sim 40 \text{ mL}$) were sonicated using Bandelin Sonopuls HD 3200 homogenizer operated at 20 kHz (200 W, amplitude 20 %) and equipped with titanium horn (TT-13 titanium tip) for 1 h. The resulting suspensions were placed in 100 ml Teflon autoclaves and treated under hydrothermal or hydrothermal-microwave conditions at 180°C for 24 h or 1 h, respectively. After cooling the autoclaves, the precipitates were repeatedly washed using distilled water and dried at 60°C in air. The synthesis scheme is shown in Fig. 1.

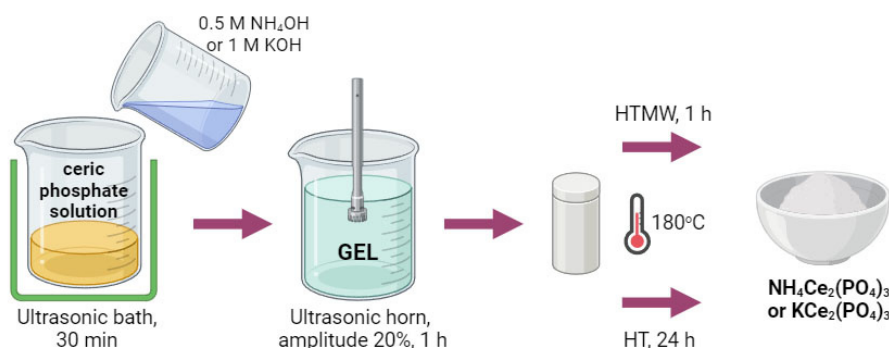


FIG. 1. The scheme of double ceric phosphates synthesis using ultrasonic-assisted hydrothermal-microwave (HTMW) or conventional hydrothermal (HT) treatment

As a reference, $\text{NH}_4\text{Ce}_2(\text{PO}_4)_3$ and $\text{KCe}_2(\text{PO}_4)_3$ samples, previously synthesized under hydrothermal conditions without the use of microwave or ultrasonic treatment [19, 23], have been obtained. These samples were designated as NCeP and KCeP, respectively.

Powder X-ray diffraction (PXRD) patterns were acquired with a DX-2700BH (Haoyuan, China) diffractometer, using $\text{Cu K}\alpha_{1,2}$ radiation in the 2θ range of $5^\circ - 80^\circ$ with 0.02° 2θ steps and a counting time of no less than 1 s per step. The identification of the diffraction peaks was carried out using the ICDD database. The full-profile analysis of diffraction patterns with quantitative determination of the coherent scattering domains (CSD) sizes, was performed using the Rietveld method realized in the MAUD software (version 2.99).

Scanning electron microscopy (SEM) images were obtained using an Amber GMH (Tescan, Czech Republic) microscope operated at an accelerating voltage of 5 kV using a secondary electron (Everhart–Thornley) detector. Particle size analysis was carried out using the ImageJ software (version 1.53t). For each sample, the sizes of at least 150 particles were measured, after which the particle size distributions were approximated by a lognormal function. Energy-dispersive X-ray spectroscopy (EDX) was performed using an Ultim Max (Oxford Instruments, UK) detector at an accelerating voltage of 20 kV.

Fourier transform infrared (FTIR) spectra of the samples were recorded using an InfraLUM FT-08 (Lumex, Russia) spectrometer in the range of $400 - 4000 \text{ cm}^{-1}$ in attenuated total reflectance mode.

Absorption spectra of $\text{NH}_4\text{Ce}_2(\text{PO}_4)_3$ and $\text{KCe}_2(\text{PO}_4)_3$ samples for band gap (E_g) determination were acquired in a diffuse reflection mode on a Lambda 950 (PerkinElmer, USA) spectrometer in the 200 – 1000 nm range. The sun protection factor (SPF) and protection factor against UV-A radiation (UVAPF) values were determined in accordance with the ISO 24443-2016, the measurement procedure and calculation formulas have previously been reported [12]. For this study, suspensions containing 10 wt.% of double ceric phosphates and 90 wt.% of a solution consisting of 9.9 wt.% H_2O , 90 wt.% glycerol and 0.1 wt.% sodium dodecyl sulfate were prepared in an agate mortar. Then, 0.035 g of each suspension was evenly spread over the surface of the 3M Transpore Tape 1527-2 film (27.5 cm^2 area). The total transmittance spectra of the films coated with the suspensions were recorded in the range of 290 – 400 nm on a Lambda 950 (PerkinElmer, USA) spectrometer using an integrating sphere (150 mm diameter). 3M Transpore Tape 1527-2 coated with a similar formulation without adding double ceric phosphates, was used as a reference sample.

3. Results and discussion

According to the PXRD data, after the hydrothermal treatment of the reaction mixtures obtained by mixing ceric phosphate solutions with a 0.5 M NH_4OH aqueous solution, $\text{NH}_4\text{Ce}_2(\text{PO}_4)_3$ phase formed (Fig. 2a). Note, that in case of hydrothermal treatment (24 h) of sonicated ceric phosphate gel an admixture of CePO_4 with monazite structure (PDF2 [00-032-199]) was detected in the sample. The presence of Ce(III) phosphate admixture in the products of hydrothermal treatment of ceric phosphate gels has been repeatedly reported [16, 19, 29, 30], what may be due to Ce(IV) reduction under specific synthesis conditions. Using the 1 M KOH aqueous solution as a precursor led to the single phase $\text{KCe}_2(\text{PO}_4)_3$ formation in all the cases (Fig. 2b). The unit cell parameters refinement as well as CSD evaluation were performed using Rietveld analysis of the PXRD patterns for $\text{NH}_4\text{Ce}_2(\text{PO}_4)_3$ and $\text{KCe}_2(\text{PO}_4)_3$ phases (Table 1). The obtained results agree well with previously published data and confirm that these double ceric phosphates are isostructural to each other [17, 19].

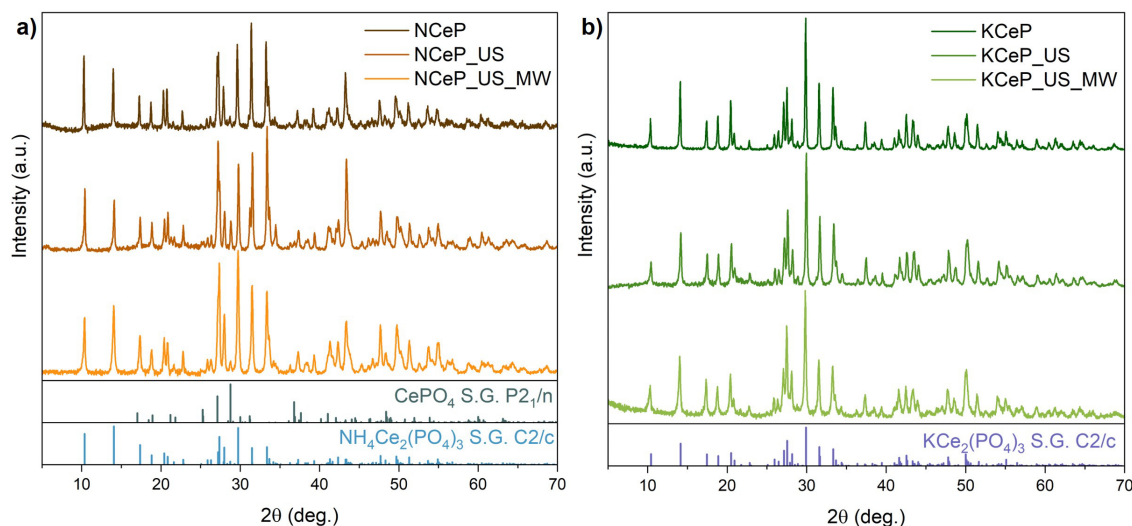


FIG. 2. Powder X-ray diffraction patterns of the products of HTMW or HT treatment of ceric phosphate gels formed upon the addition of 0.5 M NH_4OH (a) or 1 M KOH (b) to ceric phosphate solutions. The corresponding Bragg peak positions are shown below

Based on the X-ray diffraction analysis results, it was found that the use of hydrothermal-microwave treatment in comparison with conventional hydrothermal synthesis resulted in decreasing of $\text{NH}_4\text{Ce}_2(\text{PO}_4)_3$ and $\text{KCe}_2(\text{PO}_4)_3$ particle sizes. This is consistent with the findings of Tronev et al. [23], indicating the same dependence. Moreover, the same trend is observed when comparing samples obtained with or without ultrasonic pre-treatment (Table 1). Thus, the phases $\text{NH}_4\text{Ce}_2(\text{PO}_4)_3$ and $\text{KCe}_2(\text{PO}_4)_3$ with the least crystallite sizes of 60 and 65 nm, respectively, were obtained by combining microwave and ultrasonic treatment of the reaction mixtures.

IR spectroscopy data (Fig. 3) confirm the results of the PXRD analysis, indicating that the type of hydrothermal treatment and ultrasonic pre-treatment virtually has no influence on the structure of the samples. The general appearance of the IR spectra of the samples obtained is almost the same and agree well with the previously reported data for $\text{NH}_4\text{Ce}_2(\text{PO}_4)_3$ and $\text{KCe}_2(\text{PO}_4)_3$ phases [17, 19]. In the regions of $1100 - 900$ and $650 - 440 \text{ cm}^{-1}$ the absorption bands are observed, which are related to the stretching and bending vibrations of the phosphate anions, respectively [31, 32]. Furthermore, the IR spectra of $\text{NH}_4\text{Ce}_2(\text{PO}_4)_3$ samples exhibit absorption bands at $2800 - 3300 \text{ cm}^{-1}$ (broad) and 1425 cm^{-1} (sharp), which correspond to the vibrations of the NH_4^+ ion [33–35].

The particle size dependence on the synthetic method used, as observed through X-ray diffraction analysis, is clearly demonstrated in the scanning electron microscopy images (Fig. 4). Table 2 presents the mean particle sizes and standard deviations obtained from lognormal distribution as determined from scanning electron microscopy data. The mean particle sizes of $\text{KCe}_2(\text{PO}_4)_3$ samples appear to be similar to the crystallite sizes determined from XRD data. The overestimation of the corresponding values for $\text{NH}_4\text{Ce}_2(\text{PO}_4)_3$ samples is explained by the anisotropic microstructure of this phase, for which the length of single crystallites from SEM images was measured. Note that the most uniform particle size distribution is achieved through the combination of microwave and ultrasonic effects (Fig. 5).

TABLE 1. Structural parameters and crystallite sizes for the products of HTMW or HT treatment of ceric phosphate gels formed upon the addition of 0.5 M NH₄OH or 1 M KOH to ceric phosphate solutions

Sample	NCeP	NCeP_US	NCeP_US_MW	KCeP	KCeP_US	KCeP_US_MW
Precipitating agent	NH ₄ OH	NH ₄ OH	NH ₄ OH	KOH	KOH	KOH
Ultrasonic treatment	–	+	+	–	+	+
Type of hydrothermal treatment	HT	HT	HTMW	HT	HT	HTMW
Duration of hydrothermal treatment, h	24	24	1	24	24	1
Phase composition	NH ₄ Ce ₂ (PO ₄) ₃	NH ₄ Ce ₂ (PO ₄) ₃ : 89.0±1.0 wt.% CePO ₄ : 11.0±0.5 wt.%	NH ₄ Ce ₂ (PO ₄) ₃	KCe ₂ (PO ₄) ₃	KCe ₂ (PO ₄) ₃	KCe ₂ (PO ₄) ₃
Lattice parameters	$a = 17.491(1) \text{ \AA}$ $b = 6.7751(5) \text{ \AA}$ $c = 8.0051(6) \text{ \AA}$ $\beta = 102.868(3)^\circ$	NH ₄ Ce ₂ (PO ₄) ₃ : $a = 17.4691(9) \text{ \AA}$ $b = 6.7672(4) \text{ \AA}$ $c = 8.0011(4) \text{ \AA}$ $\beta = 102.802(3)^\circ$ CePO ₄ : $a = 6.799(4) \text{ \AA}$ $b = 7.016(1) \text{ \AA}$ $c = 6.4675(9) \text{ \AA}$ $\beta = 103.67(4)^\circ$	$a = 17.4804(8) \text{ \AA}$ $b = 6.7711(3) \text{ \AA}$ $c = 8.0001(4) \text{ \AA}$ $\beta = 102.836(3)^\circ$	$a = 17.373(1) \text{ \AA}$ $b = 6.7272(6) \text{ \AA}$ $c = 7.9687(6) \text{ \AA}$ $\beta = 102.350(3)^\circ$	$a = 17.372(1) \text{ \AA}$ $b = 6.7299(4) \text{ \AA}$ $c = 7.9693(5) \text{ \AA}$ $\beta = 102.351(4)^\circ$	$a = 17.376(1) \text{ \AA}$ $b = 6.7315(5) \text{ \AA}$ $c = 7.9701(6) \text{ \AA}$ $\beta = 102.306(5)^\circ$
Crystallite size, nm	> 100	NH ₄ Ce ₂ (PO ₄) ₃ : > 100 CePO ₄ : 72±2	60±2	> 100	75±3	65±2

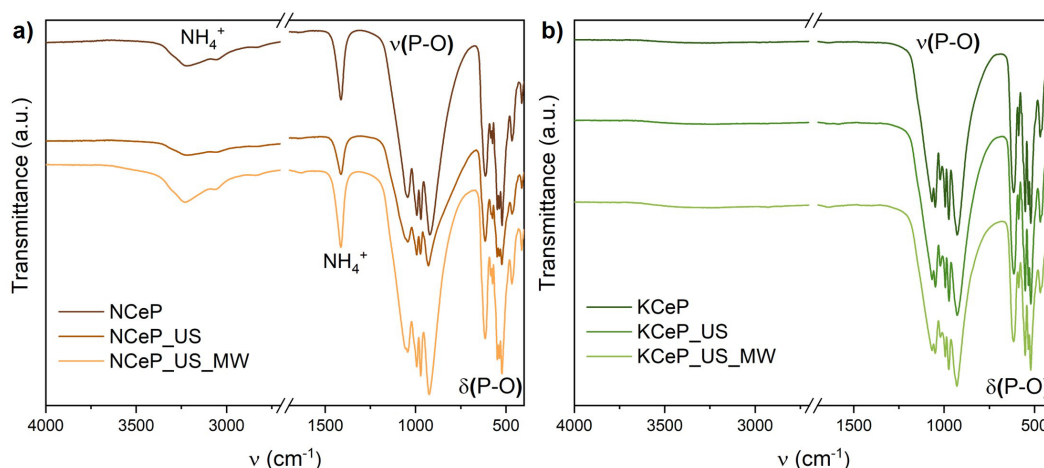


FIG. 3. IR spectra for products of HTMW or HT treatment of ceric phosphate gels formed upon the addition of 0.5 M NH_4OH (a) or 1 M KOH (b) to ceric phosphate solutions

Based on the obtained data, the ultrasonic treatment significantly affects the crystallization of double ceric phosphates under hydrothermal conditions. This observation is in line with the results of the previous studies, devoted to other inorganic systems (see e.g. [36–38]). In particular, on the example of mixed oxide particles [39] and silicoaluminophosphate molecular sieves [40] it was shown that preliminary ultrasonication inhibits the crystallite growth and leads to formation of smaller crystals with more uniform size distribution.

TABLE 2. The mean particle sizes and standard deviation determined from the SEM images for $\text{NH}_4\text{Ce}_2(\text{PO}_4)_3$ and $\text{KCe}_2(\text{PO}_4)_3$ samples

Sample	NCeP	NCeP_US	NCeP_US_MW	KCeP	KCeP_US	KCeP_US_MW
Mean particle size, nm	275	352	244	138	105	58
Standard deviation, nm	114	217	63	39	20	11

The UV-vis absorption spectra of $\text{NH}_4\text{Ce}_2(\text{PO}_4)_3$ and $\text{KCe}_2(\text{PO}_4)_3$ samples are almost identical within each series. To determine the optical band gap, optical absorption spectra were rebuilt using Tauc plot for allowed indirect transition (Fig. 6). The estimated E_g values of $\text{NH}_4\text{Ce}_2(\text{PO}_4)_3$ (2.57 – 2.61 eV) samples coincide with the previously published data [12, 23]. The corresponding values for $\text{KCe}_2(\text{PO}_4)_3$ samples (2.63 eV) were determined for the first time and are close to those of $\text{NH}_4\text{Ce}_2(\text{PO}_4)_3$.

The SPF and UVAPF values obtained in accordance with the ISO 24443-2016 international standard are shown in the Table 3. Note that the absolute values for the NCeP sample are lower than those for the $\text{NH}_4\text{Ce}_2(\text{PO}_4)_3$ sample, obtained earlier under similar conditions (SPF=2.7, UVAPF=2.5) [12]. However, even when considering the values presented in the previous work, the NCeP_US_MW sample has the highest SPF and UVAPF values. The samples produced using both ultrasonic and microwave treatment exhibit the highest UV protection properties. It is noteworthy that SPF and UVAPF values for NCeP_US_MW and KCeP_US_MW samples are higher than previously reported corresponding values for other ceric phosphates and even nanocrystalline cerium dioxide [12, 41].

TABLE 3. Sun protection factor and UVAPF protection factor values for $\text{NH}_4\text{Ce}_2(\text{PO}_4)_3$ and $\text{KCe}_2(\text{PO}_4)_3$ samples

Sample	NCeP	NCeP_US_MW	KCeP	KCeP_US_MW
SPF	1.9±0.1	4.0±0.2	3.3±0.3	3.9±0.4
UVAPF	1.9±0.1	3.9±0.3	3.5±0.5	3.5±0.4

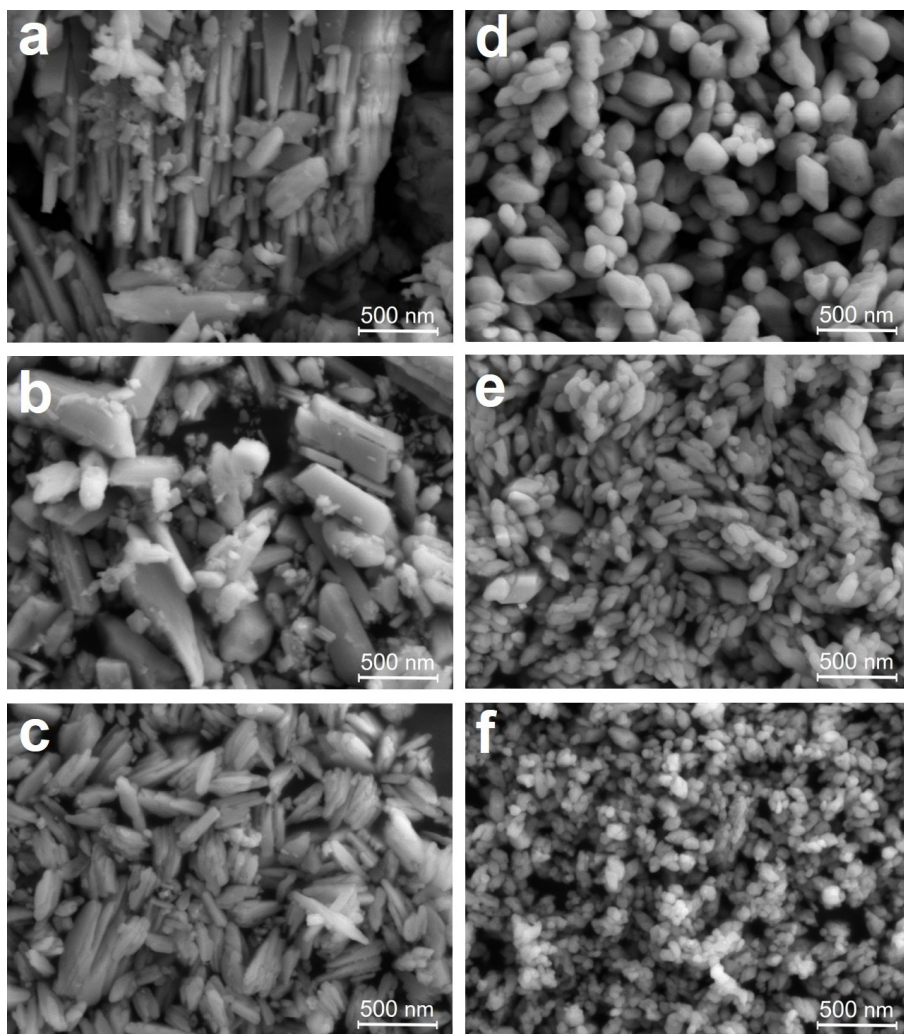


FIG. 4. SEM images of a) NCeP, b) NCeP_US, c) NCeP_US_MW, d) KCeP, e) KCeP_US, f) KCeP_US_MW samples

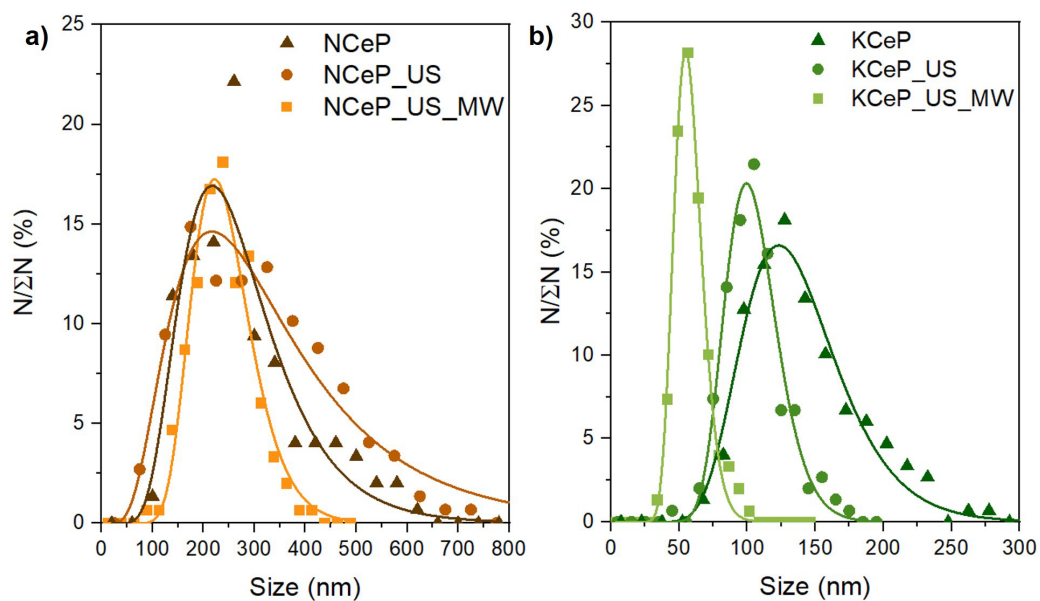


FIG. 5. Size distribution of the particles of $\text{NH}_4\text{Ce}_2(\text{PO}_4)_3$ and $\text{KCe}_2(\text{PO}_4)_3$ samples calculated from SEM data. Solid lines correspond to the results of data fitting using a lognormal distribution function

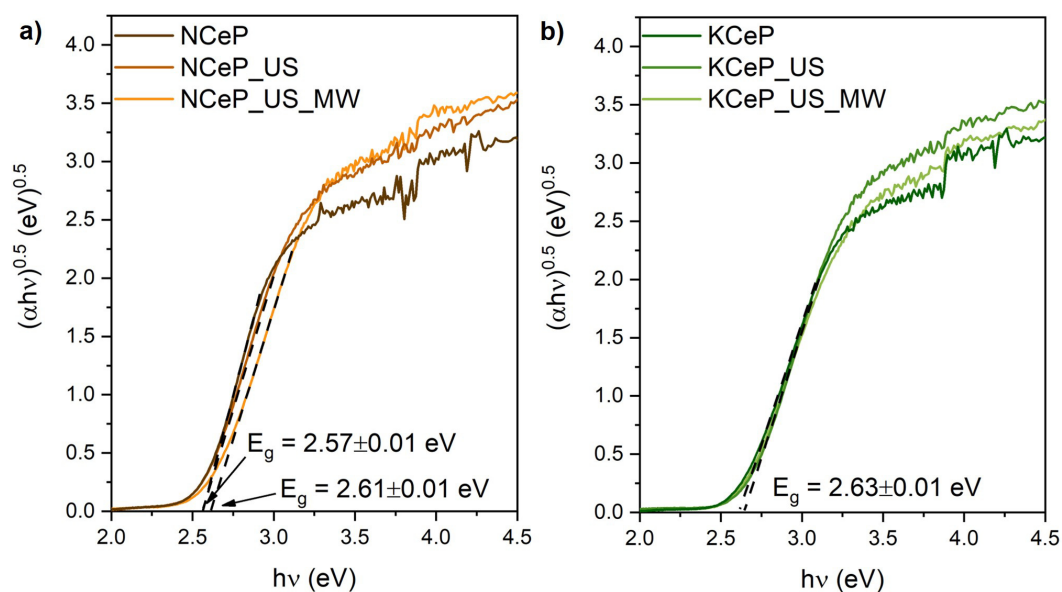


FIG. 6. Plots for band gap energy (indirect transition) determination for $\text{NH}_4\text{Ce}_2(\text{PO}_4)_3$ (a) and $\text{KCe}_2(\text{PO}_4)_3$ (b) samples

Taking into account that the optical absorption spectra of $\text{NH}_4\text{Ce}_2(\text{PO}_4)_3$ and $\text{KCe}_2(\text{PO}_4)_3$ samples are similar within each series, the increase in SPF and UVAPF values is likely due to the particle size decrease. Note, that some previous studies [42–45] also have stated the impact of inorganic filler size on the sunscreens UV shielding effect. Smaller particles contribute to a denser film formation that likely caused larger absorption in the UV region.

4. Conclusions

The study investigated the particle size distributions and UV radiation protective effects of isostructural $\text{NH}_4\text{Ce}_2(\text{PO}_4)_3$ and $\text{KCe}_2(\text{PO}_4)_3$ phases synthesized through hydrothermal and hydrothermal microwave methods, including those combined with ultrasonic pre-treatment. It has been demonstrated that the sonication of starting ceric phosphate gels followed by hydrothermal-microwave treatment allows for the production of double ceric phosphates with the smallest crystallite sizes (approximately 60 nm) and the narrowest particle size distribution. For the first time, it has been shown that the crystallite sizes of $\text{NH}_4\text{Ce}_2(\text{PO}_4)_3$ and $\text{KCe}_2(\text{PO}_4)_3$ affect their UV shielding properties. The study revealed that the sun protection factor and protection factor against UV-A radiation increase as the mean particle size of the materials decreases. The SPF and UVAPF values obtained (up to 4) are significantly higher than previously published values for similar ceric compounds.

References

- [1] Gallagher R.P., Lee T.K. Adverse Effects of Ultraviolet Radiation: A Brief Review. *Prog. Biophys. Mol. Biol.*, 2006, **92**, P. 119–131.
- [2] González S., Fernández-Lorente M., Gilaberte-Calzada Y. The Latest on Skin Photoprotection. *Clin. Dermatol.*, 2008, **26**, P. 614–626.
- [3] Wang S.Q., Balagula Y., Osterwalder U. Photoprotection: A Review of the Current and Future Technologies. *Dermatol. Ther.*, 2010, **23**, P. 31–47.
- [4] Egambaram O.P., Kesavan Pillai S., Ray S.S. Materials Science Challenges in Skin UV Protection: A Review. *Photochem. Photobiol.*, 2020, **96**, P. 779–797.
- [5] Schneider S.L., Lim H.W. A Review of Inorganic UV Filters Zinc Oxide and Titanium Dioxide. *Photodermatol. Photoimmunol. Photomed.*, 2019, **35**, P. 442–446.
- [6] Onoda H., Iwashita M. Synthesis of Novel White Pigments by Shaking Cerium Compounds with Phosphoric Acid. *Emergent Mater.*, 2023, **6**, P. 1089–1095.
- [7] Onoda H., Tanaka R. Synthesis of Cerium Phosphate White Pigments from Cerium Carbonate for Cosmetics. *J. Mater. Res. Technol.*, 2019, **8**, P. 5524–5528.
- [8] Achary S.N., Bevara S., Tyagi A.K. Recent Progress on Synthesis and Structural Aspects of Rare-Earth Phosphates. *Coord. Chem. Rev.*, 2017, **340**, P. 266–297.
- [9] Sato T., Li R., Sato C., Yin S. Synthesis and Photochemical Properties of Micaceous Cerium Phosphates. *Phosphorus Res. Bull.*, 2007, **21**, P. 44–47.
- [10] Sato T., Sato C., Yin S. Optimization of Hydrothermal Synthesis of Plate-Like Hydrated Cerium Phosphates and Their Photochemical Properties. *Phosphorus Res. Bull.*, 2008, **22**, P. 17–21.
- [11] Sato T., Yin S. Morphology Control of Cerium Phosphates for UV-Shielding Application. *Phosphorus Res. Bull.*, 2010, **24**, P. 43–48.
- [12] Kozlova T.O., Popov A.L., Kolesnik I. V., Kolmanovich D.D., Baranchikov A.E., Shcherbakov A.B., Ivanov V.K. Amorphous and Crystalline Cerium(IV) Phosphates: Biocompatible ROS-Scavenging Sunscreens. *J. Mater. Chem. B*, 2022, **10**, P. 1775–1785.
- [13] Nazaraly M., Quarton M., Wallez G., Chanéac C., Ribot F., Jolivet J.P. $\text{Ce}(\text{H}_2\text{O})(\text{PO}_4)_{3/2}(\text{H}_3\text{O})_{1/2}(\text{H}_2\text{O})_{1/2}$, a Second Entry in the Structural Chemistry of Cerium(IV) Phosphates. *Solid State Sci.*, 2007, **9**, P. 672–677.
- [14] Nazaraly M., Chanéac C., Ribot F., Wallez G., Quarton M., Jolivet J.P. A New Story in the Structural Chemistry of Cerium(IV) Phosphate. *J. Phys. Chem. Solids*, 2007, **68**, P. 795–798.

- [15] Nazaraly M., Wallez G., Chanéac C., Tronc E., Ribot F., Quarton M., Jolivet J.P. Synthesis and Characterization of $\text{CeIV}(\text{PO}_4)(\text{HPO}_4)_{0.5}(\text{H}_2\text{O})_{0.5}$. *J. Phys. Chem. Solids*, 2006, **67**, P. 1075–1078.
- [16] Brandel V., Clavier N., Dacheux N. Synthesis and Characterization of Uranium (IV) Phosphate-Hydrogenphosphate Hydrate and Cerium (IV) Phosphate-Hydrogenphosphate Hydrate. *J. Solid State Chem.*, 2005, **178**, P. 1054–1063.
- [17] Shekunova T.O., Istomin S.Y., Mironov A. V., Baranchikov A.E., Yapryntsev A.D., Galstyan A.A., Simonenko N.P., Gippius A.A., Zhurenko S.V., Shatalova T.B., Skogareva L.S., Ivanov V.K. Crystallization Pathways of Cerium(IV) Phosphates Under Hydrothermal Conditions: A Search for New Phases with a Tunnel Structure. *Eur. J. Inorg. Chem.*, 2019, **2019**, P. 3242–3248.
- [18] Kozlova T.O., Mironov A.V., Istomin S.Y., Birichevskaya K.V., Gippius A.A., Zhurenko S.V., Shatalova T.B., Baranchikov A.E., Ivanov V.K. Meet the Cerium(IV) Phosphate Sisters: $\text{Ce}^{\text{IV}}(\text{OH})\text{PO}_4$ and $\text{Ce}_2^{\text{IV}}\text{O}(\text{PO}_4)_2$. *Chem. – A Eur. J.*, 2020, **26**, P. 12188–12193.
- [19] Kozlova T.O., Vasilyeva D.N., Kozlov D.A., Teplonogova M.A., Baranchikov A.E., Simonenko N.P., Ivanov V.K. Synthesis and Thermal Behavior of $\text{KCe}_2(\text{PO}_4)_3$, a New Full-Member in the $\text{A}^{\text{I}}\text{M}_2^{\text{IV}}(\text{PO}_4)_3$ Family. *Nanosyst. Phys. Chem. Math.*, 2023, **14**, P. 112–119.
- [20] Serpone N., Dondi D., Albini A. Inorganic and Organic UV Filters: Their Role and Efficacy in Sunscreens and Suncare Products. *Inorganica Chim. Acta*, 2007, **360**, P. 794–802.
- [21] Ngoc T., Moon C., Park L. Recent Trends of Sunscreen Cosmetic: An Update Review. *Cosmetics*, 2019, **6**, 64.
- [22] Geoffrey K., Mwangi A.N., Maru S.M. Sunscreen Products: Rationale for Use, Formulation Development and Regulatory Considerations. *Saudi Pharm. J.*, 2019, **27**, P. 1009–1018.
- [23] Tronev I.V., Sheichenko E.D., Razvorotneva L.S., Trufanova E.A., Minakova P.V., Kozlova T.O., Baranchikov A.E., Ivanov V.K. Microwave-Assisted Hydrothermal Synthesis of Ceric-Ammonium Phosphates $(\text{NH}_4)_2\text{Ce}(\text{PO}_4)_2 \cdot \text{H}_2\text{O}$ and $\text{NH}_4\text{Ce}_2(\text{PO}_4)_3$. *Russ. J. Inorg. Chem.*, 2023, **68**, P. 263–269.
- [24] Yapryntsev A.D., Baranchikov A.E., Ivanov V.K., Tret'yakov Y.D. Chromium(III) Oxyhydroxide Synthesis under Intense Sonication. *Dokl. Chem.*, 2012, **446**, P. 180–182.
- [25] Yapryntsev A.D., Baranchikov A.E., Gubanov N.N., Ivanov V.K., Tret'yakov Y.D. Synthesis of Nanocrystalline ZrO_2 with Tailored Phase Composition and Microstructure under High-Power Sonication. *Inorg. Mater.*, 2012, **48**, P. 494–499.
- [26] Yang G., Lin W., Lai H., Tong J., Lei J., Yuan M., Zhang Y., Cui C. Understanding the Relationship between Particle Size and Ultrasonic Treatment during the Synthesis of Metal Nanoparticles. *Ultrason. Sonochem.*, 2021, **73**, 105497.
- [27] Kozlova T.O., Baranchikov A.E., Birichevskaya K.V., Kozlov D.A., Simonenko N.P., Gavrikov A.V., Teplonogova M.A., Ivanov V.K. On the Thermal Decomposition of Cerium(IV) Hydrogen Phosphate $\text{Ce}(\text{PO}_4)(\text{HPO}_4)_{0.5}(\text{H}_2\text{O})_{0.5}$. *Russ. J. Inorg. Chem.*, 2021, **66**, P. 1624–1632.
- [28] Baranchikov A.E., Polezhaeva O.S., Ivanov V.K., Tret'yakov Y.D. Lattice Expansion and Oxygen Non-Stoichiometry of Nanocrystalline Ceria. *CrystEngComm*, 2010, **12**, P. 3531–3533.
- [29] Shekunova T.O., Baranchikov A.E., Ivanova O.S., Skogareva L.S., Simonenko N.P., Karavanova Y.A., Lebedev V.A., Borilo L.P., Ivanov V.K. Ceric Phosphate Gels: Synthesis, Thermal Decomposition and Hydrothermal Crystallization Paths. *J. Non. Cryst. Solids*, 2016, **447**, P. 183–189.
- [30] Kozlova T.O., Vasil'eva D.N., Kozlov D.A., Teplonogova M.A., Birichevskaya K.V., Baranchikov A.E., Gavrikov A.V., Ivanov V.K. On the Chemical Stability of $\text{Ce}^{\text{IV}}(\text{PO}_4)(\text{HPO}_4)_{0.5}(\text{H}_2\text{O})_{0.5}$ in Alkaline Media. *Russ. J. Inorg. Chem.*, 2022, **67**, P. 1901–1907.
- [31] Skogareva L.S., Shekunova T.O., Baranchikov A.E., Yapryntsev A.D., Sadovnikov A.A., Ryumin M.A., Minaeva N.A., Ivanov V.K. Synthesis of Cerium Orthophosphates with Monazite and Rhabdophane Structure from Phosphoric Acid Solutions in the Presence of Hydrogen Peroxide. *Russ. J. Inorg. Chem.*, 2016, **61**, P. 1219–1224.
- [32] Clavier N., Mesbah A., Szenknect S., Dacheux N. Monazite, Rhabdophane, Xenotime & Churchite: Vibrational Spectroscopy of Gadolinium Phosphate Polymorphs. *Spectrochim. Acta – Part A Mol. Biomol. Spectrosc.*, 2018, **205**, P. 85–94.
- [33] Petit S., Righi D., Madejová J. Infrared Spectroscopy of NH_4^+ -Bearing and Saturated Clay Minerals: A Review of the Study of Layer Charge. *Appl. Clay Sci.*, 2006, **34**, P. 22–30.
- [34] Petit S., Righi D., Madejová J., Decarreau A. Interpretation of the Infrared NH_4^+ Spectrum of the NH_4^+ -Clays: Application to the Evaluation of the Layer Charge. *Clay Miner.*, 1999, **34**, P. 543–549.
- [35] Klopogge J.T., Broekmans M., Duong L.V., Martens W.N., Hickey L., Frost R.L. Low Temperature Synthesis and Characterisation of Lecontite, $(\text{NH}_4)\text{Na}(\text{SO}_4)_2 \cdot \text{H}_2\text{O}$. *J. Mater. Sci.*, 2006, **41**, P. 3535–3539.
- [36] Kopitsa G.P., Baranchikov A.E., Ivanova O.S., Yapryntsev A.D., Grigoriev S. V., Pranzas P.K., Ivanov V.K. Effect of High Intensity Ultrasound on the Mesostructure of Hydrated Zirconia. *J. Phys. Conf. Ser.*, 2012, **340**, 012057.
- [37] Ivanov V.K., Kopitsa G.P., Sharikov F.Y., Baranchikov A.Y., Shaporev A.S., Grigoriev S.V., Pranzas P.K. Ultrasound-Induced Changes in Mesostructure of Amorphous Iron (III) Hydroxide Xerogels: A Small-Angle Neutron Scattering Study. *Phys. Rev. B*, 2010, **81**, 174201.
- [38] Kuznetsova V.A., Almjasheva O.V., Gusarov V.V. Influence of Microwave and Ultrasonic Treatment on the Formation of CoFe_2O_4 under Hydrothermal Conditions. *Glas. Phys. Chem.*, 2009, **35**, P. 205–209.
- [39] Rezaei P., Rezaei M., Meshkani F. Ultrasound-Assisted Hydrothermal Method for the Preparation of the $\text{M-Fe}_2\text{O}_3 \cdot \text{CuO}$ (M: Mn, Ag, Co) Mixed Oxides Nanocatalysts for Low-Temperature CO Oxidation. *Ultrason. Sonochem.*, 2019, **57**, P. 212–222.
- [40] Chorghand M., Haghighi M., Saedy S., Aghamohammadi S. Efficient Hydrothermal Synthesis of Nanostructured SAPO-34 Using Ultrasound Energy: Physicochemical Characterization and Catalytic Performance toward Methanol Conversion to Light Olefins. *Adv. Powder Technol.*, 2014, **25**, P. 1728–1736.
- [41] Kolesnik I.V., Shcherbakov A.B., Kozlova T.O., Kozlov D.A., Ivanov V.K. Comparative Analysis of Sun Protection Characteristics of Nanocrystalline Cerium Dioxide. *Russ. J. Inorg. Chem.*, 2020, **65**, P. 960–966.
- [42] Goh E.G., Xu X., McCormick P.G. Effect of Particle Size on the UV Absorbance of Zinc Oxide Nanoparticles. *Scr. Mater.*, 2014, **78–79**, P. 49–52.
- [43] Shi W., Lin Y., Zhang S., Tian R., Liang R., Wei M., Evans D.G., Duan X. Study on UV-Shielding Mechanism of Layered Double Hydroxide Materials. *Phys. Chem. Chem. Phys.*, 2013, **15**, 18217.
- [44] Kim J.H., Choi J., Choi S., Kim W., Lee S. Study on the Dependence of Sun Protection Factor on Particle Size Distribution of Mica Using Gravitational Field-Flow Fractionation. *Bull. Korean Chem. Soc.*, 2020, **41**, P. 66–72.
- [45] Silva M.R.F., Alves M.F.R.P., Cunha J.P.G.Q., Costa J.L., Silva C.A., Fernandes M.H.V., Vilarinho P.M., Ferreira P. Nanostructured Transparent Solutions for UV-Shielding: Recent Developments and Future Challenges. *Mater. Today Phys.*, 2023, **35**, 101131.

Information about the authors:

Taisiya O. Kozlova – Kurnakov Institute of General and Inorganic Chemistry of the Russian Academy of Sciences, Leninsky prospect, 31, Moscow, 119991, Russia; ORCID 0000-0002-9757-9148; taisia.shekunova@yandex.ru

Ekaterina D. Sheichenko – Kurnakov Institute of General and Inorganic Chemistry of the Russian Academy of Sciences, Leninsky prospect, 31, Moscow, 119991, Russia; National Research University Higher School of Economics, Moscow, Myasnitskaya str., 20, 101000, Russia; ORCID 0000-0003-3485-1842; kseterina@yandex.ru

Darya N. Vasilyeva – Kurnakov Institute of General and Inorganic Chemistry of the Russian Academy of Sciences, Leninsky prospect, 31, Moscow, 119991, Russia; National Research University Higher School of Economics, Moscow, Myasnitskaya str., 20, 101000, Russia; ORCID 0009-0004-3560-4178; dnvasilyeva_1@edu.hse.ru

Daniil A. Kozlov – Kurnakov Institute of General and Inorganic Chemistry of the Russian Academy of Sciences, Leninsky prospect, 31, Moscow, 119991, Russia; ORCID 0000-0003-0620-8016; kozlov@inorg.chem.msu.ru

Irina V. Kolesnik – Kurnakov Institute of General and Inorganic Chemistry of the Russian Academy of Sciences, Leninsky prospect, 31, Moscow, 119991, Russia; Lomonosov Moscow State University, Leninskie Gory 1, Moscow, 119991, Russia; ORCID 0000-0002-1411-6691; kolesnik.iv@gmail.com

Ilya V. Tronev – Kurnakov Institute of General and Inorganic Chemistry of the Russian Academy of Sciences, Leninsky prospect, 31, Moscow, 119991, Russia; National Research University Higher School of Economics, Moscow, Myasnitskaya str., 20, 101000, Russia; ORCID 0000-0002-0718-1911; ivtronev@edu.hse.ru

Maria A. Teplonogova – Kurnakov Institute of General and Inorganic Chemistry of the Russian Academy of Sciences, Leninsky prospect, 31, Moscow, 119991, Russia; ORCID 0000-0002-4820-8498; m.teplonogova@gmail.com

Alexander E. Baranchikov – Kurnakov Institute of General and Inorganic Chemistry of the Russian Academy of Sciences, Leninsky prospect, 31, Moscow, 119991, Russia; ORCID 0000-0002-2378-7446; a.baranchikov@yandex.ru

Vladimir K. Ivanov – Kurnakov Institute of General and Inorganic Chemistry of the Russian Academy of Sciences, Leninsky prospect, 31, Moscow, 119991, Russia; ORCID 0000-0003-2343-2140; van@igic.ras.ru

Conflict of interest: the authors declare no conflict of interest.

Synthesis of magnesium ferrite by combustion of glycine-nitrate gel: the influence of reagents on the gel-precursor and the microstructure of nanopowders

Maria N. Smirnova^{1,a}, Galina E. Nikiforova^{1,b}, Olga N. Kondrat'eva^{1,c}

¹Kurnakov Institute of General and Inorganic Chemistry of the Russian Academy of Sciences, Moscow, Russia

^asmirnovamn@igic.ras.ru, ^bgen@igic.ras.ru, ^colga.kondratieva@igic.ras.ru

Corresponding author: M. N. Smirnova, smirnovamn@igic.ras.ru

PACS 61.46.+w, 61.10.cj

ABSTRACT In this study, the influence of initial reagents on the phase composition and morphology of magnesium ferrite obtained by combustion of glycine-nitrate gel was investigated. The local environment of iron ions in the gel-precursor was studied in detail using FT-IR, XANES- and EXAFS- spectroscopy. It has been established that in the gel-precursor obtained by dissolving metals (Mg, Fe) in dilute nitric acid, binuclear Fe(III) complexes are formed, while in a similar gel-precursor obtained from crystalline hydrates of nitrates of the corresponding metals, trinuclear Fe(III) complexes predominate. Combustion of a gel consisting of binuclear Fe(III) complexes leads to the formation of nanocrystalline magnesium ferrite powder, characterized by a unimodal particle size distribution.

KEYWORDS gel combustion, glycine, spinel, nanopowders, MgFe₂O₄

ACKNOWLEDGEMENTS This research was supported by the Russian Science Foundation (project No. 22-73-00185). The measurements were performed using the equipment of the Joint Research Centre (JRC PMR) IGIC RAS.

FOR CITATION Smirnova M.N., Nikiforova G.E., Kondrat'eva O.N. Synthesis of magnesium ferrite by combustion of glycine-nitrate gel: the influence of reagents on the gel-precursor and the microstructure of nanopowders. *Nanosystems: Phys. Chem. Math.*, 2024, **15** (2), 224–232.

1. Introduction

Ferrites with a spinel structure have attracted the interest of researchers for many years due to their combination of magnetic and electrical properties, chemical and thermal stability, and low toxicity. One of the representatives of this class of compounds is magnesium ferrite MgFe₂O₄ – a soft magnetic semiconductor material that is used in heterogeneous catalysis, the production of sensors, microelectronics and medicine [1–6]. The magnetic characteristics of this ferrite, and therefore the possibility of its practical use, largely depend on the particle size, degree of crystallinity and morphological homogeneity. Depending on the synthesis method, these parameters can vary within wide limits. Various methods for producing ferrites with a spinel structure are described in the literature, among which the most common are the solid-phase synthesis [5, 7], the coprecipitation method [4, 8], the hydrothermal method [9, 10] and gel combustion method [11, 12].

The main advantage of the gel combustion method is the successful combination of chemical homogenization of the starting components through the use of complexing agents and the high-temperature short-term stage of the precursor gel combustion in a self-sustaining mode, which makes this method promising for the production of highly dispersed oxide powders. Currently, there is a significant number of publications that examine the influence of the choice of organic “fuel” (for example, citric acid, glycine, urea, etc.), as well as the ratio of the initial components of the reaction (excess, deficiency or stoichiometric amount of “fuel” in relation to metal compounds) on the phase composition of the final product [13–22]. However, intermediate stages of synthesis, such as the formation and structuring of gels, as well as the influence of these processes on the characteristics of the final product, have been little studied. At the same time, this information is necessary for the targeted production of oxide materials of a given composition with certain morphological characteristics.

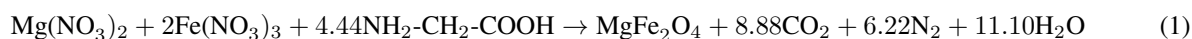
In this work, two approaches to the synthesis of magnesium ferrite MgFe₂O₄ by the gel combustion method were used and compared, one of which involves the preparation of an initial solution of nitrates by dissolving metallic magnesium and iron in dilute nitric acid, the second is based on the dissolution of crystalline hydrates of magnesium and iron nitrates in water. The purpose of this work is to study the structural features of precursor gels and to identify the existence of a connection between the choice of initial reagents and the phase and morphological properties of the final product.

2. Experimental

2.1. Synthesis MgFe₂O₄ from metals

An aqueous solution of magnesium (II) and iron (III) nitrates in a molar ratio of 1:2 was obtained by dissolving 0.279 g of metallic iron (Purissimum speciale), 0.061 g of metallic magnesium (Purissimum) in dilute (1:3) nitric acid. The number of metals was calculated so that the mass of the final product, that is MgFe₂O₄ powder, was 5 g.

To completely dissolve the metals and remove excess nitric acid, the solution was evaporated in a conical glass flask at a temperature of 80–90°C for 30 hours with constant stirring, regularly adding distilled water. The resulting nitrate solution “NM” (pH < 2) was further cooled, with an equivalent amount of glycine (0.833 g) added to it. To determine the equivalent ratio of the initial components, the balance between the valences of the oxidising and the reducing agent was used (the method of oxidising and reducing valences). Using this method, the energy released during the combustion of the mixture is assumed to be maximum when the ratio of the valence sum of the oxidising agent to the valence sum of the reducing agent is equal to one. According to calculations, 4.44 mol of glycine is required to produce 1 mol of MgFe₂O₄ (Eq. 1):



The resulting reaction mixture was evaporated in an open porcelain cup (approximately 80–90°C, for 2 hours) with constant stirring until it transformed into a gel (GM).

Subsequently, violent combustion occurred at a temperature of >100°C. Then, the powdered combustion product (PM) was kept for 30 minutes at a temperature of about 100–120°C, cooled, ground with a ball mill, and annealed at 700°C (for 6 h) in a muffle laboratory furnace.

2.2. Synthesis of MgFe₂O₄ from crystalline hydrates of metal nitrates

An aqueous solution of magnesium (II) and iron (III) nitrates in a molar ratio of 1:2 was obtained by dissolving 12.444 g of iron (III) nitrate nonahydrate and 3.756 g of magnesium (II) nitrate hexahydrate in distilled water. Before the synthesis, the water content in the crystal hydrates was specified by the gravimetric method. As a result, the number of the initial reagents was calculated for the following crystal hydrates (Fe(NO₃)₃·9.6 H₂O and Mg(NO₃)₂·5.7 H₂O) so that the mass of the final product, that is MgFe₂O₄ powder, was 5 g.

After preparing the nitrate solution “NC” (pH ~ 5), further steps of synthesis correspond to the procedure presented in Section 2.1. and include the preparation of the gel (GC), its combustion and annealing to form a powdery product (PC).

A summary scheme for synthesis of GM and GC, PM and PC samples is presented in Fig. 1.

2.3. Synthesis of iron nitrate gel (a sample-control)

To study the local atomic structure of gels by EXAFS spectroscopy, a sample-control (GF) was additionally prepared. The synthesis was carried out by dissolving metallic iron (Purissimum speciale) in dilute (1:3) nitric acid (the iron content is the same as in the sample “NM”). The resulting solution was repeatedly (5–8 times) evaporated in a conical glass flask at 80–90°C, adding distilled water regularly. Glycine was further added to the resulting solution in an equivalent amount that is required to obtain 5 g of Fe₂O₃ powder. This reaction mixture was evaporated until it transformed into a gel (GF).

2.4. Research methods

Chemical analysis of initial nitrate solutions, gels and powders was performed by inductively coupled plasma atomic emission spectrometry (ICP-AES) on an ICAP PRO XP spectrometer (Thermo Electron Corp., USA). Measurements were performed in the radial plasma view mode at the following spectrometer settings (power 1150 W, nebulizer gas flow 0.60 l/min, auxiliary gas flow 0.35 l/min, cooling gas flow 10 l/min).

FTIR spectra of gels and glycine were recorded on a Perkin Elmer Spectrum 65 FT-IR spectrometer in the region of 4000–400 cm⁻¹ with a resolution of 2 cm⁻¹.

Iron K-edge EXAFS spectra were recorded in transmission mode by measuring the intensity of the X-ray beam before and after passing through the sample using argon-filled ionization chambers. For obtaining Fe K-edge spectra Si(111) channel-cut monochromator (energy resolution $\Delta E/E \approx 2 \times 10^{-4}$) and two ion chambers filled with argon were used. A standard processing of XAS spectra was carried out in terms of IFEFFIT software package [23, 24]. Normalized EXAFS oscillations were *k*²- or *k*³-weighted, Fourier transforms were taken in a 2.5–13.0 Å⁻¹ *k*-range. The Fourier-transformed EXAFS oscillations were fitted in the range of 1.2–3.8 Å. The amplitude reduction factor for iron was taken as 1.

The phase identity and purity of magnesium ferrite were confirmed by X-ray powder diffraction (XRD), using a Bruker D8 Advance XRD diffractometer equipped with Ni-filtered CuK_{α1}-radiation ($\lambda = 1.5406 \text{ \AA}$) and a LYNXEYE detector. The sample was scanned between 10°C and 60°C 2θ with a step size of 0.0133°C and a counting time of 0.5 s per step. In order to interpret the results of XRD experiments, a Bruker DIFFRAC.EVA software package and the ICDD PDF-2 database were used.

The surface morphology and microstructure of MgFe₂O₄ powders were investigated using a Carl Zeiss NVision 40 scanning electron microscope (SEM).

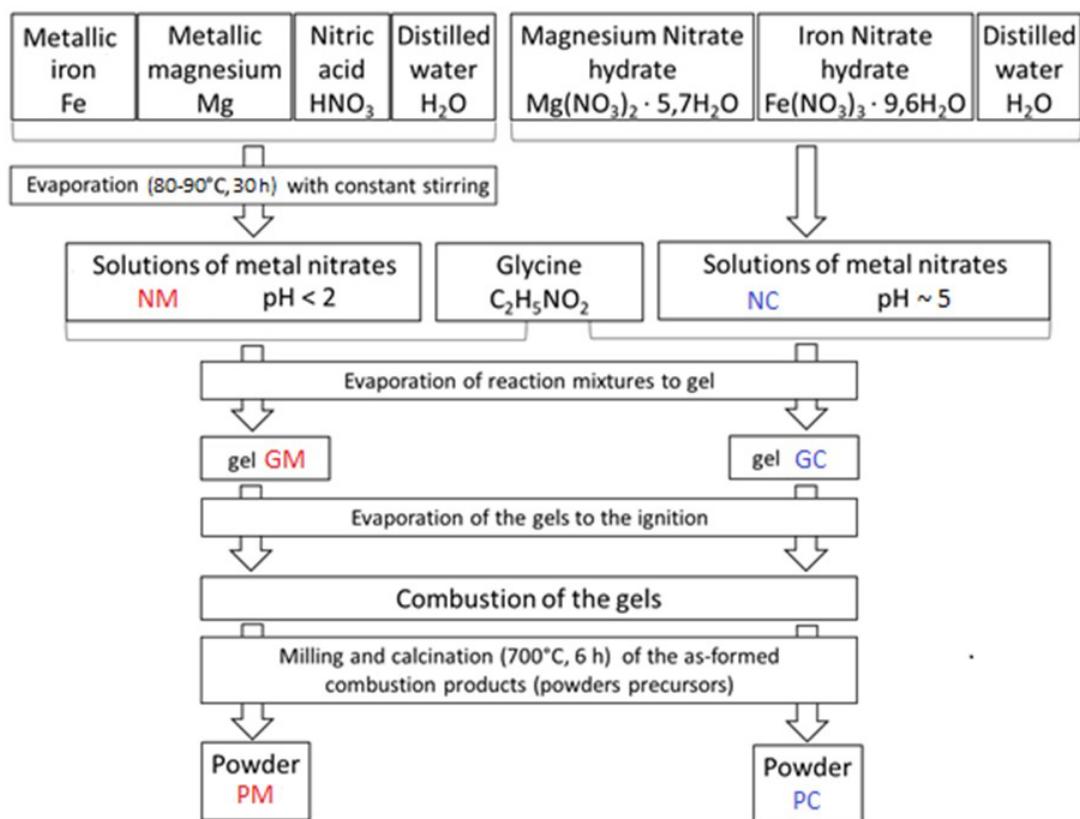


FIG. 1. Scheme of synthesis of gels (GM and GC) and powders (PM and PC)

3. Results and discussions

3.1. Elemental analysis of precursors and final product

The results of chemical analysis of precursors and finished powders are presented in Table 1. At all stages of synthesis for both samples, the ratio of elements remained constant and was close to the theoretical value. However, it should be noted that for the samples obtained from metal nitrates crystalline hydrates, a slight excess of magnesium is observed. It is likely that the use of crystalline hydrates of metal nitrates to prepare the initial solution, due to their hygroscopicity, can lead to deviations from the specified ratios of metal cations.

TABLE 1. Results of elemental analysis of nitrate solutions (NM and NC), gels (GM and GC) and powders (PM and PC)

Sample	Theoretical		Experimental	
	Mg, % wt.	Fe, % wt.	Mg, % wt.	Fe, % wt.
NM	17.6	82.4	17.9	82.1
GM			17.5	82.5
PM			17.6	82.4
NC			18.0	82.0
GC			18.1	81.9
PC			18.2	81.8

3.2. FTIR spectral analysis

To identify the role of the functional groups of the reagents in the process of formation of the structure of the gels, their Fourier transform IR spectra were initially studied, as well as the spectra of the starting glycine for comparative analysis (Fig. 2).

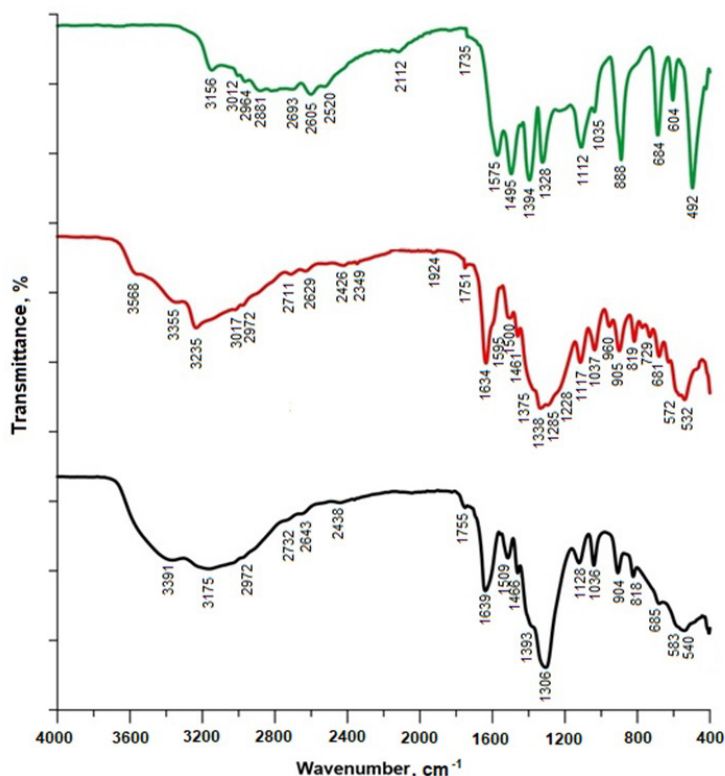


FIG. 2. FTIR spectra (from top to bottom) of glycine, GM and GC gels

The FTIR spectrum of glycine corresponds to the standard spectrum of γ -glycine [25]. The intense absorption peak at 492 cm^{-1} is due to torsional vibrations of the amino group. The bands at 604 cm^{-1} and 684 cm^{-1} are associated with bending vibrations of the COO^- group. The C–C stretching vibration produced absorption bands at 888 cm^{-1} . The peak at 1328 cm^{-1} can be attributed to both the wagging vibrations of CH_2 groups [26] and the bending vibrations of the methylene and amino groups [27]. Weak bands traced at 1035 cm^{-1} and 1112 cm^{-1} are due to C–N stretching vibrations. Three bands characteristic of the zwitterionic nature of amino acids are further observed at 1394 cm^{-1} (symmetric stretching of COO^- groups), 1495 cm^{-1} (symmetric bending of NH_3^+ ions) and 1575 cm^{-1} (asymmetric stretching of COO^- groups). In the range $2500\text{--}3200\text{ cm}^{-1}$, broad bands due to symmetric and asymmetric stretching vibrations of N–H and C–H bonds are observed [26–29].

The general appearance of the FTIR spectra of GM and GC gels differs from the spectrum of glycine. In both spectra there is no band at 492 cm^{-1} , which indicates binding of the nitro group. Moreover, additional absorption bands appear: in the region of $500\text{--}600\text{ cm}^{-1}$, associated with stretching vibrations of the Mg–O and Fe–O bonds, as well as bands located at 819 cm^{-1} and in the region of $1450\text{--}1300\text{ cm}^{-1}$, which is associated with bending vibrations of the NO_3^- group and stretching vibrations of N–O bonds [30, 31]. The position of the bands indicates a distortion of the geometry of free nitrate ions. In this case, the magnitude of the frequency separation of the bands ($\Delta\nu$) is different, which indicates the presence in the gels of nitrate groups with different types of bonds – coordination and ionic. The pronounced spectral absorption band at $1634\text{--}1639\text{ cm}^{-1}$ is associated with bending vibrations of the H–O–H bond of water. The FTIR region of $3000\text{--}3600\text{ cm}^{-1}$ indicates the presence of OH- groups in the gels involved in the formation of hydrogen bonds. It is difficult to make more precise conclusions about the nature of the bonds, since in this region the bands of stretching vibrations of OH-groups, amino-groups and the N(H)...O hydrogen bond overlap. It should be noted that for the GM gel, the above absorption bands are shifted towards higher frequencies, which indicates the formation of weaker hydrogen bonds compared to the GC gel. Another important difference in the FTIR spectra of the gels is the presence in the spectrum of the GM gel of two absorption bands at 1228 cm^{-1} and 1298 cm^{-1} , associated with vibrations of the carboxyl group and characteristic only of the cationic form of glycine [27].

3.3. X-ray Absorption Spectroscopy

At the next step of investigation GM and GC gels were studied by XAS-spectroscopy (Fig. 3). This method allows obtaining structural information of nearest environment of iron atoms in organometallic gels. For a more accurate interpretation of the results, a control sample marked as GF was additionally prepared.

The XANES spectra (Fig. 3a) of samples GC, GM and GF are almost coincident, which indicates that iron is in an octahedral environment in all gels. The most intense peak at the range of $\sim 1\text{--}2\text{ \AA}$ on the R- δ scale in the EXAFS data

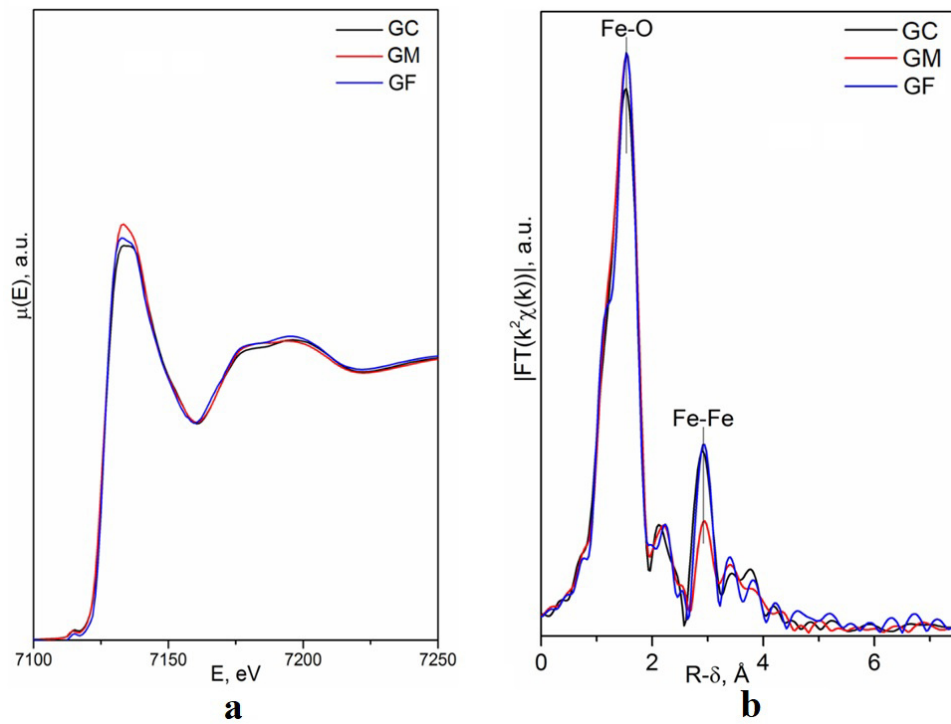


FIG. 3. XANES spectra (a) and EXAFS Fourier transforms (b) of iron K edge for organometallic gels GC, GM and GF

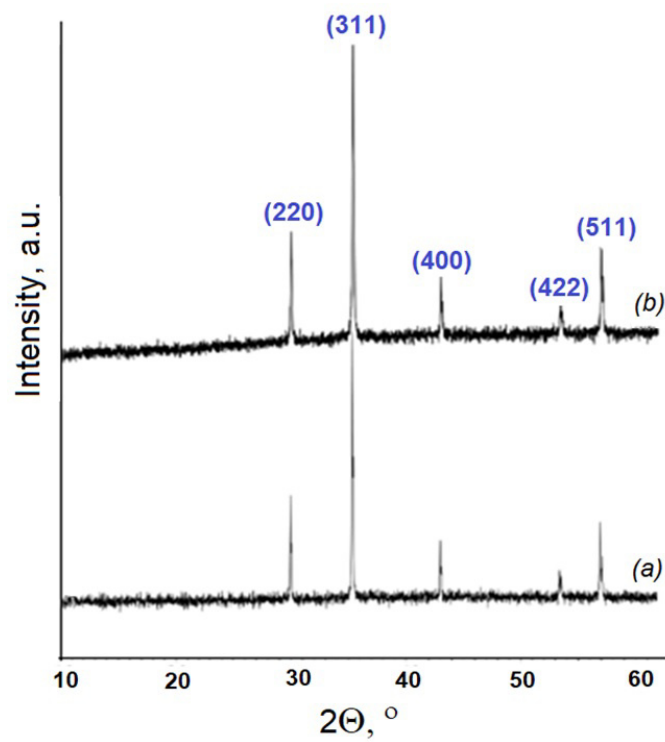


FIG. 4. X-ray diffraction patterns of PM (a) and PC (b) powders

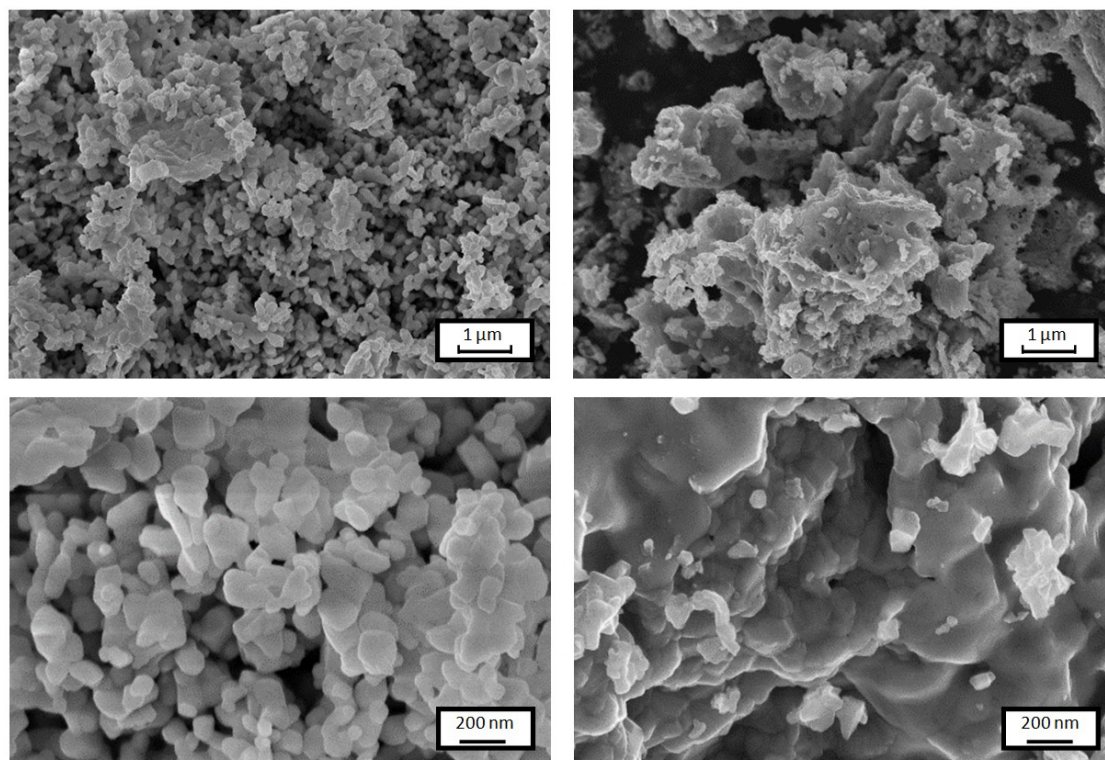


FIG. 5. SEM images of MgFe_2O_4 nanopowders (PM on the left and PC on the right) after annealing at 700°C

(Fig. 3b) refers to the oxygen atoms of the first coordination sphere of iron. The less intense peak ($R \sim 3 \text{ \AA}$) corresponds to the Fe atoms (Fig. 3b). The simulation results for the reference sample GF (Table 2) indicate the formation of a trinuclear iron (III) complex with glycine [32]. There are 6 oxygen atoms in the first coordination sphere of iron ($\sim 1.9\text{--}2.0 \text{ \AA}$) and two equidistant iron atoms at a distance of $\sim 3.31 \text{ \AA}$ in the structure of this complex (Table 2).

Applying the parameters of this model to the EXAFS data of GM and GC samples shows that the GC gel contains an iron (III) complex similar to that described above. However, in the case of the GM sample some differences are observed: the number of oxygen atoms in the first coordination sphere remains the same, but in the second coordination sphere the coordination number (CN) of iron decreases from two to one (Table 2).

It can be assumed that in the case of the GM sample, an iron complex of a slightly different composition is formed. Also, the decrease in the CN in the coordination sphere of Fe-Fe at 3.31 \AA from 2 to 1 may possibly be associated with the formation of a binuclear Fe(III) complex in the GM sample, which differs in structure from the trinuclear Fe(III) complex in the GC gel.

One possible explanation for the observed difference in the structure of GM and GC gels is the acidity of glycine-nitrate solutions prepared from metals and nitric acid (NM) or metal crystalline hydrates (NC). In NM solution at $\text{pH} \leq 2$, glycine is present predominantly in a protonated (cationic) form ($\text{H}_3\text{N}^+\text{CH}_2\text{COOH}$), which is not prone to forming complexes with metal cations. Probably, the binding of metal cations occurs through hydroxyl groups. On the other hand, the formation of the gel structure in the GC sample occurs from a weakly acidic solution with $\text{pH} \sim 5$, in which glycine is present in a more reactive form (zwitterion), which leads to the formation of a trinuclear Fe(III) complex.

3.4. XRD and SEM analysis of powders

PM and PC powders obtained after combustion the gels were heat treated in air at a temperature of 700°C for 6 hours and then investigated by XRD and SEM. According to X-ray phase analysis (Fig. 4), both powders are magnesium ferrite with a spinel structure ($Fd\text{-}3m$ space group). No reflections of impurity phases were detected. Crystallographic parameters of MgFe_2O_4 (Table 3) were found to be in a good agreement with the data of ICDD (PDF 04-012-0908, PDF 04-010-6157, PDF 04-006-6673).

The average crystallite size d_{XRD} was estimated using Scherrer's equation:

$$d_{\text{XRD}} = \frac{K \cdot \lambda}{\beta \cdot \cos \theta}, \quad (2)$$

where K is the shape factor (0.9), λ is the X-ray wavelength (0.15418 nm), θ is the diffraction angle and β is the full width at half-maximum (FWHM) intensity of the diffraction line.

TABLE 2. Fit results for the EXAFS data for the iron gels: R – interatomic distance, CN – coordination number, σ^2 – Debye factor, R – matching factor between the experimental and model spectra. Fixed parameters are marked with *, equal values designated by ”

Sample	Scattering atom	CN	σ^2 , Å ²	R, Å (model)	R, Å (from EXAFS data)	R _f , %
GF	O	3.0*	0.0043”	1.91	1.97	1.1
	O	3.0*	0.0043”	2.03	2.07	
	C	2.0*	0.0169”	2.98	3.11	
	C	2.0*	0.0169”	2.98	3.31	
	Fe	2.0*	0.0155	3.31	3.44	
	O	2.0*	0.0048”	3.32	3.47	
	O	2.0*	0.0048”	3.46	3.60	
	O	2.0*	0.0004	3.80	3.80	
	O	2.0*	0.0026	4.00	4.23	
GC	O	1.0*	0.0011	1.92	1.90	1.7
	O	5.0*	0.0047	2.03	2.03	
	C	3.1	0.0056	2.98	3.00	
	Fe	2.0*	0.0061	3.31	3.31	
	O	2.1	0.0050	3.80	3.76	
GM	O	4.0*	0.0040	1.92	1.98	1.8
	O	2.0*	0.0027	2.03	2.09	
	C	2.0*	0.0049	2.98	3.01	
	Fe	1.0*	0.0079	3.31	3.34	
	O	2.0*	0.0115	3.80	3.71	

TABLE 3. Unit cell parameters and crystalline size values for PM and PC powders

Sample	<i>a</i> , nm	<i>V</i> , nm ³	<i>d</i> _{XRD} , nm
PM	0.8380(3)	0.5885(4)	102(3)
PC	0.8391(5)	0.5908(4)	89(7)

According to SEM data (Fig. 5), PM powder consists of spherical particles 50–120 nm in size, weakly agglomerated. PC powder, on the contrary, contains large agglomerates of particles that are heterogeneous in morphology and size. This morphological difference is likely a consequence of structural differences between GM and GC gels. Probably, the structure of the GM gel ensures a uniform distribution of metal cations and is instantly destroyed upon combustion of the gel with the formation of a homogeneous nanopowder of magnesium ferrite. The authors of [30] also noted that the combustion of a glycine-nitrate gel consisting of mononuclear complexes led to the formation of a more highly dispersed powder compared to the results of combustion of a gel consisting of six-nuclear complexes.

4. Conclusion

In this study, we showed how the choice of starting reagents as well as the precursor preparation approach influences the gel structure and morphology of the final magnesium ferrite powder. The formation of GM gel, the initial nitrate solution for which was prepared by dissolving metals in nitric acid, as shown by spectroscopic studies, occurs without pronounced complex formation between glycine and metal cations. Homogenization of the starting components occurs due to the formation of aqua complexes - a system of “weak” ionic and hydrogen bonds. Such a gel is simultaneously

destroyed during the combustion process with the formation of a homogeneous magnesium ferrite powder of a given stoichiometry, the morphological features of which are characterized by nano-sized particles that are not prone to aggregation and have a uniform distribution of their sizes.

The structuring of the GC gel, for which the initial nitrate solution was an aqueous solution of metal nitrate hydrates, is largely associated with the formation of organometallic complexes. The decomposition of these complexes is probably divided in time and has a multi-stage nature, which leads to morphological heterogeneity of the final product.

Thus, the choice of initial reagents has a significant impact on the morphology of iron-magnesium ferrite particles with a spinel structure. The information obtained on the mechanisms of structuring of glycine-nitrate metal-containing gels expands the understanding of the possibilities of targeted synthesis for obtaining complex metal oxides with a given set of properties and characteristics.

References

- [1] Heidari P., Masoudpanah S.M. Structural and magnetic properties of MgFe_2O_4 powders synthesized by solution combustion method: the effect of fuel type. *J. Mater. Res. Technol.*, 2020, **9**(3), P. 4469–4475.
- [2] Nagarajan V., Thayumanavan A. MgFe_2O_4 thin films for detection of ethanol and acetone vapours. *Surf Eng.*, 2018, **34**(9), P. 711–720.
- [3] Polat K., Yurdakoc M. Solar Decolorization of Methylene Blue by Magnetic MgFe_2O_4 -MWCNT/ Ag_3VO_4 Visible Active Photocatalyst. *Water Air Soil Pollut.*, 2018, **229**, P. 331.
- [4] Liming F., Haowen C., Kang W., Xitao W. Oxygen-vacancy generation in MgFe_2O_4 by high temperature calcination and its improved Photocatalytic activity for CO_2 Reduction. *J. Alloys Compd.*, 2021, **891**, P. 161925.
- [5] Das K.Ch., Dhara S.S. Rapid catalytic degradation of malachite green by MgFe_2O_4 nanoparticles in presence of H_2O_2 . *J. Alloys Compd.*, 2020, **828**(5), P. 154462.
- [6] Nadargi D., Umar A., Nadargi J., Patil J., Mulla I., Akbar S., Suryavanshi S. Spinel Magnesium Ferrite (MgFe_2O_4): A Glycine-Assisted Colloidal Combustion and Its Potentiality in Gas-Sensing Application. *Chemosensors*, 2022, **10**(9), P. 361.
- [7] Zhang L., Wang Y., Liu B., Wang J., Han G., Zhang Y. Characterization and property of magnetic ferrite ceramics with interesting multilayer structure prepared by solid-state reaction. *Ceram. Int.*, 2021, **47**(8), P. 10927–10939.
- [8] Naaz F., Dubey H. K., Kumari C., Lahiri P. Structural and magnetic properties of MgFe_2O_4 nanopowder synthesized via co-precipitation route. *SN Applied Sciences*, 2020, **2**(5), P. 808.
- [9] Naidu K.C.B., Madhuri W. Microwave Hydrothermal Synthesis: Structural and Dielectric Properties of nano MgFe_2O_4 . *Materials Today: Proceedings*, 2016, **3**(10 B), P. 3810–3813.
- [10] Mishra B., Munisha B., Nanda J., Sankaran K.J., Suman S. Hydrothermally Synthesized Magnesium doped Zinc Ferrite Nanoparticles: An extensive study on structural, optical, magnetic, and dielectric properties, *Materials Chemistry and Physics*, 2022, **292**, P. 126791.
- [11] Komlev A.A., Gusarov V.V. Glycine-nitrate combustion synthesis of nonstoichiometric Mg-Fe spinel nanopowders. *Inorg Mater.*, 2014, **50**, P. 1247–1251.
- [12] Zhernovoi A.I., Komlev A.A., D'yachenko S.V., Magnetic characteristics of MgFe_2O_4 nanoparticles obtained by glycine–nitrate synthesis. *Tech. Phys.*, 2016, **61**, P. 302–305.
- [13] Jamdade S., Tambade P., Rathod S., Structural and magnetic study of Tb^{3+} doped zinc ferrite by sol-gel auto-combustion technique. *Nanosyst. Physics, Chem. Math.*, 2023, **14**, P. 254–263.
- [14] Varma A., Mukasyan A.S., Rogachev A.S., Manukyan K.V. Solution combustion synthesis of nanoscale materials, *Chemical Reviews*, 2016, **116**, P. 14493–14586.
- [15] Carlos E., Martins R., Fortunato E., Branquinho R. Solution combustion synthesis: towards a sustainable approach for metal oxides. *Chem.–Eur. J.*, 2020, **26**, P. 9099–9125.
- [16] Wen W., Wu J.-M. Nanomaterials via solution combustion synthesis: a step nearer to controllability. *RSC Adv.*, 2014, **4**, P. 58090.
- [17] Li F.-T., Ran J., Jaroniec M., Qiao S.Z. Solution combustion synthesis of metal oxide nanomaterials for energy storage and conversion. *Nanoscale*, 2015, **7**, P. 17590–17610.
- [18] Smirnova M.N., Glazkova I.S., Nikiforova G.E., Kop'eva M.A., Eliseev A.A., Gorbachev E.A., Ketsko V.A., Synthesis of Ce:YIG nanopowder by gel combustion, *Nanosyst. Physics, Chem. Math.*, 2021, **12**(2), P. 210–217.
- [19] Zhuravlev V.D., Dmitriev A.V., Vladimirova E.V. et al. Parameters of Glycine–Nitrate Synthesis of NiCo_2O_4 Spinel. *Russ. J. Inorg. Chem.*, 2021, **66**, P. 1895–1903.
- [20] Martinson K.D., Belyak V.E., Sakhno D.D., Kiryanov N.V., Chebanenko M.I., Popkov V.I., Effect of fuel type on solution combustion synthesis and photocatalytic activity of NiFe_2O_4 nanopowders. *Nanosyst. Physics, Chem. Math.*, 2021, **12**, P. 792–798.
- [21] Lebedev L. A., Tenevich M. I., Popkov V. I. The effect of solution-combustion mode on the structure, morphology and size-sensitive photocatalytic performance of MgFe_2O_4 nanopowders. *Condensed Matter and Interphases*, 2022, **24**(4), P. 496–503.
- [22] Mukasyan A.S., Rogachev A.S., Aruna S.T., Combustion synthesis in nanostructured reactive systems. *Adv. Powder Technol.*, 2015, **26**, P. 954–976.
- [23] Ravel B., Newville M. ATHENA, ARTEMIS, HEPHAESTUS: data analysis for X-ray absorption spectroscopy using IFEFFIT. *J. Synch. Radiat.*, 2005, **12**(4), P. 537–541.
- [24] Newville M. IFEFFIT: interactive XAFS analysis and FEFF fitting. *J. Synch. Radiat.*, 2001, **8**(2), P. 322–324.
- [25] <https://webbook.nist.gov/cgi/cbook.cgi?ID=C56406&Units=SI&Type=IR-SPEC&Index=1#IR-SPEC>
- [26] Silverstein R.M., Bassler G.C., Morrill T.C. *Spectrometric Identification of Organic Compounds*, John Wiley & Sons, New York, 1981.
- [27] Butyrskaya E.V., Nechaeva L.S., Shaposhnik V.A., Drozdova E.I. Assignment of bands in IR spectra of aqueous glycine solutions based on quantum chemical calculation. *J. Sorption and chromatographic processes*, 2012, **12**(4), P. 501–511.
- [28] Boldyreva E.V., Drebuschak V.A., Drebuschak T.N., Paukov I.E., Kovalevskaya Y.A., Shutova E.S. Polymorphism of glycine: Thermodynamic aspects. Part I - Relative stability of the polymorphs. *J. Therm. Anal. Calorim.*, 2003, **73**, P. 409–418.
- [29] Larkin P. *Infrared and Raman Spectroscopy: Principles and Spectral Interpretation*, Elsevier, 2017, 286 p.
- [30] Jain D., Sudarsan V., Patra A.K., Sastry P.U., Tyagi A.K. Effect of local ordering around Th^{4+} ions in glycine-nitrate precursor gel on the powder characteristic of gel-combusted ThO_2 . *J. Nucl. Mater.*, 2019, **527**, P. 151826.
- [31] Warriar A.V.R., Narayanan P.S. Infrared absorption spectra of single crystals of glycine silver nitrate and monoglycine nitrate. *Proc. Indian Acad. Sci.*, 1967, **66**, P. 46–54.

[32] Turte K.I., Lazaresku A.G., Simonov Yu.A., Lipkovskii Ya., Dvorkin A.A., Patron L. Structure of (μ_3 -Oxo)-hexa(μ -glycine-*O, O'*)triaquatriiron (III) Nitrate 3.5-Hydrate. *Russ. J. Coord. Chem.*, 1996, **22**(1), P. 45–53.

Submitted 28 February 2024; accepted 15 March 2024

Information about the authors:

Maria N. Smirnova – Kurnakov Institute of General and Inorganic Chemistry of the Russian Academy of Sciences, 119991, 31 Leninsky Prospect, Moscow, Russia; ORCID 0000-0003-2707-7975; smirnovamn@igic.ras.ru

Galina E. Nikiforova – Kurnakov Institute of General and Inorganic Chemistry of the Russian Academy of Sciences, 119991, 31 Leninsky Prospect, Moscow, Russia; ORCID 0000-0002-2892-6054; gen@igic.ras.ru

Olga N. Kondrat'eva – Kurnakov Institute of General and Inorganic Chemistry of the Russian Academy of Sciences, 119991, 31 Leninsky Prospect, Moscow, Russia; ORCID 0000-0003-2508-9868; olga.kondratieva@igic.ras.ru

Conflict of interest: the authors declare no conflict of interest.

Structural, magnetic and electrochemical studies on $Zn_xMg_{1-x}Fe_2O_4$ nanoparticles prepared via solution combustion method

Kirill D. Martinson^{1,a}, Alexander A. Murashkin^{2,b}, Artem A. Lobinsky^{1,c}, Danil D. Maltsev^{1,d},
Kezhen Qi^{3,e}, Jiaguo Yu^{4,f}, Oksana V. Almjasheva^{2,g}, Vadim I. Popkov^{1,h}

¹Ioffe Institute, Saint Petersburg, Russia

²Saint Petersburg Electrotechnical University “LETI”, Saint Petersburg, Russia

³College of Pharmacy, Dali University, Dali, China

⁴China University of Geosciences, Wuhan, China

^amartinsonkirill@mail.ru, ^bmurashkin1999@list.ru, ^clobinski.a@mail.ru, ^ddm.work.ac@gmail.com,

^eqkzh2003@aliyun.com, ^fyujiaquo93@cug.edu.cn, ^galmjasheva@mail.ru, ^hvip-07@yandex.ru

Corresponding author: K. D. Martinson, martinsonkirill@mail.ru

PACS 61.46Df, 75.50.Gg, 75.75.Fk

ABSTRACT Zinc-manganese ferrite nanoparticles, denoted as $Zn_xMg_{1-x}Fe_2O_4$ where x ranges from 0 to 1, were synthesized via solution combustion employing glycine as the organic fuel at a stoichiometric redox ratio. The resultant compositions underwent comprehensive characterization utilizing scanning electron microscopy, energy-dispersive spectroscopy, and powder X-ray diffractometry. Magnetic and electrochemical properties were meticulously examined using a vibrating magnetometer and cyclic voltmeter, respectively. Analysis revealed an average particle size ranging from 24.9 to 30.8 nm across all synthesized samples, with degrees of crystallinity reaching 93–96%. Notably, variations in the magnetic behavior were observed depending on the magnesium content within the samples. The highest magnetic parameters were recorded for $Zn_{0.4}Mg_{0.6}Fe_2O_4$ ($M_s = 27.78$ emu/g, $M_r = 3.77$ emu/g, and $H_c = 21.4$ Oe). Furthermore, the electrochemical capacity of the synthesized powders exhibited dependency on the incorporation of magnesium cations into the crystal lattice. These findings underscore the significance of magnesium content in modulating the magnetic and electrochemical properties of $Zn_xMg_{1-x}Fe_2O_4$ nanoparticles synthesized via solution combustion.

KEYWORDS zinc-manganese ferrite, nanoparticles, magnetic properties, electrochemical properties.

ACKNOWLEDGEMENTS The reported study was funded by Russian Science Foundation (grant no. 21-73-10070).

FOR CITATION Martinson K.D., Murashkin A.A., Lobinsky A.A., Maltsev D.D., Qi K., Yu J., Almjasheva O.V., Popkov V.I. Structural, magnetic and electrochemical studies on $Zn_xMg_{1-x}Fe_2O_4$ nanoparticles prepared via solution combustion method. *Nanosystems: Phys. Chem. Math.*, 2024, **15** (2), 233–239.

1. Introduction

Spinel ferrites represent a crucial category of industrial materials renowned for their diverse functional properties, rendering them applicable across a broad spectrum [1]. This class encompasses compounds with the general chemical formula AFe_2O_4 , wherein A denotes a divalent metal cation (such as Co, Ni, Zn, Mn, Mg, or Li). Notably, ferrites find significant utility in the realm of radio-electronic devices, with multicomponent lithium and nickel ferrites serving as pivotal components in the production of microwave ceramic products [2]. The prevalence of spinel ferrites in this domain stems from their distinctive magnetic and electromagnetic attributes, which exhibit variability across a wide range, often facilitated by the incorporation of transition metal cations [3]. Moreover, the incorporation of various metal cations within the crystal lattice of spinels has spurred their application in the fabrication of phase shifters, transformer cores, ferrite filters, and etc. [4].

Among spinel ferrites, multicomponent zinc ferrites assume particular significance. Pure zinc ferrite is classified as a normal spinel, characterized by the presence of 8 divalent Zn^{2+} cations at tetrahedral positions and 16 trivalent Fe^{3+} cations at octahedral positions [5]. Conversely, magnesium ferrite belongs to the inverted spinel category, with 8 divalent Mg^{2+} cations occupying 8 of the 16 available octahedral positions, and 16 trivalent Fe^{3+} cations distributed between 8 tetrahedral and 8 octahedral positions [6]. The replacement of zinc cations with magnesium counterparts at octahedral positions induces structural alterations, thereby dictating the magnetic and electromagnetic behavior of multicomponent zinc-magnesium ferrites [7]. Industrially, multicomponent magnesium and zinc ferrites find widespread application in microwave electronics, as well as in the manufacture of various sensors and transmitters [8]. Notably, the advent of

nanomaterials has ushered in new avenues for the utilization of spinel ferrites, including catalytic and photocatalytic applications [9], wastewater treatment [10], antibacterial materials [11], and MRI contrast agents [12]. However, the synthesis of ferrite nanopowders poses challenges, particularly with conventional solid-phase synthesis methods, owing to difficulties in obtaining pure single-phase samples with particles in the range of 30–40 nm [12]. Consequently, there is a pressing need to explore and develop methodologies for producing ferrite nanoparticles.

Presently, numerous methods exist for synthesizing nanopowders of multicomponent zinc-magnesium ferrites [13], including hydrothermal synthesis [14], sonochemical synthesis [15], co-precipitation method, various types of solution combustion methods [16], synthesis in activator mills [17] and sol-gel technology [18]. Notably, the solution combustion method has garnered attention due to its simplicity, cost-effectiveness, and potential for industrial scalability, offering a pathway to volumetric yields akin to classical solid-phase techniques [19]. Recent efforts within this method have seen the synthesis of zinc-magnesium ferrites employing citric acid and microwave treatment [20,21]. Although standalone studies have synthesized pure zinc and magnesium ferrites via the solution combustion method using glycine as a fuel [22, 23], investigations into the physical and chemical processes governing the formation of the $Zn_xMg_{1-x}Fe_2O_4$ system ($x = 0, 0.2, \dots, 1.0$), along with its magnetic and electrochemical properties, remain scarce.

Hence, the present study addresses the imperative to explore synthesis methodologies for multicomponent zinc-magnesium ferrites under solution combustion conditions, enabling the targeted fabrication of nanostructures. Glycine was chosen as the organic fuel due to its propensity for generating compositions with minimal amorphous content, particularly when used in stoichiometric proportions in the reaction solution. Herein, we report the synthesis of nanopowders with the composition $Zn_xMg_{1-x}Fe_2O_4$ ($x = 0, 0.2, \dots, 1.0$) under glycine-nitrate combustion conditions, followed by comprehensive analysis employing modern physicochemical techniques.

2. Experimental

The following reagents were utilized for the synthesis: $Zn(NO_3)_2 \cdot 6H_2O$ (puriss., NevaReactiv), $Mg(NO_3)_2 \cdot 6H_2O$ (puriss., NevaReactiv), $Fe(NO_3)_3 \cdot 9H_2O$ (puriss., NevaReactiv), CH_2NH_2COOH (puriss., NevaReactiv), HNO_3 (puriss., NevaReactiv), and double distilled water. The original zinc, magnesium, and iron nitrates were dissolved in 50 ml of distilled water with constant mechanical stirring until complete dissolution was achieved. Subsequently, glycine was added to the initial reaction solution in a stoichiometric amount, calculated based on the reaction for the formation of the primary combustion products [16, 23]. A small quantity of 5M nitric acid was introduced to the solution to prevent the formation of complex products. The resulting reaction solution was then heated on a ceramic tile until reaching the autoignition point, resulting in the formation of gaseous and solid combustion products. The brown powder synthesized in this manner was collected from the reaction beaker, ground mechanically in a mortar, and subjected to thermal treatment in an air atmosphere at a temperature of 500°C for 1 hour to eliminate any unreacted organic reagents.

The elemental composition and morphological characteristics of the synthesized compositions were assessed using energy-dispersive spectroscopy and scanning electron microscopy via a Tescan Vega 3 SBH scanning electron microscope equipped with an Oxford INCA attachment. X-ray phase and structural analyses were conducted based on diffraction patterns obtained through powder X-ray diffractometry employing a Rigaku SmartLab 3 diffractometer. The primary shooting parameters selected were $CuK\alpha 1$ radiation (0.154056 nm) at 40 kV and 30 mA, covering a range from 20 to 80 degrees of 2θ , with increments of 0.01° and an exposition time of 3 seconds. The average crystallite size was determined utilizing the Scherrer formula, while the crystallite size distribution was assessed through the method of fundamental parameters. The proportion of crystalline and amorphous phases, as well as unit cell parameters, were calculated using the Rigaku SmartLab Studio II software package. Magnetic M-H hysteresis loops were obtained employing a Lake Shore 7410 vibrating magnetometer at room temperature (278 K) within a field range of up to 60,000 Oe utilizing a standard cell. Cyclic voltammetry (CVA) curves were recorded using a SmartStat PS-20 potentiostat equipped with an FRA module in an alkaline electrolyte of 1 M KOH, spanning from -1700 to 700 mV relative to the silver chloride electrode. For a sample deposition, a suspension with Nafion in isopropanol was prepared.

3. Results and Discussion

Fig. 1 illustrates the morphological characteristics of the synthesized samples, employing the $Zn_{0.6}Mg_{0.4}Fe_2O_4$ sample as a representative example. The data obtained reveal that the morphology of zinc-manganese ferrite nanopowders manifests as micron-scale agglomerates, ranging in size from 3 to 10 μm , composed of nanoparticles measuring approximately 20–30 nm. Notably, the appearance of these agglomerates demonstrates minimal variation across different compositions of Mg^{2+} cations within the crystal lattice, consistent with typical solid products resulting from solution combustion. Furthermore, Fig. 1f highlights the presence of amorphous bridges in certain regions, facilitating connections between individual particles, which exhibit a predominantly spherical morphology.

Based on the acquired microphotographs, a particle size distribution was generated using the ImageJ software package, as depicted in Fig. 2. Among the depicted distributions, the smallest average particle size is observed in the $Zn_{0.4}Mg_{0.6}Fe_2O_4$ sample, measuring 24.9 nm. Pure zinc and magnesium ferrites, along with $Zn_{0.2}Mg_{0.8}Fe_2O_4$ and $Zn_{0.8}Mg_{0.2}Fe_2O_4$, exhibit relatively consistent average particle sizes ranging from 28 to 31 nm. This observation suggests that the minimum size occurs within the range of magnesium cation content ($x = 0.4$ and 0.6), possibly attributed to

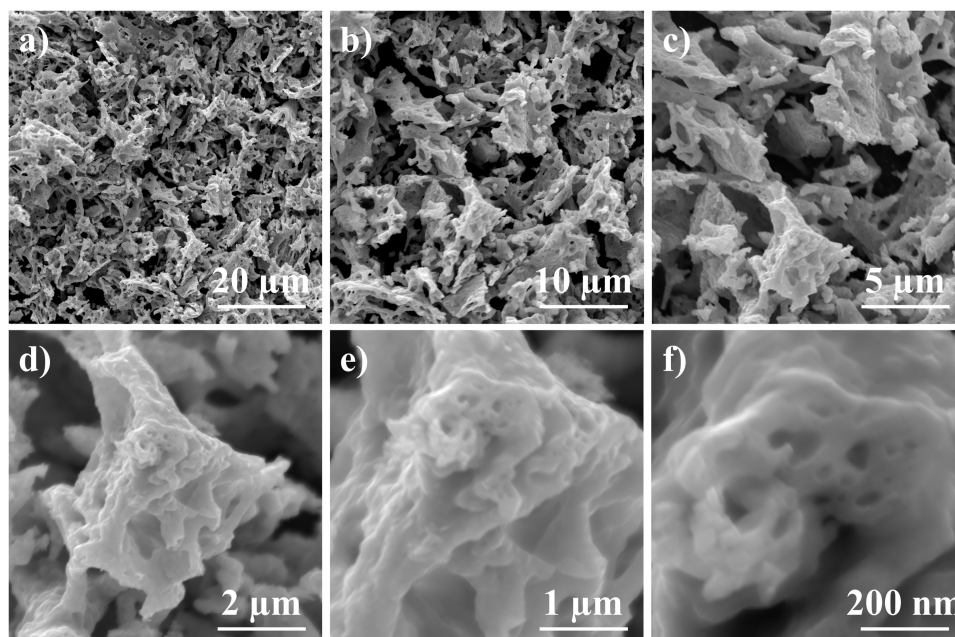


FIG. 1. SEM micrographs of $Zn_{0.6}Mg_{0.4}Fe_2O_4$ synthesized via solution combustion approach

the distribution patterns of zinc and manganese cations within the mixed spinel structure, as well as the composition of the initial reaction influencing the combustion temperature of the flame. Moreover, it is noteworthy to mention the distribution type; across all samples, there is an absence of a bimodal distribution pattern, with a distinct center of distribution evident. This indicates a high degree of uniformity in the size distribution of particles.

The elemental composition of all synthesized powders was determined using energy-dispersive spectroscopy, and the resulting data after processing the spectra are presented in Table 1, accounting for the carbon content of the conductive adhesive tape used during the sample preparation for analysis. It is noteworthy that all samples align with the experimentally derived chemical composition, with values falling within the error margin of the determination method (± 0.5 at. %).

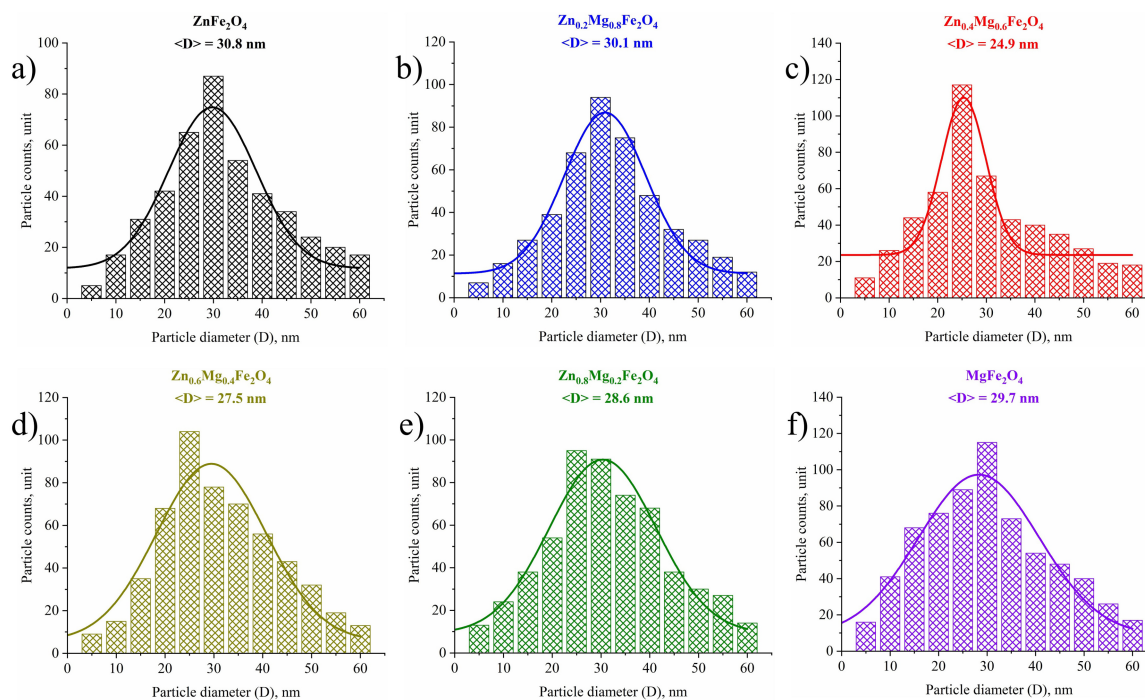


FIG. 2. Particle size distributions of $Zn_xMg_{1-x}Fe_2O_4$ ($x = 0, 0.2, \dots, 1.0$) prepared by solution combustion method

TABLE 1. Elemental composition of synthesized zinc-magnesium ferrite samples

Sample	Zn, at. %	Mg, at. %	Fe, at. %
ZnFe ₂ O ₄	32.7	0	67.3
Zn _{0.8} Mg _{0.2} Fe ₂ O ₄	26.1	6.9	67.0
Zn _{0.6} Mg _{0.4} Fe ₂ O ₄	18.6	11.8	69.6
Zn _{0.4} Mg _{0.6} Fe ₂ O ₄	11.9	18.4	69.7
Zn _{0.2} Mg _{0.8} Fe ₂ O ₄	7.1	25.8	67.1
MgFe ₂ O ₄	0	33.1	66.9

Diffraction patterns of Zn_xMg_{1-x}Fe₂O₄-type ferrites ($x = 0, 0.2, \dots, 1.0$) are depicted in Fig. 3a. It is evident that all synthesized samples exhibit a predominant phase, which, as per the ICDD PDF-2 database, corresponds to zinc-magnesium ferrite (JCPDS # 73-2211). The diffraction peaks across all samples exhibit similar width and intensity, with no discernible peaks of impurity phases, such as iron, zinc, and magnesium oxides. The average crystallite size was determined using the Scherrer formula and aligns well with the data presented in Fig. 2. Notably, the smallest crystallite size was calculated for the Zn_{0.6}Mg_{0.4}Fe₂O₄ sample, measuring 21.3 nm, slightly less than the visual estimate by SEM. This disparity is attributed to the difference between the actual particle size and the size of its crystalline core. Additionally, crystallite size distributions, as depicted in Figure 3b, were generated using the fundamental parameters method. These data also corroborate well with the results of visual assessment by SEM and calculations using the Scherrer formula. The distributions indicate that the average size across all samples falls within the range of 38 to 22 nm. Thus, the reproducibility of the results regarding average size determination was confirmed, validating the successful synthesis of Zn_xMg_{1-x}Fe₂O₄ system nanoparticles ($x = 0, 0.2, \dots, 1.0$).

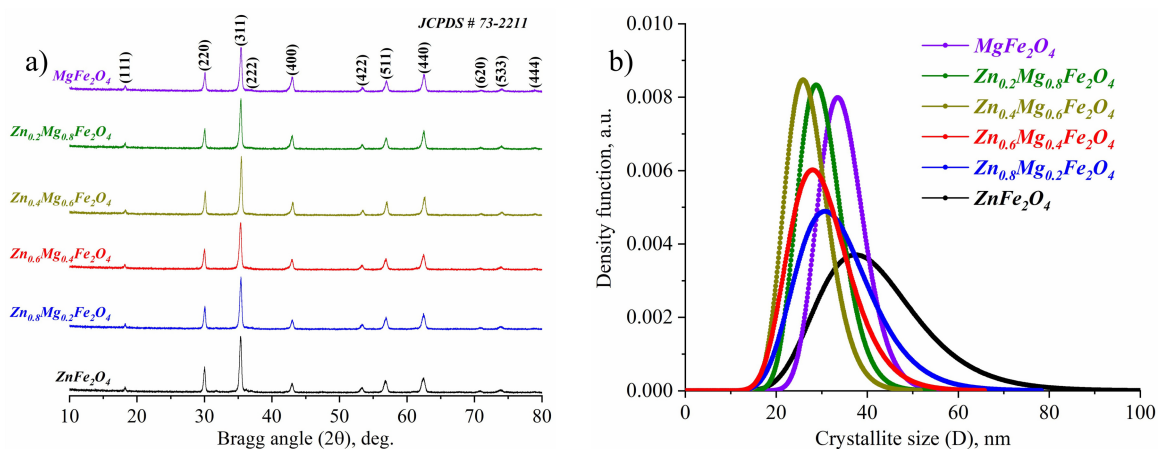


FIG. 3. Diffraction patterns of zinc-magnesium ferrite nanopowders with different amounts of magnesium

Using the Rietveld method, X-ray diffraction analysis was conducted for all synthesized compositions, enabling the determination of unit cell parameters and lattice volume. The provided values indicate minimal lattice stress across all samples, with stress levels below 0.5%. Of particular interest is the examination of changes in lattice parameters, as the substitution of Mg²⁺ cations with Zn²⁺ exerts a significant influence on these characteristics. Indeed, structural parameters play a pivotal role in dictating the magnetic and electrochemical behavior of spinel ferrites. Calculation was performed utilizing the main crystallographic directions (220), (311), (400), and (440), characterized by their high intensity and excellent agreement with standard peaks. The lattice parameter ($a = b = c$) for pure magnesium ferrite was determined to be 8.416 Å, consistent with reference card data (JCPDS # 73-2211), and decreases progressively with an increasing proportion of Mg²⁺ cations. This trend is attributed to the disparity in ionic radii between Zn²⁺ (0.82 Å) and Mg²⁺ (0.65 Å), a finding supported by existing literature [21]. However, it's worth noting that the potential for the substitution of Fe³⁺ cations at tetrahedral positions may induce slight variations in lattice parameter growth rates. This phenomenon may explain the modest decrease observed in lattice parameters for the Zn_{0.8}Mg_{0.2}Fe₂O₄ and Zn_{0.6}Mg_{0.4}Fe₂O₄ samples. Furthermore, the obtained dependencies align well with changes in average crystallite size, thereby indirectly validating structural alterations.

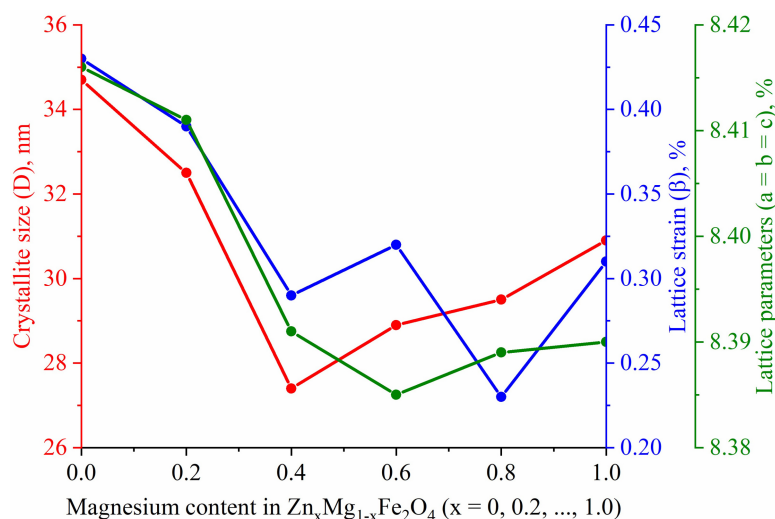


FIG. 4. Average crystallite size, lattice stress and lattice parameters of zinc-manganese ferrite nanopowders

Magnetic M-H hysteresis loops, recorded at room temperature using a standard cell, are illustrated in Fig. 4a. The appearance of these hysteresis loops distinctly showcases the influence of magnesium cation doping on the magnetic behavior of zinc-magnesium ferrites, particularly concerning saturation and coercive force.

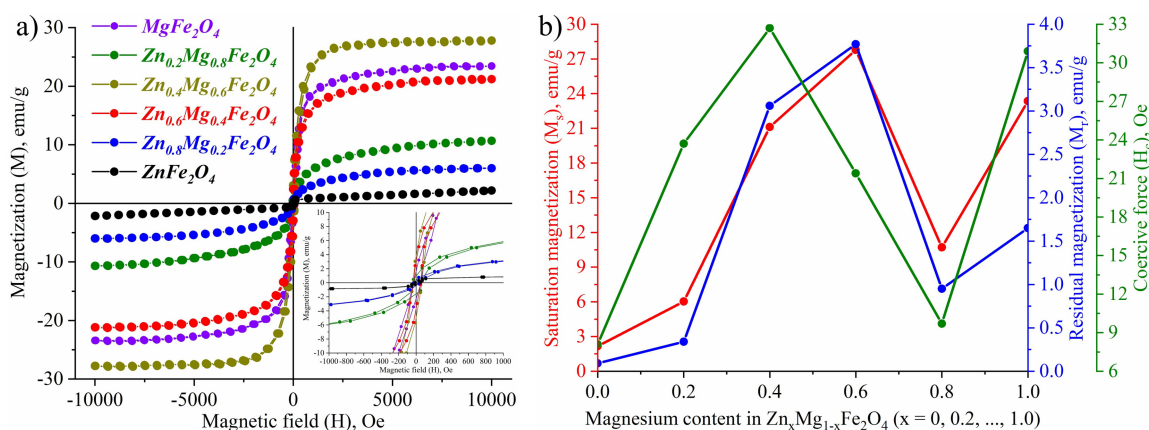


FIG. 5. M-H hysteresis loops of $Zn_{0.6}Mg_{0.4}Fe_2O_4$ synthesized by solution combustion method

To facilitate analysis of the primary magnetic parameters obtained (saturation magnetization, saturation remanent magnetization, and coercive force), their dependencies on the number of magnesium cations (x) in the sample compositions were plotted (Fig. 5b). These graphs reveal that pure zinc ferrite exhibits the lowest magnetic parameters ($M_s = 2.16$ emu/g, $M_r = 0.09$ emu/g, and $H_c = 8.1$ Oe). Moreover, a significant enhancement in magnetic characteristics is observed with increasing magnesium proportion in the spinel crystal lattice, peaking at $x = 0.4$ ($Zn_{0.4}Mg_{0.6}Fe_2O_4$ sample) with values of 27.78 emu/g, 3.77 emu/g, and 32.7 Oe, respectively. Subsequently, due to ongoing structural alterations and the substitution of Mg^{2+} cations with Zn^{2+} and Fe^{3+} cations at tetrahedral positions, magnetic characteristics begin to decline, continuing through to the $Zn_{0.2}Mg_{0.8}Fe_2O_4$ sample. Ferrite fully substituted by magnesium cations exhibits magnetic parameters characteristic of pure $MgFe_2O_4$, aligning well with literature data [24].

Fig. 6 displays cyclic voltammograms of synthesized nanoparticles of multicomponent zinc-magnesium ferrites. Measurements were conducted in a 1 M KOH alkaline electrolyte at a constant scanning speed of 10 mV/s within a potential window of $-2 - 2.0$ V, ranging from -1800 to 1600 mV relative to the silver chloride electrode. Notably, all samples, except for pure zinc ferrite, exhibit nearly identical coverage areas. The most pronounced cathodic peak is observed in the $ZnFe_2O_4$ sample at 0.58 V, while the anodic peak is recorded at 0.24 V. The appearance and retention of charge are attributed to redox reactions of the Fe^{3+}/Fe^{2+} type at the electrode. Consequently, the obtained capacity indicators primarily depend on the characteristics of these redox reactions, which are less pronounced in multicomponent zinc-magnesium and pure magnesium ferrite compared to zinc ferrite. The data suggests that all synthesized samples are theoretically suitable as starting materials for the production of electrochemical sensors.

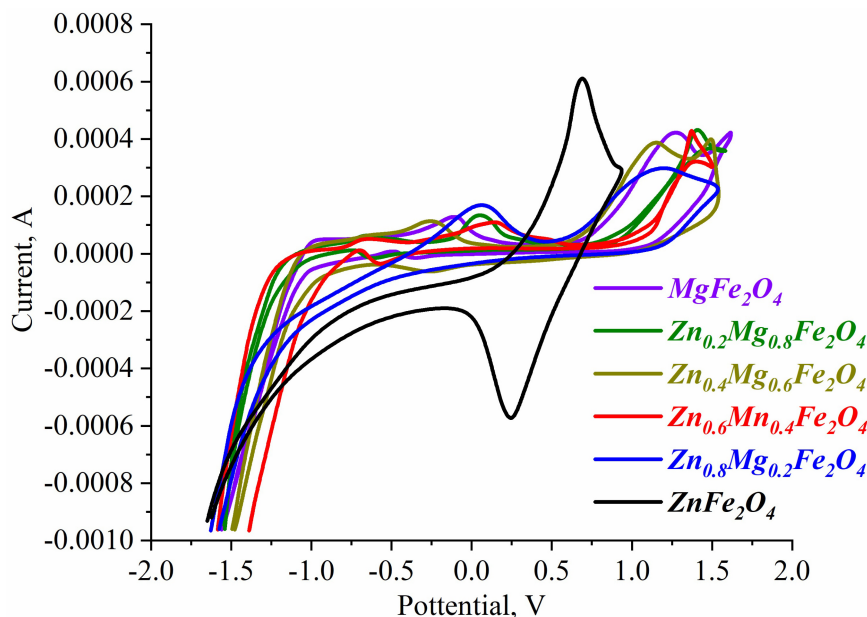


FIG. 6. M-H hysteresis loops of $\text{Zn}_{0.6}\text{Mg}_{0.4}\text{Fe}_2\text{O}_4$ synthesized by solution combustion method

4. Conclusion

In summary, this study focuses on the synthesis and characterization of multicomponent zinc-magnesium ferrites ($\text{Zn}_x\text{Mg}_{1-x}\text{Fe}_2\text{O}_4$ type, with x ranging from 0 to 1.0) via solution combustion method utilizing glycine at a stoichiometric redox ratio. The average particle size of the synthesized samples ranged from 25 to 31 nm, with the amorphous phase constituting less than 5% of the composition. Phase analysis confirmed the absence of impurity oxide phases within the compositions. Structural parameter analysis revealed variations in unit cell parameters depending on the magnesium cation content, consequently influencing the primary magnetic characteristics in a nonlinear fashion, influenced by both particle size and structural alterations. Notably, samples with higher zinc content exhibited significant changes in hysteresis loop morphology. Analysis of cyclic voltammograms provided insights into the potential utilization of the synthesized powders as electrochemical materials.

References

- [1] Varshney D., Verma K., Kumar A. Structural and vibrational properties of $\text{Zn}_x\text{Mn}_{1-x}\text{Fe}_2\text{O}_4$ ($x = 0.0, 0.25, 0.50, 0.75, 1.0$) mixed ferrites. *Materials Chemistry and Physics*, 2011, **131**, P. 413–419.
- [2] Martinson K.D., Ivanov A.A., Pantelev I.B., Popkov V.I., Effect of sintering temperature on the synthesis of LiZnMnFe microwave ceramics with controllable electro/magnetic properties. *Ceramics International*, 2021, **47**(21), P. 30071–30081.
- [3] Dippong T., Levei E.A., Cadar O. Recent Advances in Synthesis and Applications of MFe_2O_4 ($\text{M} = \text{Co}, \text{Cu}, \text{Mn}, \text{Ni}, \text{Zn}$) nanoparticles. *Nanomaterials*, 2021, **11**, P. 1560.
- [4] Salih S.J., Mahmood W.M. Review on magnetic spinel ferrite (MFe_2O_4) nanoparticles: From synthesis to application. *Heliyon*, 2023, **9**(6), P. e16601.
- [5] Sahoo P., Choudhary P., Laha S.S., Dixit A., Mefford O.T. Recent advances in zinc ferrite (ZnFe_2O_4) based nanostructures for magnetic hyperthermia applications. *Chemical Communications*, 2023, **81**(59), P. 12065–12090.
- [6] Sagayaraj R. A review on structural and magnetic properties of magnesium ferrite nanoparticles. *International Nano Letters*, 2022, **12**, P. 345–350.
- [7] Nigam A., Saini S., Singh B., Rai A.K., Pawar S.J. Zinc doped magnesium ferrite nanoparticles for evaluation of biological properties viz antimicrobial, biocompatibility, and in vitro cytotoxicity. *Materials Today: Communications*, 2022, **31**, P. 103632.
- [8] Wu K., Li J., Zhang C. Zinc ferrite based gas sensors: A review. *Ceramics International*, 2019, **45**(9), P. 11143–11157.
- [9] Mahmoodi N.M. Zinc ferrite nanoparticle as a magnetic catalyst: Synthesis and dye degradation. *Materials Research Bulletin*, 2013, **48**(10), P. 4255–4260.
- [10] Martinson K.D., Beliaeva A.D., Sakhno D.D., Beliaeva I.D., Belyak V.E., Nianikova G.G., Pantelev I.B., Naraev V.N., Popkov V.I. Synthesis, Structure, and Antimicrobial Performance of $\text{Ni}_x\text{Zn}_{1-x}\text{Fe}_2\text{O}_4$ ($x = 0, 0.3, 0.7, 1.0$) Magnetic Powders toward *E. coli*, *B. cereus*, *S. citreus*, and *C. tropicalis*. *Water*, 2022, **14**(3), P. 454.
- [11] Haghniaz R., Rabbani A., Vajhadin F., Khan T., Kousar R., Khan A.R., Montazerian H., Iqbal J., Libanori A., Kim H.-J., Wahid F. Anti-bacterial and wound healing-promoting effects of zinc ferrite nanoparticles. *Journal of Nanobiotechnology*, 2021, **19**, P. 38.
- [12] Major J.L., Parigi G., Luchinat C., Meade T.J. The synthesis and in vitro testing of a zinc-activated MRI contrast agent. *PNAS*, 2007, **104**(35), P. 13881–13886.
- [13] Rahman M.A., Islam M.T., Singh M.S.J., Samsuzzaman M., Chowdhury M.E.H. Synthesis and characterization of Mg–Zn ferrite based flexible microwave composites and its application as SNG metamaterial. *Scientific Reports*, 2021, **11**, P. 7654.
- [14] Mishra B., Munisha B., Nanda J., Sankaran K.J., Suman S. Hydrothermally Synthesized Magnesium doped Zinc Ferrite Nanoparticles: An extensive study on structural, optical, magnetic, and dielectric properties. *Materials Chemistry and Physics*, 2022, **292**, P. 126791.

- [15] Choudhury H.A., Choudhary A., Sivakumar M., Moholkar V.S., Mechanistic investigation of the sonochemical synthesis of zinc ferrite. *Ultrasonics Sonochemistry*, 2013, **20**(1), P. 294–302.
- [16] Martinson K.D., Cherepkova I.A., Sokolov V.V. Formation of cobalt ferrite nanoparticles during the burning of glycine-nitrate and their magnetic properties. *Glass Physics and Chemistry*, 2018, **44**(1), P. 21–25.
- [17] Bid S., Pradhan S.K. Preparation of Zinc Ferrite by High-Energy Ball-Milling and Microstructure Characterization by Rietveld's Analysis. *Materials Chemistry and Physics*, 2003, **82**(1), P. 27–37.
- [18] Iqbal F., Mutalib M.I.A., Shaharun M.S., Khan M., Abdullah B. Synthesis of $ZnFe_2O_4$ Using sol-gel Method: Effect of Different Calcination Parameters. *Procedia Engineering*, 2016, **148**, P. 787–794.
- [19] Riyanti F., Purwaningrum, W., Yuliasari N., Putri S., Apriani, N., Hariani P.L. The effect of fuel on the physiochemical properties of $ZnFe_2O_4$ synthesized by solution combustion method. *Turkish Journal of Chemistry*, 2022, **46**(6), P. 1875–1882.
- [20] Senthamilselvan T., Nithiyannantham S., Kogulakrishnan K., Mahalakshmi S., Lakshmigandhan T., Mohan R., Gunasekaran B. Structural, magnetic, electric and electrochemical studies on zinc doped magnesium ferrite nano particles – Sol-gel method. *Heliyon*, 2024, **10**(3), P. E25511.
- [21] Manikandan A., Vijaya J.J., Sundararajan M., Meganathan C., Kennedy L.J., Bououdina M. Optical and magnetic properties of Mg-doped $ZnFe_2O_4$ nanoparticles prepared by rapid microwave combustion method. *Superlattices and Microstructures*, 2013, **64**, P. 118–131.
- [22] Heidari P., Masoudpanah S.M. Structural and magnetic properties of $MgFe_2O_4$ powders synthesized by solution combustion method: the effect of fuel type. *Journal of Materials Research and Technology*, 2020, **9**(3), P. 4469–475.
- [23] Dyachenko S.V., Martinson K.D., Cherepkova I.A., Zhernovoi A.I. Particle size, morphology, and properties of transition metal ferrosinels of the MFe_2O_4 ($M = Co, Ni, Zn$) type, produced by glycine-nitrate combustion. *Russian Journal of Applied Chemistry*, 2016, **89**(4), P. 535–539.
- [24] Dalt S.D., Takimi A.S., Volkmer T.M., Sousa V.C., Bergmann C.P. Magnetic and Mössbauer behavior of the nanostructured $MgFe_2O_4$ spinel obtained at low temperature. *Powder Technology*, 2011, **210**(2), P. 103–108.

Submitted 7 February 2024; accepted 15 March 2024

Information about the authors:

Kirill D. Martinson – Ioffe Institute, Politekhnikeskaya st., 26, St. Petersburg, 194064, Russia; ORCID 0000-0001-9313-4267; martinsonkirill@mail.ru

Alexander A. Murashkin – St. Petersburg Electrotechnical University “LETI”, Professora Popova st., 5, St. Petersburg, 197022, Russia; murashkin1999@list.ru

Artem A. Lobinsky – Ioffe Institute, Politekhnikeskaya st., 26, St. Petersburg, 194064, Russia; lobinski.a@mail.ru

Danil D. Maltsev – Ioffe Institute, Politekhnikeskaya st., 26, St. Petersburg, 194064, Russia; ORCID 0000-0001-5787-0400; dm.work.ac@gmail.com

Kezhen Qi – College of Pharmacy, Dali University, Dali 671000, China; qkzh2003@aliyun.com

Jiaguo Yu – China University of Geosciences, 68 Jincheng St, Wuhan, 430078 P. R. China; yujiaguo93@cug.edu.cn

Oksana V. Almjashaeva – St. Petersburg Electrotechnical University “LETI”, Professora Popova st., 5, St. Petersburg, 197022, Russia; almjashaeva@mail.ru

Vadim I. Popkov – Ioffe Institute, Politekhnikeskaya st., 26, St. Petersburg, 194064, Russia; vip-07@yandex.ru

Conflict of interest: the authors declare no conflict of interest.

Pyrochlore phase in the $\text{Bi}_2\text{O}_3\text{--Fe}_2\text{O}_3\text{--WO}_3\text{--(H}_2\text{O)}$ system: its stability field in the low-temperature region of the phase diagram and thermal stability

Makariy S. Lomakin^{1,2,a}, Olga V. Proskurina^{1,3,b}, Aleksandr A. Levin^{1,c}, Vladimir N. Nevedomskiy^{1,d}

¹Ioffe Institute, St. Petersburg, Russia

²St. Petersburg Electrotechnical University “LETI”, St. Petersburg, Russia

³St. Petersburg State Institute of Technology, St. Petersburg, Russia

^alomakinmakariy@gmail.com, ^bproskurinaov@mail.ru, ^caleksandr.a.levin@mail.ioffe.ru, ^dnevedom@mail.ioffe.ru

Corresponding author: M. S. Lomakin, lomakinmakariy@gmail.com

ABSTRACT The concentration stability field localization of the pyrochlore-structured compounds of variable composition formed in the $\text{Bi}_2\text{O}_3\text{--Fe}_2\text{O}_3\text{--WO}_3$ system under hydrothermal conditions at a temperature of $T = 200^\circ\text{C}$ and a pressure of $P = 7$ MPa was determined. It was found that the pyrochlore-structured compounds stability field is longitudinally limited within the atomic ratios $0.47 < \text{Bi}/\text{W} < 1.25$, and in the transverse direction within $1.14 < \text{Bi}/\text{Fe} < 1.87$. It was shown that the pyrochlore phase cubic unit cell parameter a depends on the compound chemical composition as follows: it increases linearly from ~ 10.3319 Å to ~ 10.4199 Å with an increase in the Bi/W atomic ratio from ~ 0.47 to ~ 1.25 . It was established that from the $\text{Bi}_2\text{O}_3\text{--WO}_3$ system side, there is a region of two-phase equilibrium, in which a pyrochlore phase of variable composition coexists with the Bi_2WO_6 compound, which is formed in the form of plate-like (thickness $h \sim 50\text{--}100$ nm) nanoparticles. It was shown that from the $\text{Bi}_2\text{O}_3\text{--Fe}_2\text{O}_3$ system side, there is a region of compositions, in which the pyrochlore phase of the most enriched in bismuth oxide composition coexists with the Bi_2WO_6 compound, which is formed in the form of rod-shaped ($h \sim 10\text{--}30$ nm) nanoparticles, and with the X-ray amorphous phase composition, formed in the form of nanocrystalline particles about 10 nm in size. It was found that the higher temperature point of the pyrochlore-structured compounds stability field does not exceed 725°C , which allows them to be synthesized only by “soft chemistry” methods.

KEYWORDS pyrochlore-structured phase, hydrothermal synthesis, crystal structure, phase diagram, thermal stability

ACKNOWLEDGEMENTS XRD, SEM and EDXMA studies were performed employing the equipment of the Engineering Center of the St. Petersburg State Institute of Technology (Technical University). TEM studies and the analysis of XRD data have been carried out using the equipment and software of the Joint Research Center “Materials science and characterization in advanced technology” (Ioffe Institute). DSC/TG studies were performed employing the equipment of the First All-Russian Engineering Center for Molecular Layering Technology (St. Petersburg State Institute of Technology (Technical University)). HTXRD studies have been carried out using the equipment of the Center for X-Ray Diffraction Studies of the Research Park of St. Petersburg State University.

The authors express their deep gratitude to Corr. Mem. RAS Victor Vladimirovich Gusarov for valuable comments and advice on improving the quality of the manuscript.

The work was financially supported by the Russian Science Foundation (Project No. 20-63-47016).

FOR CITATION Lomakin M.S., Proskurina O.V., Levin A.A., Nevedomskiy V.N. Pyrochlore phase in the $\text{Bi}_2\text{O}_3\text{--Fe}_2\text{O}_3\text{--WO}_3\text{--(H}_2\text{O)}$ system: its stability field in the low-temperature region of the phase diagram and thermal stability. *Nanosystems: Phys. Chem. Math.*, 2024, **15** (2), 240–254.

1. Introduction

The pyrochlore-structured complex oxide compounds attract the researchers active attention because they have a set of interesting physicochemical properties for investigation, in particular, magnetic [1–5], dielectric [3, 5–7], transport [8, 9], photocatalytic [10–12]. Due to this, they can be considered as promising materials for the manufacture of coatings, for example, parts of gas turbines operating at elevated temperatures [13], as well as ion-exchange materials for the immobilization of radioactive waste [14]. The pyrochlore-structured compounds are characterized by a large isomorphic capacity, which determines the existence of this structural type in both binary [14–16] and more multicomponent oxide systems [1–11]. In most oxide systems, the pyrochlore-structured compounds are obtained from simple oxides by the solid-state synthesis, since, as a rule, this structural type is quite stable at elevated temperatures [17, 18]. Despite this, the application of “soft chemistry” methods, in particular, the hydrothermal method, opens up opportunities for studying

phase transformations involving the pyrochlore phase, occurring in the low-temperature region of phase diagrams [19–23]. It should be noted that, as a rule, complex oxide phases of variable composition are characterized by a narrowing of the equilibrium concentration boundaries of the stability field with increasing synthesis temperature, that is, when moving towards the melting or solid-phase decomposition temperature. Reducing the synthesis temperature of such compounds, on the contrary, leads to the possibility of widely varying their quantitative composition and, as a consequence, properties, while remaining within their stability field boundaries. It should be mentioned that when investigating phase transformations occurring in the low-temperature region of the phase diagram, it is also interesting to study the thermal stability of oxide compounds formed during hydrothermal synthesis.

Phase equilibria in the $\text{Bi}_2\text{O}_3\text{--Fe}_2\text{O}_3\text{--WO}_3$ system have not previously been the subject of systematic research, since only a few works devoted to the synthesis and characterization of compounds formed in this system are found in the scientific literature [24–26]. In particular, pyrochlore-structured compounds of variable composition were for the first time obtained and structurally characterized in a recent work by the authors [27] in 2020; however, studies of their stability field localization, as well as their thermal stability, have not been carried out to date.

The aim of this work is to determine the localization of the concentration and temperature stability fields of pyrochlore-structured compounds of variable composition in the $\text{Bi}_2\text{O}_3\text{--Fe}_2\text{O}_3\text{--WO}_3$ system.

2. Materials and Methods

2.1. Synthesis section

The synthesis procedure, which is the same for all samples, is described below. Table 1 shows the molar amounts of reagents (x , y , z) and the measured values of the precursor suspension pH corresponding to the various samples. To obtain a sample, x mmol of crystalline hydrate of bismuth (III) nitrate, $\text{Bi}(\text{NO}_3)_3 \cdot 5\text{H}_2\text{O}$ (puriss. spec.), and y mmol of crystalline hydrate of iron (III) nitrate, $\text{Fe}(\text{NO}_3)_3 \cdot 9\text{H}_2\text{O}$ (pur.), were dissolved in q ml of 6 M HNO_3 (puriss. spec.), after which h ml of distilled water was added to the resulting solution. Next, z mmol of sodium tungstate (VI) crystalline hydrate, $\text{Na}_2\text{WO}_4 \cdot 2\text{H}_2\text{O}$ (puriss. spec.), was dissolved in g ml of distilled water and the resulting solution was added dropwise into the acidic solution of bismuth and iron nitrates stirred with a magnetic stirrer at 800 rpm (~ 30 mL of distilled water was then added there and used to rinse the beaker that had contained the sodium tungstate solution). After stirring the obtained suspension for 1 h, a solution of 2 M NaOH was added to it dropwise until reaching pH of $\sim 4\text{--}5$ (Table 1). The amorphous precursor suspension obtained this way, was additionally stirred at 1000 rpm for ~ 1 h and then transferred into Teflon chambers ($\sim 80\%$ filling) and placed in steel autoclaves, which were then put in a furnace heated up to $T = 200^\circ\text{C}$. After 72 h, the autoclaves were removed from the furnace and cooled in air. The resulting precipitates were separated from the mother liquor (it was poured out), rinsed with distilled water several times by decantation and dried at 80°C for 24 h.

2.2. Characterization

The crystal structure of the samples synthesized via a hydrothermal method was analyzed by X-ray diffraction (XRD) using a Rigaku SmartLab 3 Powder X-ray Diffractometer (Rigaku Corporation, Japan). XRD patterns ($\text{Co-}K_\alpha$ radiation (average wavelength $\lambda = 1.79028 \text{ \AA}$) of an X-ray tube with a cobalt anode filtered using a $\text{Fe } K_\beta$ filter) were recorded in the Bragg-Brentano geometry at room temperature. The measurements were carried out in the symmetrical $\theta\text{--}2\theta$ mode (θ is the angle of incidence of the X-ray beam on the surface of the sample, 2θ is the diffraction angle). The recording of XRD patterns was carried out using a one-dimensional (1D) silicon strip detector D/teX Ultra 250. The measurements were carried out in the range of angles $2\theta = 10^\circ\text{--}80^\circ$ with a step of $\Delta 2\theta = 0.02^\circ$, and the total time at the point was 123 seconds (conversion from the used linear detector to a point detector).

The XRD pattern of the sample 5.12 was also obtained on the same diffractometer using a $\text{Cu-}K_\alpha$ radiation (average wavelength $\lambda = 1.54186 \text{ \AA}$) after an X-ray tube with a copper anode and a $\text{Ni } K_\beta$ filter. This measurement was carried out in the range of angles $2\theta = 6^\circ\text{--}140^\circ$ with a step of $\Delta 2\theta = 0.01^\circ$, and the total time at the point was 2560 seconds. Thus obtained XRD pattern was used to carry out the precise calculations of unit cell parameters, average crystallite size and microstrains.

High-temperature XRD (HTXRD) studies were carried out using a Rigaku Ultima IV Powder X-ray Diffractometer (Rigaku Corporation, Japan), equipped with a 1D silicon strip detector D/teX Ultra 250 and a high-temperature camera SHT-1500 (Rigaku Corporation, Japan). The XRD patterns were recorded using a $\text{Cu-}K_\alpha$ radiation of an X-ray tube with a copper anode filtered with a $\text{Ni } K_\beta$ filter (average wavelength $\lambda = 1.54186 \text{ \AA}$) in the range of angles $2\theta = 10^\circ\text{--}80^\circ$ with a step of $\Delta 2\theta = 0.02^\circ$, and the speed was $4^\circ/\text{min}$. The measurements were performed in air in the temperature range from 25°C to 585°C (step was 40°C) and in the range $585\text{--}785^\circ\text{C}$ (step was 20°C), heating rate between temperature points was $10^\circ\text{C}/\text{min}$, exposure at temperature before XRD recording was 20 minutes. The sample was prepared by deposition from an alcohol suspension onto a standard platinum substrate. The temperature was controlled using a Pt-Rh thermocouple located in close proximity to the substrate. Before the experiment, the positions of the diffraction angles were corrected using an external silicon standard.

TABLE 1. Sample names and synthesis parameters

Sample	n(Bi) (<i>x</i>), mmol	n(Fe) (<i>y</i>), mmol	n(W) (<i>z</i>), mmol	Bi ³⁺ and Fe ³⁺ nitrates solution		Sodium WO ₄ ²⁻ solution	Precursor suspension <i>pH</i>
				Vol.* of 6 M HNO ₃ (<i>q</i>), ml	Vol.* of distilled water (<i>h</i>), ml	Vol.* of distilled water (<i>g</i>), ml	
				5.3	2.779	2.799	4.242
5.6	2.012	1.791	5.777	4.8	23.9	41.3	4.50
5.8	2.744	2.340	4.313	6.5	32.7	30.8	4.77
5.9	3.096	2.620	3.609	7.4	36.9	25.8	5.03
5.12	2.010	1.386	5.781	4.8	23.9	41.3	4.55
5.16	3.388	2.432	3.025	8.1	40.3	21.6	4.88
5.17	3.717	2.682	2.367	8.8	44.2	16.9	4.48
5.18	4.040	2.928	1.720	9.6	48.1	12.3	4.58
5.20	2.354	1.273	5.092	5.6	28.0	36.4	4.58
5.21	2.688	1.530	4.425	6.4	32.0	31.6	4.57
5.22	3.015	1.782	3.769	7.2	35.9	26.9	4.42
5.34	4.186	2.360	1.427	10.0	49.8	10.2	4.69

*Volume

The crystal structure of the annealed samples was analyzed by XRD using an X-ray powder diffractometer DRON-8N (IC "Burevestnik", Russia) in the Bragg-Brentano geometry (an X-ray tube with copper anode, Ni K_{β} filter, Cu- K_{α} radiation (average wavelength $\lambda = 1.54186 \text{ \AA}$)), equipped with a position-sensitive (PSD) linear detector Mythen2 R 1D (DECTRIS Ltd., Switzerland) with an opening angle of 4.48° and with a single parabolically bent Göbel Mirror placed in the beam path so the line focus of the X-ray source. The measurements were carried out in the range of angles $2\theta = 10^{\circ} - 80^{\circ}$ with a step of $\Delta 2\theta = 0.0142^{\circ}$, and the total time at the point was 180 seconds.

The preprocessing of the measured XRD patterns of samples in order to obtain the parameters of the observed XRD reflections necessary for unit cell and microstructure calculations was carried out using the EVA program, version 5.1.0.5 (Bruker AXS, Germany). To increase the precision of the analysis, the observed values of the Bragg angles obtained by EVA were corrected for zero shift and displacement (see [28] for details). Angular corrections (zero shift and displacement) were obtained by the external standard method based on additional measurements of a 5.12 powder sample mixed with NaCl powder, which was calibrated by the internal standard method using the Si640f powder XRD standard (NIST, USA).

X-ray phase analysis (XPA) of the measured XRD patterns of samples was carried out using the Crystallographica Search-Match program, version 3.1.0.2 (Oxford Cryosystems Ltd., England) using the Powder Diffraction File-2 (PDF-2) [29] and Cambridge Structural Database (CSD) (<https://www.ccdc.cam.ac.uk/structures/>).

Scanning electron microscopy (SEM) images and bulk elemental composition of the samples were obtained on a Tescan Vega 3 SBH scanning electron microscope (Tescan Orsay Holding, Czech Republic) with an Oxford Instruments Energy Dispersive X-ray Microanalysis (EDXMA) attachment. The relative number of elements was calculated using the AZtec software. The characteristic emission spectra of each sample were accumulated from four sites with a total area of $\sim 9 \text{ mm}^2$, with a set of statistics for at least 2 million pulses at each site. The readings from each site were averaged, and the measurement error was determined at a confidence level of 0.95.

In transmission electron microscopy (TEM) studies a JEM-2100F microscope at an accelerating voltage of 200 kV is employed. Specimens from the samples were prepared by one of the traditional methods, that is, by dispersing a suspension of a weighed portion of powder in ethanol by ultrasound for 8–10 min, followed by precipitation and drying on a thin supporting carbon film.

The thermal behavior of the sample 5.16 was studied by differential scanning calorimetry (DSC) together with thermogravimetry (TG) when heating the sample in an open platinum crucible in the temperature range $30 - 900^{\circ}\text{C}$ in a

dynamic argon atmosphere (flow rate 50 ml/min) with a heating rate of $10^\circ\text{C}/\text{min}$ on a synchronous thermal analyzer Netzsch STA 449 F5 Jupiter.

3. Results and discussions

3.1. Chemical composition

The EDXMA data on the bulk chemical composition of the samples are presented in Table 2 in the form of atomic ratios and in Fig. 1 (a – nominal composition specified for the synthesis, b – bulk chemical composition) as points on the concentration triangle of the $\text{BiO}_{1.5}\text{-FeO}_{1.5}\text{-WO}_3$ system.

TABLE 2. Bulk chemical composition of samples synthesized by the hydrothermal method, in rel. at. units, according to the EDXMA data

Example	Bi/W $\pm\Delta$		Fe/W $\pm\Delta$		Bi/Fe $\pm\Delta$	
	Nom.*	Bulk	Nom.*	Bulk	Nom.*	Bulk
5.3	0.66	0.57 ± 0.05	0.66	0.50 ± 0.02	1.00	1.14 ± 0.13
5.6	0.35	0.47 ± 0.04	0.31	0.36 ± 0.02	1.13	1.30 ± 0.10
5.8	0.64	0.55 ± 0.03	0.54	0.44 ± 0.01	1.19	1.24 ± 0.05
5.9	0.86	0.79 ± 0.07	0.73	0.56 ± 0.01	1.18	1.41 ± 0.13
5.12	0.35	0.52 ± 0.03	0.24	0.28 ± 0.01	1.46	1.85 ± 0.07
5.16	1.12	1.05 ± 0.10	0.80	0.70 ± 0.02	1.40	1.49 ± 0.11
5.17	1.57	1.45 ± 0.04	1.13	0.81 ± 0.03	1.39	1.78 ± 0.07
5.18	2.35	2.09 ± 0.07	1.70	1.27 ± 0.02	1.38	1.65 ± 0.04
5.20	0.46	0.47 ± 0.03	0.25	0.25 ± 0.02	1.84	1.87 ± 0.09
5.21	0.61	0.54 ± 0.04	0.35	0.32 ± 0.01	1.74	1.71 ± 0.12
5.22	0.80	0.74 ± 0.05	0.47	0.44 ± 0.02	1.70	1.69 ± 0.12
5.34	2.93	2.41 ± 0.11	1.65	1.49 ± 0.04	1.78	1.62 ± 0.04

*Nominal composition specified for the synthesis

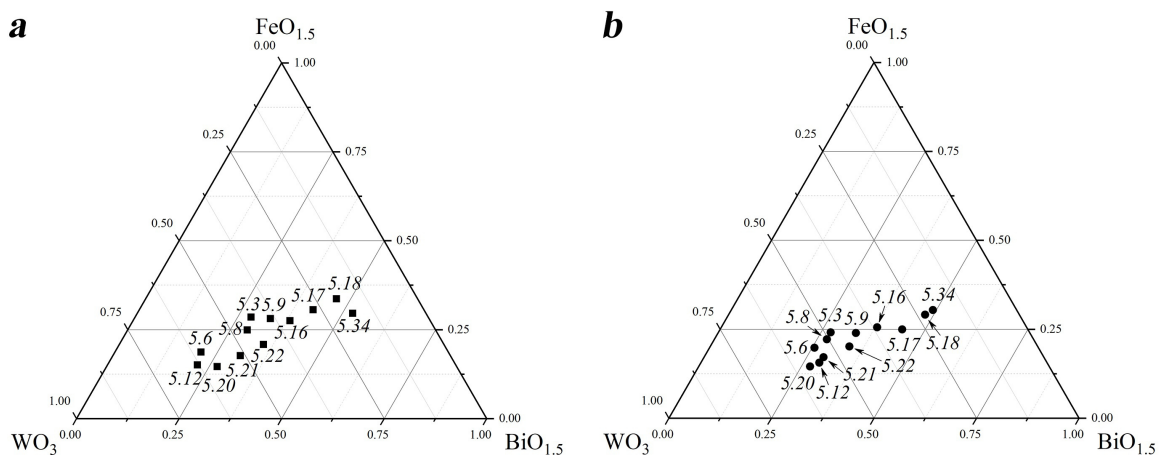


FIG. 1. (a) Nominal and (b) bulk (according to the EDXMA data) chemical composition of samples synthesized by the hydrothermal method on the concentration triangle of the $\text{BiO}_{1.5}\text{-FeO}_{1.5}\text{-WO}_3$ system

It should be noted that only for samples 5.20, 5.21, 5.22 and 5.34, there is a good agreement between their bulk and nominal compositions. For samples 5.6 and 5.12, depletion of their bulk compositions by tungsten oxide is observed, and for samples 5.3, 5.8, 5.9, 5.16, 5.17 and 5.18 – by iron oxide, relative to their corresponding nominal compositions. The

indicated depletion of the bulk composition for any component is due to the fact that some part of the components may not insert the solid phase of the hydrothermal synthesis product and remains dissolved in the cooled hydrothermal fluid, after which it will be removed from the system when rinsing the resulting precipitates.

3.2. XRD analysis

Powder X-ray diffraction patterns of samples synthesized by the hydrothermal method are shown in Fig. 2. In samples 5.3, 5.6, 5.8, 5.9 and 5.16 (Fig. 2a), only crystalline compounds with a pyrochlore structure of variable composition (CSD 1961005) were found. However, in the case of sample 5.3, when rinsing the precipitate obtained as a result of hydrothermal synthesis by decantation, it was noticed that the poured out liquid is cloudy and contains suspended particles. After drying the suspension, when studying these particles on SEM, it was found that their chemical composition was enriched with iron. Apparently, the nominal composition of sample 5.3 is beyond the stability field boundary of the pyrochlore phase from the Fe_2O_3 side, therefore, part of the iron (III) oxide does not insert into the pyrochlore phase structure and forms an impurity phase. Crystallization of iron (III) oxide, which is excessive in relation to the pyrochlore phase composition, in a slightly acidic medium of a hydrothermal fluid ($\text{pH} \sim 4-5$), is apparently difficult, since after 72 h of isothermal exposure ($T = 200^\circ\text{C}$), it is impossible to observe reflections related to any structural modifications of iron (III) oxide in the XRD pattern of the sample 5.3. It is possible to significantly accelerate the crystallization of excess iron (III) oxide by lowering the hydrothermal fluid pH to strongly acidic values ($\text{pH} < 1$), which is shown in [19, 27], where pyrochlore/ α - Fe_2O_3 composites are obtained.

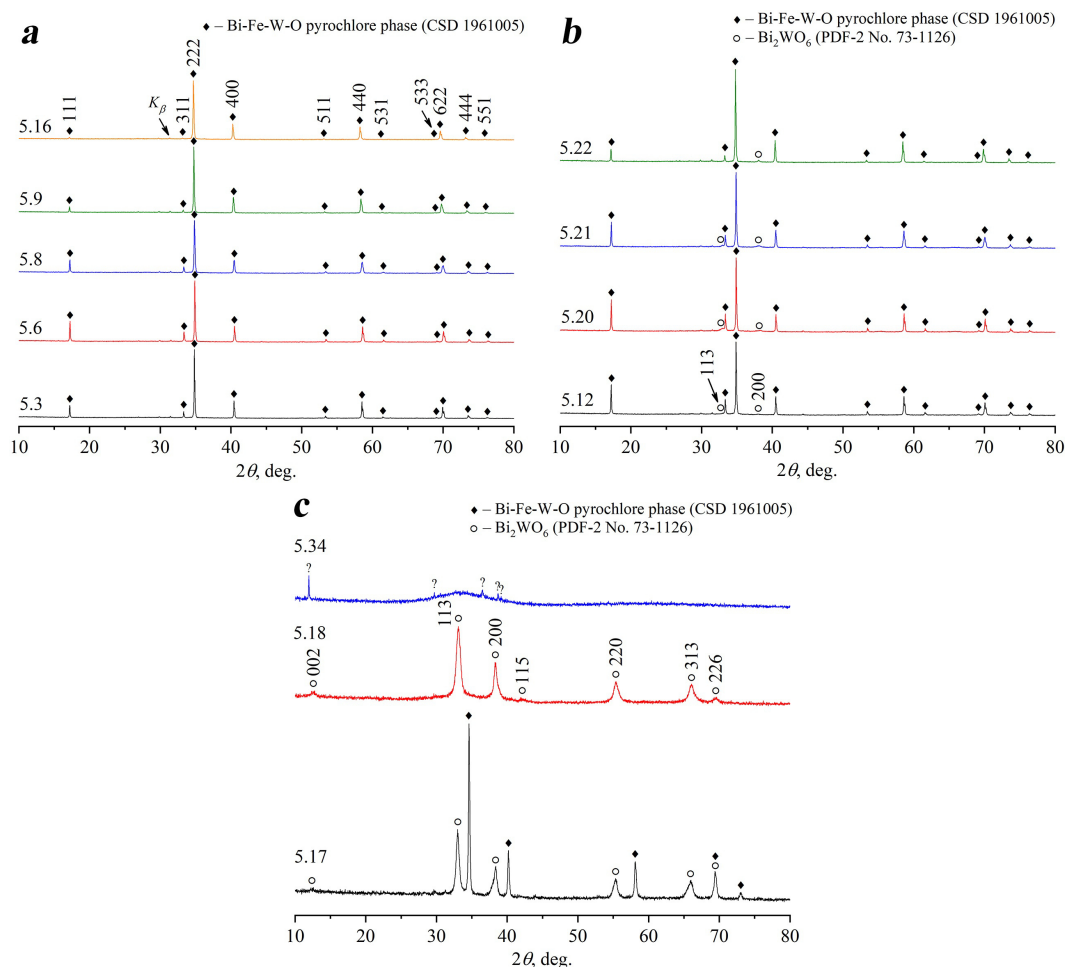


FIG. 2. Powder XRD patterns of samples synthesized by the hydrothermal method: (a) samples 5.3, 5.6, 5.8, 5.9, 5.16; (b) samples 5.12, 5.20, 5.21, 5.22; (c) samples 5.17, 5.18, 5.34 (Co- K_α radiation) (Miller indices hkl are indicated only for selected reflections)

XRD patterns of samples 5.12, 5.20, 5.21, and 5.22 (Fig. 2b) show, in addition to intense reflections of the pyrochlore phase, a set of barely noticeable reflections, identical for all these samples and related to the compound Bi_2WO_6 (PDF-2 No. 73-1126), crystallizing in the structural type of the Aurivillius phase. As a result of the pyrochlore-structured compounds composition study in these samples by the local EDXMA of single particles, it was found that the compositions determined in this way do not differ from the bulk compositions of the corresponding samples within the limits of estimated standard deviations (e.s.d.s). At the same time, the local EDXMA of single Aurivillius phase particles in these

samples showed that there is no iron in their composition, which indicates namely the formation of a two-component Aurivillius phase. Thus, it can be assumed that the bulk composition of the obtained two-phase samples, in which the Bi_2WO_6 phase is present in an impurity amount and does not affect the results of the EDXMA, with some approximation corresponds to the stability field boundary of the pyrochlore phase from the side of the Bi_2WO_6 phase.

First, the precise value of the cubic unit cell parameter of pyrochlore ($a = 10.33193(8)$ Å) was calculated for sample 5.12 using program Celsiz, version 1.1 [30] working by the least squares method and using the Miller indices hkl of all observed pyrochlore reflections and their Bragg angles $2\theta_B$ after applying the angular corrections (to zero shift and displacement). For these calculations, the XRD pattern of sample 5.12, measured with $\text{Cu-}K_{\alpha}$ radiation and a long intensity accumulation total time in step (2560 s) was used. Note that without taking into account angular corrections, the value of a is $\sim 0.0035\%$ higher and its e.s.d. is ~ 1.5 times greater.

Further, using the same XRD pattern of sample 5.12, measured with high statistics, which is described above, estimates were made of the average size D of coherent X-ray scattering regions, also called crystallites, and the absolute value of the average microdeformation (microstrain) ε_s in these regions. To obtain these parameters D and ε_s of the microstructure, using the SizeCr program [31], a profile analysis of XRD lines (line profile analysis, LPA) was carried out utilizing the Williamson-Hall (WHP) [32] and size-strain plot (SSP) [33] graphical methods.

According to the value of the criterion (full width at half the maximum intensity) $FWHM/B_{int} = 0.70(5)$, averaged over all observed XRD reflections, where $FWHM$ is the observed $FWHM$ of the XRD reflection, and $B_{int} = \frac{I_{int}}{I_{max}}$ is its integral width (I_{int} and I_{max} are integral and maximum reflection intensities, respectively), the observed reflections of sample 5.12 are characterized by a pseudo-Voigt (pV) type [34]. The observed values of the $FWHM$ were corrected for instrumental broadening (hereinafter the corrected $FWHM$ referred to as $FWHM_{corr}$) using the SizeCr program adopting procedures that take into account the type of XRD reflections [31–33]. Also, taking into account the type of XRD reflections, the program SizeCr calculates the points of the WHP and SSP graphs using the corrected values, $FWHM_{corr}$ and $2\theta_B$. The coefficients $K_{Scherrer} = 0.94$ in the Scherrer equation [35] and $K_{strain} = 4$ in the Wilson-Stokes equation [36] were used in the calculations, relating the contributions to the broadening of reflections with the values D and ε_s , respectively. When constructing the WHP and SSP graphs, the coefficient of determination R_{cod} was calculated (see its definition in [31, 33]), showing how well the experimental points fit on the approximation line $Y = A + B \cdot X$ (ideally, when all points fit on the line, $R_{cod} = 100\%$).

Fig. 3 shows the obtained SSP and WHP graphs for sample 5.12.

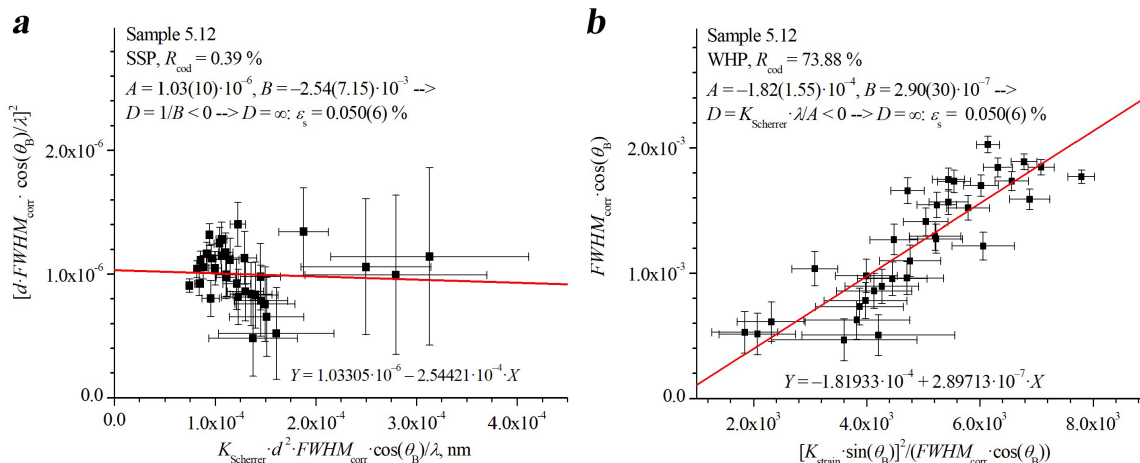


FIG. 3. (a) SSP and (b) WHP graphs constructed using XRD line profile analysis performed for sample 5.12. Approximation straight line $Y = A + B \cdot X$ of SSP (and WHP) dependence is shown in the corresponding Figures, where the values Y and X are indicated along the ordinate and abscissa axes, respectively. The symbol d means the interplanar distance corresponding to the reflection with Miller indices hkl and Bragg angle $2\theta_B$ (Bragg angle corrections are applied), and $\lambda = 1.540598$ Å is the wavelength of $\text{Cu-}K_{\alpha 1}$ radiation (after correcting the contribution of $\text{Cu-}K_{\alpha 2}$).

For sample 5.12, SSP shows low reliability, which is reflected by a large spread of points around the approximation line and a low value of the coefficient $R_{cod} = 0.39\%$ (Fig. 3a). At the same time, the WHP method for sample 5.12 (Fig. 3b) is characterized by a sufficiently large value $R_{cod} = 73.88\%$. Nevertheless, both methods give one the same results, indicating large crystallite sizes and confirming each other. In particular, as can be seen from Fig. 3a,b, the approximation straight line $Y = A + B \cdot X$ for sample 5.12 in the case of SSP is characterized by a negative slope ($B < 0$), and in the case of WHP its intersection with the Y axis occurs in the region of negative values ($A < 0$). In both cases, this formally corresponds to the infinite size of the crystallites ($D = \infty$). In the case of $D = \infty$, the values ε_s^{hkl} of

the microstrain corresponding to each observed reflection with Miller hkl indices were calculated by the SizeCr program from the Wilson-Stokes equation [36]. Indeed, for sample 5.12, the dependence $\varepsilon_s^{hkl}(2\theta_B)$ shows an almost uniform distribution of experimental ε_s^{hkl} values around the mean value $\varepsilon_s = 0.050(6)\%$ obtained by root-mean-square averaging (Fig. 4).

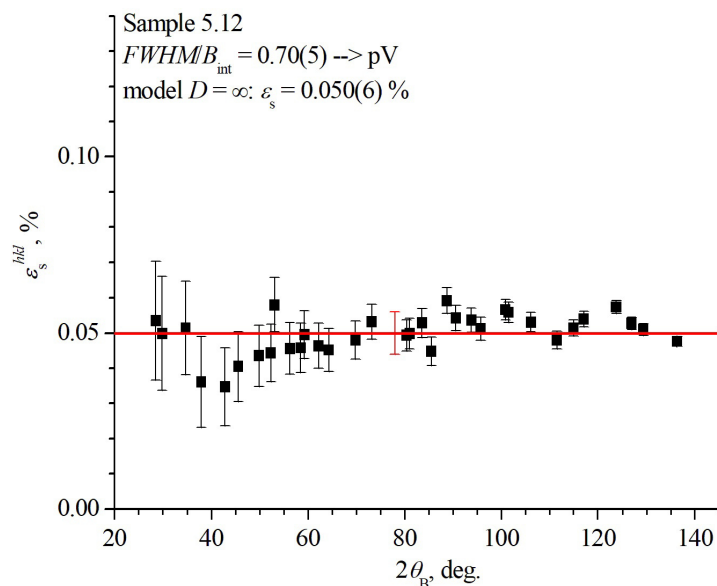


FIG. 4. Distribution of microstrain values ε_s^{hkl} along the Bragg angles $2\theta_B$. The ε_s^{hkl} values are calculated for reflections hkl within the framework of the $D = \infty$ model. The horizontal line corresponds to the mean value ε_s obtained by the root-mean-square averaging of the ε_s^{hkl} values

Taking into account that the observed values of the $FWHM$ of the pyrochlore phase reflections in other samples differ only slightly from those in sample 5.12, there is no reason to expect significant differences in the calculated values of the average crystallite sizes and microstrains for the crystalline pyrochlore phase in other synthesized samples.

Fig. 5 shows the dependence of the pyrochlore phase cubic unit cell parameter a on the phase composition expressed in Bi/W (at.) atomic ratio and assumed to be equal to the bulk composition of the samples 5.3, 5.6, 5.8, 5.9, 5.16, 5.12, 5.20, 5.21, and 5.22. The unit cell parameter a of these samples was calculated in the Celsiz program in the same way as described above for sample 5.12, based on the results obtained from the analysis of their XRD patterns measured with Co- K_α radiation and total time of 123 s of the intensity accumulation in point step (except for sample 5.12, for which the precise parameter a value was used, obtained as described above). According to the data presented in Fig. 5, the unit cell parameter increases linearly with an increase in the atomic ratio Bi/W, which, apparently, is due to an increase in the number of Bi^{3+} cations having a large radius in the structure due to their occupation of cation vacancies in the A_2O' sublattice.

In the XRD pattern of the sample 5.17 (Fig. 2c), reflections of the pyrochlore phase are detected, the unit cell parameter of which is $a = 10.4199(6)$ Å. The pyrochlore phase composition in this sample corresponds to the pyrochlore phase stability field boundary from the Bi_2O_3 - Fe_2O_3 system side and can be indirectly determined through the unit cell parameter when it is substituted into the equation $a = f(\text{Bi}/\text{W}, \text{at.})$ shown in Fig. 5: determined in this way Bi/W atomic ratio is ~ 1.25 .

In addition to the pyrochlore phase reflections, a set of reflections is observed in sample 5.17, which can be equally attributed to both the compound Bi_2WO_6 (PDF-2 No. 73-1126) and the compound of the formal composition $\text{Bi}_{1.5}\text{Fe}_{0.5}\text{WO}_6$ (PDF-2 No. 38-1285). The same set of reflections is observed in the XRD pattern of sample 5.18, while the pyrochlore phase reflections are absent (Fig. 2c). Both compounds (Bi_2WO_6 and $\text{Bi}_{1.5}\text{Fe}_{0.5}\text{WO}_6$) belong to the class of Aurivillius phases and have the same set of reflections, apparently differing in the number and nature of perovskite-like layers. It is extremely difficult to distinguish these compounds in XRD patterns, which requires the use of additional research methods, in particular, the analysis of these compounds particles chemical composition by the local EDXMA. In samples 5.17 and 5.18, it was not possible to carry out such an analysis (see Section 3.3), as was done for other samples described above. However, TEM studies confirmed the formation of a single-layer Aurivillius phase Bi_2WO_6 in them. In sample 5.17 the Aurivillius phase Bi_2WO_6 crystallite size in the crystallographic direction [113] was calculated using the Scherrer method and amounted to ~ 20 nm. Two amorphous halos are observed in the XRD pattern of sample 5.34 (Fig. 2c), against which narrow but low-intensity reflections of an unknown phase are visible.

When comparing the chemical composition of samples 5.17, 5.18, and 5.34 with the results of XRD, it can be concluded that they contain a phase, which chemical composition enriched in bismuth and iron oxides and the reflections

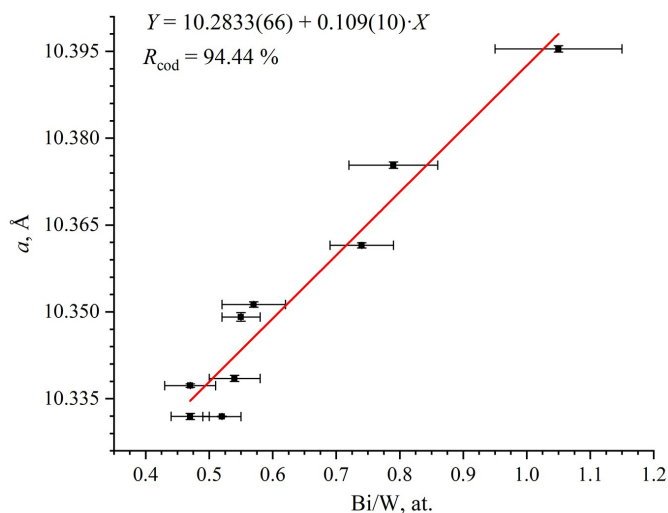


FIG. 5. Dependence of the pyrochlore phase cubic unit cell parameter a on the phase composition expressed in Bi/W (at.) atomic ratio and assumed to be equal to the bulk composition of the samples 5.3, 5.6, 5.8, 5.9, 5.16, 5.12, 5.20, 5.21, and 5.22

of which cannot be detected in XRD patterns, and the amount of this phase increases with an increase in the content of these oxides in the bulk chemical composition of the samples.

Fig. 6 shows a concentration triangle, which compares the results of determining the bulk chemical and phase composition of the obtained samples. The shaded area indicates the localization of the pyrochlore-structured compounds concentration stability field in the $\text{BiO}_{1.5}\text{-FeO}_{1.5}\text{-WO}_3$ system at $T = 200^\circ\text{C}$, which is longitudinally limited within the atomic ratios $0.47 < \text{Bi}/\text{W} < 1.25$, and in the transverse direction within $1.14 < \text{Bi}/\text{Fe} < 1.87$.

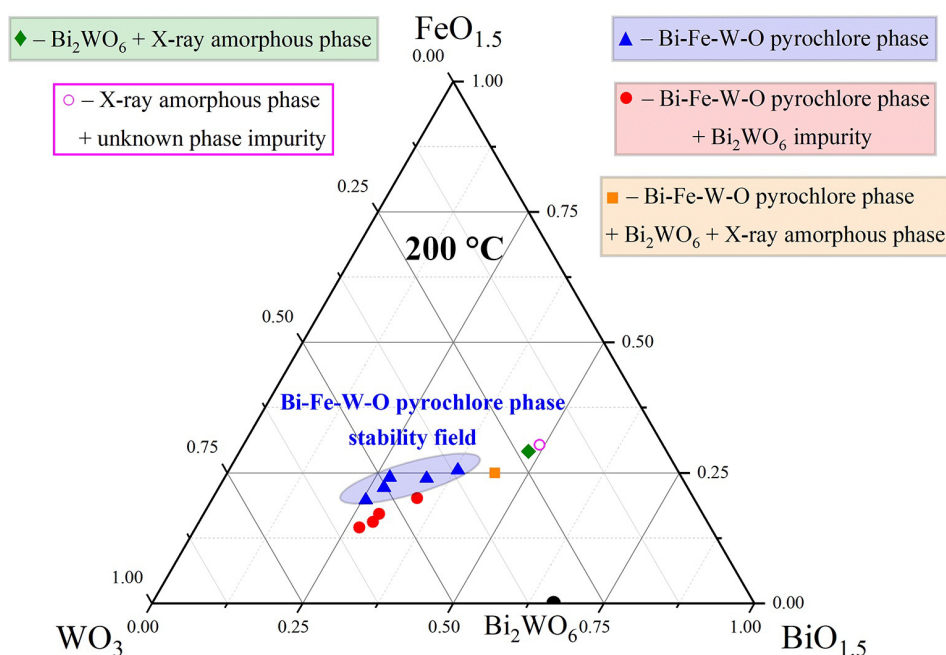


FIG. 6. Comparison of the bulk chemical composition and phase composition of the samples synthesized by the hydrothermal method on the concentration triangle of the $\text{BiO}_{1.5}\text{-FeO}_{1.5}\text{-WO}_3$ system (the shaded area indicates the localization of the pyrochlore-structured compounds concentration stability field at $T = 200^\circ\text{C}$)

3.3. SEM

The SEM data for the samples synthesized by the hydrothermal method are shown in Fig. 7 ((a) 5.6, (b) 5.8, (c) 5.9, (d) 5.16, (e) 5.12 and (f) 5.17). In samples 5.3 (not shown), 5.6, 5.8, 5.9 and 5.16, the only crystalline phase in which, according to the XRD data, is the pyrochlore phase, submicron particles of only one morphological motif are observed.

In sample 5.6, the particles have an almost spherical shape, resembling a poorly faceted octahedron, while in samples 5.3 (not shown), 5.8, 5.9 and 5.16 the particles have a predominantly clear octahedral shape. The octahedral morphology of the pyrochlore phase particles is determined by their synthesis conditions, mainly by the *pH* value of the hydrothermal fluid ($\text{pH} \sim 4\text{--}5$), as shown in [20].

In sample 5.12, in addition to the pyrochlore phase particles, which make up the bulk of the sample, rare plate-like particles with a thickness of $\sim 50\text{--}100$ nm are observed, fused with each other along flat edges into layered aggregates (Bi_2WO_6 phase). For other samples also containing impurity amounts of the Bi_2WO_6 phase (5.20, 5.21 and 5.22), a similar situation is observed, while micrographs of sample 5.17 are different, despite the qualitatively identical phase composition, according to XRD data.

Three morphological motifs are observed in micrographs of sample 5.17: (1) pyrochlore phase octahedral particles; (2) rod-shaped nanoparticles, which are, apparently, compounds with the Aurivillius phase structure; (3) agglomerates of nanoparticles, the morphology of which is difficult to determine according to SEM data. Since the reflections belonging to only two crystalline phases were detected in the XRD pattern of sample 5.17, the (3) nanoparticles observed in micrographs are apparently X-ray amorphous. Precise determination of the crystalline pyrochlore phase and Aurivillius phase individual particles composition in this sample employing the local EDXMA is complicated by the fact that the above-mentioned X-ray amorphous nanoparticles are localized, including on their surface. In micrographs of sample 5.18 (not shown), a similar situation is observed, but the pyrochlore phase particles are not detected in this case, which is consistent with XRD data. In micrographs of sample 5.34 (not shown), in which, according to XRD data, barely noticeable reflections of an unknown phase are observed against the background of an amorphous halo, the entire array of particles is represented by agglomerates of X-ray amorphous nanoparticles. In order to determine the nature and size of these nanoparticles, as well as the structure of rod-shaped nanoparticles, samples 5.17 and 5.18 were studied by the TEM method.

3.4. TEM

The TEM data for the samples synthesized by the hydrothermal method are shown in Fig. 8: (a,b,c,d) – 5.17 and (e,f) – 5.18. Three morphological motifs are observed in sample 5.17, which can be correlated with the XRD data as follows: (1) large octahedral particles of submicron sizes are pyrochlore-structured compounds (Fig. 8a); (2) rod-shaped nanoparticles of various lengths having a thickness of $\sim 10\text{--}30$ nm are, most likely, compounds with the Aurivillius phase structure (Bi_2WO_6 , PDF-2 No. 73-1126) (Fig. 8a,b,c); (3) almost spherical nanoparticles, which size is about 10 nm, are an X-ray amorphous phase (Fig. 8a,b,c). In sample 5.18, only (2) and (3) morphological motifs can be observed, which, apparently, correlate with the results of XRD in a similar way (Fig. 8e). The above assumptions are confirmed when considering nanoparticles in the high resolution mode (HRTEM), as well as when studying them using electron diffraction.

In the HRTEM, the structure of rod-shaped nanoparticles resembles a layered structure formed by alternating atomic planes composed of various sorts of atoms, as indicated by the different brightness of the atomic planes and the different interplanar distance between them (Fig. 8c). The Bi_2WO_6 compound is the simplest member of the Aurivillius phases family, the structure of which can be represented as two alternating layers: a fluorite-like layer $\text{Bi}_2\text{O}_2^{2+}$ and a perovskite-like layer WO_4^{2-} , while the unit cell parameter c is ~ 16.43 Å. In the micrograph of a rod-shaped nanoparticle obtained in the HRTEM, exactly such a layered structure is observed (Fig. 8c). If the left side of the nanoparticle is considered, then the following sequence of atomic planes alternation can be noted: two adjacent atomic planes having the same brightness, the distance between which is less than the distance from any of them to the nearest neighboring, brighter atomic plane, form a fluorite-like layer $\text{Bi}_2\text{O}_2^{2+}$, while the brighter atomic plane is a perovskite-like layer WO_4^{2-} . When comparing the observed structure with the Bi_2WO_6 compound unit cell structure, the average value of the parameter $c \sim 16.33$ Å over several unit cells was determined. When considering the right side of the same nanoparticle, a similar structure is observed, however, in this case, the atomic planes that make up the fluorite-like layer $\text{Bi}_2\text{O}_2^{2+}$ are brighter than the atomic plane, which is the perovskite-like layer WO_4^{2-} . The measured in this case average value of parameter c was ~ 16.07 Å over several unit cells. Similar measurements made for another rod-shaped nanoparticle (not shown) give a result close to the previous ones ~ 16.59 Å. When averaging all measured values of the unit cell parameter c , its value is ~ 16.33 Å, which indicates the formation of a single-layer Bi_2WO_6 phase and does not confirm an increase in the number of layers of the perovskite-like block. It should be noted that the rod-shaped nanoparticles observed in sample 5.18 have a similar structure and are the Bi_2WO_6 compound.

In Fig. 8c, in addition to the rod-shaped nanoparticle, several almost spherical nanoparticles can be noted, the size of which is about 10 nm. For nanoparticles that are found in the Bragg position, it is possible to observe sets of atomic planes that have the same brightness and a single interplanar distance within a particle. This, firstly, indicates the crystalline nature of such nanoparticles and, secondly, suggests that they are not layered compounds. In the electron diffraction pattern obtained from a certain group of such nanoparticles (Fig. 8d), the set of diffraction rings can be observed, while a broadened ring from the amorphous phase is not observed, which indicates the absence of an amorphous component.

In Fig. 8e (sample 5.18), a certain number of rod-shaped (Bi_2WO_6 compound) and almost spherical (X-ray amorphous phase) nanoparticles can be observed, the electron diffraction pattern from which is shown in Fig. 8f. When

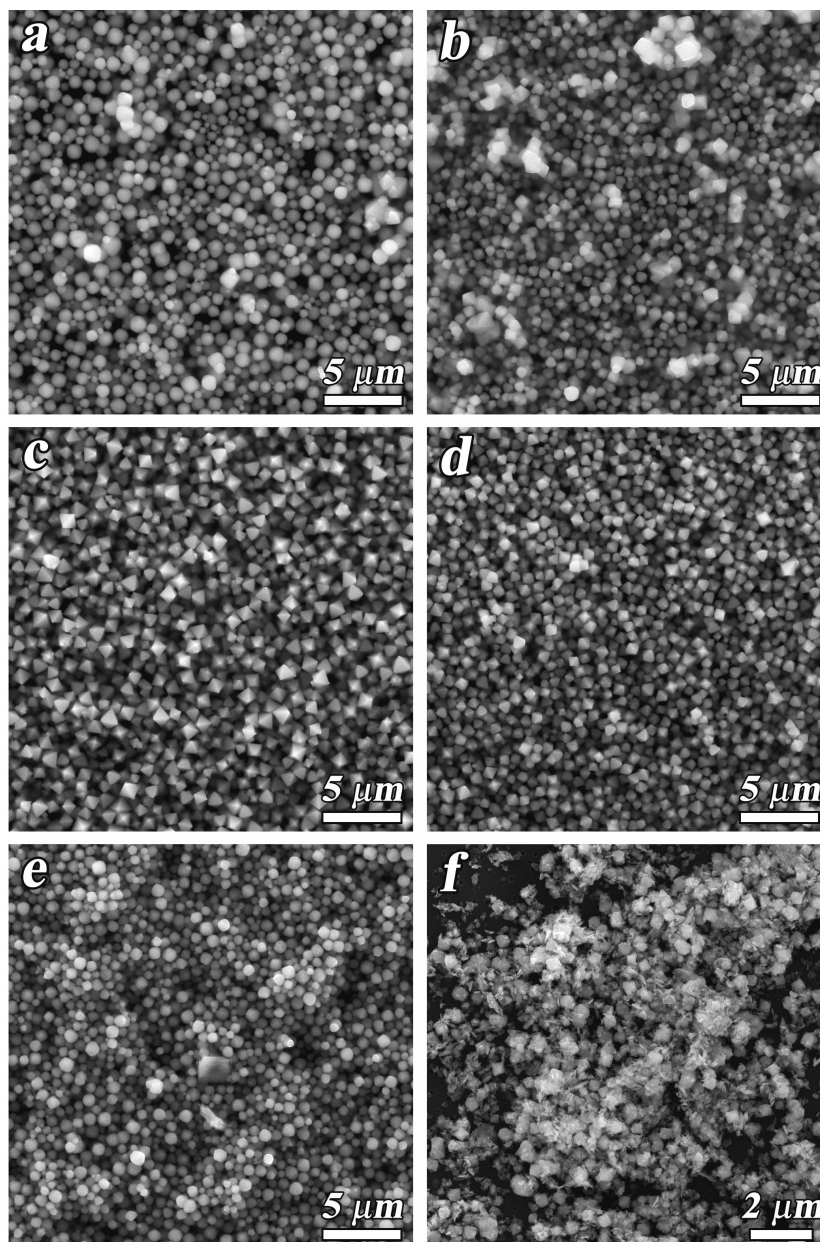


FIG. 7. SEM images of samples synthesized by the hydrothermal method: (a) 5.6, (b) 5.8, (c) 5.9, (d) 5.16, (e) 5.12 and (f) 5.17)

comparing the interplanar distances calculation results with a characteristic set of those for the Bi_2WO_6 compound, it was possible to establish a reliable match for eight of the ten indicated in Fig. 8f diffraction rings (Table 3). Two diffraction rings (3 and 10), the appearance of which is slightly different from the others, relate to diffraction from the substrate. It is not possible to perform a precise calculation of interplanar distances using other diffraction rings, that not indicated in Fig. 8f, due to their low brightness. It is important to note that the diffraction rings attributed to the Bi_2WO_6 compound may also relate to diffraction from nanoparticles of the X-ray amorphous phase, as well as other less bright and therefore not indicated in Fig. 8f diffraction rings.

3.5. Thermal stability

The thermal stability of the pyrochlore-structured compounds synthesized by the hydrothermal method was studied using sample 5.16 as an example. Two kinetic regimes were studied: (1) nonequilibrium (HTXRD and DSC/TG) and (2) quasi-equilibrium (annealing-quenching).

The data of the HTXRD of sample 5.16 (Fig. 9) indicate that no phase transformations occur in the sample up to a temperature of 545°C . Starting with a temperature of 585°C , the appearance of reflections belonging to the compound Bi_2WO_6 (PDF-2 No. 73-1126) is observed in HTXRD patterns. With a further increase in temperature to 765°C , the intensities of the Bi_2WO_6 phase reflections constantly increase, however, the pyrochlore-structured compound remains

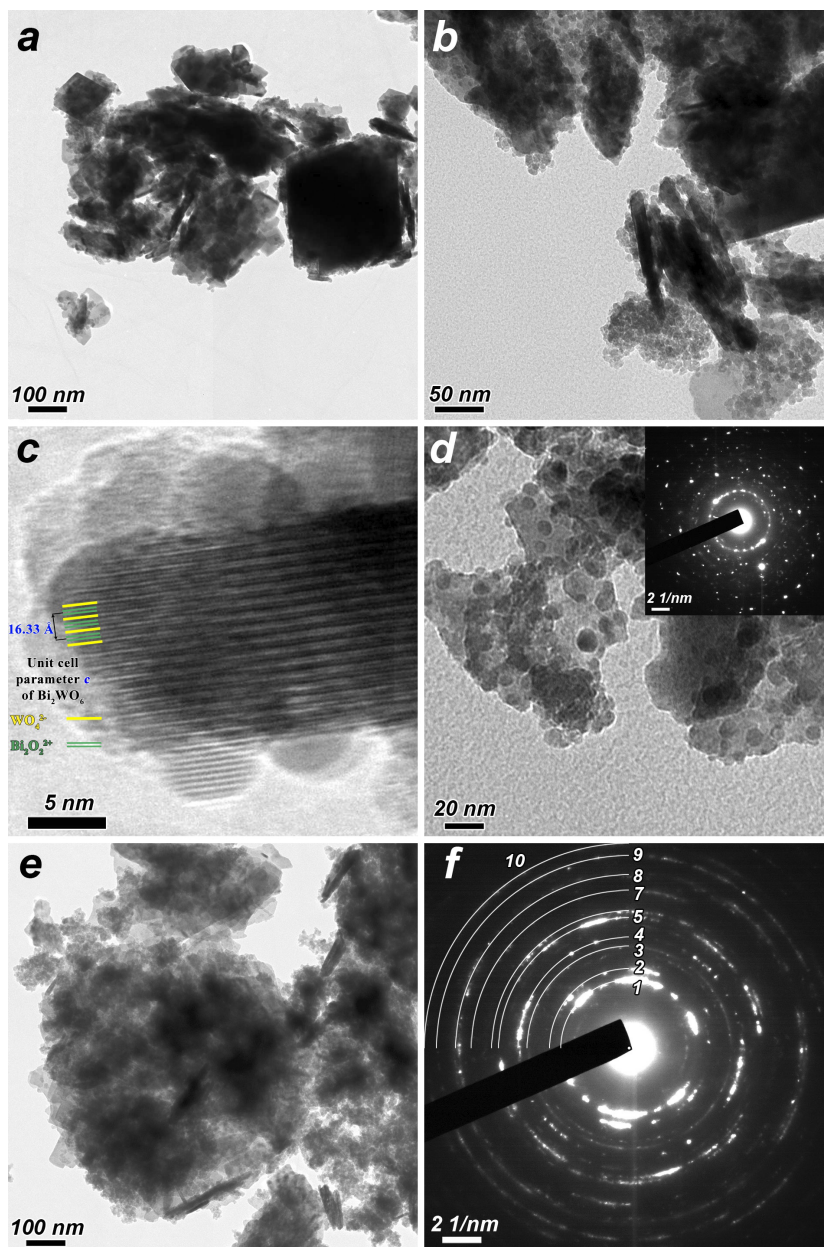


FIG. 8. TEM images of samples synthesized by the hydrothermal method: (a, b, c, d) 5.17 and (e, f) 5.18

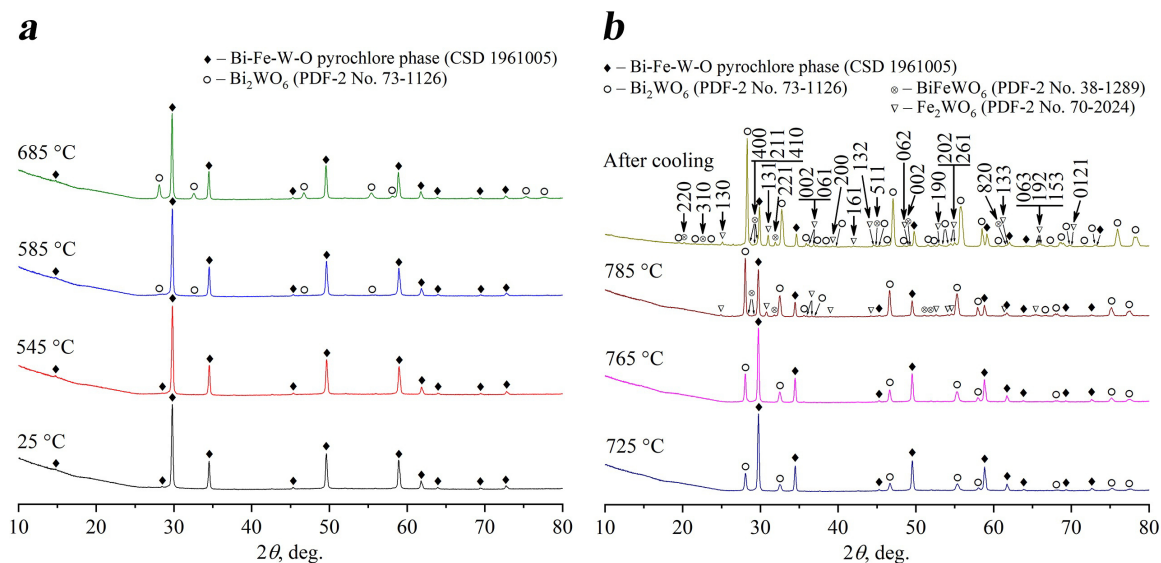
the predominant phase. The pyrochlore phase unit cell parameter increases in the temperature range 585–765°C, however, its change with increasing temperature is due not only to thermal lattice expansion, but also to a change in the composition of the compound during its gradual decomposition. At a temperature of 785°C, qualitative and significant quantitative changes can be noted in the HTXRD pattern: reflections of two new phases appear – Fe_2WO_6 (PDF-2 No. 70-2024) and BiFeWO_6 (PDF-2 No. 38-1289), and the amount of pyrochlore phase decreases sharply relative to the Bi_2WO_6 phase. No qualitative changes are observed in the XRD pattern obtained after cooling the sample from 785°C to room temperature in the natural mode (40–50 min), however, a further decrease in the amount of the pyrochlore phase is clearly noticeable compared to the amounts of Bi_2WO_6 , Fe_2WO_6 and BiFeWO_6 phases.

The presented results of HTXRD studies of sample 5.16 allow to conclude that in the temperature range 585–765°C the equilibrium composition of the pyrochlore phase changes, which corresponds to its continuous decomposition with the formation of the Bi_2WO_6 phase with an increase in temperature, while at a temperature of 785°C instantaneous decomposition of the pyrochlore phase of the composition corresponding to the higher temperature point of the pyrochlore stability field is observed.

The DSC/TG data for sample 5.16 are presented in Fig. 10. At the initial stage of heating in the range from 75°C to 230°C, a weak endothermic effect is observed on the DSC curve with a maximum at 130°C, which corresponds to a noticeable weight decrease of 1.37% on the TG curve. With further heating, weight loss is observed up to a temperature of 580°C, however, in the range of 230–580°C it proceeds more slowly and amounts to only 0.47%. Apparently, the

TABLE 3. The results of comparing the interplanar distances calculated from electron diffraction data with those for the Bi_2WO_6 compound (PDF-2 No. 73-1126)

The designation in Fig. 8f	Interplanar distances (d) according to the electron diffraction data (Fig. 8f), Å	Miller indices hkl of Bi_2WO_6 compound reflections
1	3.132	113
2	2.704	006 200 020
3	2.101	substrate
4	1.911	206 026 220 018
5	1.635	119 313 208 133
6	1.553	226 0110 218
7	1.353	0012 400 040 038
8	1.209	145 2012 0212 406 420 046 0310 240 238
9	1.103	2212 426 246 2310
10	1.036	substrate

FIG. 9. Powder XRD patterns of sample 5.16, measured *in situ* at various heating temperatures: (a) from 25 °C to 685 °C; (b) from 725 °C to 785 °C and after cooling from 785 °C to room temperature in the natural mode (Cu-K_α radiation) (Miller indices hkl are indicated only for selected reflections)

loss of weight at this stage of heating is due to further water removal, but decomposition of impurity carbonates formed during the hydrothermal synthesis is also possible. Further, when the sample is heated to a temperature of 815 °C, its mass practically does not change. On the DSC curve in the range from 230 °C to 795 °C, it is not possible to distinguish thermal effects due to their low intensity. According to the data of HTXRD analysis (Fig. 9), the pyrochlore phase decomposition occurs in the temperature range of 585–785 °C. This process, like most solid-phase reactions, is kinetically hindered and has small thermal effects, which makes it much more difficult to detect on the DSC curve. In the temperature range of 795–900 °C, three consecutive endothermic effects are observed, which can be associated with the melting of the phases formed during the pyrochlore phase decomposition.

Sample 5.16 was annealed sequentially to temperatures of 585 °C, 685 °C and 725 °C (Fig. 11), and quenching was carried out to room temperature in air by removing the crucible with the sample from a hot furnace. The duration of each annealing was 12 h, and the duration of cooling of the samples to room temperature was ~ 10–15 min. The sample obtained by annealing to a temperature of 585 °C, after XRD analysis, was used for annealing to a temperature of 685 °C

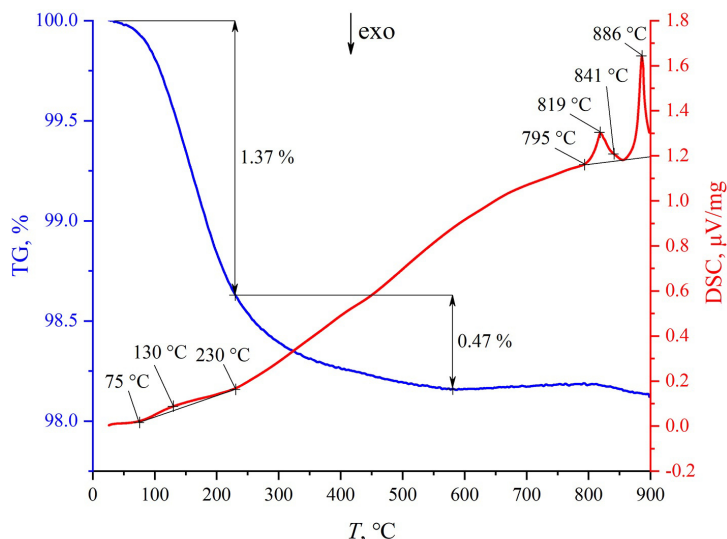
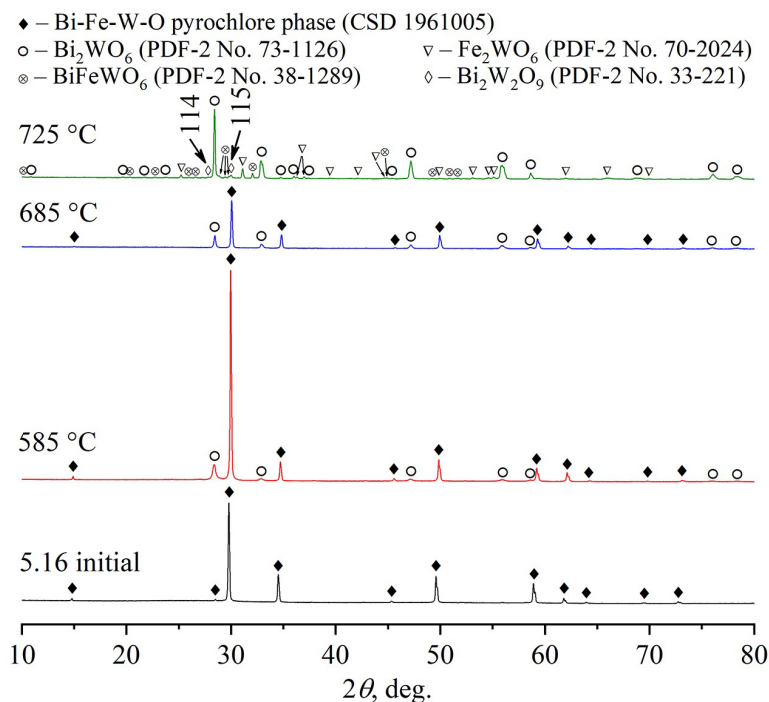


FIG. 10. DSC/TG curves obtained by heating the sample 5.16

FIG. 11. Powder XRD patterns of samples obtained by annealing sample 5.16 to various temperatures (585°C, 685°C, and 725°C) with quenching to room temperature. The measurements were carried out at room temperature (Cu- K_{α} radiation) (Miller indices hkl are indicated only for selected reflections)

and so on. The bulk chemical compositions of the samples obtained as a result of annealing-quenching correspond within the limits of e.s.d.s to the initial sample composition, which indicates the absence of noticeable volatilization of the components.

In the XRD pattern of the sample obtained by annealing to 585°C, the appearance of the nanocrystalline Bi_2WO_6 (PDF-2 No. 73-1126) phase reflections is observed. The Aurivillius phase Bi_2WO_6 crystallite size in the crystallographic direction [113] was calculated using the Scherrer method and amounted to ~ 28 nm, however, the intensity of its reflections turns out to be several times greater than observed according to HTXRD data at this temperature (Fig. 9a,11). In the XRD pattern of the sample obtained by annealing to 685°C (Fig. 11), a further increase in the Bi_2WO_6 phase reflections intensity can be noted, which is qualitatively consistent with the HTXRD data (Fig. 9). Significant qualitative and quantitative changes are observed in the XRD pattern of the sample obtained by annealing to 725°C: the appearance of three new phases is recorded – Fe_2WO_6 (PDF-2 No. 70-2024), BiFeWO_6 (PDF-2 No. 38-1289) and barely noticeable amounts

of $\text{Bi}_2\text{W}_2\text{O}_9$ (PDF-2 No. 33-221), and the reflections of the pyrochlore phase are not observed, which indicates the completed decomposition of the pyrochlore phase having the composition corresponding to the higher temperature point of its stability field. Comparing the phase composition of the sample obtained by annealing to 725°C and the HTXRD data obtained in the temperature range $725\text{--}785^\circ\text{C}$ (Fig. 9b,11), it can be concluded that the temperature readings when recording the XRD pattern *in situ* are more than 60°C ahead of the temperature at which the phase composition observed on the HTXRD is equilibrium.

4. Conclusions

Pyrochlore-structured compounds of variable composition formed in the $\text{Bi}_2\text{O}_3\text{--Fe}_2\text{O}_3\text{--WO}_3$ system under hydrothermal conditions ($T = 200^\circ\text{C}$, $P = 7$ MPa, hydrothermal fluid $\text{pH} \sim 4\text{--}5$) were obtained in the form of single-phase materials and as part of composite nanomaterials, and characterized.

The concentration stability field localization of the pyrochlore-structured compounds was established and phase equilibria involving these compounds were studied. It was shown that under the studied hydrothermal synthesis conditions, a pyrochlore-structured compounds were obtained in the form of submicron particles, predominantly of a clear octahedral shape, which indicates the intensification of their growth processes under such conditions. At the same time, it was found that the phases coexisting with these compounds are formed in nanocrystalline form: in the region of two-phase equilibrium from the $\text{Bi}_2\text{O}_3\text{--WO}_3$ system side, plate-like (thickness $h \sim 50\text{--}100$ nm) nanoparticles of the Bi_2WO_6 compound are formed; in the region of compositions from the $\text{Bi}_2\text{O}_3\text{--Fe}_2\text{O}_3$ system side, rod-shaped ($h \sim 10\text{--}30$ nm) nanoparticles of the Bi_2WO_6 compound are formed, which crystallite size in the crystallographic direction [113] is ~ 20 nm, as well as X-ray amorphous nanoparticles with a size of about 10 nm.

The presented results of pyrochlore-structured compounds thermal stability investigation allow to conclude that in the temperature range from $\sim 585^\circ\text{C}$ to $\sim 725^\circ\text{C}$ the equilibrium composition of the pyrochlore phase changes, which corresponds to its continuous decomposition with the formation of the nanocrystalline Bi_2WO_6 phase with an increase in temperature, while at a temperature of 725°C instantaneous decomposition of the pyrochlore phase of the composition corresponding to the higher temperature point of the pyrochlore stability field is observed.

References

- [1] Ellert O.G., Egorysheva A.V., Gajtko O.M., Kirdyankin D.I., Svetogorov R.D. Highly Frustrated Bi–Cr–Sb–O Pyrochlore with Spin-Glass Transition. *Journal of Magnetism and Magnetic Materials*, 2018, **463**, P. 13–18.
- [2] Egorysheva A.V., Ellert O.G., Maksimov Y.V., Volodin V.D., Efimov N.N., Novotortsev V.M. Subsolidus Phase Equilibria and Magnetic Characterization of the Pyrochlore in the $\text{Bi}_2\text{O}_3\text{--Fe}_2\text{O}_3\text{--Sb}_2\text{O}_x$ System. *Journal of Alloys and Compounds*, 2013, **579**, P. 311–314.
- [3] Koroleva M.S., Piir I.V., Ryabkov Yu.I., Korolev D.A., Chezhina N.V. Synthesis and Properties of Chromium-Containing Bismuth Titanates with the Pyrochlore Structure. *Russian Chemical Bulletin, International Edition*, 2013, **62**(2), P. 408–411.
- [4] Babu G.S., Bedanta S., Valant M. Evidence of the spin glass state in $(\text{Bi}_{1.88}\text{Fe}_{0.12})(\text{Fe}_{1.42}\text{Te}_{0.58})\text{O}_{6.87}$ pyrochlore. *Solid State Communications*, 2013, **158**, P. 51–53.
- [5] Lufaso M.W., Vanderah T.A., Pazos I.M., Levin I., Roth R.S., Nino J.C., Provenzano V., Schenck P.K. Phase Formation, Crystal Chemistry, and Properties in the System $\text{Bi}_2\text{O}_3\text{--Fe}_2\text{O}_3\text{--Nb}_2\text{O}_5$. *Journal of Solid State Chemistry*, 2006, **179**(12), P. 3900–3910.
- [6] Jusoh F.A., Tan K.B., Zainal Z., Chen S.K., Khaw C.C., Lee O.J. Novel pyrochlores in the $\text{Bi}_2\text{O}_3\text{--Fe}_2\text{O}_3\text{--Ta}_2\text{O}_5$ (BFT) Ternary System: Synthesis, Structural and Electrical Properties. *Journal of Materials Research and Technology*, 2020, **9**(5), P. 11022–11034.
- [7] Liu W., Wang H. Enhanced Dielectric Properties of $\text{Bi}_{1.5}\text{ZnNb}_{1.5}\text{O}_7$ Thick Films via Cold Isostatic Pressing. *Journal of Electroceramics*, 2012, **29**(3), P. 183–186.
- [8] Piir I.V., Koroleva M.S., Ryabkov Y.I., Korolev D.A., Chezhina N.V., Semenov V.G., Panchuk V.V. Bismuth Iron Titanate Pyrochlores: Thermostability, Structure and Properties. *Journal of Solid State Chemistry*, 2013, **204**, P. 245–250.
- [9] Krasnov A.G., Piir I.V., Koroleva M.S., Sekushin N.A., Ryabkov Y.I., Piskaykina M.M., Sadykov V.A., Sadovskaya E.M., Pelipenko V.V., Ereemeev N.F. The Conductivity and Ionic Transport of Doped Bismuth Titanate Pyrochlore $\text{Bi}_{1.6}\text{M}_x\text{Ti}_2\text{O}_{7-\delta}$ ($M\text{--Mg, Sc, Cu}$). *Solid State Ionics*, 2017, **302**, P. 118–125.
- [10] Egorysheva A.V., Gajtko O.M., Rudnev P.O., Ellert O.G., Ivanov V.K. Synthesis of Bi–Fe–Sb–O Pyrochlore Nanoparticles with Visible-Light Photocatalytic Activity. *European Journal of Inorganic Chemistry*, 2016, **13–14**, P. 2193–2199.
- [11] Bencina M., Valant M., Pitcher M.W., Fanetti M. Intensive Visible-Light Photoactivity of Bi- and Fe-Containing Pyrochlore Nanoparticles. *Nanoscale*, 2014, **6**(2), P. 745–748.
- [12] Allured B., Delacruz S., Darling T., Huda M.N., Subramanian V.(R.) Enhancing the visible light absorbance of $\text{Bi}_2\text{Ti}_2\text{O}_7$ through Fe-substitution and its effects on photocatalytic hydrogen evolution. *Appl. Catal. B Environ.*, 2014, **144**, P. 261–268.
- [13] Pyrochlorine Materials and thermal barrier coating with these pyrochlore materials, Patent. 2454477 Russia: MPK C22C 29/12, C23C 30/00, Malov T., Oexchep M., N 2009116606/02, Issue N 18, 27.06.2012.
- [14] Xue J., Zhang K., He Z., Zhao W., Li W., Xie D., Luo B., Xu K., Zhang H. Rapid Immobilization of Simulated Radioactive Soil Waste Using Self-Propagating Synthesized $\text{Gd}_2\text{Ti}_2\text{O}_7$ Pyrochlore Matrix. *Materials*, 2019, **12**(7), P. 1163.
- [15] Benčina M., Valant M. $\text{Bi}_2\text{Ti}_2\text{O}_7$ -based pyrochlore nanoparticles and their superior photocatalytic activity under visible light. *Journal of the American Ceramic Society*, 2017, **101**(1), P. 82–90.
- [16] Castellano C., Berti G., Rubio-Marcos F., Lamura G., Sanna S., Salas-Colera E., Brambilla A., Muñoz-Noval Á., Duò L., Demartin F. Anomalous local lattice disorder and distortion in $\text{A}_2\text{Mo}_2\text{O}_7$ pyrochlores. *Journal of Alloys and Compounds*, 2017, **723**, P. 327–332.
- [17] Zhuk N.A., Krzhizhanovskaya M.G., Koroleva A.V., Semenov V.G., Selyutin A.A., Lebedev A.M., Nekipelov S.V., Sivkov D.V., Kharton V.V., Lutoev V.P., Makeev B.A. Fe,Mg-Codoped Bismuth Tantalate Pyrochlores: Crystal Structure, Thermal Stability, Optical and Electrical Properties, XPS, NEXAFS, ESR, and ^{57}Fe Mössbauer Spectroscopy Study. *Inorganics*, 2023, **11**(1), P. 8.
- [18] Guskov V.N., Gagarin P.G., Tyurin A.V., Khoroshilov A.V., Guskov A.V., Gavrichev K.S. Heat capacity of solutions $\text{LaLnZr}_2\text{O}_7$ ($\text{Ln} = \text{Sm, Gd, Dy}$) with the structure of pyrochlore in the temperature range of $10\text{--}1400$ K. *Russian Journal of Physical Chemistry A*, 2020, **94**(2), P. 233–239.

- [19] Lomakin M.S., Proskurina O.V., Gusarov V.V. Pyrochlore phase in the $\text{Bi}_2\text{O}_3\text{-Fe}_2\text{O}_3\text{-WO}_3\text{-(H}_2\text{O)}$ system: its formation by hydrothermal synthesis in the low-temperature region of the phase diagram. *Nanosystems: Phys. Chem. Math.*, 2023, **14**(2), P. 242–253.
- [20] Lomakin M.S., Proskurina O.V., Levin A.A., Sergeev A.A., Leonov A.A., Nevedomskiy V.N., Voznesenskiy S.S. Pyrochlore Phase in the $\text{Bi}_2\text{O}_3\text{-Fe}_2\text{O}_3\text{-WO}_3\text{-(H}_2\text{O)}$ System: its Formation by Hydrothermal-Microwave Synthesis and Optical Properties. *Russ. J. Inorg. Chem.* 2022, **67**(6), P. 820–829.
- [21] Lomakin M.S., Proskurina O.V., Abiev R.Sh., Nevedomskiy V.N., Leonov A.A., Voznesenskiy S.S., Gusarov V.V. Pyrochlore phase in the $\text{Bi}_2\text{O}_3\text{-Fe}_2\text{O}_3\text{-WO}_3\text{-(H}_2\text{O)}$ system: physicochemical and hydrodynamic aspects of its production using a microreactor with intensively swirled flows. *Advanced Powder Technology*, 2023, **34**(7), 104053.
- [22] Daniels L.M., Playford H.Y., Grenèche J.-M., Hannon A.C., Walton R.I. Metastable $(\text{Bi}, M)_2(\text{Fe}, \text{Mn}, \text{Bi})_2\text{O}_{6+x}$ ($M = \text{Na}$ or K) Pyrochlores from Hydrothermal Synthesis. *Inorganic Chemistry*, 2014, **53**(24), P. 13197–13206.
- [23] Egorysheva A.V., Gajtko O.M., Rudnev P.O., Ellert O.G., Ivanov V.K. Synthesis of Bi–Fe–Sb–O Pyrochlore nanoparticles with visible-light photocatalytic activity. *Eur. J. Inorg. Chem.*, 2016, **13–14**, P. 2193–2199.
- [24] Radha R., Srinivasan A., Manimuthu P., Balakumar S. Tailored sunlight driven nano-photocatalyst: bismuth iron tungstate (BiFeWO_6), *J. Mater. Chem. C*, 2015, **3**(39), P. 10285–10292.
- [25] Annamalai K., Radha R., Vijayakumari S., Kichanov S.E., Balakumar S. Insight into the investigation on nanostructured defect pyrochlore $\text{Bi}_{2-x}\text{Fe}_x\text{WO}_6$ and its photocatalytic degradation of mixed cationic dyes. *Materials Science in Semiconductor Processing*, 2022, **150**, 2022, P. 106961.
- [26] Wang Y., Zhang S., Zhong Q., Zeng Y., Ou M., Cai W. Hydrothermal synthesis of novel uniform nanooctahedral $\text{Bi}_3(\text{FeO}_4)(\text{WO}_4)_2$ solid oxide and visible-light photocatalytic performance. *Ind. Eng. Chem. Res.*, 2016, **55**(49), P. 12539–12546.
- [27] Lomakin M.S., Proskurina O.V., Danilovich D.P., Panchuk V.V., Semenov V.G., Gusarov V.V. Hydrothermal Synthesis, Phase Formation and Crystal Chemistry of the pyrochlore/ Bi_2WO_6 and pyrochlore/ $\alpha\text{-Fe}_2\text{O}_3$ Composites in the $\text{Bi}_2\text{O}_3\text{-Fe}_2\text{O}_3\text{-WO}_3$ System. *J. Solid State Chem.*, 2020, **282**, P. 121064.
- [28] Narykova M.V., Levin A.A., Prasolov N.D., Lihachev A.I., Kardashev B.K., Kadomtsev A.G., Panfilov A.G., Sokolov R.V., Brunkov P.N., Sultanov M.M., Kuryanov V.N., Tyshkevich V.N. The structure of the near-surface layer of the AAAC overhead power line wires after operation and its effect on their elastic, microplastic, and electroresistance properties. *Crystals*, 2022, **12**, P. 166.
- [29] Fawcett T.G., Kabekkodu S.N., Blanton J.R., Blanton T.N. Chemical analysis by diffraction: the Powder Diffraction File™. *Powder Diffr.*, 2017, **32**, P. 63–71.
- [30] Maunders C., Etheridge J., Wright N., Whitfield H.J. Structure and microstructure of hexagonal $\text{Ba}_3\text{Ti}_2\text{RuO}_9$ by electron diffraction and microscopy. *Acta Crystallogr. B.*, 2005, **61**, P. 154–159.
- [31] Levin A.A. Program *SizeCr* for calculation of the microstructure parameters from X-ray diffraction data. preprint ResearchGate, 2022.
- [32] Terlan B., Levin A.A., Börrnert F., Simon F., Oschatz M., Schmidt M., Cardoso-Gil R., Lorenz T., Baburin I.A., Joswig J.-O., Eychmüller A. Effect of Surface Properties on the Microstructure, Thermal, and Colloidal Stability of VB_2 Nanoparticles. *Chem. Mater.*, 2015, **27**, P. 5106–5115.
- [33] Terlan B., Levin A.A., Börrnert F., Zeisner J., Kataev V., Schmidt M., Eychmüller A. A Size-Dependent Analysis of the Structural, Surface, Colloidal, and Thermal Properties of $\text{Ti}_{1-x}\text{B}_2$ ($x = 0.03\text{--}0.08$) Nanoparticles. *Eur. J. Inorg. Chem.*, 2016, **6**, P. 3460–3468.
- [34] Langford L., Cernik R. J., Louer D. The Breadth and Shape of Instrumental Line Profiles in High-Resolution Powder Diffraction. *J. Appl. Phys.*, 1991, **24**, P. 913–919.
- [35] Scherrer P. Bestimmung der Grösse und der inneren Struktur von Kolloidteilchen mittels Röntgenstrahlen. *Nachr. Königl. Ges. Wiss. Göttingen.*, 1918, **26**, P. 98–100. (in German)
- [36] Stokes A.R., Wilson A.J.C. The diffraction of X-rays by distorted crystal aggregates. *Proc. Phys. Soc. London*, 1944, **56**, P. 174–181.

Submitted 26 October 2023; revised 20 November 2023; accepted 5 December 2023

Information about the authors:

Makariy S. Lomakin – Ioffe Institute, 26, Politekhnicheskaya St., 194021, St. Petersburg, Russia; St. Petersburg Electrotechnical University “LETI”, 5, Professor Popov St., 197376, St. Petersburg, Russia; ORCID 0000-0001-5455-4541; lomakinmakariy@gmail.com

Olga V. Proskurina – Ioffe Institute, 26, Politekhnicheskaya St., 194021, St. Petersburg, Russia; St. Petersburg State Institute of Technology, 26, Moskovsky Ave., 190013, St. Petersburg, Russia; ORCID 0000-0002-2807-375X; proskuri-naov@mail.ru

Aleksandr A. Levin – Ioffe Institute, 26, Politekhnicheskaya St., 194021, St. Petersburg, Russia; ORCID 0000-0001-9258-3204; aleksandr.a.levin@mail.ioffe.ru

Vladimir N. Nevedomskiy – Ioffe Institute, 26, Politekhnicheskaya St., 194021, St. Petersburg, Russia; ORCID 0000-0002-7661-9155; nevedom@mail.ioffe.ru

Conflict of interest: the authors declare no conflict of interest.

Numerical model of temperature-dependent thermal conductivity in $M_{1-x}R_xF_{2+x}$ heterovalent solid solution nanocomposites where M stands for alkaline-earth metals and R for rare-earth metals

Pavel A. Popov¹, Alexander V. Shchelokov¹, Pavel P. Fedorov²

¹Petrovsky Bryansk State University, Bryansk, Russia

²Prokhorov General Physics Institute of the Russian Academy of Sciences, Moscow, Russia

Corresponding author: Pavel P. Fedorov, ppfedorov@yandex.ru

ABSTRACT We propose a mathematical model to fit the temperature-dependent thermal conductivity of $M_{1-x}R_xF_{2+x}$ heterovalent solid solutions where M stands for alkaline-earth metals and R for rare-earth metals. These solid solutions experience composition-driven transition from the crystal-like to glass-like behavior of thermal conductivity. When tested on $Ca_{1-x}Yb_xF_{2+x}$ solid solutions, the model showed a potential for use with an option for further improvements.

KEYWORDS thermal conductivity, thermal resistance, temperature dependence, solid solution, mathematical model

FOR CITATION P. A. Popov, A. V. Shchelokov, P. P. Fedorov Numerical model of temperature-dependent thermal conductivity in $M_{1-x}R_xF_{2+x}$ heterovalent solid solution nanocomposites where M stands for alkaline-earth metals and R for rare-earth metals. *Nanosystems: Phys. Chem. Math.*, 2024, **15** (2), 255–259.

1. Introduction

Heat transfer in solids is related to many diverse factors, including the crystal structure, structure perfection and symmetry, chemical composition, temperature, and some others. Accordingly, extant theoretical models used to fit the behavior of the thermal conductivity coefficient are intricate and ineffective (see, e.g., [1–6]). These models are frequently far from providing good fits even for structurally simple and perfect single crystals. Especially serious problems arise in the mathematical description of thermal conductivity in solid solutions with heterovalent ion substitutions.

Rare-earth (R) fluoride solid solutions in fluorite matrices, $M_{1-x}R_xF_{2+x}$ (where $M = Ca, Sr, Ba, Cd, \text{ or } Pb$), are some types of nanocomposites [7]. Association of oppositely charged point defects generates nanosized defect clusters in these solid solutions; as the rare-earth doping level (x) increases, percolation of defect areas occurs. What we call an “*anti-glass*” is thus formed, that is, a material where the short-range order is destroyed while the long-range order intrinsic to the fluorite structure is preserved [7]. The R_6F_{36} associates are typical clusters of defects embedded in the fluorite lattice with the replacement of the corresponding fragments M_6F_{32} of the crystal lattice. The size of these associates is about 1.5 nm. Each cluster is surrounded by a deformation zone. This evolution of the defect structure brings about a radical change in physical properties of crystals. A solid solution has its thermal conductivity decreasing dramatically in response to increasing rare-earth concentration; ultimately, the material becomes a heat insulator. The thermal conductivity coefficient $k(T)$ changes its temperature-dependent trend from that typical of crystals with a low-temperature peak to a glass-like monotone curve with k ascending as temperature rises.

There is now a significant amount of experimental thermal conductivity data for $M_{1-x}R_xF_{2+x}$ fluoride solid solutions where M stands for Ca, Sr, or Ba and R for rare-earth elements (see, e.g., [8–12]). When $M = Ca$, the transition from single crystals to anti-glass nanocomposites is particularly clear-cut because of the greatest difference in weight between calcium ions and substituent ions R^{3+} .

Liu et al. [13, 14] proposed a numerical model to fit the temperature-dependent thermal conductivity in $M_{1-x}R_xF_{2+x}$ solid solutions. This is a synthetic model combining Gaumé et al.’s model for the prediction of thermal conductivity in pure and doped insulating crystals [6] and a simple third-order polynomial for the thermal conductivity coefficient of an amorphous material. The correlation relation of Liu et al.’s model [13] is

$$k = A\beta\sqrt{\frac{k_0}{d}} \cdot \arctan\left(\frac{\sqrt{k_0d}}{\beta}\right) + (1 - A)(BT + CT^3), \quad (1)$$

where A is a parameter related to the crystal-like heat transfer behavior, β is a dopant-dependent parameter related to the non-crystalline heat transfer behavior, k_0 is the thermal conductivity coefficient of an undoped crystal, d is the dopant concentration, and B and C are the factors of the polynomial for the thermal conductivity coefficient of an amorphous material.

It is evidently an interesting and promising idea to sum-up the terms relating to crystalline and amorphous states. However, the summing-up of thermal conductivity coefficients may have physical meaning only when the heat flow passes in the sample *along parallel* dislike layers that have differing properties. The presence of diverse phonon scattering centers in solid solutions makes it more appropriate to consider the sequential passage of heat flow *through* areas with different thermal resistances. The Matthiessen rule [15] of the additivity of specific resistances in the approximation of independence of scattering centers is fulfilled both for the electric current and for the heat flow [16].

Figure 1 illustrates the results we obtained when applying equation (1) to some $\text{Ca}_{1-x}\text{Yb}_x\text{F}_{2+x}$ solid solution samples [8]. We set $k_0 = 3193T^{-1}$, as Liu et al. did [13]. Liu et al. [13] obtained this simple expression as a fit to the $k(T)$ data set for the $\text{Ca}_{1-x}\text{Yb}_x\text{F}_{2+x}$ sample that had the least dopant level ($x = 0.01$ mol %) taken from our data [8]. The fitted curves and datapoints show an appreciable divergence in the dopant concentration range from 0.7 to 9 mol %. The measured $k(T)$ values exhibit like trends for the 0.7, 1, 1.5, and 3 % rare-earth samples, with temperature-diffuse $k(T)$ peaks typical of appreciably disordered crystal structures. However, not only do the fitted curves deviate strongly from the datapoints, but their runs are also different: for the 0.7, 1, and 1.5 % rare-earth samples, the fitted $k(T)$ curves decline throughout the range of temperatures studied (50 – 300 K), while for the 3 % sample the curve is typical of an amorphous material.

Liu et al.'s model [13] gave a satisfactory fit of temperature-dependent thermal conductivity coefficient $k(T)$ data for $\text{Ca}_{1-x}\text{Yb}_x\text{F}_{2+x}$ solid solution crystals [8] only when equation (1) was used in “three stages”. For low dopant concentration levels, Liu et al. [13] confined the model to the first term of the expression, which relates to crystalline thermal conductivity. For moderate dopant concentrations, the entire temperature range was divided into a pair of areas. In the

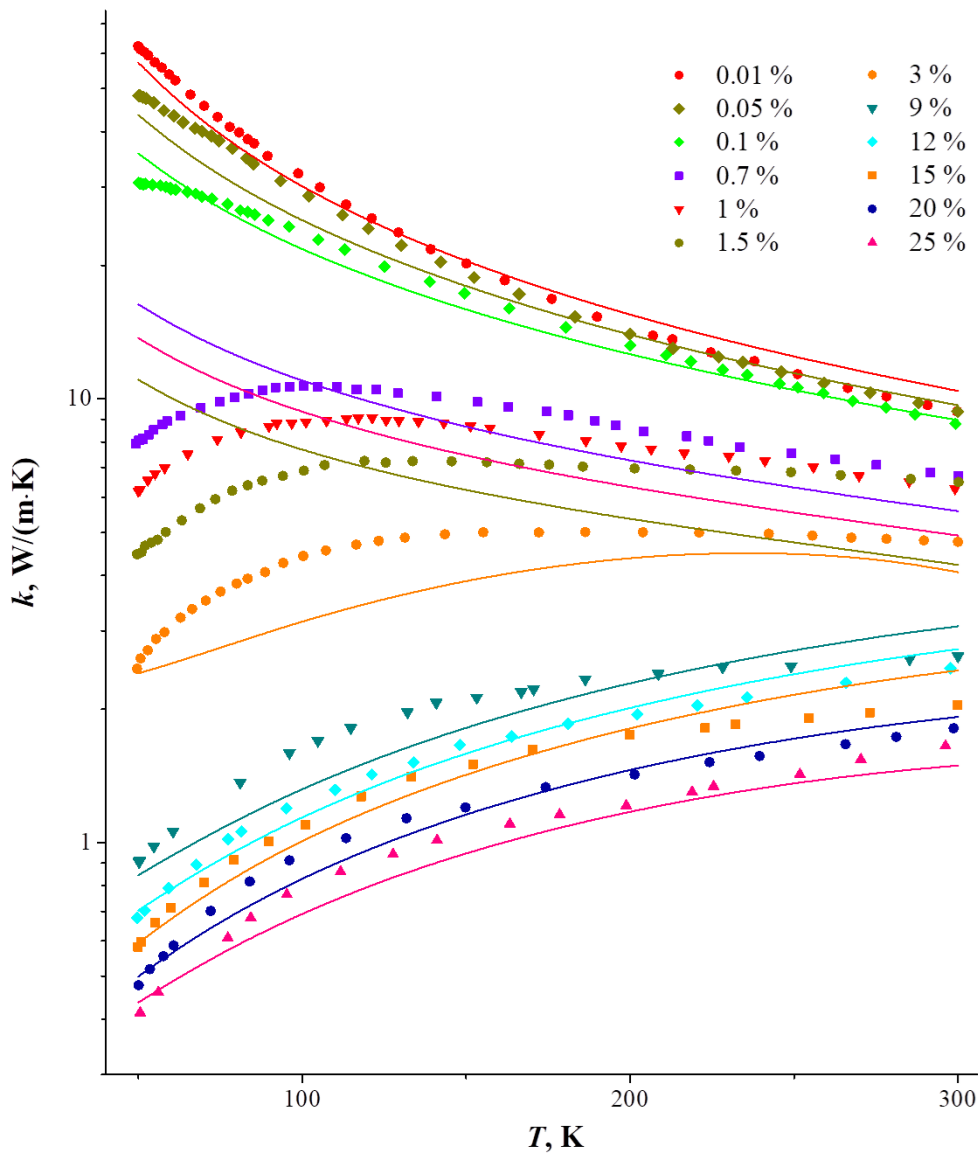


FIG. 1. Temperature-dependent thermal conductivity coefficient in $\text{Ca}_{1-x}\text{Yb}_x\text{F}_{2+x}$ solid solution single crystals: symbols refer to measured data points [8], and lines are fitted curves calculated by model (1)

range 50 – 100 K, the rise in thermal conductivity coefficient was fitted by the above polynomial, while after $k(T)$ passed the peak temperature, the whole equation (1) was applied. For high dopant concentrations, this equation was applied to fit the increasing thermal conductivity over the entire temperature range (50 – 300 K) with low values of the parameter A .

Our goal was to modify Liu et al.'s model [13] using Matthiessen's rule.

2. Results and discussion

The model we proposed and used to calculate the temperature-dependent thermal conductivity coefficient for $M_{1-x}R_xF_{2+x}$ heterovalent solid solutions is as follows

$$\frac{1}{k} = \frac{1 - A}{\beta \sqrt{\frac{k_0}{d}} \cdot \arctan\left(\frac{\sqrt{k_0 d}}{\beta}\right)} + \frac{A}{D + BT + CT^2}, \quad (2)$$

where A is the amorphous specific resistance contribution; β is the parameter depending on the dopant; k_0 is the thermal conductivity coefficient of an undoped crystal; d is the dopant concentration; and D , B and C are factors of the polynomial for the amorphous thermal conductivity coefficient.

Keeping in mind that the range of temperatures we studied starts at 50 K, which is not a very low temperature, and the heat capacity, which directly influences the thermal conductivity coefficient, rises more slowly than by the $C \sim T^3$ law, we lowered the polynomial order to the second order. Also, we added the zero order factor D , whose meaning is the "remnant" thermal conductivity when the $k(T)$ is extrapolated to $T = 0$. Liu et al. [13] took k_0 as $k_0 = 3193T^{-1}$. Liu et al. [13] obtained this simple expression as a fit to the $k(T)$ data set for the $\text{Ca}_{1-x}\text{Yb}_x\text{F}_{2+x}$ sample that had the least dopant level ($x = 0.01$ mol %) taken from our data [8]. However, the $k \sim T^{-1}$ law is approximately fulfilled only within a limited (near-room) temperature range, and only for some compounds. Without making serious corrections and complications, we selected $k_0 = 4575T^{-1.08}$ with the least deviations from experimental data, similar to the expression Liu et al. used [13]. As the parameter β , we took $\beta = 0.20$, which slightly differs from the $\beta = 0.16$ in Liu et al.'s model [13].

Figure 2 shows the fits by our model (2) for the entire dataset comprised of the $k(T)$ values we measured for twenty $\text{Ca}_{1-x}\text{Yb}_x\text{F}_{2+x}$ solid solution compositions. In all cases, model (2) was used in the same manner, in the same form, and for the entire range of temperatures studied (50 – 300 K). One can observe a very close match of the behaviors of measured and fitted $k(T)$ curves over the entire concentration range.

As for the parameter A , its values that we selected show a concentration dependence little differing from the one described by a log function with a constant term (Fig. 3).

3. Conclusion

Altogether, our mathematical model has shown a good ability to fit the temperature-dependent behavior of the thermal conductivity coefficient in heterovalent fluoride solid solutions, with their diversity, which solid solutions experience a composition-driven transition from the crystal-like to glass-like behavior of thermal conductivity. When tested for $\text{Ca}_{1-x}\text{Yb}_x\text{F}_{2+x}$ solid solution, the model has shown a promise for use with an option for further improvements.

In the future, we intend to correct the expressions for the model parameters and test the model for a wider range of similar compounds, as well as to analyze the model parameters depending on the type of compound.

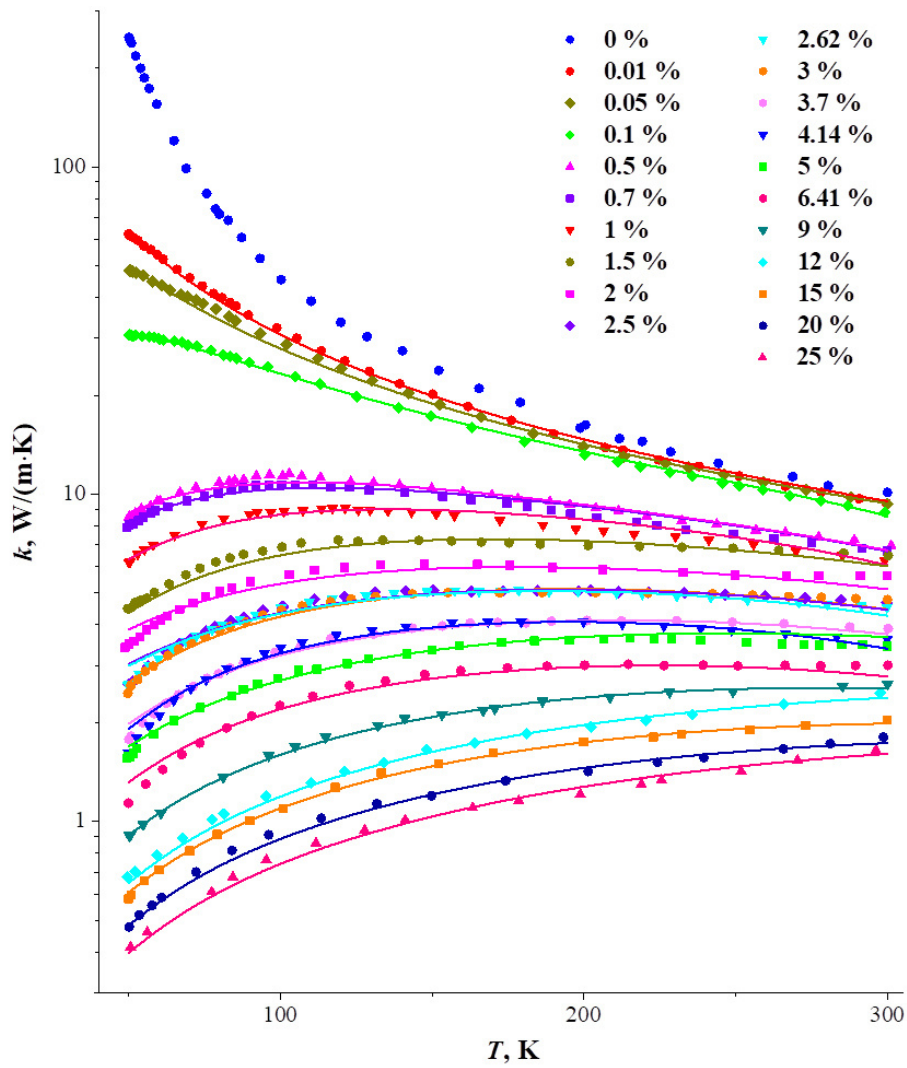


FIG. 2. Temperature-dependent thermal conductivity coefficient for $\text{Ca}_{1-x}\text{Yb}_x\text{F}_{2+x}$ solid solution single crystals: symbols refer to measured data points [8], and lines are fitted curves calculated by model (2)

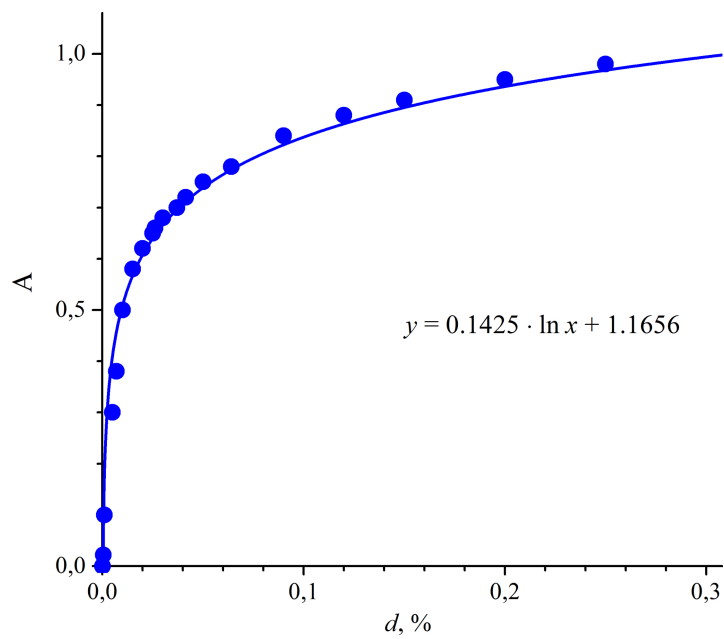


FIG. 3. Parameter A versus YbF_3 concentration in $\text{Ca}_{1-x}\text{Yb}_x\text{F}_{2+x}$ solid solution

References

- [1] Peierls R. Zur kinetischen theorie der wärmeleitung in kristallen. *Annalen der Physik*, 1929, **3**, P. 1055–1101.
- [2] Klemens P.G. Thermal conductivity and lattice vibrational modes. *Solid State Phys.*, 1958, **7**, P. 1–98.
- [3] Callaway J. Model for lattice thermal conductivity at low temperatures. *Phys. Rev.*, 1959, **113** (4), P. 1046–1051.
- [4] Callaway J., Baeyer H.C. Effect of point imperfections on lattice thermal conductivity. *Phys. Rev.*, 1960, **120** (4), P. 1149–1154.
- [5] Berman R. *Thermal Conduction in Solids*. Clarendon Press, Oxford, 1976.
- [6] Gaumé R., Viana B., Vivien D., Roger J.-P., Fournier D. A simple model for the prediction of thermal conductivity in pure and doped insulating crystals. *Appl. Phys. Lett.*, 2003, **83** (7), P. 1355–1358.
- [7] Kuznetsov S.V., Osiko V.V., Tkatchenko E.A., Fedorov P.P. Inorganic nanofluorides and related nanocomposites. *Russ. Chem. Rev.*, 2006, **75** (12), P. 1065–1082.
- [8] Popov P.A., Fedorov P.P., Kuznetsov S.V., Konyushkin V.A., Osiko V.V., Basiev T.T. Thermal conductivity of single crystals of $\text{Ca}_{1-x}\text{Yb}_x\text{F}_{2+x}$ solid solutions. *Doklady Physics*, 2008, **53** (4), P. 198–200.
- [9] Popov P.A., Fedorov P.P., Kuznetsov S.V., Konyushkin V.A., Osiko V.V., Basiev T.T. Thermal conductivity of single crystals of $\text{Ba}_{1-x}\text{Yb}_x\text{F}_{2+x}$. *Doklady Physics*, 2008, **53** (7), P. 353–355.
- [10] Popov P.A., Fedorov P.P., Reiterov V.M., Garibin E.A., Demidenko A.A., Mironov I.A., Osiko V.V. Thermal conductivity of single crystals of $\text{Ca}_{1-x}\text{Er}_x\text{F}_{2+x}$ and $\text{Ca}_{1-x}\text{Tm}_x\text{F}_{2+x}$ solid solutions. *Doklady Physics*, 2012, **57** (3), P. 97–99.
- [11] Popov P.A., Fedorov P.P., Konyushkin V.A. Heat Conductivity of $\text{Ca}_{1-x}\text{R}_x\text{F}_{2+x}$ (R= La, Ce, or Pr; $0 \leq x \leq 0.25$) Heterovalent Solid Solutions. *Crystallogr. Rep.*, 2015, **60** (5), P. 744–748.
- [12] Popov P.A., Fedorov P.P. *Thermal conductivity of fluoride optical materials*. Bryansk: “Desyatochka” Group of Companies, 2012. (in Russian)
- [13] Liu K., Bian G., Zhang Z., Ma F., Su L. Modelling and analyzing the glass-like heat transfer behavior of rare-earth doped alkaline earth fluoride crystals. *CrystEngComm*, 2022, **24**, 6468.
- [14] Liu K., Bian G., Zhang Z., Ma F., Su L. Simulation and demonstration of glass-like heat transfer equations in rare-earth doped alkaline earth fluoride crystals. *Chinese J. of Physics*, 2024, **88**, P. 584–593.
- [15] Matthiessen A., Vogt C. On the Influence of Temperature on the Electric Conducting-Power of Alloys. *Philosophical Transactions of the Royal Society of London*, 1864, **154**, P. 167–200.
- [16] Lifshits I.M. *Electron Theory of Metals*. Springer, 1973.

Submitted 22 February 2024; revised 9 March 2024; accepted 12 March 2024

Information about the authors:

Pavel A. Popov – Petrovsky Bryansk State University, 14 Bezhitskaya str., Bryansk, 241036 Russia; ORCID 0000-0001-7555-1390; tfbgubry@mail.ru

Alexander V. Shchelokov – Petrovsky Bryansk State University, 14 Bezhitskaya str., Bryansk, 241036 Russia; ORCID 0009-0001-4090-2506; alexandershchelokov@mail.ru

Pavel P. Fedorov – Prokhorov General Physics Institute of the Russian Academy of Sciences, 38 Vavilova str., Moscow, 119991 Russia; ORCID 0000-0002-2918-3926; ppfedorov@yandex.ru

Conflict of interest: the authors declare no conflict of interest.

Synthesis of redox-active $\text{Ce}_{0.75}\text{Bi}_{0.15}\text{Tb}_{0.1}\text{F}_3$ nanoparticles and their biocompatibility study *in vitro*

Nikita N. Chukavin^{1,a}, Danil D. Kolmanovich^{1,b}, Arina D. Filippova^{2,c}, Maria A. Teplonogova^{2,d}, Vladimir K. Ivanov^{2,e}, Anton L. Popov^{1,f}

¹Institute of Theoretical and Experimental Biophysics of the Russian Academy of Sciences, 142290, Russia

²Kurnakov Institute of General and Inorganic Chemistry of the Russian Academy of Sciences, Moscow, 119991, Russia

^achukavinnik@gmail.com, ^bkdd100996@mail.ru, ^carifilippova@yandex.ru, ^dm.teplonogova@gmail.com, ^evan@igic.ras.ru, ^fantonpopovleonid@gmail.com

Corresponding author: Anton L. Popov, antonpopovleonid@gmail.com

ABSTRACT Cerium fluoride (CeF_3) nanoparticles (NPs), being a unique nanozyme and redox-active nanomaterial, show high promise for advanced biomedical applications. Doping of CeF_3 NPs with the other chemical elements allow one to increase their catalytic activity, impart them new functional properties, and also to increase the efficiency of their interaction with ionizing radiation, which is important in the development of novel nanoradiosensitizers. In this article, we synthesized citrate-stabilized $\text{Ce}_{0.75}\text{Bi}_{0.15}\text{Tb}_{0.1}\text{F}_3$ nanoparticles, which demonstrate high colloidal stability, have good luminescent properties and radiation-induced redox activity. Cytotoxicity analysis of $\text{Ce}_{0.75}\text{Bi}_{0.15}\text{Tb}_{0.1}\text{F}_3$ NPs using normal and tumor cells *in vitro* showed the sensitivity of B16/F10 and EMT6 tumor cell lines to the nanoparticles at high concentrations (0.5 – 1 mM). Obtained experimental results allow us to consider $\text{Ce}_{0.75}\text{Bi}_{0.15}\text{Tb}_{0.1}\text{F}_3$ nanoparticles as a possible platform for the development of a new class of nanoradiosensitizers for radiation therapy purposes.

KEYWORDS nanoparticles, cytotoxicity, fluoride, cerium

ACKNOWLEDGEMENTS The work was supported by the Russian Science Foundation (project no. 22-73-10231, <https://rscf.ru/project/22-73-10231/>).

FOR CITATION Chukavin N.N., Kolmanovich D.D., Filippova A.D., Teplonogova M.A., Ivanov V.K., Popov A.L. Synthesis of redox-active $\text{Ce}_{0.75}\text{Bi}_{0.15}\text{Tb}_{0.1}\text{F}_3$ nanoparticles and their biocompatibility study *in vitro*. *Nanosystems: Phys. Chem. Math.*, 2024, **15** (2), 260–267.

1. Introduction

Nanocrystalline materials based on cerium(IV) oxide are currently widely used in various fields of biomedicine due to their unique catalytic properties and high degree of biocompatibility [1–4]. Due to their redox activity and the ability to mimic the activity of various enzymes, CeO_2 nanoparticles have become the most promising inorganic nanozymes [5–8]. Catalytic activity of these nanoparticles is based on the unique reversible $\text{Ce}^{3+}/\text{Ce}^{4+}$ transition, which determines its role as prooxidant and reactive oxygen species (ROS) generator at low pH values in tumor cells, or as an antioxidant and ROS inactivator under normal physiological pH conditions [9]. Meanwhile, earlier we have demonstrated for the first time the catalytic activity of CeF_3 nanoparticles, the mechanism of action of which differs from that of CeO_2 nanoparticles. We have shown that CeF_3 NPs demonstrate selective cytotoxicity to tumor cells, inhibiting their proliferative activity and DNA repair under X-ray irradiation [10]. Also, we have reported the ability of CeF_3 NPs to stimulate planarian regeneration [11] and to act as an effective radioprotector under X-ray irradiation [12]. In a number of studies, authors have shown that doping of REE fluorides provides them with unique properties [13–17]. Particularly, additional chemical modification of CeF_3 NPs provides them with new functional properties. For instance, doping of CeF_3 crystal lattice with Yb and Tm ions allows for the formation of theranostic luminescent systems with enhanced upconversion ($\text{CeF}_3:\text{Yb}$, $\text{Tm}@\text{SiO}_2\text{-CD36/OPN}$) [18]. Wang et al. synthesized biocompatible $\text{CeF}_3:\text{Tb}@\text{LaF}_3$ NPs with pronounced luminescent properties [19], which could be used for bioimaging, biolabeling, biodetection and bioprobeing. $\text{Ce}_x\text{La}_{1-x}\text{F}_3$ NPs have been proposed for the use in nanoscintillator-photosensitizer systems, in which excitation of nanoparticles by ionizing irradiation leads to energy transfer to photosensitizer molecules, effectively combining the effects of radiation and photodynamic therapy [20].

Nanoparticle-based radioenhancement is considered as a promising approach to improve therapeutic effect of radiation therapy [21–23]. Mechanisms of nanoparticle-based radiosensitizers action can include: physical, chemical and

biological. Ionizing radiation leads to the ejection of secondary electrons which can interact with water, causing ROS generation. In turn, ROS interact with different components of the cell, including cell membrane, mRNA, DNA and, consequently, triggering cell death. Thus, the use of nanoparticles based on high-Z elements and on elements with low ionization potential can significantly increase the efficiency of radiation therapy [24–26]. In particular, the drug NBTXR3/Hensify® (Nanobiotix, Paris, France) based on hafnium oxide has already been approved and is being used [27], and the drug AGuIX® (NH TherAguix, Lyon, France) based on gadolinium is undergoing clinical trials [28]. Thus, synthesis and comprehensive analysis of new theranostic agents for radiotherapy is an urgent task.

In this study, we have synthesized citrate-stabilized $Ce_{0.75}Bi_{0.15}Tb_{0.1}F_3$ nanoparticles, analyzed their physico-chemical characteristics and studied their cytotoxicity to normal and tumor cells *in vitro*.

2. Materials and methods

2.1. Synthesis scheme

For the synthesis of $Ce_{0.75}Bi_{0.15}Tb_{0.1}F_3$ colloidal solutions the following substances were used: $Ce(NO_3)_3 \cdot 6H_2O$ (puriss., Lanhit), $Tb(NO_3)_3 \cdot 6H_2O$ (puriss., Lanhit), $Bi(NO_3)_3 \cdot 5H_2O$ (pur., Reachem), HF (puriss. spec., Sigma Tec), ammonium citrate dibasic (puriss., Sigma-Aldrich), isopropanol (puriss. spec., Chimmed), ethylene glycol (puriss., Sigma Aldrich). Samples of rare earth elements (REE) nitrates (1.628 g $Ce(NO_3)_3 \cdot 6H_2O$, 0.228 g $Tb(NO_3)_3 \cdot 6H_2O$, 0.363 g $Bi(NO_3)_3 \cdot 5H_2O$) were suspended in 30 mL of ethylene glycol upon heating to 60 °C and intense stirring on a magnetic stirrer. 0.885 mL of 40 % HF was dissolved in 150 mL of isopropanol. The obtained solution was added drop by drop to mixed REE nitrates solution with intensive stirring until the suspension was formed. The precipitate was separated by filtration through a paper filter (2 – 3 μm), washed with isopropanol, placed in an oven for 30 – 60 minutes at 50 °C to remove isopropanol. Wet gel-like precipitate was re-dispersed in 100 mL of deionized water. Ammonium citrate solution (1.134 g of ammonium citrate in 100 mL of deionized water) was added to the resulting suspension with intense stirring. The resulting sol was mixed at 30 – 35 °C until remnant isopropanol was removed. The concentration of the resulting sol was 7.6 mM.

2.2. Characterization of $Ce_{0.75}Bi_{0.15}Tb_{0.1}F_3$ NPs

Powder X-ray diffraction analysis (XRD) of the samples was carried out on a Haoyuan DX-2700BH diffractometer ($CuK\alpha$ radiation, $\lambda = 1.54184 \text{ \AA}$) in the range of 5 – 60° 2θ with a step of 0.02° and a shutter speed of 1 sec/step. The diffractograms were indexed using the ICDD PDF2 database. The concentration of the $Ce_{0.75}Bi_{0.15}Tb_{0.1}F_3$ NPs sols was determined gravimetrically. The corundum crucibles pre-annealed at 900 °C for 2 hours were weighted on analytical scales to establish their initial weight. Then 3 mL of sol was placed in each crucible and heated in a muffle furnace at 900 °C for 2 hours with slow heating ($\sim 3 \text{ }^\circ/\text{min}$). After cooling to room temperature, the crucibles were weighted. The weight of the dry residue of the annealing product was determined and the concentration of the initial sols was calculated. The study of the elemental composition of the obtained materials was carried out using energy dispersive X-ray spectroscopy (EDX) using a Tescan Amber GMH microscope equipped with an Ultim MAX detector with 100 mm² active area (Oxford Instruments) at an accelerating voltage of 20 kV. EDX data were processed using the AZtec software (5.0). An UV5 Nano spectrophotometer (Mettler Toledo, Columbus, Ohio, USA) was used to measure $Ce_{0.75}Bi_{0.15}Tb_{0.1}F_3$ NPs sols absorbance in the UV-visible range. Measurements were carried out in the wavelength range from 200 to 600 nm in 0.1 nm increments. The sizes and ζ -potentials of nanoparticles were determined by dynamic and electrophoretic light scattering at 25 °C using a BeNano analyzer (BetterSize, Dandong, China).

2.3. Cell culture

The experiments were performed using 5 types of cell cultures: B16F10 (murine melanoma), EMT6/P (murine adenocarcinoma), MNNG/HOS (human osteosarcoma), MCF-7 (human adenocarcinoma), NCTC L929 (murine fibroblasts) obtained from Theranostics and Nuclear Medicine Laboratory cryostorage (ITEB RAS, Pushchino, Russia). The cells were cultured in a DMEM/F12 (1:1) culture medium containing 50 $\mu g/mL$ of penicillin, 50 $\mu g/mL$ of streptomycin, 10 % of fetal bovine serum (FBS) and 1 % of L-glutamine at a temperature of 37 °C in a 95 % humidity atmosphere containing 95 % air and 5 % CO₂. The cells were seeded on 96-well plates at a density of 25000 cells/cm². 6 hours after cell attachment the culture medium was then replaced with a fresh culture medium containing different concentrations of $Ce_{0.75}Bi_{0.15}Tb_{0.1}F_3$ NPs (0.1 – 1 mM). Cells from the control groups were cultured without the addition of $Ce_{0.75}Bi_{0.15}Tb_{0.1}F_3$ NPs.

2.4. MTT assay

Cell viability was assessed using MTT assay which is based on the reduction of a yellow tetrazolium salt (3-[4,5-dimethylthiazole-2-yl]-2,5-diphenyl tetrazolium bromide, MTT) to insoluble formazan crystals having purple color. After 48 hours of cultivation, 0.5 mg/mL MTT reagent solution, dissolved in culture medium without FBS, was added to the wells. The optical density of the formed formazan was measured at $\lambda = 570 \text{ nm}$ using an INNO-S plate reader (LTEK, Korea).

2.5. Live/Dead assay

The cytotoxic effect of $\text{Ce}_{0.75}\text{Bi}_{0.15}\text{Tb}_{0.1}\text{F}_3$ NPs was assessed using a Live/Dead assay. This method is based on measuring the percentage of dead cells to their total number after their incubation with $\text{Ce}_{0.75}\text{Bi}_{0.15}\text{Tb}_{0.1}\text{F}_3$ NPs. Cells were labeled via staining with a combination of the fluorescent dyes Hoechst 33342 (binds to DNA of all cells, $\lambda_{ex} = 350$ nm, $\lambda_{em} = 460$ nm) and propidium iodide (binds to DNA of dead cells, $\lambda_{ex} = 535$ nm, $\lambda_{em} = 615$ nm). After 24, 48, and 72 hours of incubation with nanoparticles, the culture medium was replaced with a mixture of Hoechst 33342 and propidium iodide in Hanks' buffer solution (PanEko, Moscow, Russia). After 15 min of incubation with dyes, the cells were washed three times with Hanks' buffer solution. Then, cells were photographed using a ZOE fluorescent imager (Bio-Rad, USA). ImageJ software was used to count the number of cells. Three different cell areas on the field were analyzed on three different microphotographs. Quantitative analysis results were presented as mean \pm SD.

2.6. Measuring of mitochondrial membrane potential

The mitochondrial membrane potential (MMP) was measured by staining cells with TMRE (tetramethylrhodamine, ethyl ester, ThermoFisher, Carlsbad, CA, USA) fluorescent dye followed by fluorescence microscopy analysis. After 24, 48, and 72 hours of incubation with nanoparticles, the culture medium was replaced with TMRE solution in Hanks' buffer (PanEko, Moscow, Russia). After 15 min of incubation with dye, the cells were washed three times with Hanks' buffer solution. Then, the cells were photographed using a ZOE fluorescent imager (Bio-Rad, USA). TMRE fluorescence intensity, which directly correlates with the MMP of cells, was measured using the ImageJ software. Three different areas on the field were analyzed on three different microphotographs. Quantitative analysis results were presented as mean \pm SD.

2.7. Statistical analysis

Three independent experiments with three independent repetitions for each $\text{Ce}_{0.75}\text{Bi}_{0.15}\text{Tb}_{0.1}\text{F}_3$ NPs concentration were performed. Experimental results were compared with untreated control. Statistical analysis was performed using the methods of variation statistics (ANOVA, Student's t-test). The mean values and the standard deviations (SD) were determined. The obtained data were processed using the GraphPad Prism 8.0 software.

3. Results and discussion

The scheme of $\text{Ce}_{0.75}\text{Bi}_{0.15}\text{Tb}_{0.1}\text{F}_3$ NPs synthesis is shown in Fig. 1a. EDX analysis confirms the elemental composition of the nanoparticles, where the peaks of cerium, bismuth and terbium are easily discernible (Fig. 1b). Quantitative EDX analysis revealed the following cation ratios: Ce : Bi : Tb = 79 : 14 : 7. Fig. 1c shows a fluorescence spectrum of the $\text{Ce}_{0.75}\text{Bi}_{0.15}\text{Tb}_{0.1}\text{F}_3$ NPs, Fig. 1d shows the UV-visible absorption spectrum of $\text{Ce}_{0.75}\text{Bi}_{0.15}\text{Tb}_{0.1}\text{F}_3$ NPs. The spectrum contains characteristic absorption peaks of Ce^{3+} ions (245 nm) and citric acid (225 nm), which confirms the presence of these components in the composition of nanoparticles. The diffraction pattern of $\text{Ce}_{0.75}\text{Bi}_{0.15}\text{Tb}_{0.1}\text{F}_3$ NPs corresponds well to the structure of CeF_3 (PDF2 card No. 8-45), however, due to the significant broadening of diffraction maxima, it is not possible to clarify the unit cell parameters (Fig. 1e). The significant broadening of diffraction maxima of $\text{Ce}_{0.75}\text{Bi}_{0.15}\text{Tb}_{0.1}\text{F}_3$ NPs confirms the small size of the nanoparticles. The distribution of the hydrodynamic diameters of $\text{Ce}_{0.75}\text{Bi}_{0.15}\text{Tb}_{0.1}\text{F}_3$ NPs in water indicates the polydispersity of these nanoparticles (PDI = 0.238) (Fig. 1f). Analysis of the ζ -potential of $\text{Ce}_{0.75}\text{Bi}_{0.15}\text{Tb}_{0.1}\text{F}_3$ NPs indicates the colloidal stability of the aqueous sol of these nanoparticles (ζ -potential -36 mV) (Fig. 1g).

Routine MTT assay was used to study $\text{Ce}_{0.75}\text{Bi}_{0.15}\text{Tb}_{0.1}\text{F}_3$ NPs cytotoxicity. The NAD(P)H-dependent cytosolic oxidoreductases activity measured during MTT assay is associated with the metabolic activity of cells, which, in turn, is one of the main indicators of cell viability [29]. According to the results of the study of the metabolic activity of B16F10, EMT6/P, MNNG/HOS, MCF-7, NCTC L929 cell cultures, the pronounced dose-dependent effect was revealed after 24 hours of coinubation of the cells with $\text{Ce}_{0.75}\text{Bi}_{0.15}\text{Tb}_{0.1}\text{F}_3$ NPs (Fig. 2). It was shown that the viability of B16/F10, EMT6/P, MNNG/HOS and MCF-7 cells decreased by 25 %, while NCTC L929 cells viability decreased by 50 % after 24 hours of incubation with $\text{Ce}_{0.75}\text{Bi}_{0.15}\text{Tb}_{0.1}\text{F}_3$ NPs at a 1 mM concentration. Moreover, the viability of B16/F10, EMT6/P and NCTC L929 cells decreased by 75 % after 72 hours of incubation with 1 mM $\text{Ce}_{0.75}\text{Bi}_{0.15}\text{Tb}_{0.1}\text{F}_3$ NPs. MCF-7 and MNNG/HOS cells were found to be the most resistant cell lines to cytotoxic effect of $\text{Ce}_{0.75}\text{Bi}_{0.15}\text{Tb}_{0.1}\text{F}_3$ NPs.

According to the measured live/dead cells ratios (Fig. 3), the pronounced cytotoxic effect of $\text{Ce}_{0.75}\text{Bi}_{0.15}\text{Tb}_{0.1}\text{F}_3$ NPs was revealed on EMT6/P, MCF-7 and NCTC L929 cell lines after 72 hours of incubation with these nanoparticles. This effect consisted in an increase in the percentage of dead cells. The maximum percentage of dead cells was about 50 % at a $\text{Ce}_{0.75}\text{Bi}_{0.15}\text{Tb}_{0.1}\text{F}_3$ NPs concentration of 1 mM. However, nanoparticles showed significantly lower cytotoxicity to B16/F10 and MNNG/HOS cells (20 % cell death). Thus, it can be concluded that the cell viability decrease caused by $\text{Ce}_{0.75}\text{Bi}_{0.15}\text{Tb}_{0.1}\text{F}_3$ NPs does not necessarily lead to the development of apoptosis and cell death, as it has been shown for mouse melanoma cells. The revealed differences in the behavior of the cells may also be due to the different efficiency of endocytosis of this type of nanoparticles, which directly correlates with their effect on cell viability.

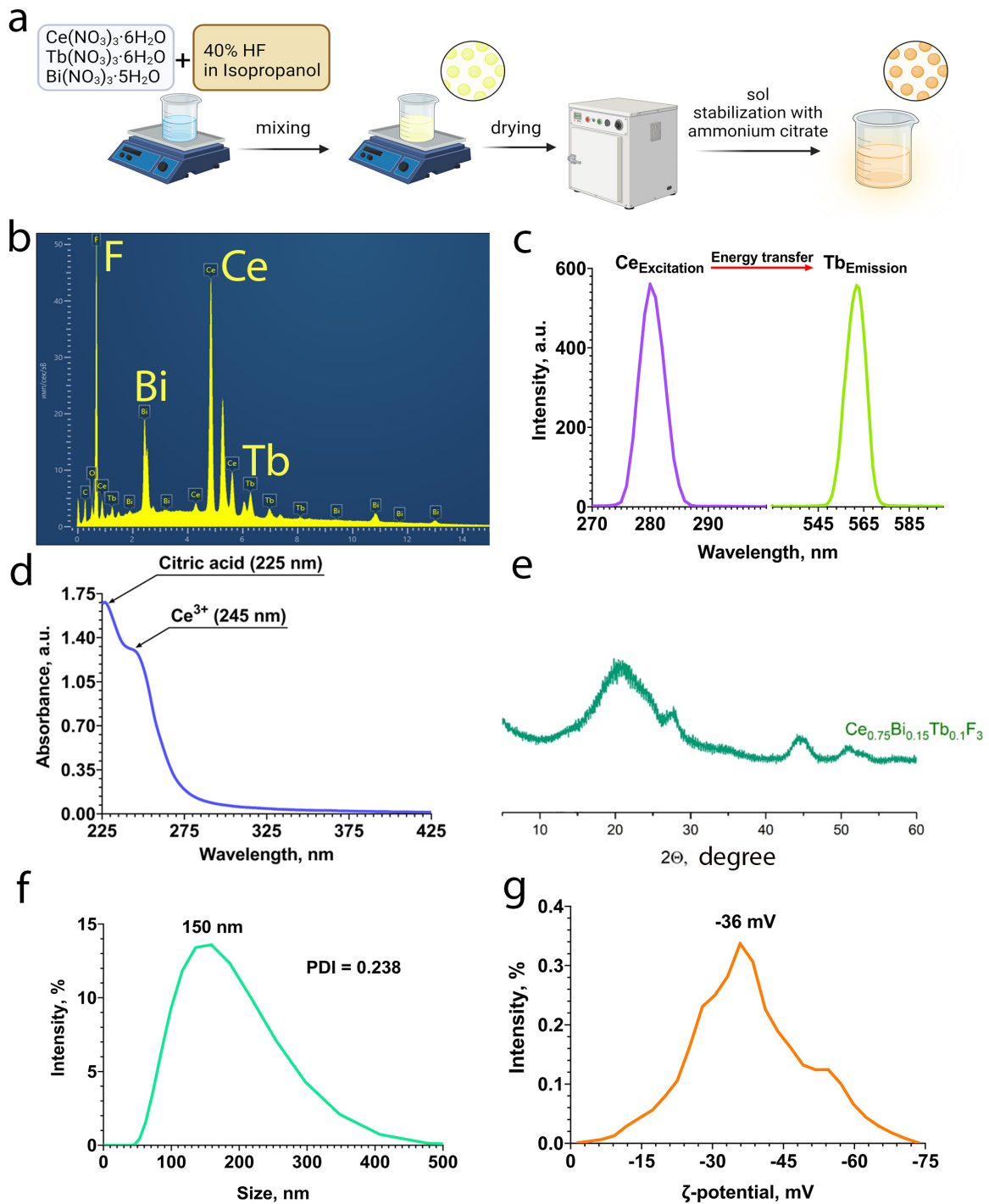


FIG. 1. Synthesis scheme (a), EDX spectrum (b), fluorescence spectrum (c), UV-visible absorbance spectrum (d), diffraction pattern (e), hydrodynamic diameter distribution (f) and ζ -potential distribution (g) of the $Ce_{0.75}Bi_{0.15}Tb_{0.1}F_3$ NPs

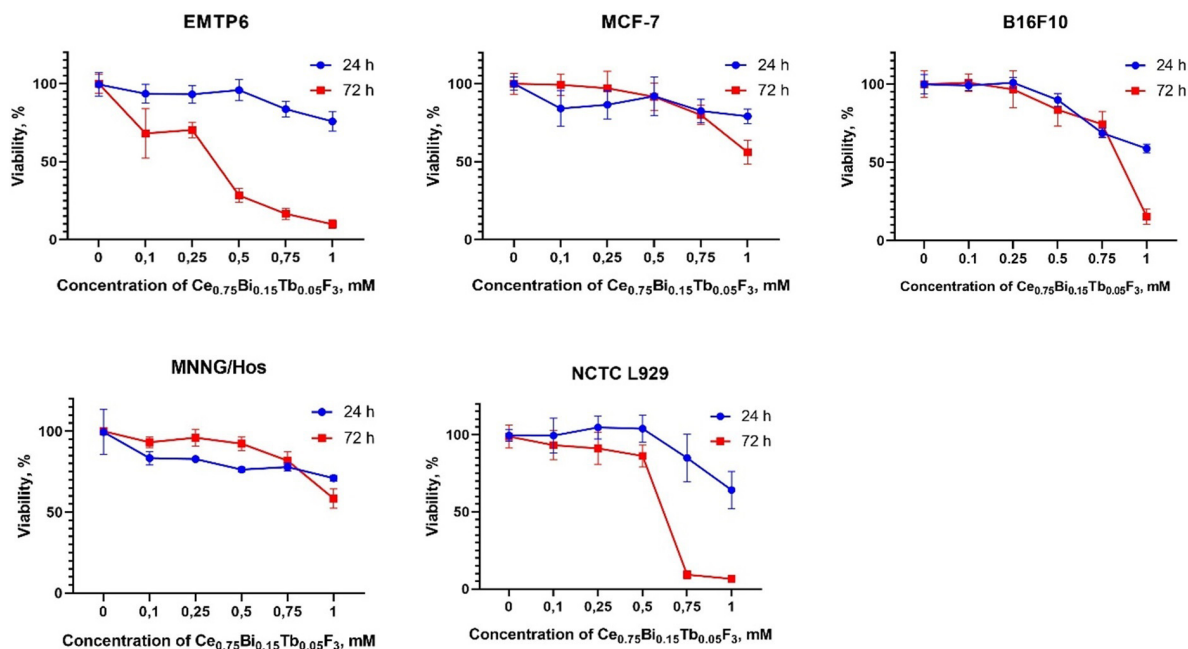


FIG. 2. Viability of cancer (B16F10, EMTP6, MCF-7, MNNG/HOS) and normal (NCTC L929) cells according to MTT assay. The cells were incubated with $Ce_{0.75}Bi_{0.15}Tb_{0.05}F_3$ NPs (0.1–1 mM) for 24 and 72 hours

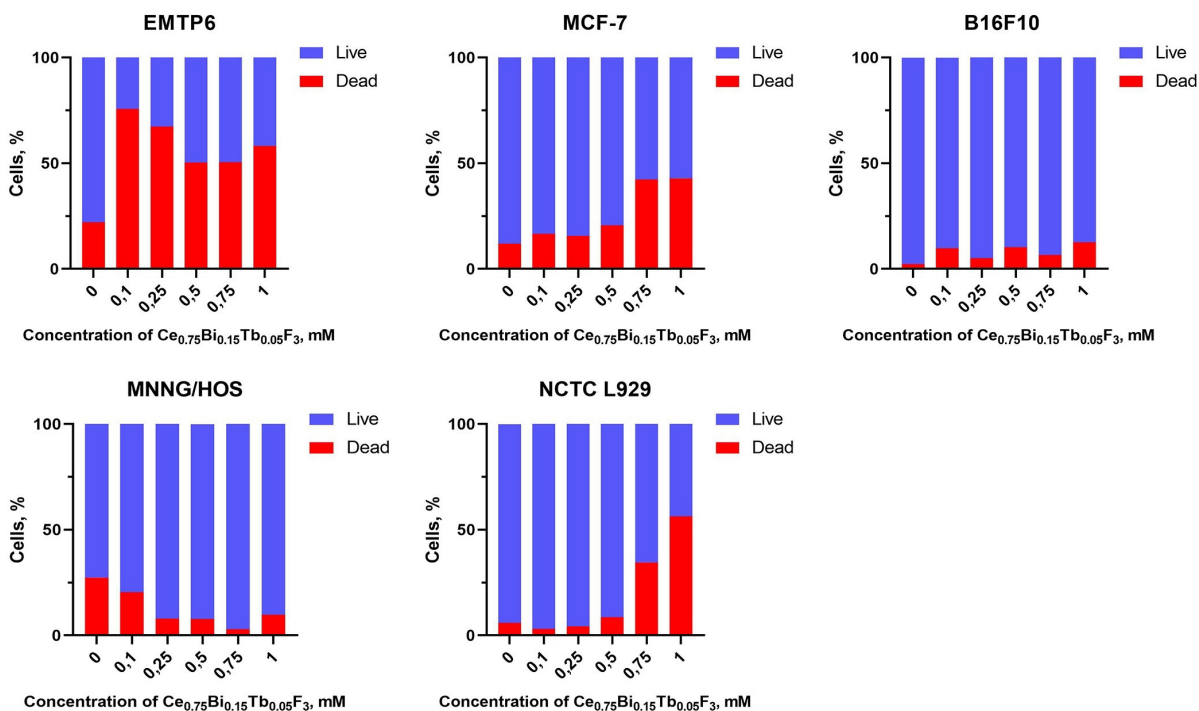


FIG. 3. Ratios of live/dead cancer (B16/F10, EMTP6/P, MCF-7, MNNG/HOS) and normal (NCTC L929) cells after 72 hours of incubation with $Ce_{0.75}Bi_{0.15}Tb_{0.05}F_3$ NPs (0.1 – 1 mM)

Using fluorescent tetramethylrhodamine (TMRE) dye, which is accumulated in mitochondria in a voltage-dependent manner, we analyzed the mitochondrial membrane potential (MMP) of cell cultures after 72 hours of incubation with $Ce_{0.75}Bi_{0.15}Tb_{0.1}F_3$ NPs (Fig. 4). The significant decrease of MMP in the presence of nanoparticles was shown for human osteosarcoma MMNG/HOS and human adenocarcinoma MCF-7 cells. In addition, the pronounced cytotoxic effect of $Ce_{0.75}Bi_{0.15}Tb_{0.1}F_3$ NPs in the form of a dose-dependent MMP decrease was revealed for normal murine fibroblasts. Oppositely, MMP of murine melanoma B16/F10 cells did not change significantly after incubation with nanoparticles in the entire studied concentrations range (0.1 – 1 mM). The redox activity of cerium-containing nanoparticles can lead to mitochondrial dysfunction in tumor cells. In particular, Aplak et al. demonstrated, using human melanoma A375 cells, that cerium dioxide nanoparticles initiate an increase of mitochondrial ROS levels accompanied by an increase in mitochondrial thiol oxidation [30]. Also, the authors revealed changes in mitochondrial bioenergetics and crista morphology that led to the death of tumor cells.

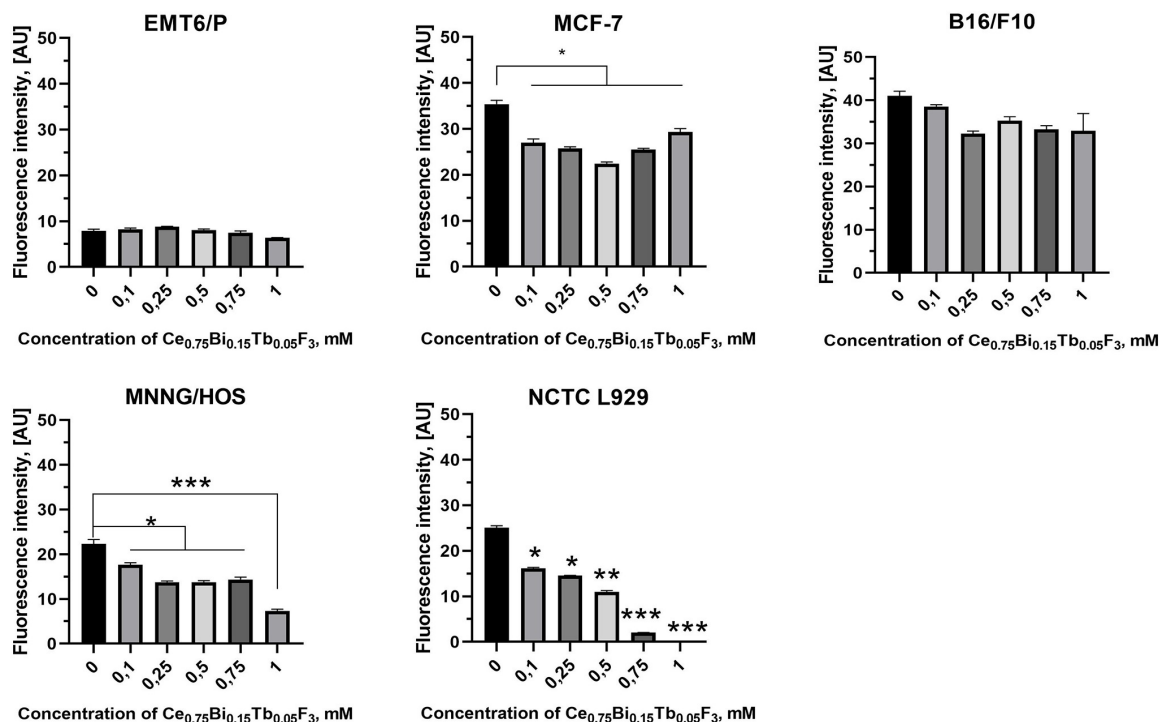


FIG. 4. Quantitative assessment of the mitochondrial membrane potential (MMP) of cancer (B16F10, EMT6/P, MCF-7, MNNG/HOS) and normal (NCTC L929) cells after 72 hours of incubation with $Ce_{0.75}Bi_{0.15}Tb_{0.1}F_3$ NPs at a concentration of 0.1 – 1 mM. Cells were stained with TMRE. Mean \pm standard deviation (SD) is plotted for five replicates, * $p < 0.05$, ** $p < 0.01$, *** $p < 0.005$

Analysis of the $Ce_{0.75}Bi_{0.15}Tb_{0.1}F_3$ NPs redox-activity under X-ray irradiation in aqueous solution was performed using the method of enhanced chemiluminescence in the iodophenol-horseradish peroxidase system (Fig. 5a). High sensitivity of this method makes it possible to determine changes in hydrogen peroxide concentrations up to 1 nM. X-ray irradiation (1 Gy) of the control group (solution without NPs) led to the formation of about 80 nM of hydrogen peroxide (Fig. 5b). $Ce_{0.75}Bi_{0.15}Tb_{0.1}F_3$ NPs colloidal solution (0.5 mM) demonstrated prooxidant activity which was expressed in a twofold increase in the level of hydrogen peroxide after irradiation at a dose of 1 Gy. This effect was observed regardless of the pH value of the colloidal solution.

Earlier, we have shown that cerium fluoride nanoparticles, including those doped with REE (for example, gadolinium), exhibit prooxidant activity under acidic pH conditions [31]. Thus, irradiation of tumor cells, containing $Ce_{0.75}Bi_{0.15}Tb_{0.1}F_3$ NPs, would lead to enhanced intracellular ROS generation, resulting in an accelerated radiation-induced cell death.

4. Conclusions

Citrate-stabilized $Ce_{0.75}Bi_{0.15}Tb_{0.1}F_3$ nanoparticles were synthesized by a facile precipitation technique. Analysis of the $Ce_{0.75}Bi_{0.15}Tb_{0.1}F_3$ NPs confirmed the composition and structure of these nanoparticles, as well as their good luminescent properties due to the presence of terbium ions in the crystal lattice of nanoparticles. $Ce_{0.75}Bi_{0.15}Tb_{0.1}F_3$ NPs at a concentration of 0.5 – 1 mM exhibit different cytotoxicity to normal and tumor cell lines, suppressing their

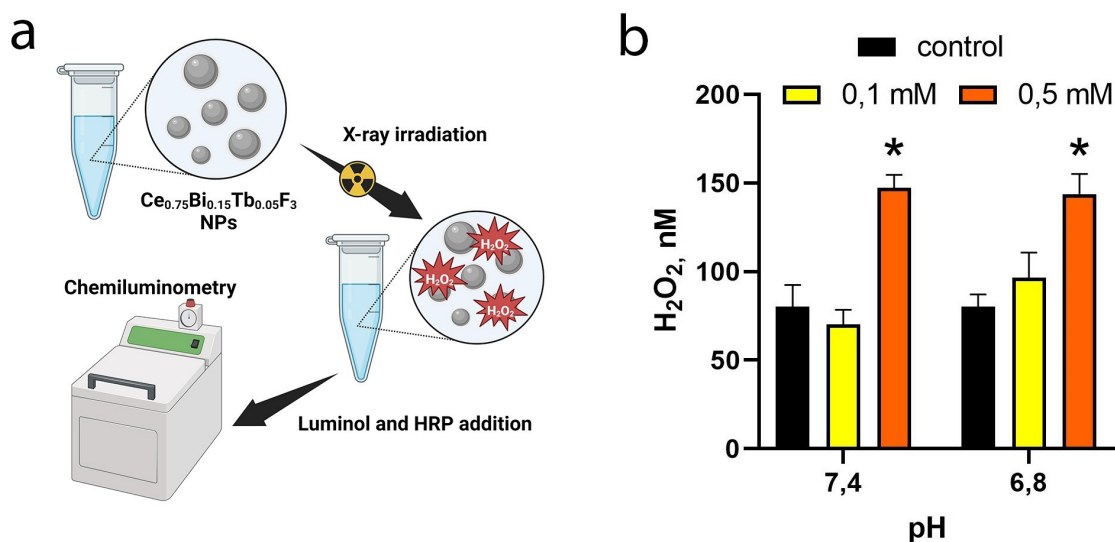


FIG. 5. Redox activity of $\text{Ce}_{0.75}\text{Bi}_{0.15}\text{Tb}_{0.1}\text{F}_3$ NPs under X-ray irradiation (1 Gy). Schematic representation of the experiment (a). Concentration of hydrogen peroxide after X-ray irradiation (total dose 1 Gy) of the $\text{Ce}_{0.75}\text{Bi}_{0.15}\text{Tb}_{0.1}\text{F}_3$ NPs colloid solution at pH 6.8 and pH 7.2 (b). The level of hydrogen peroxide was determined by the chemiluminescent method, using iodophenol-horseradish peroxidase system

viability and MMP and contributing to their death. Radiation-induced redox activity of $\text{Ce}_{0.75}\text{Bi}_{0.15}\text{Tb}_{0.1}\text{F}_3$ NPs was revealed upon X-ray irradiation that confirms the possibility of their application as a radiosensitizer in various tumor models *in vitro* and *in vivo*.

References

- [1] Tang J.L.Y., Moonshi S.S., Ta H.T. Nanoceria: An Innovative Strategy for Cancer Treatment. *Cell. Mol. Life Sci.*, 2023, **80**, 46.
- [2] Li H., Xia P., Pan S., Qi Z., Fu C., Yu Z., Kong W., Chang Y., Wang K., Wu D., et al. The Advances of Ceria Nanoparticles for Biomedical Applications in Orthopaedics. *Int. J. Nanomedicine*, 2020, **15**, P. 7199–7214.
- [3] Garzón-Manjón A., Aranda-Ramos A., Melara-Benítez B., Bensarghin I., Ros J., Ricart S., Nogués C. Simple Synthesis of Biocompatible Stable CeO_2 Nanoparticles as Antioxidant Agents. *Bioconjug. Chem.*, 2018, **29**, P. 2325–2331.
- [4] Banavar S., Deshpande A., Sur S., Andreescu S. Ceria Nanoparticle Theranostics: Harnessing Antioxidant Properties in Biomedicine and Beyond. *J. Phys. Mater.*, 2021, **4**, 042003
- [5] Popov A.L., Shcherbakov A.B., Zhlobak N.M., Baranchikov A.E., Ivanov V.K. Cerium Dioxide Nanoparticles as Third-Generation Enzymes (Nanozymes). *Nanosyst. Phys. Chem. Math.*, 2017, **8** (6), P. 760–781.
- [6] Liu H., Liu J. Self-Limited Phosphatase-Mimicking CeO_2 Nanozymes. *ChemNanoMat*, 2020, **6**, P. 947–952.
- [7] Ma Y., Tian Z., Zhai W., Qu Y. Insights on Catalytic Mechanism of CeO_2 as Multiple Nanozymes. *Nano Res.*, 2022, **15**, P. 10328–10342.
- [8] Luo Q., Li Y., Huo X., Li J., Li L., Wang W., Li Y., Chen S., Song Y., Wang N. Stabilizing Ultrasmall Ceria-Cluster Nanozyme for Antibacterial and Antibiofouling Applications. *Small*, 2022, **18**, 2107401.
- [9] Nelson B.C., Johnson M.E., Walker M.L., Riley K.R., Sims C.M. Antioxidant Cerium Oxide Nanoparticles in Biology and Medicine. *Antioxidants*, 2016 **5**, 15.
- [10] Chukavin N.N., Filippova K.O., Ermakov A.M., Karmanova E.E., Popova N.R., Anikina V.A., Ivanova O.S., Ivanov V.K., Popov A.L. Redox-Active Cerium Fluoride Nanoparticles Selectively Modulate Cellular Response against X-Ray Irradiation In Vitro. *Biomedicines*, 2024, **12**, 11.
- [11] Ermakov A., Popov A., Ermakova O., Ivanova O., Baranchikov A., Kamenskikh K., Shekunova T., Shcherbakov A., Popova N., Ivanov V. The First Inorganic Mitogens: Cerium Oxide and Cerium Fluoride Nanoparticles Stimulate Planarian Regeneration via Neoblastic Activation. *Mater. Sci. Eng. C*, 2019, **104**, 109924.
- [12] Filippova K.O., Ermakov A.M., Popov A.L., Ermakova O.N., Blagodatsky A.S., Chukavin N.N., Shcherbakov A.B., Baranchikov A.E., Ivanov V.K. Mitogen-like Cerium-Based Nanoparticles Protect Schmidtea Mediterranea against Severe Doses of X-Rays. *Int. J. Mol. Sci.*, 2023, **24**, 1241.
- [13] Jacobsohn L.G., Kucera C.J., James T.L., Sprinkle K.B., DiMaio J.R., Kokuoz B., Yazgan-Kukouoz B., DeVol T.A., Ballato J. Preparation and Characterization of Rare Earth Doped Fluoride Nanoparticles. *Materials*, 2010, **3**, P. 2053–2068.
- [14] Secco H. de L., Ferreira F.F., Péres L.O. Simple Preparation of Fluorescent Composite Films Based on Cerium and Europium Doped LaF_3 Nanoparticles. *J. Solid State Chem.*, 2018, **259**, P. 43–47.
- [15] Huang D.T.M., Tien N.T., Vu L.V., Long N.N. Synthesis and Optical Characterization of Samarium Doped Cerium Fluoride Nanoparticles. *VNU J. Sci. Math.-Phys.*, 2015, **31**.
- [16] Greis O., Haschke J.M. Rare Earth Fluorides. In *Handbook on the Physics and Chemistry of Rare Earths*, Elsevier, 1982, **5**, P. 387–460.
- [17] Pudovkin M.S., Morozov O.A., Korableva S.L., Rakhmatullin R.M., Semashko V.V., Ginkel A.K., Rodionov A.A., Kiiamov A.G. EPR and Optical Study of Erbium-Doped CeO_2 and $\text{CeO}_2/\text{CeF}_3$ Nanoparticles. *Ceram. Int.*, 2024, **50**, P. 9263–9269.
- [18] Cheng Y., Xu H., Cao W., Gao W., Tang B. Cerium Fluoride Nanoparticles as a Theranostic Material for Optical Imaging of Vulnerable Atherosclerosis Plaques. *J. Am. Ceram. Soc.*, 2023, **106**, P. 2375–2383.
- [19] Wang J., Ansari A.A., Malik A., Syed R., Ola M.S., Kumar A., AlGhamdi K.M., Khan S. Highly Water-Soluble Luminescent Silica-Coated Cerium Fluoride Nanoparticles Synthesis, Characterizations, and In Vitro Evaluation of Possible Cytotoxicity. *ACS Omega*, 2020, **5**, P. 19174–19180.

- [20] Cooper D.R., Kudinov K., Tyagi P., Hill C.K., Bradforth S.E., Nadeau J.L. Photoluminescence of Cerium Fluoride and Cerium-Doped Lanthanum Fluoride Nanoparticles and Investigation of Energy Transfer to Photosensitizer Molecules. *Phys. Chem. Chem. Phys.*, 2014, **16**, P. 12441–12453.
- [21] Gerken L.R.H., Gerdes M.E., Pruschy M., Herrmann I.K. Prospects of Nanoparticle-Based Radioenhancement for Radiotherapy. *Mater. Horiz.*, 2023, **10**, P. 4059–4082.
- [22] Deng J., Xu S., Hu W., Xun X., Zheng L., Su M. Tumor Targeted Stealthy and Degradable Bismuth Nanoparticles for Enhanced X-Ray Radiation Therapy of Breast Cancer. *Biomaterials*, 2018, **154**, P. 24–33.
- [23] Fan W., Tang W., Lau J., Shen Z., Xie J., Shi J., Chen X. Breaking the Depth Dependence by Nanotechnology-Enhanced X-Ray-Excited Deep Cancer Theranostics. *Adv. Mater.*, 2019, **31**, 1806381.
- [24] Yuan Z., Liu X., Ling J., Huang G., Huang J., Zhu X., He L., Chen T. In Situ-Transition Nanozyme Triggered by Tumor Microenvironment Boosts Synergistic Cancer Radio-/Chemotherapy through Disrupting Redox Homeostasis. *Biomaterials*, 2022, **287**, 121620.
- [25] Liu S., Fang L., Ding H., Zhang Y., Li W., Liu B., Dong S., Tian B., Feng L., Yang P. Alternative Strategy to Optimize Cerium Oxide for Enhanced X-Ray-Induced Photodynamic Therapy. *ACS Nano*, 2022, **16**, P. 20805–20819.
- [26] Zhu X., Wu J., Liu R., Xiang H., Zhang W., Chang Q., Wang S., Jiang R., Zhao F., Li Q., et al. Engineering Single-Atom Iron Nanozymes with Radiation-Enhanced Self-Cascade Catalysis and Self-Supplied H₂O₂ for Radio-Enzymatic Therapy. *ACS Nano*, 2022, **16**, P. 18849–18862.
- [27] Bagley A.F., Ludmir E.B., Maitra A., Minsky B.D., Li Smith G., Das P., Koong A.C., Holliday E.B., Taniguchi C.M., Katz M.H.G., et al. NBTXR3, a First-in-Class Radioenhancer for Pancreatic Ductal Adenocarcinoma: Report of First Patient Experience. *Clin. Transl. Radiat. Oncol.*, 2022, **33**, P. 66–69.
- [28] Lux F., Tran V.L., Thomas E., Dufort S., Rossetti F., Martini M., Truillet C., Doussineau T., Bort G., Denat F., et al. AGuIX® from Bench to Bedside-Transfer of an Ultrasmall Theranostic Gadolinium-Based Nanoparticle to Clinical Medicine. *Br. J. Radiol.*, 2019, **92**, 20180365.
- [29] Ghasemi M., Turnbull T., Sebastian S., Kempson I. The MTT Assay: Utility, Limitations, Pitfalls, and Interpretation in Bulk and Single-Cell Analysis. *Int. J. Mol. Sci.*, 2021, **22**, 12827.
- [30] Aplak E., Montfort C. von, Haasler L., Stucki D., Steckel B., Reichert A.S., Stahl W., Brenneisen P. CNP Mediated Selective Toxicity on Melanoma Cells Is Accompanied by Mitochondrial Dysfunction. *PLOS ONE*, 2020, **15**, e0227926.
- [31] Kolmanovich D.D., Chukavin N.N., Savintseva I.V., Mysina E.A., Popova N.R., Baranchikov A.E., Sozarukova M.M., Ivanov V.K., Popov A.L. Hybrid Polyelectrolyte Capsules Loaded with Gadolinium-Doped Cerium Oxide Nanoparticles as a Biocompatible MRI Agent for Theranostic Applications. *Polymers*, 2023, **15**, 3840.

Submitted 15 January 2024; accepted 28 February 2024

Information about the authors:

Nikita N. Chukavin – Institute of Theoretical and Experimental Biophysics of the Russian Academy of Sciences, 142290, Russia; ORCID 0000-0001-8431-4485; chukavinnik@gmail.com

Danil D. Kolmanovich – Institute of Theoretical and Experimental Biophysics of the Russian Academy of Sciences, 142290, Russia; ORCID 0000-0003-3391-7889; kdd100996@mail.ru

Arina D. Filippova – Kurnakov Institute of General and Inorganic Chemistry of the Russian Academy of Sciences, Moscow, 119991, Russia; ORCID 0000-0002-2725-8891; arifilippova@yandex.ru

Maria A. Teplonogova – Kurnakov Institute of General and Inorganic Chemistry of the Russian Academy of Sciences, Moscow, 119991, Russia; ORCID 0000-0002-4820-8498; m.teplonogova@gmail.com

Vladimir K. Ivanov – Kurnakov Institute of General and Inorganic Chemistry of the Russian Academy of Sciences, Moscow, 119991, Russia; ORCID 0000-0003-2343-2140; van@igic.ras.ru

Anton L. Popov – Institute of Theoretical and Experimental Biophysics of the Russian Academy of Sciences, 142290, Russia; ORCID 0000-0003-2643-4846; antonpopovleonid@gmail.com

Conflict of interest: the authors declare no conflict of interest.

Nanocomposites of aromatic poly(amide-imide) with nanotubular Mg-Fe hydrosilicate

Svetlana V. Kononova¹, Galina K. Lebedeva¹, Valery S. Kozlov², Eleonora N. Korytkova³, Tatyana P. Maslennikova³, Elena V. Kruchinina¹, Elena N. Vlasova¹, Natalia N. Saprykina¹, Galina N. Gubanova¹, Milana E. Vylegzhanina¹, Vasiliy T. Lebedev²

¹Institute of Macromolecular Compounds Russian Academy of Science, St. Petersburg, Russia

²Petersburg Nuclear Physics Institute named by B. P. Konstantinov of National Research Centre “Kurchatov Institute”, Gatchina, Russia

³Russian Academy of Science, Grebenshchikov Institute of Silicate Chemistry, St. Petersburg, Russia

Corresponding author: Svetlana V. Kononova, svetlanavkononova@gmail.com

ABSTRACT Composite films based on aromatic polyamide imide with carboxyl-containing fragments in repeating units (PAI-Ac) containing hydrosilicate nanotubes $(\text{Mg,Fe})_3\text{Si}_2\text{O}_5(\text{OH})_4$ are structurally sensitive to the molecular weight of the polymer used. According to Mössbauer spectroscopy data, nanotubes introduced into a polymer matrix generally retain their original structure. When using a polymer with a relatively low molecular weight, composite films are formed that are not stable during the pervaporation of cyclohexane and ethanol. In the case of a high-molecular polymer, the resulting MMM-type membranes are stable during pervaporation. They are more permeable to polar liquids compared to the base polymer and MMMs containing $\text{Mg}_3\text{Si}_2\text{O}_5(\text{OH})_4$ nanotubes. Analysis of the found differences in the properties of the studied nanocomposites with iron-containing nanotubes in the PAI-Ac matrix from similar nanocomposites with magnesium-containing nanotubes leads to the conclusion about the need to study MMMs with iron-containing nanoparticles of a different structure.

KEYWORDS poly(amide-imide), pervaporation, liquid separation, synthesis, hydrosilicate nanotubes, Mössbauer spectroscopy, morphology, composite materials, mixed matrix membranes (MMM), electron microscopy, atomic force microscopy

ACKNOWLEDGEMENTS The work was carried out within State Programs of IMC RAS (Project No. 122012000452-9).

FOR CITATION Kononova S.V., Lebedeva G.K., Kozlov V.S., Korytkova E.N., Maslennikova T.P., Kruchinina E.V., Vlasova E.N., Saprykina N.N., Gubanova G.N., Vylegzhanina M.E., Lebedev V.T. Nanocomposites of aromatic poly(amide-imide) with nanotubular Mg-Fe hydrosilicate. *Nanosystems: Phys. Chem. Math.*, 2024, **15** (2), 268–284.

1. Introduction

The development of inorganic/polymer nanocomposite materials assumes a new importance not only for the experts in the area of polymer mechanics and thermal physics, but for the researchers engaged in membrane technologies whose aim is to design useful materials with valuable mechanical and thermal properties as well as good transport parameters. The works in this field have always been dependent on the availability of nanoparticles and the possibility of synthesis of novel nanosized objects with unique properties. In a number of research papers, it was demonstrated that hybrid systems frequently possessed new characteristics differing from those of the initial compounds [1–3]. These differences are most pronounced upon the formation of filled polymers. The effect is related to the processes of distribution of nanosized inorganic particles in a polymer matrix and is primarily determined by the following factors: (i) the amount and type of reactive groups; (ii) the ability of the initial components to interact with each other; (iii) the presence of “potential ligands” for the selected filler in the polymer structure; (iv) the structure of a filler; (v) the size of filler particles. The rational variation of physico-chemical properties of a polymer by addition of fillers leads to the creation of structural materials with improved characteristics [4–6]. This approach is also used in the development of industrial polymer membranes that should be stable under rigid conditions of the separation process [7]. Composites containing nano-sized inorganic fillers are of particular interest. For example, in a series of publications [8–10], the authors considered the influence of zeolite 4A or carbon molecular sieves introduced into the polyimide matrix on its properties. It has been demonstrated that if the components of a polymer-based composite were well compatible, the ordered nanoporous structure of the inorganic component was responsible for the gas separation efficiency [11, 12]. There are well-known works devoted to the introduction of inorganic (mostly crystalline) additives into a polymeric membrane matrix with the objective of improving its barrier properties with respect to both gases and liquids. This idea was used in the development of composite

membrane materials with decreased gases and liquids permeabilities [13, 14]. Using carbon nanotubes as an example, the high efficiency of using nanoparticles with a tubular structure in membrane materials has been demonstrated [15–17]. First of all, the interest in carbon nanotubes is caused by their high specific surface area, which leads to the formation of large amounts of nanometer-sized voids and cavities. It has been shown that diffusion and sorption characteristics of carbon nanotubes were superior to those of the known materials [18–20].

The development of easy synthetic methods for non-carbon (most often oxide and oxyhydroxide) tubular structures of various morphologies and surface activities [21] offers possibilities of preparing catalytic and pervaporation composite membranes. It has been shown that morphology of nanotubes, their shape, length and the ratio between internal and external diameters could determine morphological features of a composite [22].

In world practice, the applicability of natural nanomaterials with chrysotile structure in preparation of nanocomposites has been demonstrated [22]. Chrysotile is a lamellar silicate mineral of the serpentine group; its idealized structural formula is $\text{Mg}_3\text{Si}_2\text{O}_5(\text{OH})_4$. According to the modern views, the structural elements of chrysotile are crystalline fibrils in the shape of nanotubes with the average internal diameters of 5 – 7 nm and the average external diameters of 30 – 40 nm. The nanotube (NT) walls are formed by twisting of the double layers due to small mismatch of their diameters (Fig. 1); one of those layers is composed of silicon-oxygen tetrahedrons, and another consists of brucite octahedrons. The thickness of this elementary layer is about 0.75 nm, and the number of layers forming the NT walls usually varies from 20 to 25 [20].

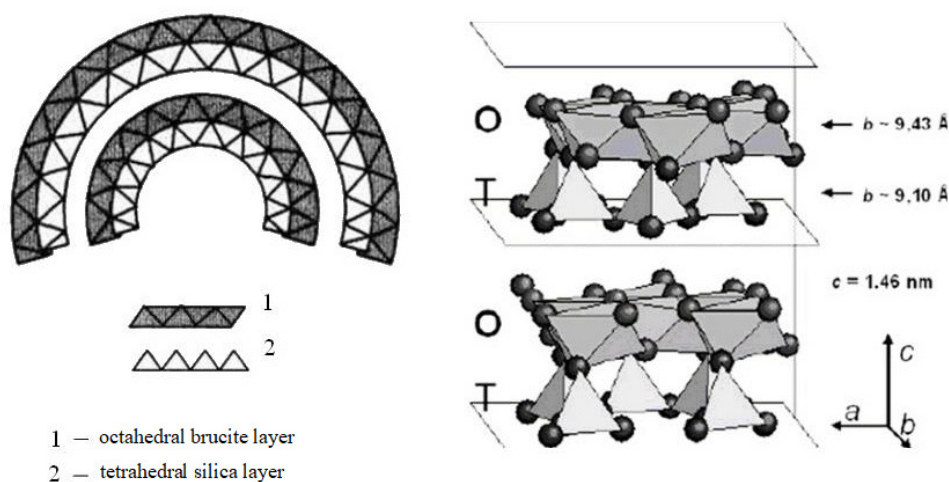


FIG. 1. Structure of chrysotile nanotubes [20]

The transport of liquids and gases through polymer composites containing lamellar nanoparticles with chrysotile structure MMT-15A has been described; the pervaporation nanocomposite membranes containing these chrysotile particles have been prepared [22]. However, the presence of impurities in the natural materials frequently limits the use of natural chrysotile [23]. The use of synthetic nanoparticles with the chrysotile structure made it possible not only to avoid the negative influence of impurities but also to observe a number of specific effects related to the unique structural, morphological, and physical properties of the developed materials.

In this connection, of great interest were the design of new composite materials based on aromatic poly(amide-imide)s filled with inorganic nanotubes of magnesium hydrosilicate $\text{Mg}_3\text{Si}_2\text{O}_5(\text{OH})_4$ (chrysotile) and investigation of the obtained composites (their morphological features, mechanical and transport properties) [22]. The choice of filler material was also caused by the structure of chrysotile nanoparticles, whose surfaces contain polar OH-groups. The methods for controlled hydrothermal synthesis of hydrosilicate NTs were developed and optimized, making it possible to regulate the structure, morphology and size of NTs by varying the synthesis modes and composition of the reaction media [24]. It should be considered that cations of d-elements (Ni, Co, Fe) that partially substitute magnesium in the octahedral layer of the chrysotile structure may change diameter and length of synthetic NTs and affect thermal stability, electric and magnetic characteristics of synthetic substituted hydrosilicates.

The introduction of magnesium-hydrosilicate NTs into polyimide films has been studied earlier; it has been revealed that the presence of this filler resulted in the considerable improvement of mechanical characteristics of the polymer [2,20]. In our earlier works, it has been shown that introduction of hydrosilicate NTs with the chrysotile structure into chemically stable poly(amide-imide) (PAI) led to a new material, the microcomposite whose transport characteristics, thermal stability, and glass transition temperature were significantly higher than those of the initial polymer [25]. This composite consisted of a polymer matrix (poly(diphenyloxide-amide-N-phenylphthalimide)) with NT agglomerates dispersed inside; the size of one such agglomerate approximately corresponded to 10 external diameters of a NT. When a more hydrophilic

polymer (PAI-Ac containing carboxylic groups in diamine fragments of repeating monomer units) was used as a matrix, morphological studies demonstrated more homogeneous distribution of the filler in the matrix; the average amount of NTs in one agglomerate decreased down to 2 – 3 [26].

The studies of transport properties of non-porous films of PAI-based nanocomposites filled with $\text{Mg}_3\text{Si}_2\text{O}_5(\text{OH})_4$ or $\text{Ni}_3\text{Si}_2\text{O}_5(\text{OH})_4$ NTs revealed their increased permeability with respect to polar liquids (water, methanol, ethanol). At the same time, a significant decrease in permeability with respect to weakly polar liquids (toluene, cyclohexane) was observed; in the limiting case, the nanocomposite film even demonstrated barrier properties (very low permeability) [20, 27].

The possibility of modification of transport properties of filled polymer films by variation of their structural and morphological characteristics is widely discussed in scientific literature; these works are reviewed in [20]. Several possible mechanisms of transport of gases and liquids through diffusion membranes of this type were proposed. However, the majority of existing literature data are particular cases and sometimes contradictory observations; they cannot be used to reliably predict transport properties of the developed membranes. One of the problems is the difficulty of analysis of multifactor and multicomponent systems containing low (or very low) amounts of nanosized fillers. The information about the influence of nanoparticles on the properties of nanocomposite membranes is fragmentary, and the factors determining the diffusion transport in these objects are not revealed.

To summarize, the general principles of components combination and regularities of transport of gases and liquids through polymer/NT composites are still poorly understood. It remains unclear what happens to NTs upon immersion into a polymer matrix. The roles of the internal channels of NTs and the external NT/polymer interface in the formation of nanocomposites and the appearance of new mechanical, thermophysical and transport properties have not been explained. To answer these questions, it is necessary to propose an empirical model and to study it using the available physical methods. In this work, the selected model was the PAI-Ac-based nanocomposite containing iron-hydrosilicate NTs with the chrysotile structure. This system was chosen because the hydrothermal synthetic method for morphologically similar NTs containing magnesium, iron, and nickel atoms has been already developed. The nanocomposites on the basis of aromatic PAIs containing magnesium $\text{Mg}_3\text{Si}_2\text{O}_5(\text{OH})_4$ and nickel $\text{Ni}_3\text{Si}_2\text{O}_5(\text{OH})_4$ hydrosilicates with tubular structure have been obtained and investigated earlier. However, the main factor is that the structure of iron-containing nanoparticles can be studied by Mössbauer spectroscopy. To reveal structural features of inorganic nanofillers present in a polymer matrix in low amounts (less than 2 wt.% with respect to polymer mass), it is necessary to use special analytical methods. Mössbauer spectroscopy is a highly sensitive tool for the study of crystalline and amorphous materials; it is absolutely selective to ^{57}Fe isotope and allows one to monitor changes in local environment of iron atoms and to obtain information about phase composition of iron-containing domains. Therefore, it is expected that the use of this method in the studies of correctly chosen model composites will enable one to reveal possible changes in the structure of NTs after their immersion into a polymer matrix.

The aim of the present study is the development of new nanocomposite materials based on aromatic PAI (which was synthesized from diacid chloride of 2-(4-carboxyphenyl)-1,3-dioxoisindoline-5-carboxylic acid and 3,5-diaminobenzoic acid) filled with iron-containing hydrosilicate NTs.

2. Experimental

2.1. Materials

MgO (“analytical grade”), Fe_2O_3 (“analytical grade”), Fe (“special purity grade”), $\text{SiO}_2 \cdot n\text{H}_2\text{O}$ (silica gel GOST 3056-76), N-methyl-2-pyrrolidone (N-MP) and propylene oxide (Sigma Aldrich, 99 %, CAS 106-89-8) were used without additional purification.

2-(4-carboxyphenyl)-1,3-dioxoisindoline-5-carboxylic acid was prepared by condensation of trimellitic anhydride ($\text{C}_9\text{H}_4\text{O}_5$) and p-aminobenzoic acid; then the dicarboxylic acid obtained was converted to its diacid chloride by reaction with thionyl chloride as described in [28].

2.2. Polymer synthesis

Synthesis of PAI-Ac (Fig. 2) was performed according to the following protocol [28]. 3,5-Diaminobenzoic acid was dissolved in N-MP containing no more than 0.035 wt.% of moisture at room temperature. Diacid chloride of 2-(4-carboxyphenyl)-1,3-dioxoisindoline-5-carboxylic acid was added to cooled solution at stirring, then the reaction mixture was left to stand at room temperature for 1.5 h. After cooling the polymer solution and adding propylene oxide, the resulting mixture was stirred at room temperature for 60 min.

PAI-Ac was isolated by precipitation from 10 wt.% polymer solution in N-MP into water. The resulting polymer fibers were filtered, washed with ethanol and dried in oven at 70 °C.

The reduced viscosity of 0.5 wt.% solution of the synthesized PAI-Ac was determined in N-MP at 20 °C and the values of the reduced viscosity η_{red} of two different samples were 1.4 and 1.9 dl/g, which corresponds to molecular masses of 57 and 98 kDa, respectively.

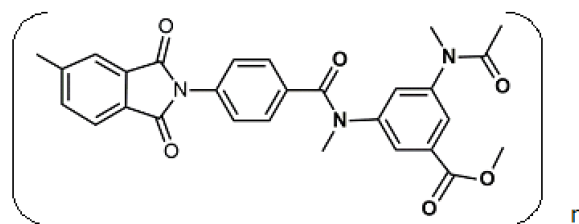


FIG. 2. Chemical structure of PAI-Ac

2.3. Synthesis of nanotubes

Hydrothermal synthesis of $(\text{Mg}, \text{Fe}_2^+, \text{Fe}_3^+)_3\text{Si}_2\text{O}_5(\text{OH})_4$ hydrosilicate was carried out according to the procedure described in [29].

The specially synthesized $(\text{Mg}, \text{Fe})\text{SiO}_3$ solid solution containing 25 wt.% FeO was used as an iron-containing starting component. $(\text{Mg}, \text{Fe})\text{SiO}_3$ was obtained from MgO, Fe_2O_3 , Fe, and $\text{SiO}_2 \cdot n\text{H}_2\text{O}$ (silica gel) by solid-phase synthesis performed for 2 – 3 hours in argon atmosphere at a temperature of 1200 °C. Additional component $(\text{Mg}, \text{Fe})\text{O}$ was introduced into the reaction mixture to create the required chrysotile stoichiometry $(\text{MgO} + \text{FeO}) : \text{SiO}_2 = 3 : 2$. The mixture of $(\text{Mg}, \text{Fe})\text{SiO}_3$ and $(\text{Mg}, \text{Fe})\text{O}$ was subjected to hydrothermal treatment in 1/5 – 2 wt.% NaOH solution (400 °C, 70 MPa, 24 h).

2.4. Preparation of samples for studies

2.4.1. Model samples

Preparation of 15 wt.% solution of PAI-Ac polymer in N-MP: N-MP was added to dry polymer and left to stay for 12 hours until the polymer was completely dissolved.

Preparation of nanoparticle suspension: NTs (30 wt.% with respect to the weight of dry polymer) were suspended in N-MP. The suspension was subjected to ultrasound treatment for 1 hour at stirring.

The prepared solution of the PAI-Ac polymer was added to this NT suspension. The concentration of the resulting dispersion (12 wt.% with respect to the weight of dry polymer) was adjusted to 10 wt.% by adding N-MP; after stirring for 20 hours, the dispersion was filtered through a Schott filter.

Model films were prepared by applying a layer of dispersion on a glass plate and removing the solvent during sequential heat treatment at 50 °C for 15 h followed by heating to 150 °C.

2.4.2. Membrane samples

Preparation of 10 wt.% solution of the PAI-Ac polymer in N-MP (5.05 g): 4.55 g of N-MP was added to 0.50 g of dry polymer and left to stay for 12 hours until the polymer was completely dissolved.

Preparation of nanoparticle suspension: nanoparticles (0.0051 g, 1 wt.% with respect to the weight of dry polymer) were suspended in 1.25 g of N-MP. The suspension was subjected to ultrasound treatment for 1 hour at stirring.

The prepared 10 wt.% solution of the PAI-Ac polymer was added to the resulting suspension. The resulting dispersion (NT concentration 8 wt.% with respect to the weight of dry polymer) was stirred for 20 hours, then filtered through a Schott filter. Films were cast onto the surface of glass plates and subjected to heat treatment at 50 °C for 15 h followed by stepwise heating to 150 °C.

2.5. Methods

2.5.1. IR spectroscopy

FTIR spectra were recorded on a Vertex 70 IR-Fourier spectrometer (“Bruker”) with a resolution of 4 cm^{-1} , the number of scans was 60. The spectrometer was equipped with a single attenuated total internal reflection (SATR) microattachment (“Pike”) with a ZnSe working element. When recording the ATR spectra, a correction was introduced to take into account the penetration depth depending on the wavelength.

2.5.2. ^1H NMR spectroscopy

^1H NMR spectra were obtained using a Bruker AC-400 spectrometer in deuterated dimethylsulfoxide (DMSO-d_6).

The spectra contain signals at 10.86 ppm and 10.63 ppm that are assigned to NH protons of the amide groups of PAI-Ac.

2.5.3. XRay diffraction analysis

The phase composition of hydrosilicate samples was determined using X-ray diffractometry data (DRON-3M, Cu $K\alpha$, Ni filter, $\lambda = 1.54 \text{ \AA}$). Identification of peaks in diffraction patterns was carried out using the PDWin 4.0 software package with a powder diffraction data base based on the ICDD PDF-2 card index.

2.5.4. Electron microscopy

TEM: Transmission electron microscopy studies of NTs were carried out using a JEM 2100-F transmission electron microscope with an accelerating voltage U_{ac} up to 200 kV.

SEM: Film samples were studied with a Supra 55VP scanning electron microscope (ZEISS, Germany) with a secondary electron (SE2) detector. To impart electroconductive properties to the surfaces of tested films and to increase the contrast of obtained images, they were coated with a thin gold layer (15 – 20 nm) by cathode sputtering on a Quorum 150 apparatus (Quorum Technologies Ltd, Laughton, UK).

2.5.5. Mössbauer spectroscopy

Mössbauer spectra of the synthesized samples were recorded on an MS-1-003 electrodynamic spectrometer in the constant acceleration mode with a ^{57}Co (Rh) source at an absorber temperature of 300 K. Isomeric shifts and calibration of the velocity scale were carried out relative to the generally accepted $\alpha\text{-Fe}$ standard. Mössbauer spectra were processed in the MOSSFIT program assuming a Lorentzian line shape. The samples were prepared by pressing a certain amount of the tested substance together with a neutral filler (powdered sugar) into tablets about 0.7 mm thick.

2.5.6. Pervaporation experiments

Pervaporation performance of the obtained membranes was tested for different penetrants (sequence \rightarrow cyclohexane \rightarrow methanol \rightarrow ethanol \rightarrow water or reverse sequence water \rightarrow ethanol \rightarrow methanol \rightarrow cyclohexane) using the autonomous noncontinuous flow laboratory cell, as described in [30] with an operating membrane area of $1.38 \cdot 10^{-3} \text{ m}^2$. The process was carried out at constant temperature of $40 \text{ }^\circ\text{C}$, at continuous stirring. Permeate vapors were condensed in a receiver using liquid nitrogen. Then the permeate was weighed, and the flux value J ($\text{kg} \cdot \text{m}^{-2} \cdot \text{h}^{-1}$) was calculated using the following equation:

$$J = mS^{-1}t^{-1}, \quad (1)$$

where m is the mass of penetrants permeated through membrane area S in a period t ; P ($\mu\text{m} \cdot \text{kg} \cdot \text{m}^{-2} \cdot \text{h}^{-1}$) is the flux (permeation rate) of penetrants normalized to $1 \mu\text{m}$ membrane thickness.

3. Results and discussion

As discussed in Introduction, immersion of magnesium or nickel-containing nanoparticles of tubular morphology with a chrysotile structure into a polymer matrix can lead to changes in thermophysical and transport properties of a polymer. First of all, this applies to samples belonging to the Mixed Matrix Membranes (MMM) type used in pervaporation. This effect was observed for nanocomposites containing an optimal amount of nanosized inorganic filler; the amount depends on chemical structure of the matrix polymer. This dependence is related to the process of distribution of nanoparticles in the polymer film. In particular, the distribution process is controlled by possible interactions between functional groups present on the surface of nanoparticles and functional groups of the matrix polymer.

When tubular nanoparticles of the general formula $\text{Mg}_3\text{Si}_2\text{O}_5(\text{OH})_4$ synthesized under identical conditions are used as a filler, it is possible to influence the nature of the interaction between inorganic (NT) and organic (polymer) phases. Specifically, we need to select polymers with (or without) functional groups capable of interacting with hydroxyl groups on the outer surface of the NTs. The most significant change in properties (compared to the original polymer) was observed in the case of nanocomposites based on aromatic PAI that was synthesized from 1,3-diaminobenzoic acid. This polymer includes carboxyl-containing fragments in the diamine component of the repeating unit. In polymer-inorganic composites based on this polymer, agglomerates of 1 – 2 NTs are distributed fairly evenly throughout the entire thickness of the film composites. The permeability of composite membranes differs significantly from the permeability of unfilled polymer (Table 1). As shown in Table 1, the PAI-Ac-Mg-NT nanocomposite film is more permeable to both non-polar penetrants (cyclohexane) and polar penetrants (water), but the water permeability increases significantly.

At first glance, the reason for the increase in the permeability of the nanocomposite to water seems obvious, since during its preparation, nanoparticles with hydrophilic groups on the surface are introduced into the polymer matrix. However, a test involving introduction of $\text{Ni}_3\text{Si}_2\text{O}_5(\text{OH})_4$ NTs of a similar structure into PAI under the same conditions showed a slight decrease in water permeability. Consequently, the question of how NTs participate in the preferential mass transfer of water through polymer-inorganic films remains open.

In addition to studying structural and morphological characteristics of the composites, it would be wise to investigate whether the changes occur in the structure of the inorganic dopants themselves after immersion in a polymer matrix. However, this complex problem may be solved only after special additional experiments, possibly involving the preparation of model composites. For this reason, we selected iron-containing NTs of the general formula $\text{Me}_3\text{Si}_2\text{O}_5(\text{OH})_4$

TABLE 1. Pervaporation properties of PAI-Ac-NT in comparison with the base polymer

N	Type of sample	C_{NT} , wt.%	l , μm	T , $^{\circ}\text{C}$	penetrant	J , $\text{kg}\cdot\text{m}^{-2}\text{h}^{-1}$	P , $\text{kg}\cdot\mu\text{m}\cdot\text{m}^{-2}\text{h}^{-1}$	$P(\text{PAI-Ac-NT})/ P(\text{PAI-Ac})$
1	PAI-Ac	—	20	40	water	$6.6 \cdot 10^{-2}$	1.3	—
				20	cyclohexane	$5.0 \cdot 10^{-4}$	$1.0 \cdot 10^{-2}$	—
				40		$9.0 \cdot 10^{-4}$	$1.8 \cdot 10^{-2}$	
2	PAI-Ac – Mg-NT	2	22	40	water	$2.8 \cdot 10^{-1}$	6.2	4.8
				18	cyclohexane	$6.0 \cdot 10^{-4}$	$1.3 \cdot 10^{-2}$	~ 1.3
3	PAI-Ac – Fe-NT	1	15	40	water	$6.1 \cdot 10^{-1}$	9.1	7.0
				40	cyclohexane	$2.3 \cdot 10^{-3}$	$3.4 \cdot 10^{-2}$	1.9

with a chrysotile structure as a filler for preparation of model and membrane composites. This choice was dictated by the possibility of using Mössbauer spectroscopy to study the structure of nanoparticles.

3.1. Inorganic nanoparticles

To form polymer-inorganic composite films, iron-containing hydrosilicate nanoparticles from Mg, Fe-enstatite were synthesized.

According to the XRD data (Fig. 3), the sample is a hydrosilicate with a chrysotile structure.

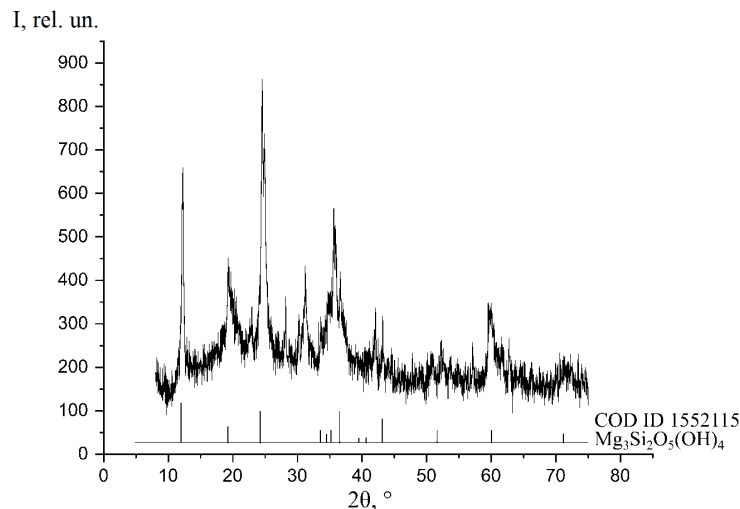


FIG. 3. X-ray diffraction pattern of synthetic $(\text{Mg,Fe})_3\text{Si}_2\text{O}_5(\text{OH})_4$

Chemical composition of the sample (in mass %): MgO – 31.25, FeO – 9.85, Fe_2O_3 – 5.83, SiO_2 – 40.21 and H_2O – 12.93.

According to the electron microscopy data (Fig. 4), the sample contains cylindrical tubes with a certain amount of “sleeves” type particles with the following geometric dimensions: length 1 – 5 μm , outer diameter 30 – 50 nm, inner diameter 5 – 6 nm.

To investigate crystallinity and chemical structure of the synthesized hydrosilicate NTs, Mössbauer spectroscopy was used. It is known that the Mössbauer spectroscopy, which is a highly sensitive tool for studying crystalline and amorphous materials, has absolute selectivity for the Mössbauer isotope ^{57}Fe . It allows one to obtain valuable information about the coordination position, oxidation state of Fe ions, relative concentration of iron atoms in various states, magnetic structure, etc. [31, 32].

The original synthetic sample of iron-containing chrysotile hydrosilicate NTs from Mg, Fe (enstatite) was studied by the Mössbauer spectroscopy. It should be noted that the results of the Mössbauer research on natural chrysotile were reported in numerous publications [33–35]. From a brief review of publications on the Mössbauer spectroscopy of

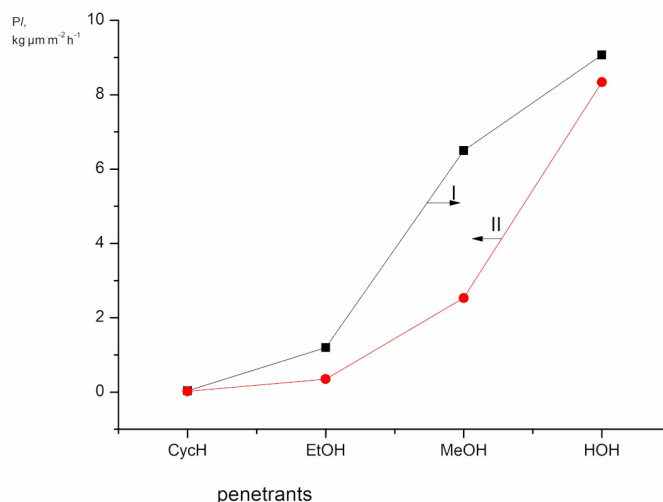


FIG. 5. Pervaporation properties of the MMM membrane containing $(\text{Mg,Fe})_3\text{Si}_2\text{O}_5(\text{OH})_4$ nanotubes. Flux normalized to membrane thickness [$\text{kg}\cdot\mu\text{m}\cdot\text{m}^{-2}\cdot\text{h}^{-1}$] for penetrants of different polarities when passed through the sample at 40°C in the following sequences: (I) – cyclohexane (CycH), ethanol (EtOH), methanol (MeOH), water (HOH); (II) – water, methanol, ethanol, cyclohexane

After that, the membrane permeability with respect to polar liquids decreases (in the pervaporation rote from cyclohexane to water), but the cyclohexane permeability of the membrane after this pervaporation cycle remains virtually unchanged.

The permeability of the composite material of the second type exceeds the permeability of the base polymer; this difference is more pronounced than that in the case of magnesium-containing NTs (Table 1). It was assumed that the amounts of surface hydroxyl groups in $\text{Mg}_3\text{Si}_2\text{O}_5(\text{OH})_4$ and $(\text{Mg,Fe})_3\text{Si}_2\text{O}_5(\text{OH})_4$ tubes are approximately equal. Therefore, we have to discard the idea that an increase in hydrophilicity of the material after its modification determines its permeability.

This pervaporation behavior of composites cannot be explained by irreversible swelling of the membrane in polar liquids either, as evidenced by the data in Fig. 5. The cyclohexane flux normalized to the thickness of the membrane at the beginning of pervaporation is almost equal to that after a full cycle of passing penetrants of different polarities. This also indicates the integrity of the composite film.

It remains unclear why the introduction of Fe-NTs leads to such a significant change in the properties of the polymer. To answer this question, it is necessary to investigate the structure and morphology of the prepared membranes and model composites.

3.2.2. Structural features of polymer and nanocomposite films

3.2.2.1. IR spectroscopy

Using FTIR spectroscopy, the pure PAI-Ac films were compared with nanocomposites of the first type (PAI-Ac films filled with chrysotile).

The FTIR spectrum of pure PAI-Ac contains the bands characteristic of this class of compounds. They are: the band at 3290 cm^{-1} (N-H stretching vibrations of the amide group); bands at 1780 cm^{-1} and 1716 cm^{-1} (symmetric and antisymmetric vibrations of the C=O group of the imide ring); the band at 1659 cm^{-1} (vibrations of the C=O acid group and C=O amide bond); the peak at 1546 cm^{-1} (bending vibrations of the N-H amide bond); and the band at 1367 cm^{-1} (stretching vibrations of the C-N group of the amide ring). In addition, the spectrum exhibits the wide band with a maximum at 3400 cm^{-1} related to the residual solvent (a mixture of amide solvent and water). The peaks assigned to vibrations of OH groups appear near 3400 cm^{-1} .

The important thing to observe here is that the intensity of the broad band with a maximum at 3400 cm^{-1} (vibrations of OH groups) is higher in the spectra of filled films. That is, the OH content in the filled films is higher than that in the PAI-Ac film. An increase in the content of OH groups can occur both due to the presence of hydroxyl groups on the surface of the filler and to more intense sorption of water on the composites (which is probably also related to the filler).

In addition, when the filler is introduced, the band of antisymmetric vibrations of the C=O imide ring at 1716 cm^{-1} shifts to 1719 cm^{-1} and expands into the high-frequency region, which indicates weakening of the hydrogen bonds associated with this band. Further, the intensity of the band at 1367 cm^{-1} , which is attributed to the C-N stretching vibrations of the imide ring, decreases significantly. A change in the system of hydrogen bonds is also indicated by a change in the intensities of the Amide I band (1653 cm^{-1}) and Amide II band (1543 cm^{-1}).

On the other hand, spectral changes in the region of $1716 - 1740\text{ cm}^{-1}$ can be associated with the formation of ester bonds between the COOH groups of the polyacid and OH groups on the surface of the filler. The formation of the

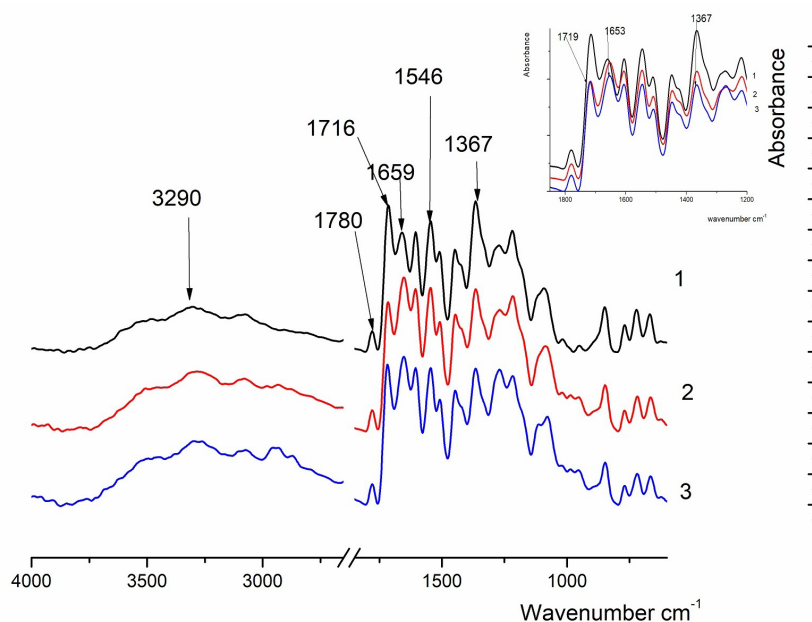


FIG. 6. FTIR spectra of PAI-Ac (1), PAI-Ac-Fe-NT films before pervaporation (2), and PAI-Ac-Fe-NT films after pervaporation (3)

ester bond involving an aromatic acid should lead to the appearance of a new absorption band in the region of $1730 - 1717 \text{ cm}^{-1}$. The appearance of a certain number of ester groups in the system is also accompanied by a change in the system of hydrogen bonds. It should be noted that the esterification reaction is highly likely to occur when a sample is heated above $130 \text{ }^\circ\text{C}$, and studied composite films were formed at $150 \text{ }^\circ\text{C}$.

However, the formed PAI-Ac based nanocomposite films of the first type (defect-free, judging by the result of a vacuum test on a dry membrane in a pervaporation cell) containing 1 wt.% Fe-NTs showed high permeability to cyclohexane during pervaporation and low stability after direct contact with alcohols (n-ethanol, n-propanol) as penetrants. The films studied during the pervaporation process were re-examined by IR spectroscopy (see above). It was shown that after pervaporation, the shift and broadening of the 1716 cm^{-1} band into the high-frequency region continued. This result indicates gradual weakening of hydrogen bonds involving the C=O groups of the imide ring.

This effect may be related to swelling of the composite film to the point where it loses integrity.

The observed effect in combination with pervaporation properties (see above) absolutely contradicts the results of our previous research (the study of PAI-Ac-based nanocomposite film membranes containing magnesium/nickel hydrosilicate nanoparticles formed under similar conditions). The above works show that the introduction of magnesium or nickel hydrosilicate NTs reduces the permeability of the material to cyclohexane, but significantly increases the permeability to alcohols and water. A consistent explanation for this effect can be provided: the introduced NTs contain hydroxyl groups capable of forming hydrogen bonds. What is the reason of completely different pervaporation behavior exhibited by the Fe-NT-filled composites based on the same PAI-Ac matrix? This is an important question, especially since the used NTs have a similar structure (chrysotile $(\text{Me})_3\text{Si}_2\text{O}_5(\text{OH})_4$).

Of course, the NTs themselves differed morphologically. While magnesium- or nickel-containing NTs were cylindrical nanoscrolls, then Fe-NTs were cylindrical tubes containing a certain amount of “sleeves” type particles. This difference could lead to differences in the morphology of the composite films.

3.2.2.2. Atomic Force Microscopy (AFM)

Numerous NTs and their fragments located in the near-surface region are observed on the free surface of the film composite (Fig. 7). As seen in Fig. 7, the NTs are uniformly distributed, virtually no aggregates are observed. Taking into account the thickness of polymer coating, the NT thickness was estimated to be $\sim 200 \text{ nm}$ by the linear profile of the surface area.

The obtained results indicate that the morphology of composites of the first type changes upon contact with cyclohexane, which correlates with the pervaporation data. Although the surface topography practically does not change after swelling in the cyclohexane vapors, the number of NTs observed on the surface increases (due to their ejection from the near-surface region). At the same time, the thickness of the NTs decreases slightly (up to 150 nm) due to the absence of a polymer coating on their surface. It should be noted that the roughness parameters of the matrix surface vary slightly (for a 20×20 micron scanning matrix – $R_a = 3.7 \text{ nm}$, $R_q = 5.4 \text{ nm}$ for the initial composite, $R_a = 3.4 \text{ nm}$, $R_q = 5.9 \text{ nm}$ for the composite after swelling).

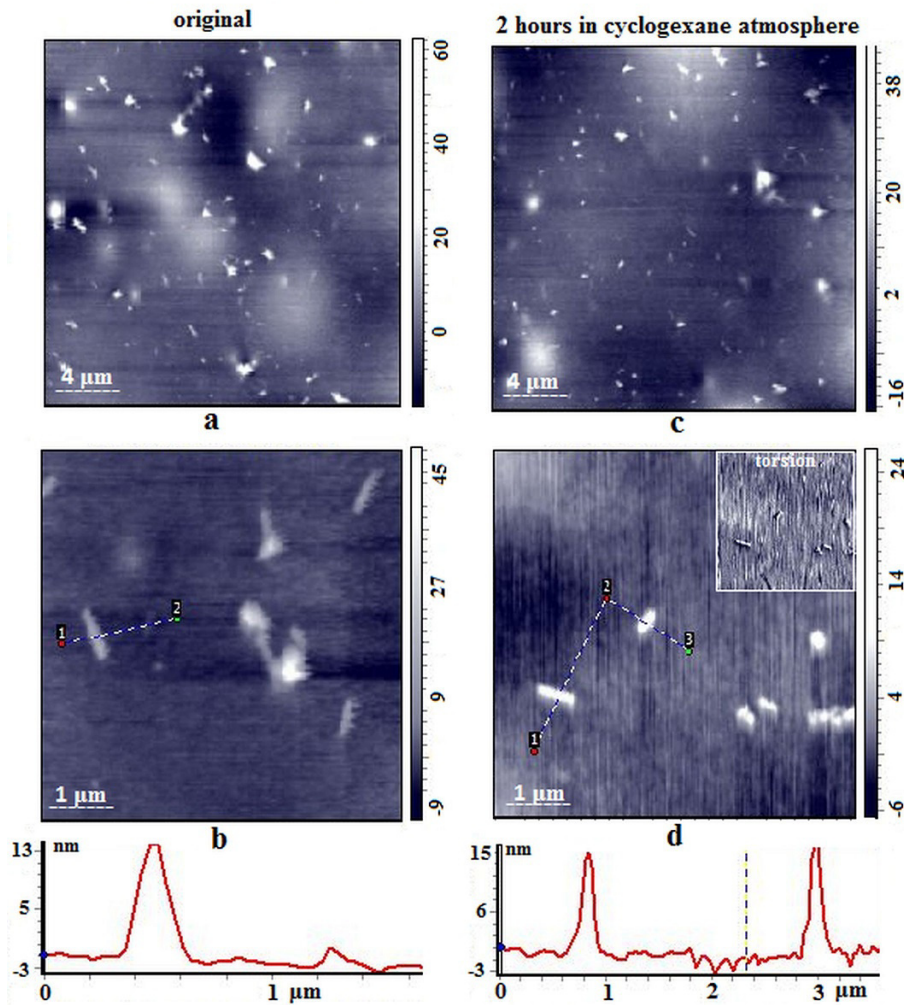


FIG. 7. AFM images of the height of the free surface of the composite: a, b – original; c, d – after 2 hours in cyclohexane atmosphere

Significant changes in the surface topography are visible in the image showing the surface facing the substrate (Fig. 8). The initial surface is characterized by the presence of a large number of cavities; besides, fragments of NTs and their replicas are clearly visible on the surface of the matrix at high magnification. After 2 hours of swelling in cyclohexane vapors, significant morphological changes are observed. Micron-sized aggregates consisting of NT associates and the swollen matrix protrude on the surface, which is seen more clearly in the image taken in the lateral force contrast mode (torsion). At the same time, there are significant changes in the morphology of the fine structure of the sample surface: the surface becomes more friable, nanoporous, the surface roughness increases.

After storage at room temperature for 20 hours, large aggregates of NTs and swollen areas of the matrix are visible over the entire surface of the composite, while the morphology of the matrix changes. The surface is smoothed, the pores are sewn up, the replicas from the fallen NTs are clearly visible.

This tendency of swelling of the film composite with subsequent smoothing of the surface is confirmed by the roughness values. Thus, for the initial film for the 12×12 micron scanning matrix, the values are $R_a = 5.3$ nm, $R_q = 8.1$ nm, after 2 hours of swelling in cyclohexane vapors – $R_a = 30.2$ nm, $R_q = 38.5$ nm, after 20 hours at room temperature $R_a = 12.7$ nm, $R_q = 19.7$ nm.

3.2.2.3. Scanning Electron Microscopy (SEM)

3.2.2.3.1. SEM of MMM. The morphology of cross sections of the nanocomposite film was studied using scanning electron microscopy (Fig. 9) before and after pervaporation.

It was important to reveal structural and morphological properties of the internal layers of the MMM, since the film was formed from the dispersion containing a solvent (N-MP), a polymer (PAI-Ac), and nanoparticles (Fe-NT). NTs were found in the inner layers of the membrane (Fig. 9) and were most clearly seen in the image of the denser film after pervaporation (Fig. 9d,e). It is interesting that the internal structure of the PAI-Ac polymer characteristic of unfilled samples and described in detail by us in [38] is most clearly visible in the samples that passed the pervaporation test.

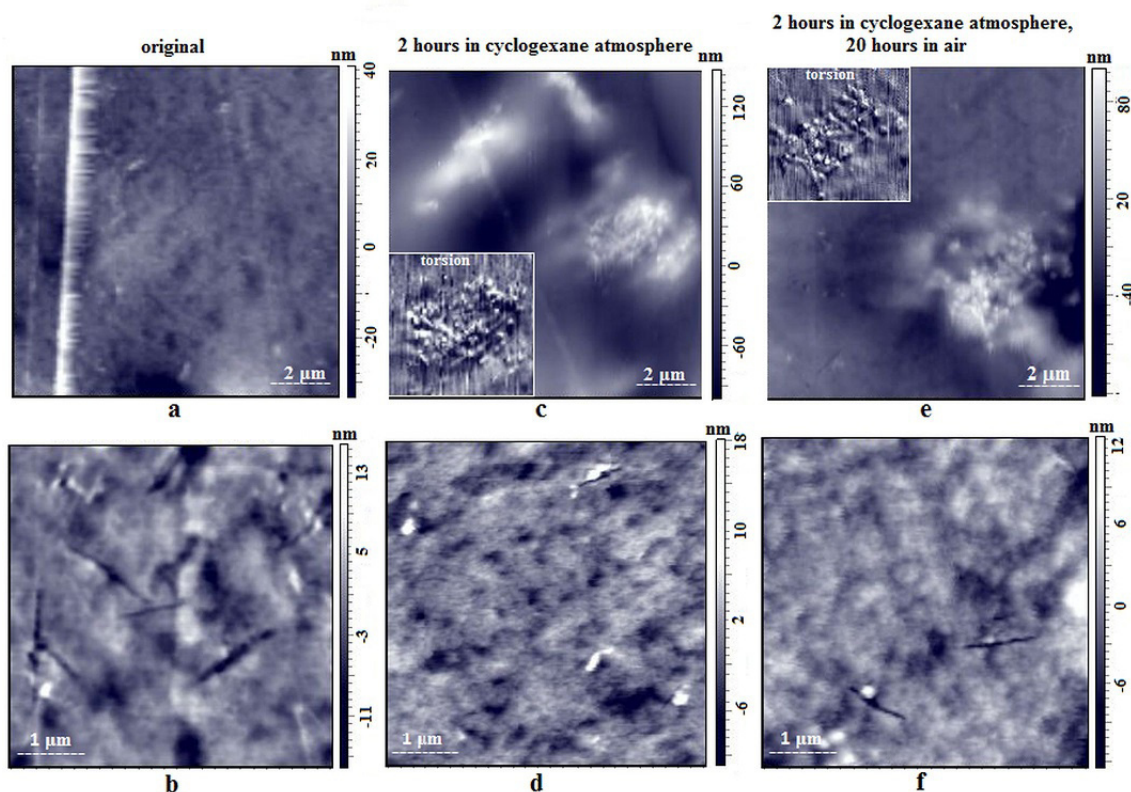


FIG. 8. AFM images of the height of the surface to substrate of the composite: a, b – original; c, d – after 2 hours in cyclohexane atmosphere; e, f – after 2 hours in cyclohexane atmosphere, then 20 hours in air

Apparently, in the case of samples of the first type, the introduction of iron-containing NTs does not cause significant changes in the structural and morphological characteristics of PAI-Ac. However, the formed films are loose and contain cavities, which are larger than those typical of unfilled PAI. After pervaporation and drying, the sample shrinks to form a film of denser morphology. In this case, the NTs come closer together, their concentration in the matrix increases; as a result, they are clearly visible in the inner layers of the membrane (Fig. 9e).

During the pervaporation process and further drying, the film changed its size at least twice, which led to the appearance of pronounced cracks and internal defects. Therefore, it is understandable why after repeated introduction into the pervaporation cell, the membrane failed the vacuum test and was no longer suitable for measurements.

3.2.2.3.2. SEM of the model composite. The question remained as to the state of NTs of this type after immersion in the polymer matrix using the method described in the Experimental Section. To investigate this issue, model composites with a high content of NTs were prepared in the presence of PAI-Ac. This question arose because membranes and model composites were formed by casting dispersions in N-MP; according to the literature data, metal-containing hydrosilicate NTs can change their characteristics in the presence of solvents [39].

As shown in Fig. 10, the polymer covers the entire surface of the sample despite the fact that the inorganic phase (which consists of a set of nanoparticles) predominates in this sample. The NTs coated with a thin layer of polymer are clearly visible in the near-surface region of the sample.

Micrographs of the cross section and internal layers of the sample show that the polymer has penetrated into the sample and formed regions in the interlayer space bordering the inorganic phase. This distribution of the polymer and inorganic phases is confirmed by the data of energy dispersive analysis (EDAS, Table 2) that correspond to the image of the surface of the inner layer of the model film at a magnification of 2000 (Fig. 11). It can be seen that in the regions corresponding to spectra 1, 2, 3, 4, the average concentration of nanoparticles is low (silicon concentration 2.2–2.8 wt.%), and in the “point” regions corresponding to spectra 5, 6, 7, nanoparticles are localized. Spectrum 8 shows the presence of voids in the interlayer space of the sample.

Thus, in this model composite, the concentration of nanoparticles is so high that it is possible to study them in a limited time using the Mössbauer method, while the concentration of the polymer and its distribution allow one to trace its influence on the state of the inorganic phase. Recall that the model composites were obtained by the same method and under the same conditions as the membranes (casting from dispersions in N-MP).

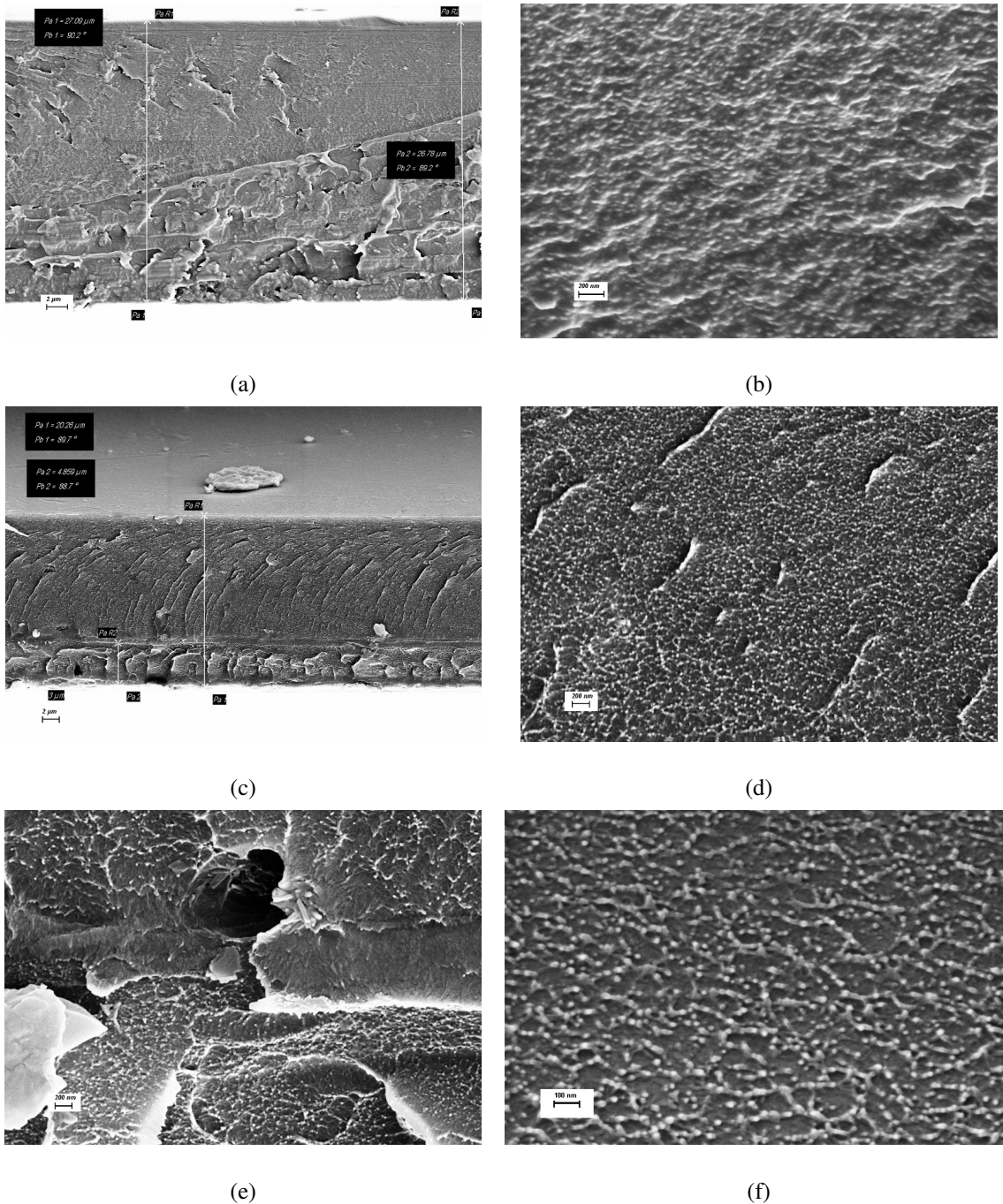


FIG. 9. SEM-images of the cross section (a – e) and internal layers (b,d,e) of a 27 μm thick MMM sample before (a,b) and after (c – e) pervaporation; SEM – image of the cross section of the PAI-Ac film (f)

It is interesting that the nature of the internal structure of the model films (Fig. 10f) is dictated by the polymer matrix, and their structural and morphological features are similar to the structure of the PAI-Ac films [38], as well as the MMM-film presented in Fig. 9.

3.2.2.4. Mössbauer spectroscopy

We attempted to use Mössbauer spectroscopy to analyze structural features of NTs immersed in a polymer matrix.

Figure 12 shows the Mössbauer spectra of chrysotile hydrosilicate NTs (original sample) and nanotubes included in the composite film (PAI-K + MgFe chrysotile NTs).

The results of the mathematical decomposition into individual subspectra of these samples are presented in Table 3. The data presented above show that the Fe ions in the samples exist in the magnetic (magnetite) and paramagnetic (chrysotile) phases. The areas under the Mössbauer absorption lines were used to calculate the distribution of total iron

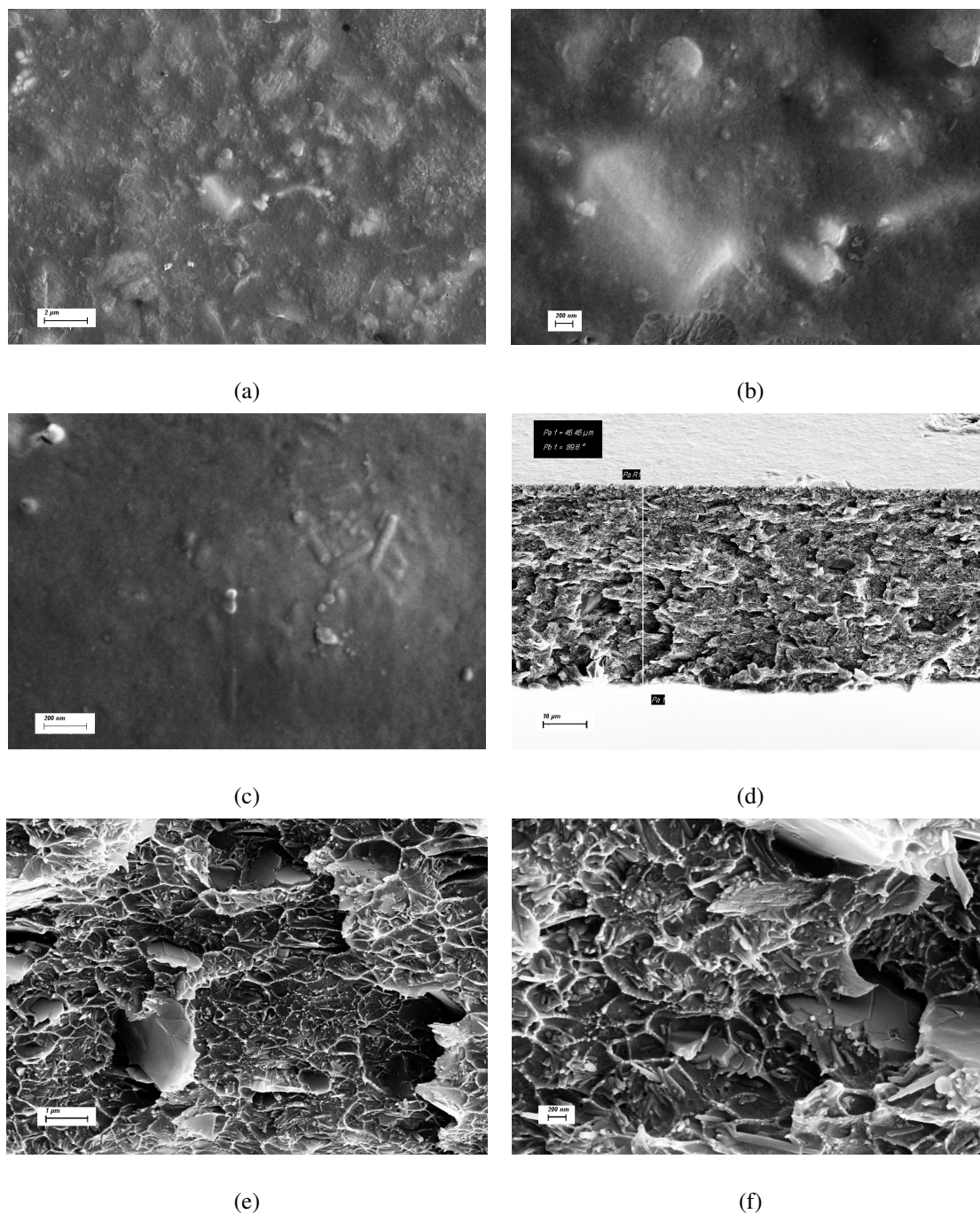


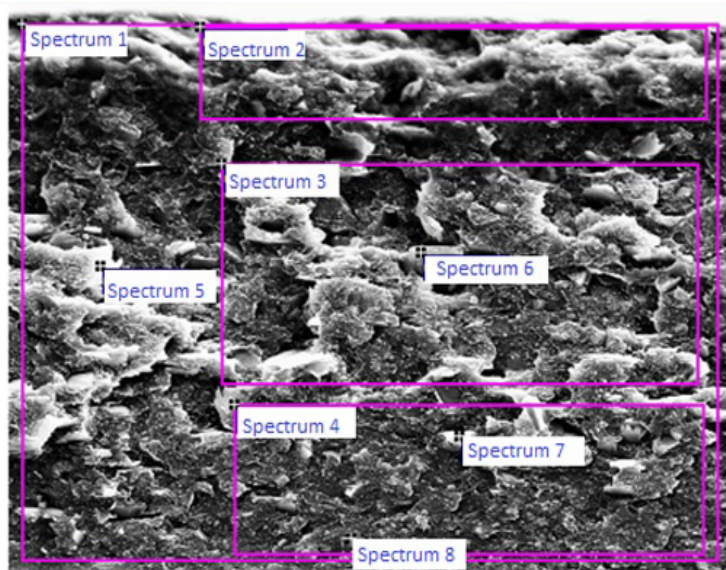
FIG. 10. SEM images of the model sample: (a, b, c) surface fragments, (d) cross-section, (e, f) internal layers

between the Fe^{2+} and Fe^{3+} states and the ratio of iron amounts in magnetite and chrysotile NTs (~ 1 in the original sample, 1.29 in the composite). It is known that magnetite is a mixed-valence system and crystallizes into an inverted spinel structure at room temperature. This structure contains tetrahedral positions with Fe^{3+} cations and octahedral positions with an equal number of randomly distributed Fe^{3+} and Fe^{2+} cations. As a result of rapid electron exchange between iron ions of different valences in the octahedral position, an intermediate electronic state with an average value of the isomer shift parameter appears. The Mössbauer spectroscopy allows one to qualitatively distinguish the distribution of Fe^{2+} and Fe^{3+} ions between tetrahedral and octahedral positions in magnetite based on the characteristic H_{eff} values (see Table 3).

The paramagnetic part of the spectrum of the initial sample consists of two doublets, which, according to the typical IS and QS values (Table 3), can be attributed to Fe ions of different valences in the tetrahedral and octahedral ($\text{Fe}^{3+}_{\text{tet}}$ and $\text{Fe}^{2+}_{\text{oct}}$) positions of the chrysotile structure. Fe^{2+} and Mg^{2+} ions are isomorphic; therefore, Fe^{2+} replaces Mg in the brucite (outer) layer of the chrysotile NT. It should be noted that inclusion of Fe^{3+} in the octahedral position was not detected in the original sample, in contrast to the spectra of natural chrysotiles of various origins, as well as those of the synthetic layered hydrosilicate of variable composition with a chrysotile structure [36]. Obviously, under the synthetic

TABLE 2. Elemental EDAS analysis (normalized; concentrations in mass %) of the surface of the inner layer of the sample in accordance with Fig. 11

Spectrum	C	N	O	Na	Mg	Si	Cl	Fe	Total
1	60.97	8.39	22.45	0.56	2.82	2.40	0.75	1.65	100.00
2	59.96	5.24	20.56	2.28	2.35	2.73	3.89	2.99	100.00
3	61.06	6.73	23.86	0.32	3.32	2.77	0.22	1.72	100.00
4	62.12	8.40	22.75	0.24	2.72	2.23	0.08	1.47	100.00
5	75.19	0.00	16.54	0.35	3.59	4.33	0.00	0.00	100.00
6	38.52	0.00	39.67	0.52	8.66	6.29	0.00	6.35	100.00
7	55.18	0.00	28.84	0.32	7.42	6.17	0.06	2.02	100.00
8	69.69	0.00	25.25	0.17	2.30	1.80	0.00	0.79	100.00
Average	60.34	3.60	24.99	0.60	4.15	3.59	0.62	2.12	100.00
Std. deviation	10.79	3.97	6.91	0.69	2.46	1.79	1.35	1.92	

FIG. 11. SEM image of the surface of the inner layer of the model sample at a magnification of $\times 2000$

conditions for the initial sample, Fe^{3+} only enters into the tetrahedral position. Thus, the possibility exists of targeted synthesis of samples with predetermined properties.

The Mössbauer parameters in the sample of chrysotile NTs included in composite films underwent minor changes. Mössbauer parameters (IS, QS, H_{eff}) remained the same within the measurement error. A slight increase in the error in the calculated values of the Mössbauer parameters $\text{Fe}^{2+}_{\text{oct}}$ in the composite sample is correlated with a decrease in the overall magnitude of the Mossbauer resonance absorption effect, which may be associated with the preparation conditions of this film composite. The $\text{Fe}^{3+}/\text{Fe}^{2+}$ ratio in the paramagnetic part of the sample in the polymer film decreased to 4.4 compared to the original sample (5.2), mainly due to a change in the relative fraction of magnetite.

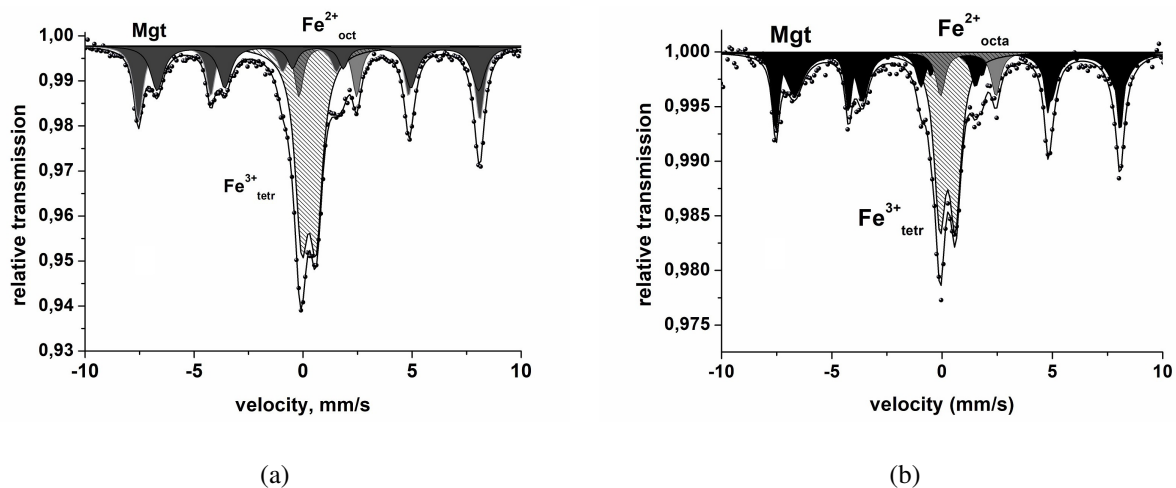


FIG. 12. Mössbauer spectra of chrysotile hydrosilicate nanotubes: a – original sample; b – nanotubes in the composite

TABLE 3. Mössbauer effect parameters of the samples (a – original sample; b – nanotubes in the composite) at 300 K

Sample	Spectral component	IS, mm/s	QS, mm/s	S, %	Heff, T
a	Fe ³⁺ tetr	0.27 ± 0.01	0.66 ± 0.01	41.56	—
	Fe ²⁺ oct	1.14 ± 0.02	2.65 ± 0.04	8.05	—
	Fe ³⁺ tetr	0.29 ± 0.01	0.02 ± 0.02	26.13	48.64 ± 0.09
	Mgt				
	(Fe ²⁺ + Fe ³⁺) oct	0.68 ± 0.02	0.01 ± 0.02	24.25	45.77 ± 0.18
b	Fe ³⁺ tetr	0.25 ± 0.04	0.70 ± 0.08	35.57	—
	Fe ²⁺ oct	1.18 ± 0.12	2.51 ± 0.25	8.08	—
	Fe ³⁺ tetr	0.27 ± 0.01	0.01 ± 0.02	25.87	48.49 ± 0.11
	Mgt				
	(Fe ²⁺ + Fe ³⁺) oct	0.66 ± 0.03	-0.02 ± 0.06	30.48	45.74 ± 0.29

Note: IS – isomer shift (Isomer shift); QS – quadrupole splitting, (Quadrupole splitting); S – relative fraction of iron atoms in a particular position; Heff – ultrafine magnetic field, tesla (Hyperfine field, T)

4. Conclusions

Introduction of hydrosilicate NTs $(\text{Mg,Fe})_3\text{Si}_2\text{O}_5(\text{OH})_4$ with a chrysotile structure into the PAI-Ac polymer matrix leads to the formation of two types of composite membranes, depending on the molecular weight of PAI. When the polymer with relatively low molecular weight is used, the so-called “composite films of the first type” are formed. They are not stable during pervaporation that involves contact with organic penetrants such as cyclohexane and ethanol. Membranes of this type exhibit high permeability to cyclohexane compared to the base polymer. However, they swell significantly during pervaporation and cannot be reused, because defects appear in films after drying. Membranes of the “second type” prepared of the polymer with higher molecular weight are stable during pervaporation. Besides, they are more permeable to polar liquids (compared to the base polymer and MMMs containing $\text{Mg}_3\text{Si}_2\text{O}_5(\text{OH})_4$ NTs). Thus, the introduction of iron-containing NTs into PAI-Ac leads to an increase in the permeability of MMM. The results obtained correlate

with the structural characteristics of the membranes. The introduction of NTs into the polymer does not cause significant changes in the structural characteristics of the nanoparticles. However, a slight increase in the amount of magnetite in NTs indicates that some part of NTs are destructed in the process of formation of the “first type composites”.

The properties of the obtained MMMs deserve further study; a possible line of investigation is introduction of iron-containing nanoparticles of other structure and morphology into the PAI-Ac polymer matrix.

References

- [1] Sreekumar T.V., Liu T., Min B.G., Guo H., Kumar S., Hauge R.H., Smalley R.E. Polyacrylonitrile Single-Walled Carbon Nanotube Composite Fibers. *Adv. Mat.*, 2004, **16** (1), 58.
- [2] Yudin V.E., Otaigbe J.U., Gladchenko S., Olson B.G., Nazarenko S., Korytkova E.N., Gusarov V.V. New polyimide nanocomposites based on silicate type nanotubes: Dispersion, processing and properties. *Polymer*, 2007, **48**, P. 1306–1315.
- [3] Zhen-Liang X.U., Li-Yun Y.U., Ling-Feng H.A.N. Polymer-nanoinorganic particles composite membranes: a brief overview. *Front. Chem. Eng. China*, 2009, **3** (3), 318.
- [4] Samad A., Lau K.Y., Khan I.A., Khoja A.H., Jaffar M.M., Tahir M. Structure and breakdown property relationship of polyethylene nanocomposites containing laboratory-synthesized alumina, magnesia and magnesium aluminate nanofillers. *J. Phys. Chem. Solids*, 2018, **120**, P. 140–146.
- [5] Li S., Lin M.M., Toprak M.S., Kim D.K., Muhammed M. Nanocomposites of polymer and inorganic nanoparticles for optical and magnetic applications. *Nano Reviews*, 2010, **1**, 5214.
- [6] Jeon I-Y., Baek J-B. Nanocomposites Derived from Polymers and Inorganic Nanoparticles. *Materials*, 2010, **3** (6), 3654.
- [7] Sawunyama L., Ajiboye T.O., Oyewo O., Onwudiwe D.C. Ceramic-polymer composite membranes: Synthesis methods and environmental applications. *Ceramics Int.*, 2024, **50**, P. 5067–5079.
- [8] Vu De Q., Koros W. J., Miller S. J. High Pressure CO₂/CH₄ Separation Using Carbon Molecular Sieve Hollow Fiber Membranes. *Industrial & engineering chemistry research* 2002, **41** (3), 367.
- [9] Mahajan R., Koros W.J., Thundiyil M. Mixed matrix membranes: important and challenging. *Membrane Technology*, 1999, **105**, 6.
- [10] Moaddeb M., Koros W.J. Occlusion of pores of polymeric membranes with colloidal silica. *J. Membrane Sci.*, 1997, **136** (1), P. 273–277.
- [11] Koros W.J., Coleman M.R., Walker D.R.B. Controlled permeability polymer membranes. *Annu. Rev. Mater. Sci.*, 1992, **22**, P. 47–89.
- [12] Singh-Ghosal A., Koros W.J. Energetic and entropic contributions to mobility selectivity in glassy polymers for gas separation membranes. *Ind. Eng. Chem. Res.*, 1999, **38**, 3647.
- [13] Pinnau I., He Z.J., Morisato A. Nanostructured poly (4-methyl-2-pentyne)/silica hybrid membranes for gas separation. *Abstr. Pap. Am. Chem. Soc. Part 2*, 2001, **222**, U368.
- [14] Nunes S.P., Peinemann K.V., Ohlrogge K., Alpers A., Keller M., Pires A.T.N. Membranes of poly(ether imide) and nanodispersed silica. *J. Membrane Sci.*, 1999, **157**, 219.
- [15] Potschke P., Fomes T.D., Paul D.R. Rheological behavior of multiwalled carbon nanotube/polycarbonate composites. *Polymer*, 2000, **41**, 3861.
- [16] Baughman R.H., Zakhidov A.A., Heer W.A. Carbon Nanotubes – the Route Toward Applications. *Science*, 2002, **297** (5582), 787.
- [17] Sholl D.S., Johnson J.K. Making High-Flux Membranes with Carbon Nanotubes. *Science*, 2006, **312** (5776), P. 1003–1004.
- [18] McGinnis R.L., Reimund K., Ren J., Xia L., Chowdhury M.R., Sun X., Abril M., Moon J.D., Merrick M.M., Park J., Stevens K.A., McCutcheon J.R., Freeman B.D. Large-scale polymeric carbon nanotube membranes with sub-1.27 nm pores. *Sci. Adv.*, 2018, **4** (3), 1700938.
- [19] Geise G.M., Paul D.R., Freeman B.D. Fundamental water and salt transport properties of polymeric materials. *Progress in Polymer Science*, 2014, **39** (1), P. 1–42.
- [20] Kononova S.V., Gubanova G.N., Korytkova E.N., Sapegin D.A., Setnickova K., Petrychkovych R., Uchytel P. Polymer Nanocomposite Membranes. *Appl. Sci.*, 2018, **8**, 1181.
- [21] Korytkova E.N., Maslov A.V., Pivovarova L.N., Drozdova I.A., Gusarov V.V. Formation of Mg₃Si₂O₅(OH)₄ nanotubes under hydrothermal conditions. *Glass Phys. Chem. (Engl. Transl.)*, 2004, **30** (1), P. 51–55.
- [22] Kononova S.V., Korytkova E.N., Romashkova K.A., Kuznetsov Y.P., Gofman I.V., Svetlichnyi V.M., Gusarov V.V. Nanocomposite based on polyamidoimide with hydrosilicate nanoparticles of varied morphology. *Russian J. of Applied Chemistry*, 2007 **80** (12), P. 2142–2148.
- [23] Skuland T., Maslennikova T., Lag M., Gatina E., Serebryakova M., Trulioff A., Kudryavtsev I., Klebnikova N., Kruchinina I., Schwarze P. E., Refsnes M. Synthetic hydrosilicate nanotubes induce low pro-inflammatory and cytotoxic responses compared to natural chrysotile in lung cell cultures. *Basic & Clinical Pharmacology & Toxicology*, 2019, **126** (2), 13341.
- [24] Korytkova E.N., Pivovarova L.N., Drozdova I.A., Gusarov V.V. Synthesis of nanotubular nickel hydrosilicates and nickel-magnesium hydrosilicates under hydrothermal conditions. *Glass Physics and Chemistry*, 2005, **31** (6), P. 797–802.
- [25] Gubanova G.N., Kononova S.V., Vylegzhanina M.E., Sukhanova T.E., Grigor'ev A.I., Romashkova K.A., Svetlichnyi V.M., Korytkova E.N., Christi M., Timpu D., Harabagiu V. Structure, morphology, and thermal properties of nanocomposites based on polyamidoimides and hydrosilicate nanotubes. *Russian J. of Applied Chemistry*, 2010, **83** (12), P. 2175–2181.
- [26] Kononova S.V., Korytkova E.N., Maslennikova T.P., Romashkova K.A., Kruchinina E.V., Potokin I.L., Gusarov V.V. Polymer-inorganic nanocomposites based on aromatic polyamidoimides effective in the processes of liquids separation. *Russ. J. Gen. Chem.*, 2010, **80**, 1136.
- [27] Gubanova G.N., Sukhanova T.E., Vylegzhanina M.E., Lavrentiev V.K., Romashkova K.A., Kutin A.A., Maslennikova T.P., Kononova S.V. Analysis of the surface morphology, structure and properties of polyamidoimide nanocomposites with tubular hydrosilicates. *J. of Surf. Invest.: X-ray, Synchrotron and Neutron Techniques*, 2017, **11** (5), 1022.
- [28] Gusinskaya V.A., Koton M.M., Batrakova T.V., Romashkova K.A. Poly(amino) imides based on symmetrical and asymmetrical imido acid dichlorides. *Polymer Science U.S.S.R.*, 1976, **A18** (12), P. 3062–3068.
- [29] Korytkova E.N., Pivovarova L.N., Semenova O.E., Drozdova I.A., Povinich V.F., Gusarov V.V. Hydrothermal synthesis of nanotubular Mg-Fe hydrosilicate. *Russian J. of Inorganic Chemistry*, 2007, **52** (3), P. 338–344.
- [30] Kononova S.V., Kremnev R.V., Suvorova E.I., Baklagina Y.G., Volchek B.Z., Uchytel P., Shabsels B.M., Romashkova K.A., Setnickova K., Reznickova J. Pervaporation membranes with poly(γ -benzyl-L-glutamate) selective layers for separation of toluene–n-heptane mixtures. *J. Membr. Sci.*, 2015, **477**, 14.
- [31] Eckhard Bill, in *⁵⁷Fe-Mössbauer Spectroscopy and Basic Interpretation of Mössbauer Parameters*, (Eds: Crichton R.R., Louro R.O.), Elsevier, 2013, **5**, P. 109–130.
- [32] Eckhard Bill, in *⁵⁷Fe-Mössbauer spectroscopy and basic interpretation of Mössbauer parameters*, (Eds: Crichton R.R., Louro R.O.), Elsevier, 2020, **6**, P. 201–228.

- [33] Boulatov F.M., Ivoilova E.Kh. Structural features of chrysotile asbestos according to Mössbauer spectroscopy data. *Mineralogical J.*, 1985, **7** (2), P. 22–29.
- [34] Ristić M., Czako-Nagy I., Musić S., Vértes A. Spectroscopic characterization of chrysotile asbestos from different regions. *J. of Molec. Struct.*, 2011, **993**, 120.
- [35] Lemos B.R.S., Teixeira A.P.C., Ardisson J.D., Macedo W.A.A., Fernandes-Outon L.E., Amorim C.C., Moura F.C.C., Lago R.M. Magnetic Amphiphilic Composites Applied for the Treatment of Biodiesel Wastewaters. *Appl. Sci.*, 2012, **2** (2), 513.
- [36] Krasilin A.A., Panchuk V.V., Semenov V.G., Gusarov V.V. Formation of variable-composition iron(III) hydrosilicates with the chrysotile structure. *J. of Gen. Chem.*, 2016, **86** (12), 1943.
- [37] Kozlov V.S., Maslennikova T.P., Korytkova E.N., Kononova S.V. Mössbauer study of iron ions localization in the structure of synthetic chrysotile-asbestos hydrosilicate nanotubes. *Neutron Scattering in Condensed Matter Research (RNICS-2021)*, Russia, Ekaterinburg, 2021, **306**.
- [38] Gubanova G.N., Timpu D., Cristea M., Kononova S.V., Korytkova E.N., Sapegin D.A., Saprykina N.N., Volkov A.Y., Klechkovskaya V.V. Nanocomposites Based on Poly(Amide-Imide) Matrix with Na–Mg Triple Chain Hydrosilicate. *Crystallography Reports*, 2021, **66** (7), 1185.
- [39] Kryazheva K.S., Korytkova E.N., Maslennikova T.P., Ugolkov V.L. Interacton of chrisotyl nanotubes with water-alcohol solutons at different temperature-time parameters. *Glass Phys. Chem.*, 2012, **38** (1), 122.

Submitted 2 April 2024; revised 5 April 2024; accepted 6 April 2024

Information about the authors:

Svetlana V. Kononova – Institute of Macromolecular Compounds Russian Academy of Science, 199004, Bolshoy pr. 31, St. Petersburg, Russia; ORCID 0000-0001-5468-3909; svetlanavkononova@gmail.com

Galina K. Lebedeva – Institute of Macromolecular Compounds Russian Academy of Science, 199004, Bolshoy pr. 31, St. Petersburg, Russia; ORCID 0000-00002-2384-1422; constanta2011.lebedeva@mail.ru

Valery S. Kozlov – Petersburg Nuclear Physics Institute named by B.P. Konstantinov of National Research Centre “Kurchatov Institute”, Gatchina, Russia; kozlov_vs1@pnpi.nrcki.ru

Eleonora N. Korytkova – Russian Academy of Science, Grebenshchikov Institute of Silicate Chemistry, St. Petersburg, Russia; elkor@list.ru

Tatyana P. Maslennikova – Russian Academy of Science, Grebenshchikov Institute of Silicate Chemistry, St. Petersburg, Russia; ORCID 0000-0001-9459-8960; sveta.k@hq.macro.ru

Elena V. Kruchinina – Institute of Macromolecular Compounds Russian Academy of Science, 199004, Bolshoy pr. 31, St. Petersburg, Russia; ORCID 0000-0002-3628-0863; evkruchinina@mail.ru

Elena N. Vlasova – Institute of Macromolecular Compounds Russian Academy of Science, 199004, Bolshoy pr. 31, St. Petersburg, Russia; ORCID 0000-0002-4644-0445; spectra@imc.macro.ru

Natalia N. Saprykina – Institute of Macromolecular Compounds Russian Academy of Science, 199004, Bolshoy pr. 31, St. Petersburg, Russia; ORCID 0000-0002-9240-1690; nataly-saprykina@yandex.ru

Galina N. Gubanova – Institute of Macromolecular Compounds Russian Academy of Science, 199004, Bolshoy pr. 31, St. Petersburg, Russia; ORCID 0000-0003-548-9976; gubanovagn@yandex.ru

Milana E. Vylegzhanina – Institute of Macromolecular Compounds Russian Academy of Science, 199004, Bolshoy pr. 31, St. Petersburg, Russia; ORCID 0000-0002-5468-7595; v.e.milana@gmail.com

Vasiliy T. Lebedev – Petersburg Nuclear Physics Institute named by B.P. Konstantinov of National Research Centre “Kurchatov Institute”, Gatchina, Russia; ORCID 0000-0003-4894-0862; lebedev_vt@pnpi.nrcki.ru

Conflict of interest: the authors declare no conflict of interest.

Green approach to production of porous char adsorbents via oxidative carbonization in fluidized catalyst bed

Petr M. Yeletsky, Nikolay A. Yazykov, Yury V. Dubinin, Maksim M. Borodaevskiy, Svetlana A. Selishcheva, Vadim A. Yakovlev

Federal Research Center Boreskov Institute of Catalysis SB RAS, Novosibirsk, Russia

Corresponding author: Petr M. Yeletsky, yeletsky@catalysis.ru

ABSTRACT A green and energy-efficient technique for production of porous carbon-mineral chars from agricultural wastes (rice husk, wheat bran) and sedimentary carbonaceous feedstocks (high-ash peat, coal) was developed. It is based on partial combustion in fluidized bed of a deep oxidation catalyst at low temperatures (465 – 600 °C). This technique yields porous chars with an elevated mineral content that depends on a feedstock used, and gaseous products of complete oxidation. It was found that the obtained chars have developed porosity with BET specific surface area of ca. 50 – 170 m²g⁻¹, pore volume of 0.05 – 0.17 ml·g⁻¹, and ash content of 16 – 79 wt. %. They were additionally characterized by TGA and FTIR. Their testing as adsorbents for heavy metal ions (by the example of Cu²⁺) and organic dyes (by the example of methyl green) revealed that their adsorption capacities are comparable to those of chars produced by the conventional pyrolytic approaches.

KEYWORDS biochar, biomass, rice husk, bran, fluidized catalyst bed, composite

ACKNOWLEDGEMENTS The work was supported by the Ministry of Science and Higher Education of the Russian Federation within the governmental order for Boreskov Institute of Catalysis (project FWUR-2024-0038). The authors also thank Dr. Roman B. Tabakaev from University of Tyumen for providing feedstock (wheat bran and high-ash peat).

FOR CITATION Yeletsky P.M., Yazykov N.A., Dubinin Y.V., Borodaevskiy M.M., Selishcheva S.A., Yakovlev V.A. Green approach to production of porous char adsorbents via oxidative carbonization in fluidized catalyst bed. *Nanosystems: Phys. Chem. Math.*, 2024, **15** (2), 285–299.

1. Introduction

Nowadays, a lot of literature is devoted to the study of various processes of conversion of plant biomass to obtain solid carbonaceous products (biochar) that find applications in many fields of science and technology. Biochar is considered as a cheap environmentally friendly adsorbent with a developed porous structure and a high content of oxygen-containing surface functional groups. In addition, it also used to increase soil fertility and for remediation, for wastewater treatment, as a feedstock for activated carbons, as well as an energy carrier with a higher calorific value and density than the feedstock [1, 2]. Biochar from plant biomass can be obtained by gasification [3], hydrothermal carbonization [4] as well as various types of pyrolysis – torrefaction [5], slow and fast pyrolysis with both the conventional heating [6, 7], and microwave one [8]. Almost all of the above approaches are characterized by the need to create an environment (e.g., inert or aqueous) as well as supplying energy on the heating. Currently, pyrolysis is considered to be a more attractive process for obtaining these materials. Depending on the process time together with the temperature, this approach can be divided into the following types: slow ($t = 5 - 30$ min at $T = 300 - 600$ °C), intermediate ($t = 10 - 30$ s at $T = 500 - 600$ °C), fast ($t < 2$ s, at $T = 450 - 600$ °C) and flash pyrolysis ($t < 0.5$ s at $T = 800 - 1000$ °C) [9]. The last two types of pyrolysis are usually carried out in a fluidized bed of a heat carrier, which is usually quartz sand. Particles of raw materials are suspended in a fluidized bed of a heated heat carrier, due to which the intense heat and mass transfer is attained. These properties of the fluidized bed make it suitable for the processing of particulate feedstock. In addition, processes using fluidized bed reactors are very flexible in terms of feed calorific value, moisture content, particle size, density and heteroatom content [10]. A significant increase in the efficacy of this process can be achieved by carrying it out in the presence of oxygen, as well as using particles of a catalyst instead of the sand. Partial oxidation allows the process to be carried out in an auto- or exothermic mode, i.e. to reduce power inputs, or even – to receive heat energy, and the use of catalysts – more efficiently control the process direction [11]. However, currently, catalysts are rarely used for biomass pyrolysis in a fluidized bed. Except zeolite ZSM-5 that utilized to increase the yield of fast pyrolysis oil [11, 12], there are practically no other examples of utilization of catalysts of other formulations. Therefore, the search and application of more suitable and stable catalytic systems is urgent.

At the Boreskov Institute of Catalysis, the technology based combustion in a fluidized bed of a deep oxidation catalysts has been developed, that was successfully tested for combustion of various fuels [13, 14], including such difficult

to utilize ones like shale heavy coal-tar products [15], heavy high-sulfuric oils [16, 17], as well as sewage sludge [18]. The use of the deep oxidation catalyst for fuel combustion allows heat production and extraction to be carried out within the same fluidized bed at a near stoichiometric air-to-fuel ratio. Furthermore, this technology can be related to truly green, since:

- all the combustion products are being practically completely oxidized to CO₂ and water, with a content of harmful substances within the Environmental Standards;
- allows for reduction of combustion temperature from 800 – 1000 °C to 450 – 750 °C, thus diminishing requirements to heat resistance of the construction materials, as well as avoiding the high-temperature NO_x formation.

Thus, all the above advantages make this technology suitable for clean, facile and energy-efficient production of char from biomass and other carbon-containing feedstocks [19].

Recently, in the previous work, a set of chars from two biomass wastes (wheat bran and rice husk) as well as two sedimentary feedstocks (highly-mineralized peat, and coal) were obtained via partial combustion in the fluidized catalyst bed (FCB) reactor at 465 – 600 °C and evaluated as precursors of porous carbons via acid leaching of the char mineral phase [20]. The goal of this work is to investigate the obtained materials with a wider set of characterization techniques that include FTIR and TGA, as well as estimate properties of the synthesized chars as potential adsorbents for wastewater treatment through the removal of inorganic and organic industrial pollutants. As such pollutants, heavy metal ions (by the example of Cu²⁺) and organic dyes (by the example of methyl green) were selected.

2. Material and methods

2.1. Feedstock carbonization in reactor with fluidized catalyst bed

For the study, the following feedstocks have been used: 1) wheat bran (WB) obtained from Kemerovo region (Russia); 2) rice husk (RH, Krasnodar region, Russia); 3) highly mineralized peat Sukhovskoy from deposit Sukhovskoye (Tomsk region, Russia); 4) coal, grade DOMSSH from “Vinogradovsky” coal mine (Kemerovo region, Russia). The composition of the feedstocks, including their mineral component, is provided in Tables 1 – 2. The properties of the used WB are presented in more detail in [21], peat Sukhovskoy – in [22], and RH – in [23].

TABLE 1. Composition of the used feedstocks

Feedstock	W^a , wt. %	A^{d2} , wt. %	V^{daf3} , wt. %	FC^{daf4} , wt. %	CHNS-O-composition, wt. %				
					C^{daf}	H^{daf}	N^{daf}	S^{daf}	O^{daf5}
WB	8.6	6.9	81.0	12.1	49.14	6.66	3.30	0.07	40.83
RH	5.0	19.5	65.0	15.5	51.55	6.83	0.06	0.02	41.54
Peat	9.9	22.8	74.8	2.4	52.06	6.31	3.58	0.20	37.85
Coal	14.9	8.3	35.8	55.9	77.09	5.43	1.98	0.95	14.55

¹ – moisture content; ² – ash content on dry matter; ³ – volatile matter; ⁴ – fixed carbon; ⁵ – calculated by difference

TABLE 2. Composition of ash of the used feedstocks in recalculation to oxides of the corresponding elements (wt. %). WB and peat – according to the results of energy dispersive X-ray fluorescence (EDXRF) [21], RH – according to ICP-OES [23]; and coal – provided by the supplier

Feedstock	SiO ₂	Al ₂ O ₃	Fe ₂ O ₃	CaO	MgO	Na ₂ O	K ₂ O	TiO ₂	Mn ₂ O ₃	P ₂ O ₅	SO ₃
WB	1.74	26.3	0.41	0.93	16.3	28.6	17.9	–	–	7.9	–
RH	95.8	0.11	0.12	1.06	0.33	0.3	2.17	–	0.08	–	–
Peat	3.8	6.85	8.53	39.8	11.1	23.2	0.26	–	–	6.51	–
Coal	54.4	23.8	7.07	5.44	1.34	0.44	1.39	1.1	0.07	0.95	4

The previous studies have shown that mineral component of WB and RH is X-Ray amorphous, while those of coal includes quartz and those of peat contains CaCO₃ and CaO [20].

Carbonization of the feedstocks in air flow was carried out using the laboratory installation set up equipped by the fluidized catalyst bed reactor with a deep oxidation catalyst (Fig. 1). The catalyst was supplied by the Engineering Center of the Boreskov Institute of Catalysis and represents CuO–Cr₂O₃/γ-Al₂O₃ spherical particles with a diameter of 1.5 –

2.0 mm and contain Cr_2O_3 – 6.5 wt. % + CuO – 3.5 wt. %. Its BET specific surface area is $115 \text{ m}^2\text{g}^{-1}$, pore volume – $0.3 \text{ ml}\cdot\text{g}^{-1}$ and mean pore size – 10.5 nm. The installation includes a feedstock tank, from which, via of a screw driver, a feedstock is fed into a fluidized bed reactor. All the raw materials were previously ground to a particle size less than 1 mm. The FCB reactor is 75 mm i.d. and loaded with 1000 mm of the height of the fluidized catalyst bed ($\sim 3.5 \text{ L}$ in volume). Preheated airflow is supplied to the bottom of the reactor and controlled by rotameters. After the reactor outlet, the carbonized feedstock is separated from the exhaust in the cyclone and falls into the collecting tank. Carbonization trials were carried out in isothermal mode along with the bed height.

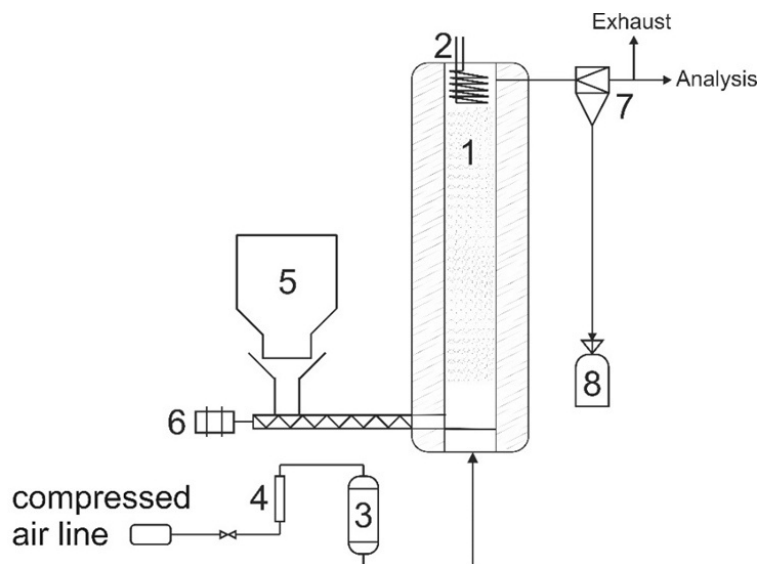


FIG. 1. A scheme of laboratory installation for combustion of solid fuels in a fluidized bed of catalyst. 1 – reactor; 2 – heat exchanger; 3 – electric air heater; 4 – rotameter; 5 – feedstock tank; 6 – screw feeder; 7 – cyclone; 8 – carbonized feedstock collection tank

Sample designations: feedstocks combusted in the FCB reactor are designated as “XTTT”, where “X” is the abbreviation of a feedstock (X = P – peat, C – coal, B – wheat bran, and RH – rice husk) and “TTT” designates the carbonization temperature – 465, 550 or $600 \text{ }^\circ\text{C}$.

2.2. Characterization techniques

The elemental composition of samples was determined by means of a VARIO EL CUBE CHNS analyzer (Elementar Analysensysteme GmbH, Germany).

The porous structure of the chars was characterized with nitrogen adsorption at 77 K. Nitrogen adsorption isotherms were measured by a surface area and pore size analyzer Autosorb 6B (Quantachrome Instruments, Austria). Before the measurements, all the samples were degassed under vacuum to remove moisture and other adsorbed contaminations. The char samples were pretreated at $150 \text{ }^\circ\text{C}$ for 4 h. The specific surface area was calculated by the standard BET method according to IUPAC recommendations [24], micropore volume was estimated by the α_S -plot method using the non-porous carbon Cabot BP 280 as a reference material [25]. The differential pore size distributions (PSD) were computed by means of Quenched Solid Density Functional Theory Method (QSDFT) equilibrium model for nitrogen adsorption at 77 K in cylinder-like pores of carbon, applied to the adsorption branch of an isotherm, using software supplied with the above instrument.

Samples of the chars were investigated by FTIR spectroscopy using a Bruker Alpha II spectrometer equipped the Platinum Diamond ATR unit (Bruker, USA), in the diapason of $400 - 4000 \text{ cm}^{-1}$ with a resolution of 4 cm^{-1} and accumulation of 32 scans.

Synchronous thermal analysis (STA), which includes simultaneous thermogravimetric determination (TG) of differential scanning calorimetry (DSC) and mass spectrometric analysis of the recovered gas (ABG-MS), was performed on a STA 449F1 Jupiter® instrument combined with a quadrupole mass-spectrometer QMS 403D Aëolos® (NETZSCH, Germany). The experiments were carried out using a high-temperature furnace with a graphite heater and water cooling. We used a measuring sensor DSC/TG Cp S TC: type S ($0 \dots 1650 \text{ }^\circ\text{C}$). The experiments were carried out in open Al_2O_3 crucibles, within a temperature range of $30 - 900 \text{ }^\circ\text{C}$, in the Ar atmosphere with the heating rate of $10 \text{ }^\circ\text{C}/\text{min}$, and the Ar flow rate of $20 \text{ ml}/\text{min}$. The processing of the experimental data was carried out using the Proteus analysis software package (NETZCH, Germany).

2.3. Adsorption tests by methyl green and Cu^{2+}

As model pollutants, aqueous solutions of methyl green (MG, Fig. 2) with an initial concentration of $0.019 \text{ g}\cdot\text{L}^{-1}$ and copper sulfate with a concentration of copper ions of $0.20 \text{ g}\cdot\text{L}^{-1}$ were used.

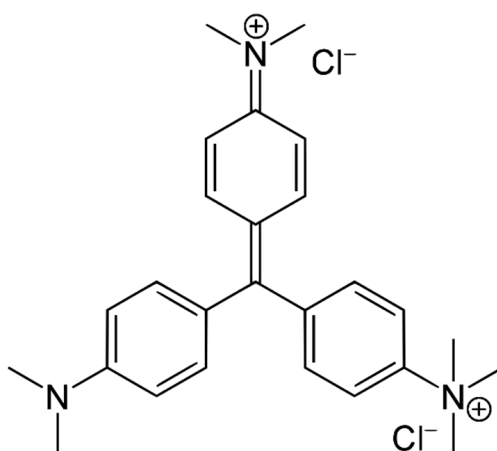


FIG. 2. Structure formula of methyl green

The experiments were carried out in glass vials with a volume of 35 ml. Acidity of the medium during the adsorption was controlled using a buffer solution with $\text{pH} = 4$. A weighed portion of a sorbent (15 mg) was added to a solution with the known concentration, followed by leaving the mixture without access to the light for a specified period of time. Upon the process finishing, an adsorbent was separated on a paper filter. The contaminant concentration in the filtrate was measured by visible spectrophotometry on a Cary 300 instrument (Agilent Technologies Inc., USA) in quartz cuvettes with an optical path length of 1.0 cm. The following extinction coefficients were determined in the calibration tests: $4.08 \cdot 10^4 \text{ L}\cdot\text{g}^{-1}\cdot\text{cm}^{-1}$ for MG (632 nm); and $5.00 \cdot 10^4 \text{ L}\cdot\text{g}^{-1}\cdot\text{cm}^{-1}$ for copper ions (805 nm). When determining the adsorption capacity, solutions with a volume of 25 ml were left for a week.

3. Results and discussion

Carbonization of biomass and sedimentary feedstocks in fluidized catalyst bed reactor allowed for obtaining of a set of porous carbon-mineral char samples. Their yields and ash contents (used as the basis for calculation of the yields) are presented in Fig. 3.

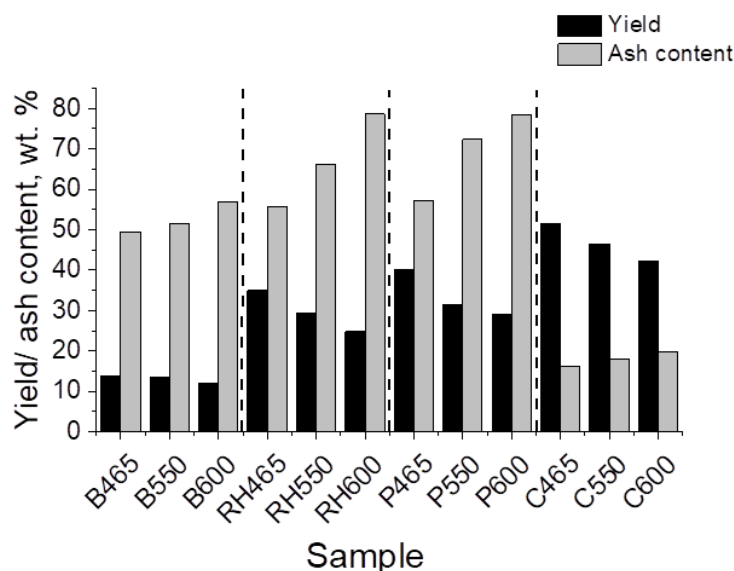


FIG. 3. Yield and ash content of chars from the feedstock carbonized in FCB reactor at 465 – 600 °C

As can be seen, in all the cases, as expected, with the temperature increase, yield of chars from every feedstock drops and mineral phase content increases. Carbonization of wheat bran in the fluidized catalyst bed resulted in the lowest

yield of the chars compared to other feedstocks. This can be caused by such factors as a low content of fixed carbon (12.1 wt. %) and the highest contents of alkaline metals (> 46 wt. %, in the recalculation to oxides) well-known as gasification catalysts [26, 27]. Furthermore, the high content of dispersed alumina (26.3 wt. %) can also contribute to gasification via facilitating processes of cracking of the biopolymers [28].

For RH, yields of the biochar are significantly higher that seems to be due to the initially high content of the mineral component (19.5 wt. %) consisting mainly of pure silica, which does not exhibit any notable catalytic activity in the carbonization conditions. This SiO₂ forms a rigid mineral matrix hindering the diffusion of volatile carbonization products, making them to transform inside RH particles.

Yields and ash contents in carbonized peat are similar to RH despite it has the lowest fixed carbon content and a high content of Na. This can also be caused by the initially high ash content (22.8 wt. %) comparable to those of RH, and the same probable diffusion limitations for volatile oxidative pyrolysis products from the feedstock particles, thus, leading to the pyrolysis processes inside the solid feedstock particles.

For the coal, the highest yields with the lowest ash contents are observed. At the similar to WB ash content, coal contains the highest fixed carbon content (*ca.* 56 wt. %) due to the highest maturation degree. Thus, the carbon-containing phase of the coal can be characterized by the highest stability to both pyrolysis and oxidation that results in the lowest burn off degree compared to other raw materials. For example, it was previously found that another feedstock, having similar composition of carbon-containing phase – petroleum coke, was impossible to be burnt completely in the fluidized catalyst bed reactor even at 750 °C using similar deep oxidation catalyst [29].

The obtained chars were characterized by the following techniques.

3.1. Low-temperature nitrogen adsorption

BET specific surface area, and total pore volume of the samples are presented in Fig. 4 (in more detail, texture characteristics are provided in Table A1), their nitrogen adsorption isotherms and pore size distributions are shown in Figs. 5 – 8. In the case of wheat bran, the porous chars were found to have BET specific surface area (A_{BET}) of *ca.* 40 – 90 m²g⁻¹ and predominantly mesoporous texture (Fig. 5).

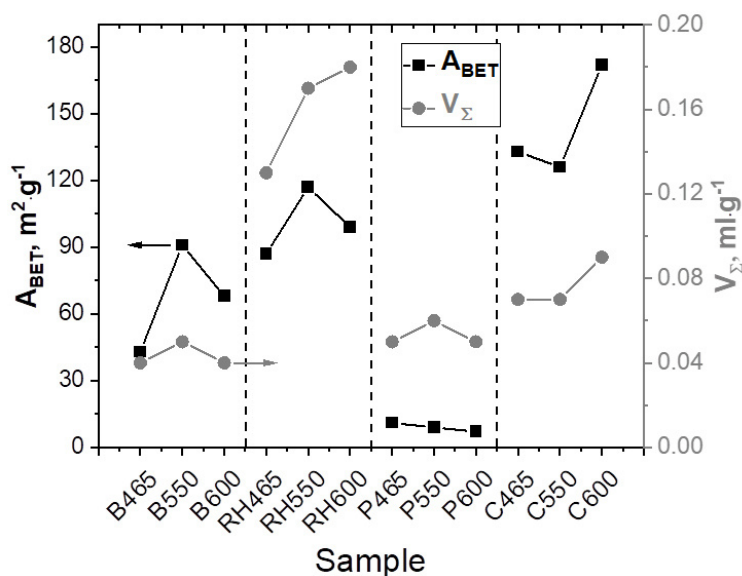


FIG. 4. A_{BET} and total pore volume of char samples from wheat bran (B465 – B600), rice husk (RH465 – RH600), peat (P465 – P600) and coal (C465 – C600) obtained via carbonization in FCB reactor at 465 – 600 °C

The nitrogen adsorption isotherms can be related to Type II [30], they indicate the presence of meso- and macropores in the samples. Their desorption branches, as can be seen, do not follow the adsorption ones most probably due to the phenomenon of swelling and/or deformation [31]. The maximally developed porosity of the sample obtained at 550 °C can be explained by the fact that it mainly depends on the carbon phase porosity, which is, probably, not developed enough at the lowest temperature, and at 600 °C the effect of mineral phase seems to dominate. The carbon-silica biochar samples from RH have more mesoporous structure (Fig. 6). Nitrogen adsorption isotherms appeared to be similar to those of WB, including the swelling effect.

The char samples have A_{BET} of *ca.* 90 – 120 m²g⁻¹ and a high pore volume of 0.13 – 0.18 cm³g⁻¹. In this case, their A_{BET} values are also maximal at 550 °C. However, unlike bran, they are higher and closer, probably due to the greater dispersity of the silica phase, which is less prone to sintering due to the high purity, and with an increase in its contribution at 600 °C, A_{BET} also decreases, but to a lesser extent.

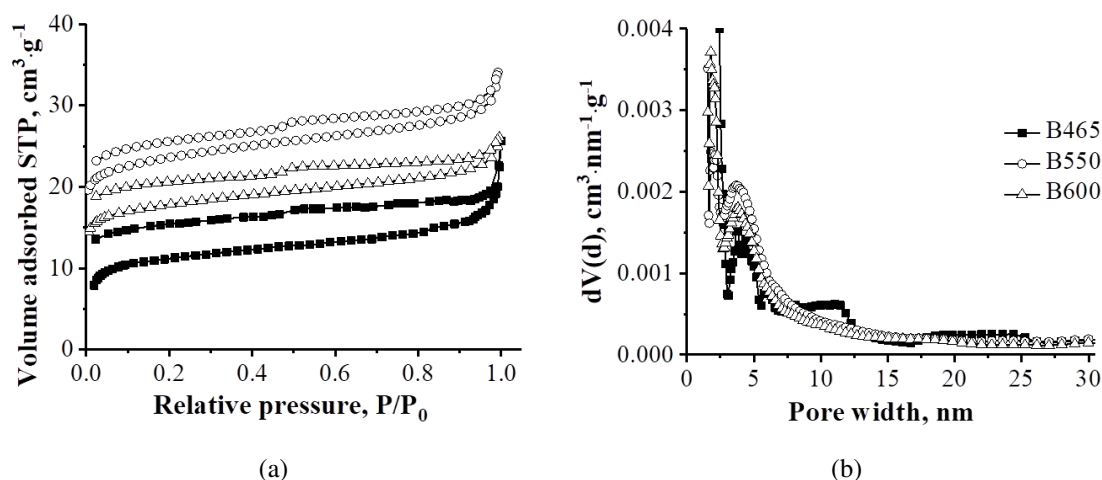


FIG. 5. Nitrogen adsorption isotherms (a) and differential pore size distributions (b) on biochars obtained from wheat bran via carbonization in the FCB reactor at 465 – 600 °C

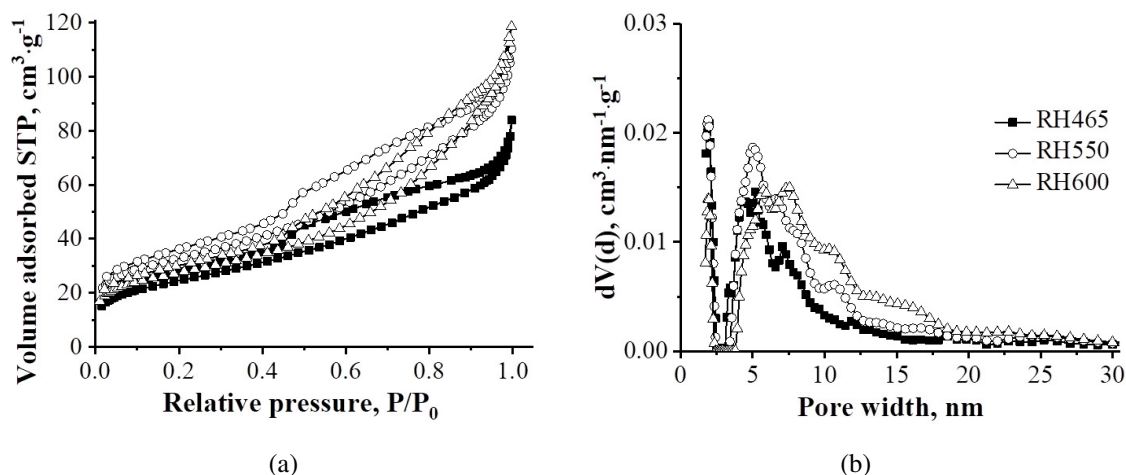


FIG. 6. Nitrogen adsorption isotherms (a) and differential pore size distributions (b) on biochars obtained from rice husk via carbonization in the FCB reactor at 465 – 600 °C

Peat-derived chars were found to be mesoporous and having a low A_{BET} (ca. $10 \text{ m}^2 \text{ g}^{-1}$). The adsorption isotherms are close to Type III [30], indicating on a poorly developed porosity and the presence of large mesopores (Fig. 7). This, probably, points on the fact that the carbon-containing phase is burnt out/decomposed around the mineral phase particles evenly, without porous structure development. The mineral phase is composed of large non-porous particles that seem to be practically not contributing to the porosity. Furthermore, the low-developed porosity can be connected with the fact that unlike biomass feedstocks, carbon-containing phase of peat is represented by partially repolymerized components of biomass practically not forming porous structure during carbonization, only gasifying and burning out without a significant pore formation.

Coal-derived char samples appeared to have significantly different textural properties. Nitrogen adsorption isotherms and differential PSD of the samples are presented in Fig. 8. They indicate that the chars are microporous and exhibit the adsorption isotherms of Type I [30]. Similar texture characteristics of samples obtained at 465 and 550 °C, and the eminent properties of the char obtained at 600 °C can be connected with a high degree of maturation of the coal carbon-containing phase that stable to the oxidative treatment in the carbonization conditions.

Thus, the porosity development in the carbon-derived char samples is predominantly occurred due to burning off the most active, least matured fragments of the carbon-containing phase, resulted in the development mainly of microporosity.

3.2. FTIR spectroscopy

FTIR spectra of the studied chars are presented in Fig. 9. The spectra of WB-derived samples (Fig. 9a) include absorption bands of SiO_2 at 490, 880 and 1118 cm^{-1} corresponding to the bending vibration of O–Si–O, symmetric and asymmetric components of the stretching vibration of Si–O–Si, respectively [32]. Furthermore, the spectra show a band

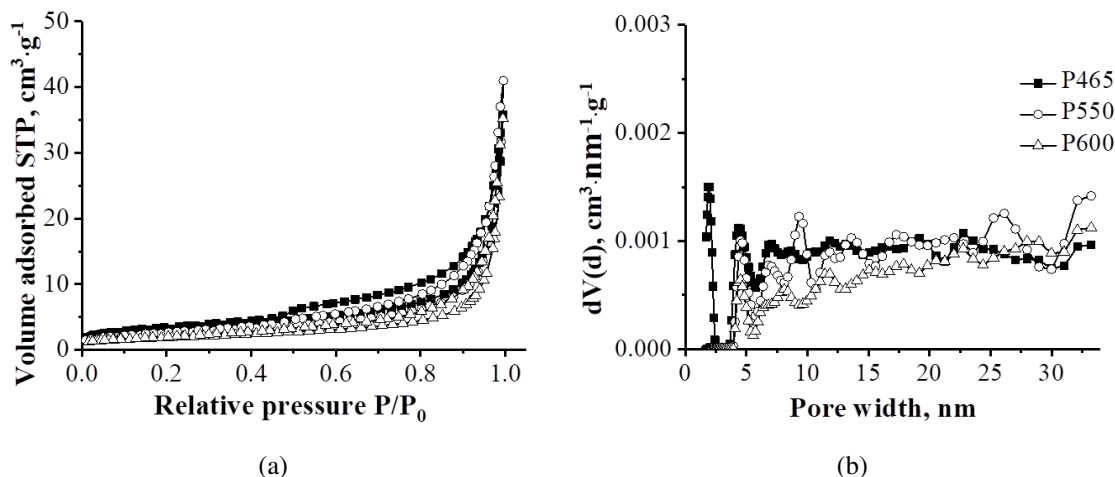


FIG. 7. Nitrogen adsorption isotherms (a) and differential pore size distributions (b) on chars obtained from Sukhovskoy highly-mineralized peat carbonized in the FCB reactor at 465 – 600 °C

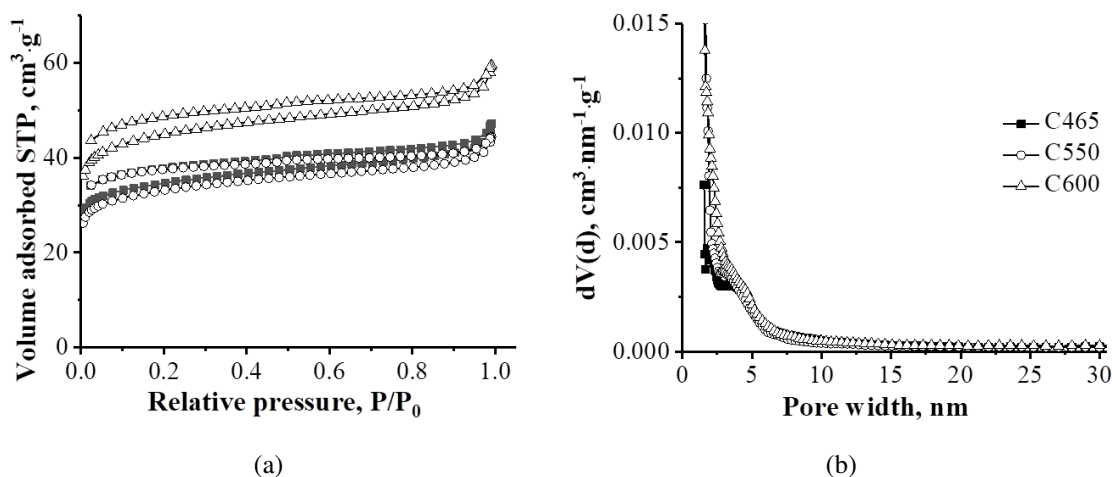


FIG. 8. Nitrogen adsorption isotherms (a) and differential pore size distributions (b) of coal carbonized in the FCB reactor at 465 – 600 °C

at 750 cm⁻¹, which can be attributed to the symmetric stretching vibrations of Si–O–Al, characteristic of aluminosilicates [33,34]. The bands corresponding to Al–O vibrations of alumina (554 and 915 cm⁻¹ for aluminum in tetrahedral and octahedral positions, respectively), in this case overlap with other bands in this region. The band at 1580 cm⁻¹ may refer to C=C stretching vibrations [35].

FTIR spectra of the RH-derived biochars (Fig. 9b) also exhibit absorption bands characteristic of silica. The bands at 450 and 1055 cm⁻¹ characterize the bending vibration of O–Si–O in the SiO₄ tetrahedron and the asymmetric stretching vibration of Si–O (Si), respectively, and the band at 793 cm⁻¹ is a superposition of bands corresponding to the symmetric stretching vibration of Si–O–Si and vibrations of silanol Si–OH and siloxane Si–O–Si–OH groups [36,37]. The broad low-intensity band in the region of 3000 – 3750 cm⁻¹ refers to the vibrations of hydrogen-bonded OH-groups formed by silanol Si–OH groups and OH-groups of water adsorbed on the surface. For the RH600 sample, this band is the least pronounced in intensity. The band at 1593 cm⁻¹ can also be referred to C=C stretching vibrations [35].

For the peat-derived chars (Fig. 10a), a number of intense bands characteristic of calcium carbonate are observed [38]. The bands at 713 and 873 cm⁻¹ refer to bending CO₃²⁻ vibrations, and the bands at 1040 and 1410 cm⁻¹ to symmetric and asymmetric stretching C–O vibrations within the CO₃²⁻ fragment [39].

For the FTIR spectra of coal (Fig. 10b), the absorption bands of silica are also observed. The band at 460 cm⁻¹, corresponding to bending vibration of O–Si–O in the silicate tetrahedrons, two bands in the area of 780 – 800 cm⁻¹, associated with symmetric stretching Si–O–Si vibrations, and the band near 1030 cm⁻¹, characterizing asymmetric symmetric stretching Si–O–Si vibrations [32,40]. A doublet in the range of 780 – 800 cm⁻¹ is characteristic of the low-temperature type of quartz [38]. The band at 1580 cm⁻¹ can be attributed to C=C stretching vibrations in polyaromatic compounds [35].

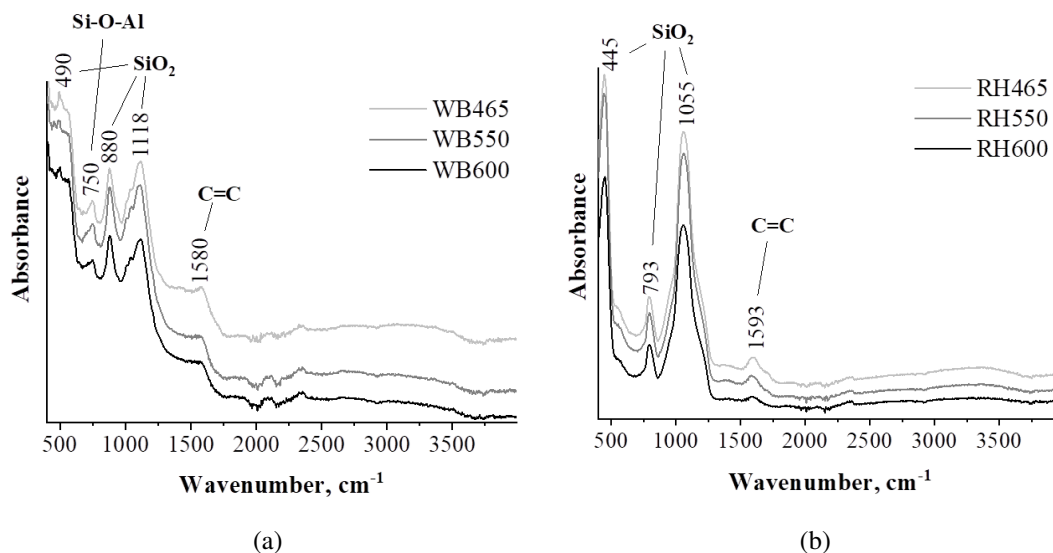


FIG. 9. FTIR spectra of WB (a) and RH (b) carbonized in fluidized catalyst bed reactor at 465 – 600 °C

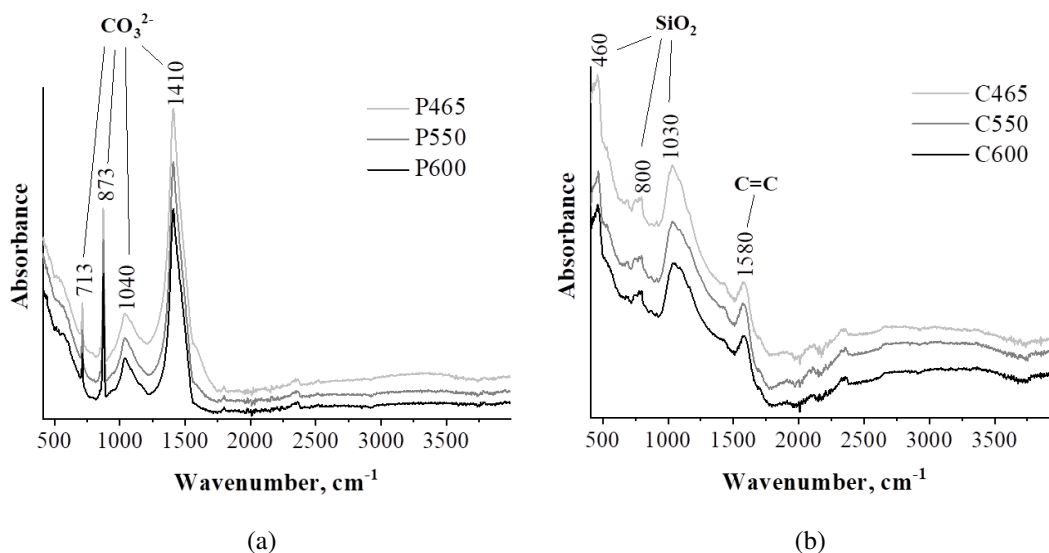


FIG. 10. FTIR spectra of peat (a) and coal (b) carbonized in fluidized catalyst bed reactor at 465 – 600 °C

3.3. TGA

Thermogravimetric and differentiating scanning calorimetry (DSC) profiles of the studied chars are provided in Appendix in Figs. A1–A4. For all samples, the thermal stability directly depends on the carbonization temperature: with the temperature increase, the weight loss decreases down. Samples obtained at 465 °C are characterized by distinctively high weight losses caused by the presence in their composition of incompletely transformed organic compounds, including polymers. The losses up to 200 – 250 °C for all samples are connected with water desorption. For biochars, the weight loss in the region of 250 – 600 °C is related to decomposition of cellulose, hemicellulose and lignin. The weight losses after *ca.* 800 °C for WB-derived chars are probably caused by the gasification of carbon-containing phase via interaction with compounds of Na and K (most probably, carbonates) constituting WB ash by *ca.* a half [23, 41]. In the case of peat-derived samples, the peaks in DSC profiles at $T > 750$ °C seems to be caused by CaCO_3 decomposition [42].

The most stable chars appeared to be RH600 with the minimal weight loss of 8.3 wt. % and RH550 (11.63 wt. %), while the lowest thermal stability was exhibited by peat-derived samples with the weight losses in the interval of 23.71 – 35.29 wt. %. It is also notable, the profiles of coal-derived chars exhibited the highest similarity between each other, which, apparently, is related to the highest maturation degree of the carbon-containing phase compared to other feedstocks. Their weight losses were close and relatively low – 14.5 – 16.4 wt. %.

3.4. Adsorption tests of the chars by Cu^{2+} ions and methyl green

Adsorption capacities of the char samples are provided in Fig. 11. They were calculated according to the following equation:

$$\Gamma = (C_0 - C) \cdot \frac{V}{m_{char}},$$

where Γ is the adsorption capacity ($\text{mg} \cdot \text{g}^{-1}$); C_0 , C is the concentration of a model pollutant in a solution ($\text{mg} \cdot \text{L}^{-1}$); V is the volume of solution (L); m_{char} is the weight of the used adsorbent sample. From the graph it can be seen that the biochars have exhibited the highest adsorption capacities relating to both Cu^{2+} ions (WB) and MG (RH). The char samples obtained from peat and coal appeared to have worse adsorptive properties, especially in the case of peat. Besides, Cu^{2+} can be adsorbed via formation of complexes and electrostatic interaction with oxygen-containing groups [43]. Also, Cu^{2+} ions can substitute alkali and alkaline-earth metal ions to get bound by the corresponding O-containing surface species. In case of dyes, the adsorption mechanism is more complex and can include [44, 45]:

- surface adsorption in pores, when used char has a quite developed porosity;
- surface interaction with functional groups ($-\text{OH}$, $-\text{C}=\text{O}$ etc.) via hydrogen bonds, van der Waals force;
- $\pi-\pi$ stacking;
- electrostatic interactions.

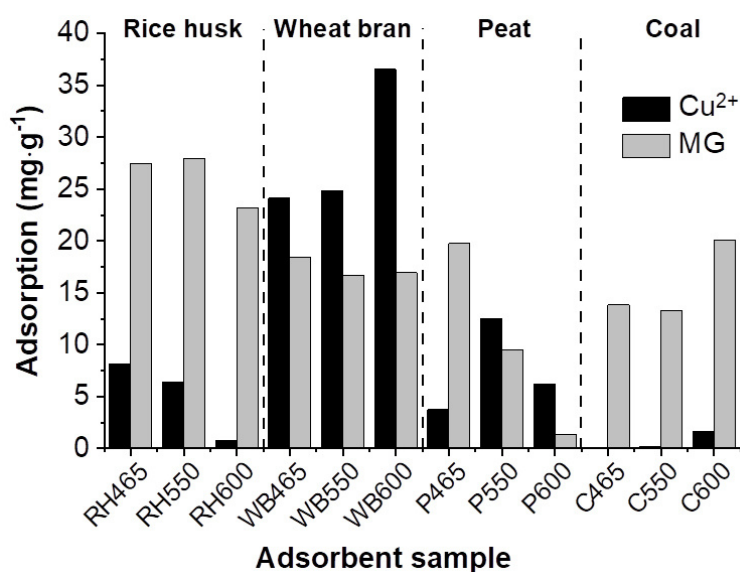


FIG. 11. Adsorption of Cu^{2+} and methyl green on the (bio)char samples obtained via carbonization in the fluidized catalyst bed reactor at 465 – 600 °C

As can be seen from the results presented in Fig. 11, adsorptive properties of the chars are weakly correlated with their BET specific surface area indicating on importance of other adsorption mechanisms. It should be noted that unlike biochars, which are usually prepared by conventional slow pyrolysis that can be conjugated with physical or chemical activation, chars prepared in this research via partial oxidation in the FCB reactor practically in all cases (except coal-derived ones) consist mainly of mineral component of the used feedstock: ash content is mostly varied from ~ 50 to 80 wt. % (Table 3). Therefore, their adsorptive properties are mainly determined by ash component, and adsorption mechanisms of both transition metal ions and organic dyes apparently governed by composition and chemical properties of the mineral part. Furthermore, in the case of biochars from RH and WB, their mineral component is distributed quite homogeneously, while in the peat and coal representing sedimentary feedstocks the mineral component is distributed in the form of large agglomerates [20, 46, 47]. All the above peculiarities should be taken in consideration in discussion of the obtained results.

Copper adsorption is correlated with carbonization temperature in the case of WB and coal and inversely correlated for RH. Such dependence is apparently related to decrease in oxygen content (Table 3) with the carbonization temperature increase, except coal, when the inverse trend is observed. It is interesting to note, that WB-derived chars exhibit the highest Cu^{2+} adsorption capacity rising with the carbonization temperature, despite the drop in O-content. This most probably is caused by the highest content of alkali and alkaline-earth metals responsible for the cation exchange (see Table 2), in particularly – sodium, potassium and magnesium.

However, for the peat-derived chars, despite similar content of sodium, calcium and magnesium, their adsorption capacity is significantly worse that seems to relate with their inaccessibility for cation exchange, unlike WB derived biochars.

TABLE 3. Composition of the char samples obtained at 465 – 600 °C via oxidative carbonization in FCB reactor

Char feedstock	Temperature, °C	W ^{a 1} , %	A ^{d 2} , %	CHNS-O composition, wt. %				
				C, %	H, %	N, %	S, %	O ³ , %
Rice husk	465	2.4	57.1	28.0	3.1	0.49	0.50	9.8
	550	2.3	67.8	17.0	3.0	0.45	0.50	10.6
	600	1.6	79.9	12.6	3.0	0.46	0.60	3.1
WB	465	2.7	50.9	36.0	3.6	3.80	0.45	4.0
	550	2.3	52.6	33.7	3.8	3.10	0.4	5.3
	600	2.0	58.2	32.0	4.0	2.60	0.27	2.1
Peat	465	2.0	58.5	20.3	1.9	1.34	0.29	16.9
	550	0.7	72.9	10.9	1.5	0.52	0.28	13.7
	600	0.7	79.1	7.1	1.3	0.26	0.25	11.9
Coal	465	2.4	16.5	69.2	2.9	2.17	0.29	6.9
	550	1.3	18.1	67.0	3.8	2.20	0.29	7.5
	600	1.2	19.9	63.0	3.4	2.16	0.27	10.3

¹ – moisture content; ² – ash content on dry matter; ³ – calculated by difference

Adsorption of the MG occurs differently compared to the copper ions. Except coal-derived chars, the MG adsorption decreases with the carbonization temperature increase. This points on a certain dependence of dye adsorption on content of the carbon-containing phase forming porous structure with such adsorption sites as functional groups, aromatic rings (via π - π stacking) and others listed above. Besides, MG adsorption depends, probably, on porous structure and it is lower for the most of microporous char obtained from coal, despite they have the highest BET surface area. For coal-derived chars MG adsorption increases with carbonization temperature probably due to increase in A_{BET} and the content of oxygen being introduced onto the char surface in the carbonization process in the form of surface functional groups that play a role as one type of adsorption sites.

On the whole, the obtained results have shown that the carbon-mineral chars are promising adsorbents for both transition metal ions and organic dyes. The obtained adsorption values are comparable with those reported in many literature sources (Table 4).

4. Conclusions

A novel approach to facile, green and energy-efficient production of porous char adsorbents from the feedstocks of various nature (wheat bran, rice husk, highly-mineralized peat and coal) is proposed. It represents oxidative carbonization in fluidized bed of deep oxidation CuO-Cr₂O₃/ γ -Al₂O₃ catalyst at low temperatures (465, 550 and 600 °C). This technique allowed for production of porous carbon-mineral char materials with different properties that depend on both temperature and characteristics of the used feedstocks. They appeared to have a quite high BET specific surface area (up to $\sim 170 \text{ m}^2\text{g}^{-1}$) as well as the content of the mineral part (16 – 79 wt. %). Due to similar nature and composition, wheat bran and rice husk exhibited similar behavior and properties of the obtained biochars: their maximal BET specific surface area was reached at 550 °C (91 and 117 m^2g^{-1} correspondingly) at similar pore size distribution. Sedimentary feedstocks (peat and coal) appeared to exhibit different both combustion behavior and properties of the chars produced. Due to the high content of Ca-containing ash component and partially decomposed biomass-originated organic phase, peat-derived chars have a relatively low texture characteristics with $A_{BET} \leq \sim 10 \text{ m}^2\text{g}^{-1}$ at the high yield and ash content. Coal-derived chars represented the highest stability to oxidation and, correspondingly, the highest yield ($\sim 40 - 50 \text{ wt. \%}$), A_{BET} (up to $172 \text{ m}^2\text{g}^{-1}$) as well as the lowest ash content ($\sim 16 - 20 \text{ wt. \%}$).

Their adsorption properties relating to the tested adsorbates were found to be quite complex that caused by the complex adsorption mechanisms. Adsorption of Cu²⁺ ions was detected to be the highest ($\sim 24 - 37 \text{ mg}\cdot\text{g}^{-1}$) for wheat bran due to, apparently, the highest content of alkali and alkali-earth metals available for the cation exchange. Adsorption of the organic dye depended on carbon content in the chars as well as porosity features and specific surface area. The

TABLE 4. Adsorption capacities of biomass, chars or activated carbons by Cu^{2+} and methyl green reported in literature

Feedstock	Synthesis conditions	A_{BET} , m^2g^{-1}	Ash content, wt. %	Maximal capacity ($\text{mg}\cdot\text{g}^{-1}$) by:		Ref.
				Cu^{2+}	MG	
Rice straw	Pyrolysis, 400 °C, 4 h	3.6	–	27.73	–	[48]
	Pyrolysis, 400 °C, 4 h followed by treatment with KMnO_4	19.4	–	71.60	–	
Spent tyres	Pyrolysis, 550 °C	–	–	~ 47	–	[49]
Pine sawdust	Hydrothermal liquefaction at 300 °C; CO_2 activation at 800 °C	425	2.9	25.18	–	[50]
Rice husk		358	59.96	22.62	–	
Date seed	Pyrolysis, 550 °C, 3 h	104.2	12.67	26.7	–	[51]
Waste tires derived acti- vated carbon	Activation with H_3PO_4 at 650 °C, 2 h	356	–	–	71.43	[52]
Almond shell	–	–	–	–	1.1	[53]

highest adsorption capacity by methyl green was achieved by RH-derived chars ($28 \text{ mg}\cdot\text{g}^{-1}$). On the whole, chars with the most attractive properties were obtained at 550 and 600 °C.

The obtained results show that the chars produced via oxidative carbonization in fluidized catalyst bed reactor with the deep oxidation catalyst can be suitable adsorbents of both heavy metal ions and organic pollutants. Thus, the developed approach can be effectively applied for production of chars from carbon-containing feedstocks of very different nature, including sedimentary one and lignocellulosic biomass.

Appendix

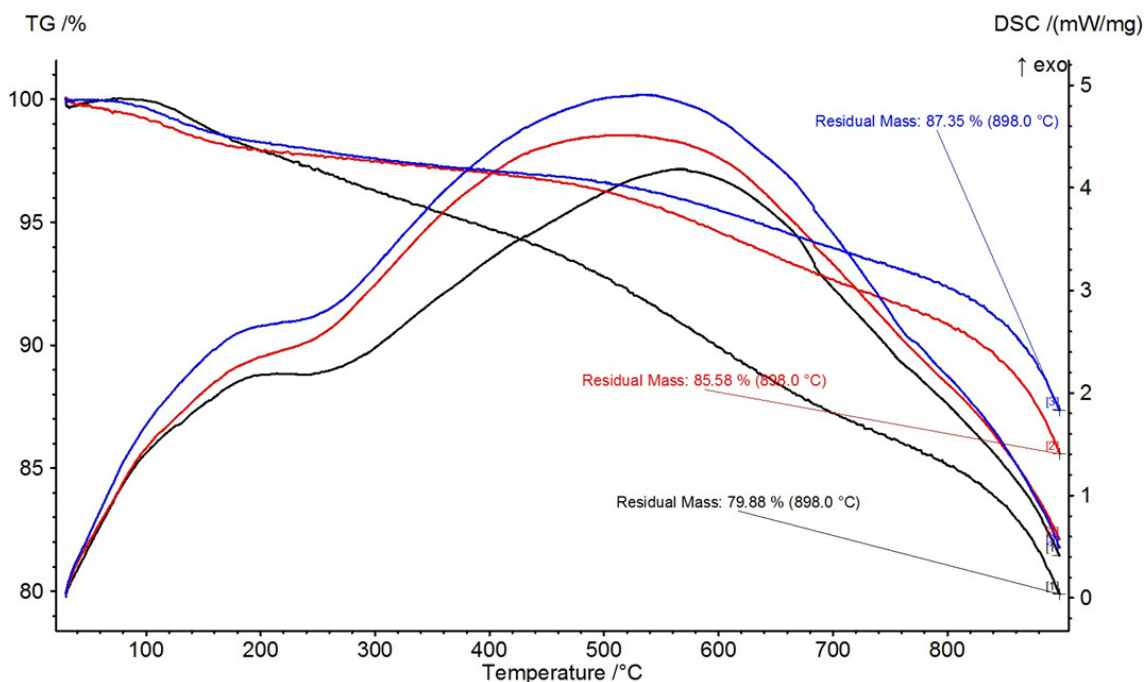


FIG. A1. TG and DSC profiles of WB-derived char samples obtained at 465 – 600 °C

TABLE A1. Texture characteristics, ash content and yield of chars from the feedstock carbonized in FCB reactor at 465 – 600 °C

Sample	A_{BET} , $m^2 g^{-1}$	A_{EXT} , $m^2 g^{-1}$	V_{Σ} , $cm^3 g^{-1}$	V_{μ} , $cm^3 g^{-1}$	$\langle d_{pore} \rangle$, nm
Bran					
B465	43	15	0.04	0.01	3.7
B550	91	40	0.05	0.02	2.2
B600	68	36	0.04	0.01	2.3
Rice husk					
RH465	87	82	0.13	0	6.0
RH550	117	102	0.17	0.01	5.8
RH600	99	78	0.18	0.01	7.4
Peat					
P465	11	11	0.05	0	19.5
P550	9	10	0.06	0	28.5
P600	7	7	0.05	0	32.7
Coal					
C465	133	61	0.07	0.03	2.1
C550	126	68	0.07	0.02	2.1
C600	172	92	0.09	0.03	2.1

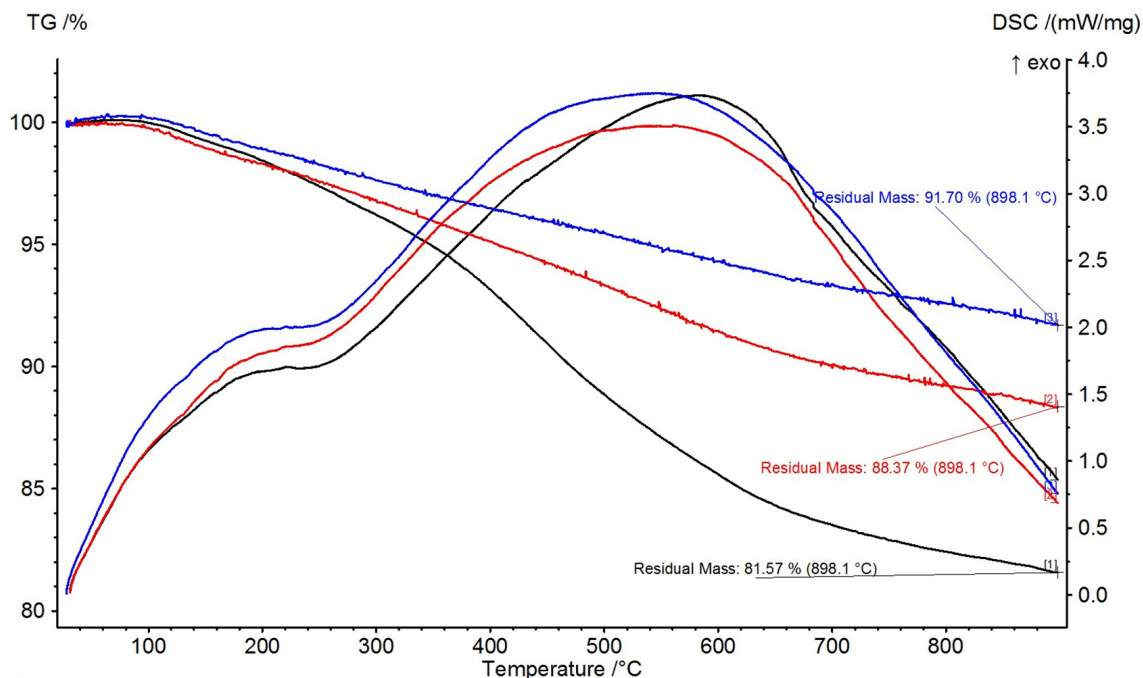


FIG. A2. TG and DSC profiles of RH-derived char samples obtained at 465 – 600 °C

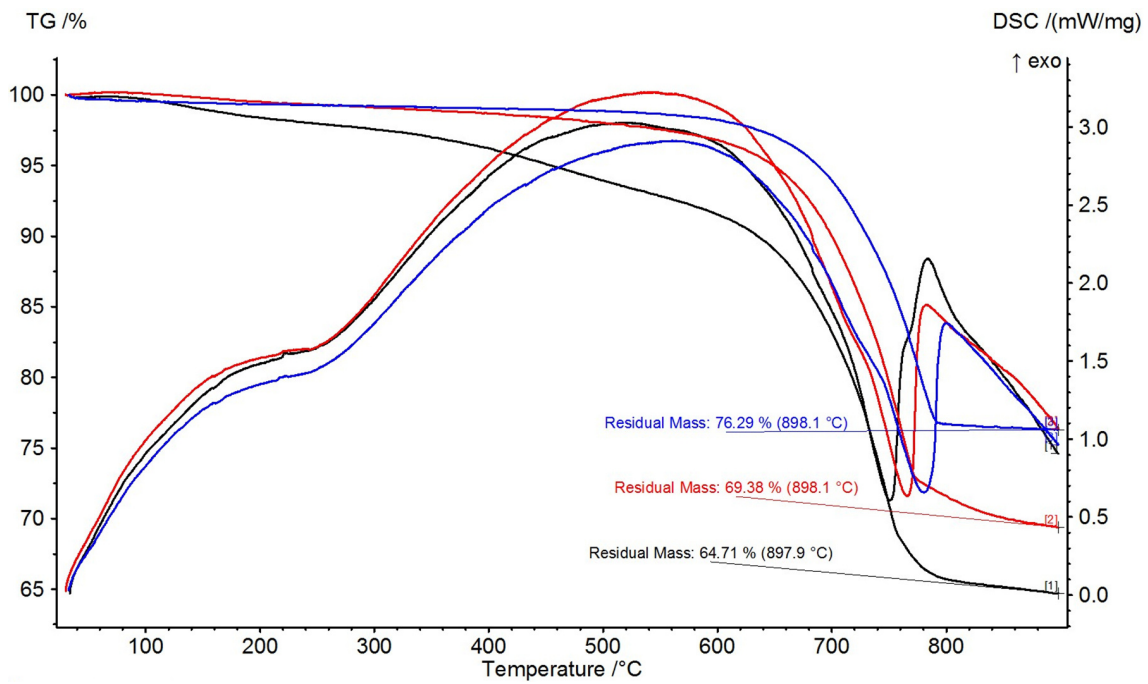


FIG. A3. TG and DSC profiles of peat-derived char samples obtained at 465 – 600 °C

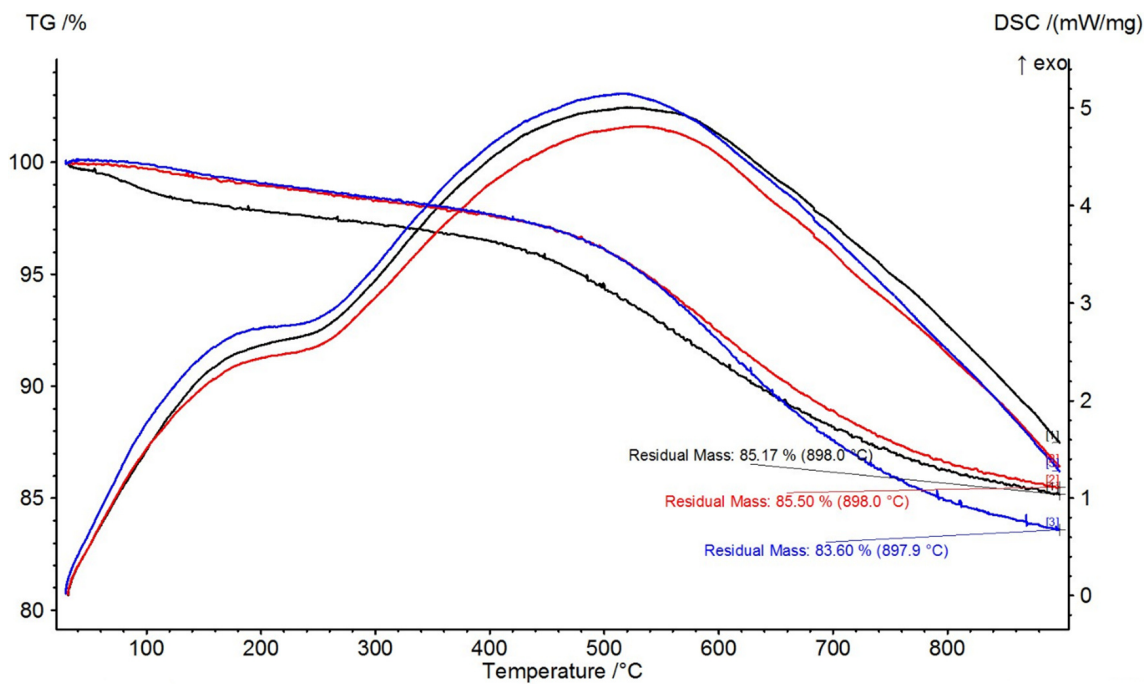


FIG. A4. TG and DSC profiles of coal-derived char samples obtained at 465 – 600 °C

References

- [1] Jeguirim M., Limousy L. *Biomass Chars: Elaboration, Characterization and Applications*, MDPI, Basel, 2018.
- [2] Xiang W., Zhang X., Chen J., Zou W., He F., Hu X., Tsang D.C.W., Ok Y.S., Gao B. Biochar technology in wastewater treatment: A critical review. *Chemosphere*, 2020, **252**, 126539.
- [3] Suárez-Almeida M., Gómez-Barea A., Ghoniem A.F., Pfeifer C. Solar gasification of biomass in a dual fluidized bed. *Chem. Eng. J.*, 2021, **406**, 126665.
- [4] Heidari M., Salaudeen S., Arku P., Acharya B., Tasnim S., Dutta A. Development of a mathematical model for hydrothermal carbonization of biomass: Comparison of experimental measurements with model predictions. *Energy*, 2021, **214**, 119020.
- [5] Liu Y., Rokni E., Yang R., Ren X., Sun R., Levendis Y.A. Torrefaction of corn straw in oxygen and carbon dioxide containing gases: Mass/energy yields and evolution of gaseous species. *Fuel*, 2021, **285**, 119044.

- [6] Mortari D.A., Perondi D., Rossi G.B., Bonato J.L., Godinho M., Pereira F.M. The influence of water-soluble inorganic matter on combustion of grape pomace and its chars produced by slow and fast pyrolysis. *Fuel*, 2021, **284**, 118880.
- [7] Braghiroli F.L., Bouafif H., Neculita C.M., Koubaa A. Influence of Pyro-Gasification and Activation Conditions on the Porosity of Activated Biochars: A Literature Review. *Waste and Biomass Valorization*, 2020, **11**, P. 5079–5098.
- [8] Li Z., Zhong Z., Zhang B., Wang W., Zhao H., Seufitelli G.V.S., Resende F.L.P. Microwave-assisted catalytic fast pyrolysis of rice husk over a hierarchical HZSM-5/MCM-41 catalyst prepared by organic base alkaline solutions. *Sci. Total Environ.*, 2021, **750**, 141215.
- [9] Pawar A., Panwar N.L., Salvi B.L. Comprehensive review on pyrolytic oil production, upgrading and its utilization. *J. Mater. Cycles Waste Manag.*, 2020, **22**, P. 1712–1722.
- [10] Iannello S., Morrin S., Materazzi M. Fluidised Bed Reactors for the Thermochemical Conversion of Biomass and Waste. *KONA Powder Part. J.*, 2020, **37**, P. 114–131.
- [11] Karmee S.K., Kumari G., Soni B. Pilot scale oxidative fast pyrolysis of sawdust in a fluidized bed reactor: A biorefinery approach. *Bioresour. Technol.*, 2020, **318**, 124071.
- [12] Mullen C.A., Boateng A.A. Accumulation of Inorganic Impurities on HZSM-5 Zeolites during Catalytic Fast Pyrolysis of Switchgrass. *Ind. Eng. Chem. Res.*, 2013, **52**, P. 17156–17161.
- [13] Yazykov N.A., Simonov A.D., Dubinin Y.V., Zaikina O.O. Catalytic Co-Combustion of Peat and Anthracite in a Fluidized Bed. *Catal. Ind.*, 2019, **11**, P. 342–348.
- [14] Simonov A.D., Fedorov N.A., Dubinin Y.V., Yazykov N.A., Yakovlev V.A., Parmon V.N. Catalytic heat-generating units for industrial heating. *Catal. Ind.*, 2013, **5**, P. 42–49.
- [15] Yazykov N.A., Simonov A.D., Aflyatunov A.S., Dubinin Y.V., Selischeva S.A., Yakovlev V.A., Stepanenko A.I. Combustion of Shale Heavy Coal-Tar Products in a Boiling Layer of a Catalyst. *Chem. Sustain. Dev.*, 2017, **25**, P. 313–321.
- [16] Yazykov N.A., Dubinin Y.V., Simonov A.D., Reshetnikov S.I., Yakovlev V.A. Features of sulfur oils catalytic combustion in fluidized bed. *Chem. Eng. J.*, 2016, **283**, P. 649–655.
- [17] Dubinin Y.V., Yazykov N.A., Reshetnikov S.I., Yakovlev V.A. Catalytic combustion of sulfur-containing liquid fuels in the fluidized bed: Experiment and modeling. *J. Ind. Eng. Chem.*, 2021, **93**, P. 163–169.
- [18] Fedorov A.V., Dubinin Y.V., Yeletsky P.M., Fedorov I.A., Shelest S.N., Yakovlev V.A. Combustion of sewage sludge in a fluidized bed of catalyst: ASPEN PLUS model. *J. Hazard. Mater.*, 2021, **405**, 124196.
- [19] Nikitin D.S., Shanenkov I.I., Yeletsky P.M., Nassyrbayev A., Tabakaev R.B., Shanenkova Y.L., Ryskulov D.N., Tsimmerman A.I., Sivkov A.A. Agricultural waste derived silicon carbide composite nanopowders as efficient coelectrocatalysts for water splitting. *J. Clean. Prod.*, 2024, **442**, 140890.
- [20] Yeletsky P.M., Dubinin Y.V., Yazykov N.A., Tabakaev R.B., Okotrub K.A., Yakovlev V.A. Conversion of natural feedstocks to porous carbons via carbonization in fluidized catalyst bed followed by leaching the feedstock mineral template phase: A comparison of biomass and sedimentary raw materials. *Fuel Process. Technol.*, 2022, **226**, 107076.
- [21] Tabakaev R., Ibraeva K., Kan V., Dubinin Y., Rudmin M., Yazykov N., Zavorin A. The effect of co-combustion of waste from flour milling and highly mineralized peat on sintering of the ash residue. *Energy*, 2020, **196**, 117157.
- [22] Tabakaev R., Astafev A., Dubinin Y., Yazykov N., Yakovlev V. Evaluation of Autothermal Peat Pyrolysis Realization for Fuel Processing Technologies. *Waste and Biomass Valorization*, 2019, **10**, P. 1021–1027.
- [23] Yeletsky P.M., Yakovlev V.A., Mel'gunov M.S., Parmon V.N. Synthesis of mesoporous carbons by leaching out natural silica templates of rice husk. *Microporous Mesoporous Mater.*, 2009, **121**, P. 34–40.
- [24] Thommes M., Kaneko K., Neimark A.V., Olivier J.P., Rodriguez-Reinoso F., Rouquerol J., Sing K.S.W. Physisorption of gases, with special reference to the evaluation of surface area and pore size distribution (IUPAC Technical Report). *Pure Appl. Chem.*, 2015, **87**, P. 1051–1069.
- [25] Kruk M., Jaroniec M., Gadkaree K.P. Nitrogen Adsorption Studies of Novel Synthetic Active Carbons. *J. Colloid Interface Sci.*, 1997, **192**, P. 250–256.
- [26] Liu Y., Yang X., Lei F., Xiao Y. Synergistic Effect of Alkali Metals in Coal and Introduced CaO during Steam Gasification. *J. Therm. Sci.*, 2020, **29**, P. 1627–1637.
- [27] Zhao M., Memon M.Z., Ji G., Yang X., Vuppaladiyam A.K., Song Y., Raheem A., Li J., Wang W., Zhou H. Alkali metal bifunctional catalyst-sorbents enabled biomass pyrolysis for enhanced hydrogen production. *Renew. Energy*, 2020, **148**, P. 168–175.
- [28] Zhu Y., Li W., Huang Y., Zheng Y., Wang D., Ye Y., Li S., Zheng Z. Catalytic pyrolysis of cellulose over solid acidic catalysts: an environment-friendly method for furan production. *Biomass Convers. Biorefinery*, 2020, **11**, P. 2695–2702.
- [29] Sosnin G.A., Yazykov N.A., Yeletsky P.M., Zaikina O.O., Yakovlev V.A. Molybdenum recovery from spent Mo-based dispersed catalyst accumulated in heavy oil steam cracking coke. *Fuel Process. Technol.*, 2020, **208**, 106520.
- [30] Sing K.S.W. Reporting physisorption data for gas/solid systems with special reference to the determination of surface area and porosity (Recommendations 1984). *Pure Appl. Chem.*, 1985, **57**, P. 603–619.
- [31] Jeromenok J., Weber J. Restricted Access: On the Nature of Adsorption/Desorption Hysteresis in Amorphous, Microporous Polymeric Materials. *Langmuir*, 2013, **29**, P. 12982–12989.
- [32] Hanna R. Infrared Absorption Spectrum of Silicon Dioxide. *J. Am. Ceram. Soc.*, 1965, **48**, P. 595–599.
- [33] Davarcioglu B., Spectral characterization of non-clay minerals found in the clays (Central Anatolian-Turkey). *Int. J. Phys. Sci.*, 2011, **6**, P. 511–522.
- [34] Mozgawa W., Król M., Dyczek J., Deja J. Investigation of the coal fly ashes using IR spectroscopy. *Spectrochim. Acta Part A Mol. Biomol. Spectrosc.*, 2014, **132**, P. 889–894.
- [35] Coates J. Interpretation of Infrared Spectra, A Practical Approach, in: *Encycl. Anal. Chem.*, John Wiley & Sons, Ltd, Chichester, UK, 2006.
- [36] Ibrahim D.M., El-Hemaly S.A., Abdel-Kerim F.M. Study of rice-husk ash silica by infrared spectroscopy. *Thermochim. Acta*, 1980, **37**, P. 307–314.
- [37] Sankar S., Sharma S.K., Kaur N., Lee B., Kim D.Y., Lee S., Jung H. Biogenerated silica nanoparticles synthesized from sticky, red, and brown rice husk ashes by a chemical method. *Ceram. Int.*, 2016, **42**, P. 4875–4885.
- [38] Yin Y., Yin J., Zhang W., Tian H., Hu Z., Ruan M., Xu H., Liu L., Yan X., Chen D. FT-IR and micro-Raman spectroscopic characterization of minerals in high-calcium coal ashes. *J. Energy Inst.*, 2018, **91**, P. 389–396.
- [39] Gunasekaran S., Anbalagan G., Pandi S. Raman and infrared spectra of carbonates of calcite structure. *J. Raman Spectrosc.*, 2006, **37**, P. 892–899.
- [40] Mozgawa W., Król M., Dyczek J., Deja J. Investigation of the coal fly ashes using IR spectroscopy. *Spectrochim. Acta Part A Mol. Biomol. Spectrosc.*, 2014, **132**, P. 889–894.
- [41] Elelskii P.M., Yakovlev V.A., Fenelonov V.B., Parmon V.N. Texture and adsorptive properties of microporous amorphous carbon materials prepared by the chemical activation of carbonized high-ash biomass. *Kinet. Catal.*, 2008, **49**, P. 708–719.
- [42] He D., Ou Z., Qin C., Deng T., Yin J., Pu G. Understanding the catalytic acceleration effect of steam on CaCO₃ decomposition by density function theory. *Chem. Eng. J.*, 2020, **379**, 122348.

- [43] Georgiou E., Mihajlović M., Petrović J., Anastopoulos I., Dosche C., Pashalidis I., Kalderis D. Single-stage production of miscanthus hydrochar at low severity conditions and application as adsorbent of copper and ammonium ions. *Bioresour. Technol.*, 2021, **337**, 125458.
- [44] Yao X., Ji L., Guo J., Ge S., Lu W., Chen Y., Cai L., Wang Y., Song W. An abundant porous biochar material derived from wakame (*Undaria pinnatifida*) with high adsorption performance for three organic dyes. *Bioresour. Technol.*, 2020, **318**, 124082.
- [45] Cuong Nguyen X., Thanh Huyen Nguyen T., Hong Chuong Nguyen T., Van Le Q., Yen Binh Vo T., Cuc Phuong Tran T., Duong La D., Kumar G., Khanh Nguyen V., Chang S.W., Jin Chung W., Duc Nguyen D. Sustainable carbonaceous biochar adsorbents derived from agro-wastes and invasive plants for cation dye adsorption from water. *Chemosphere*, 2021, **282**, 131009.
- [46] Larichev Y.V., Eletsii P.M., Tuzikov F.V., Yakovlev V.A. Porous carbon-silica composites and carbon materials from rice husk: Production technology, texture, and dispersity. *Catal. Ind.*, 2013, **5**, P. 350–357.
- [47] Eletsii P.M., Yakovlev V.A., Kaichev V.V., Yazykov N.A., Parmon V.N. Texture and surface properties of carbon-silica nanocomposite materials prepared by the carbonization of high-ash vegetable raw materials in a fluidized catalyst bed. *Kinet. Catal.*, 2008, **49**, P. 305–312.
- [48] Meng Z., Xu T., Huang S., Ge H., Mu W., Lin Z. Effects of competitive adsorption with Ni(II) and Cu(II) on the adsorption of Cd(II) by modified biochar co-aged with acidic soil. *Chemosphere*, 2022, **293**, 133621.
- [49] Shahtalebi A., Sarrafzadeh M.H., McKay G. An adsorption diffusion model for removal of copper (II) from aqueous solution by pyrolytic tyre char. *Desalin. Water Treat.*, 2013, **51**, P. 5664–5673.
- [50] Liu Z., Zhang F.-S. Removal of copper (II) and phenol from aqueous solution using porous carbons derived from hydrothermal chars. *Desalination*, 2011, **267**, P. 101–106.
- [51] Mahdi Z., Yu Q.J., El Hanandeh A. Investigation of the kinetics and mechanisms of nickel and copper ions adsorption from aqueous solutions by date seed derived biochar. *J. Environ. Chem. Eng.*, 2018, **6**, P. 1171–1181.
- [52] Belgacem A., Brahim I.O., Belmedani M., Hadoun H. Removal of Methyl Green Dye from Aqueous Solutions Using Activated Carbon Derived from Cryogenic Crushed Waste Tires. *Iran. J. Chem. Chem. Eng.*, 2022, **41**, P. 207–219.
- [53] Tanaydin M.K., Goksu A. Optimization of the adsorption of methyl green dye on almond shells using central composite design. *Desalin. Water Treat.*, 2021, **227**, P. 425–439.

Submitted 6 December 2023; revised 6 March 2024; accepted 10 March 2024

Information about the authors:

Petr M. Yeletsky – Federal Research Center Boreskov Institute of Catalysis SB RAS, Acad. Lavrentiev av., 5, Novosibirsk, 630090, Russia; ORCID 0000-0001-8899-9039; yeletsky@catalysis.ru

Nikolay A. Yazykov – Federal Research Center Boreskov Institute of Catalysis SB RAS, Acad. Lavrentiev av., 5, Novosibirsk, 630090, Russia; yazykov@catalysis.ru

Yury V. Dubinin – Federal Research Center Boreskov Institute of Catalysis SB RAS, Acad. Lavrentiev av., 5, Novosibirsk, 630090, Russia; ORCID 0000-0002-0786-0500; dubinin@catalysis.ru

Maksim M. Borodaevskiy – Federal Research Center Boreskov Institute of Catalysis SB RAS, Acad. Lavrentiev av., 5, Novosibirsk, 630090, Russia; ORCID 0009-0003-6243-5579; maxim.borodaevskiy@gmail.com

Svetlana A. Selishcheva – Federal Research Center Boreskov Institute of Catalysis SB RAS, Acad. Lavrentiev av., 5, Novosibirsk, 630090, Russia; ORCID 0000-0003-2768-9680; svetlana@catalysis.ru

Vadim A. Yakovlev – Federal Research Center Boreskov Institute of Catalysis SB RAS, Acad. Lavrentiev av., 5, Novosibirsk, 630090, Russia; ORCID 0000-0001-5015-3521; yakovlev@catalysis.ru

Conflict of interest: the authors declare no conflict of interest.

A plasmonic turn-on insulin sensing platform on centimeter scale nanostructure arrays

Thanh Thi Van Nguyen

School of Materials Science and Engineering, Hanoi University of Science and Technology, Hanoi, Vietnam

thanh.nguyenthivan@hust.edu.vn

ABSTRACT We present a plasmonic turn-on biosensing assay for insulin detection via aptamer DNA based on the plasmonic interaction of centimeter scale gold/silver double-layer nanodisk arrays and gold nanoparticles. The large-scale nanostructures were fabricated by laser interference lithography technique. The detecting optical signal-extinction spectra of the system were monitored by UV-visible spectrophotometry. The 3D finite-difference time-domain simulation was used to observe the plasmonic interaction of the sensing system. The platform exhibits an exceptionally large turn-on signal by a 120 nm red shift of the localized surface plasmonic resonance peak, results in the limit detection of 140 pM. The centimeter-scale localized surface plasmon resonance nanostructures combined with turn-on design scheme would offer a promising sensor-on-chip biosensing platform.

KEYWORDS insulin sensing, localized surface plasmon, plasmonic interaction, nanostructure

ACKNOWLEDGEMENTS This research is funded by Hanoi University of Science and Technology (HUST) under project number T2022-PC-083.

FOR CITATION Thanh Thi Van Nguyen A plasmonic turn-on insulin sensing platform on centimeter scale nanostructure arrays. *Nanosystems: Phys. Chem. Math.*, 2024, **15** (2), 300–306.

1. Introduction

Diabetes can lead to many dangerous complications therefore necessary to detect it early so that effective treatments can be intervened in the early stages [1]. Type 1 diabetes is related to the insulin deficiency leads to glucose in the blood not being absorbed [2]. Detection of insulin is critical for diagnosis of this high risk disease [3]. Conventional methods applied for insulin sensing include immunoassay methods (RIA – Radioimmunoassay [4], ELISA – Enzyme-Linked Immunosorbent Assay [5], and CLIA chemiluminescence immunoassay [6]), analytical chemistry methods (fluorescent detection [7], mass spectrometry [8], Raman spectroscopy [9]), electrochemical spectrometry [10]. These methods have their own advantages and some limitations needed to improve including selectivity, detection time, multiplex sample preparation, electronic signal reading instrumentation, and complex signal enhancement procedure [11].

Recently, the usage of localized surface plasmon resonance of nanostructures in biological sensing assays has become a promising method due to its distinctive characteristics. Localized surface plasmon resonance (LSPR) is widely known as the collective charge oscillations that arises around nanoscale structures when light is illuminated onto the surface [12]. LSPR owns highly sensitivity to the localized refractive index (RI) changes. The biomolecular attachment on the surface of the nanostructures changes the local RI in the vicinity of the sensing surface that results in a sensitive response in LSPR-induced light absorption spectrum which is used to conduct specific detection [13]. LSPR – based detection by using nanoscale structures fabricated in a large – scale area has been demonstrated to be an effective platform for biosensing offers the advantage of being easily multiplexed to enable high throughput screening in an array format [14–20].

Laser interference lithography (LIL) is one of the simple techniques to produce a large area of well ordering arrays of LSPR nanostructures [21, 22]. In addition, this technique can be used to fabricate the nanostructures array in all available rigid or flexible substrates. With one shot of laser exposure in few minutes, by manipulating carefully the laser incident beam angles as well as the relative angles between exposure times, the size, shape can be altered flexibly [23]. Previously, we fabricated 2D gold/silver nanodisks by LIL with high refractive index sensitivity and successfully used these nanodisks for DNA sensing platform [19].

Nucleic acid aptamers have been widely used as chemical antibodies in various biological sensing due to the specific recognition and tight binding to their targets [24, 25]. The insulin aptamers are single stranded DNAs containing a two-repeat sequence of the insulin-linked polymorphic region (ILPR) of the human insulin gene promoter region [26, 27]. They can fold into G-quadruplex oligonucleotides in the presence of insulin with high specificity and affinity. Many research groups have used insulin aptamers as ligands in insulin detection [28–31].

In this work, we report the experimental assay for insulin sensing with a turn-on design sensing scheme by using fabricated 2D gold/silver nanodisks, gold nanoparticles and insulin aptamers. Our objective is to integrate the high sensitivity resulting from the plasmonic interactions between gold nanoparticles and large-scale gold/silver nanodisk array and the high selectivity resulting from the specific binding of the insulin to their aptamers. The “turn-on” design means

that the lesser insulin concentration presents the higher optical signal of plasmonic system can be generated, consequently, the higher sensitivity can be achieved.

2. Detection scheme and working principle

The detection scheme is shown in Fig. 1. The detecting optical signal in this design is LSPR peak shift of the 2D gold/silver nanodisks as the gold nanoparticles are attached to the nanodisk surfaces by insulin aptamer DNA. The aptamer DNA was complementary with two different single DNA strands attached to 2D gold/silver double-layer nanodisks (capture DNA c1) and gold nanoparticles (capture DNA c2). Without the presence of insulin, the aptamers link the gold nanoparticles to the nanodisk surfaces and cause the LSPR peak shift (signal on). Since the binding affinity of insulin to insulin aptamer DNA to form G-quadruplex is much higher than that to complementary single DNA strands, the insulin aptamers have prior bindings to insulin rather than to their complementary strands. Therefore, once the insulin is introduced there is lesser available insulin aptamer DNA for attachment of gold nanoparticles to the nanodisk surfaces. As a result, smaller LSPR peak shifts of the 2D gold/silver nanodisks are generated (signal off). The presence of various concentrations of insulin in the system will modulate the attachment of gold nanoparticles due to the interaction of insulin and their aptamer, hence, insulin can be detected by the corresponding LSPR peak shift of the nanodisks. By observing the LSPR spectrum of the 2D gold/silver nanodisks, insulin could be detected selectively and sensitively.

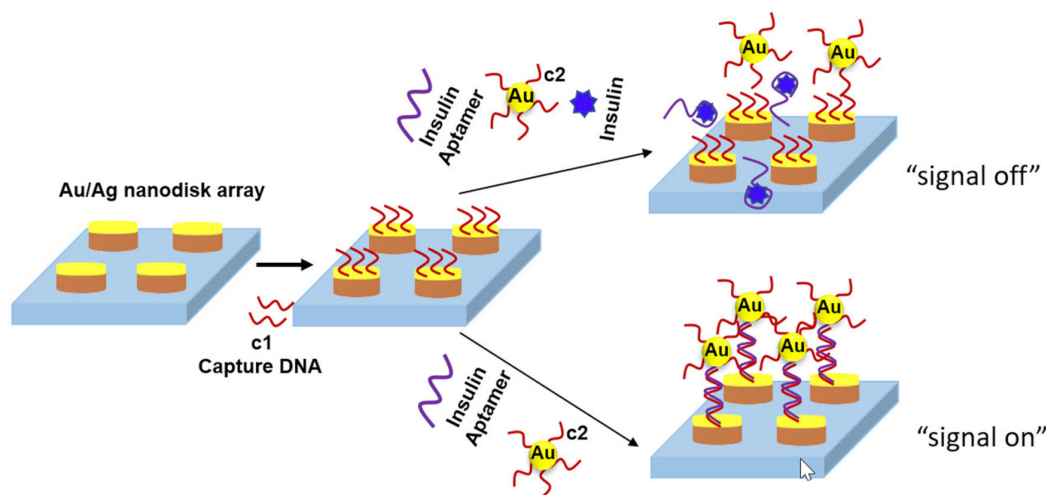


FIG. 1. "Turn on" insulin detection scheme

The gold nanoparticles in this design are sensing indicators as well as the plasmonic signal amplifying agents. Once they are brought closely enough to the nanodisk surfaces, the plasmonic interaction between them occurs [32]. As a result, the electromagnetic field surrounding them increases, the sensitivity to the localized refractive index (RI) changes of the nanodisks enhances significantly. Therefore, the lesser biological binding events on the nanodisk surfaces still cause a large LSPR peak shift for the detection.

The key point of our detection design is turn-on strategy. With the same concentration of insulin aptamer DNA introduced, the lower insulin concentration is needed to detect in the system, the more insulin aptamer DNA are left, the more gold nanoparticles are attached to the nanodisk surface, and the larger LSPR peak shift is recorded. By that turn-on principle, the detecting signal is enlarged as the concentration of the sensing agent is lessened. Hence, the lower concentration of sensing agent could be detected.

3. Materials and methods

3.1. Materials

All substrates (silicon, quartz, PEN) were bought from Photonik Pte Ltd (Singapore). The photoresist maN1407 and maR404 remover used for laser interference lithography was brought from Micro resist technology (Germany). The metallic materials used for fabrication of nanodisks (chromium, silver, gold) were supplied by MOS Group Pte Ltd (Singapore). The chemicals, insulin and DNA strands used in this study were bought from Sigma Aldrich (Singapore). The DNA sequences are shown in Table 1.

TABLE 1. DNA sequences

Name	Sequences
C1-Capture DNA	3'-ACCATCCCACAGAAGTTT [thiolC6]-5'
C2-Capture DNA	3'-[thiolC3] TTTCCACCACCCCCCCA-5'
IA-Aptamer DNA	5'-GGTGGTGGGGGGGGTTGGTAGGGGTGTC TTCTT-3'

3.2. Fabrication of 2D gold/silver double-layer nanodisks on centimeter scale substrate

All 2D gold/silver double-layer nanodisks used in this study were fabricated by laser interference lithography (LIL) technique in a homebuilt *Lloyd's-mirror* LIL system with a 325 nm He–Cd laser. The procedure was similar to the standard lithography procedure and described in our previous study in detail [19]. Shortly, the negative photoresist firstly coated on the substrates, then they were exposed to laser on the LIL system to create holes array. After that, the 20 nm thick silver layer and 10 nm thick gold layer were deposited by an electron-beam evaporator to form 30 nm thick gold/silver nanodisk arrays after lift-off process.

3.3. Capture DNA attachment to gold/silver nanodisks and gold nanoparticles

Gold nanoparticles (~ 15 nm) were synthesized by citrate reduction of HAuCl₄ method [33]. Capture DNA attachment to gold/silver nanodisks and gold nanoparticles were followed by the same procedure as were described in our previous study [19]. In brief, two types of capture DNA strands (Table 1) were used, the capture strand c_1 was attached to gold/silver nanodisks and the capture strand c_2 was attached to gold nanoparticles. These 3'- or 5'-terminal disulfide groups of single-stranded capture DNAs were first cleaved by immersing these DNA strands in a mixture of 0.1 M dithiothreitol (DTT) and phosphate buffer solution (pH = 8.0) for 2 hours, afterwards purified on NAP-5 columns (GE Healthcare). Then the corresponding purified capture DNA solution was brought to 15 nm gold nanoparticles and the gold/silver nanodisks for attachment. Finally, the rinsing process was carried out to remove the non-binding capture DNAs.

3.4. Insulin sensing experiment

At first, the attachment of capture DNA to the nanodisk arrays and gold nanoparticles was performed. Then, 1 μ M insulin aptamer DNA (IA) in insulin buffer (50 mM Tris-HCl, 10 mM KCl, 100 mM NaCl, pH = 8.0) was subject to the heating process to unfold the DNA sequences to increase the binding affinity of the aptamer to insulin. The heating process was carried out at 90 °C in 10 minutes and then the aptamer solution was cooled in 30 minutes to room temperature. After that, the insulin was introduced to the aptamer solution then allowed to incubate at room temperature in 1 hour. The sensing concentration of insulin ranged from 10 pM to 50 μ M. For the experiment with no insulin introduction, this step was skipped. Next, DNA-captured gold nanoparticles were added to the incubated mixture of insulin and their aptamers. After that, this final mixture was brought to the DNA-capture gold/silver nanodisk arrays. It was allowed to incubate in 2 hours then rinsed with insulin buffer thoroughly. Finally, the modified gold/silver nanodisk arrays were brought to the measurement step to obtain the extinction spectra. In the selectivity experiments, the same procedure was carried out with other proteins (bovine serum albumin (BSA), and alkaline phosphatase (ALP) and thrombin).

3.5. Characterization

To observe the morphology of nanodisks and the attachment of gold nanoparticles to the nanodisk surface, a scanning electron microscope (SEM) was used (NOVA NanoSEM 230-FEI, USA). The extinction spectra of the nanodisks were characterized by a UV-1800 UV-VISspectrophotometer (Shimadzu, Japan) in transmission mode.

4. Result and discussion

4.1. Observation of 2D gold/silver nanodisks

After fabrication, the 2D Au/Ag nanodisks were observed by SEM to confirm the size of the nanostructures. The diameter of the disks is 330 nm approximately. The size of the disk can be altered by changing the interference angle of LIL system. This is the smallest size of the disks that can be fabricated by our home-made LIL system. The nanodisks are double layer, the 20 nm thick silver layers are underneath and 10 nm thick gold layers are on the top. The double layer was fabricated to take advantage of the high refractive index sensing of silver and the biological compatibility of gold. The centimeter scale of nanodisks was obtained by one shot of laser exposure by LIL technique on many types of substrates. As shown in Figs. 2b and 2c, the nanodisks were fabricated on silicon, quartz and polyethylene naphthalate (PEN) substrates. In this study, all samples were fabricated on quartz substrate to get high transmittance for optical signal detection.

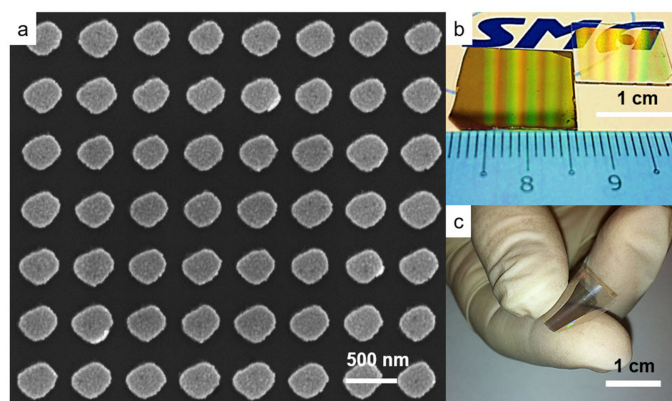


FIG. 2. Fabricated 2D gold/silver nanodisks: (a) SEM image, (b) centimeter scale of nanodisks on rigid substrate (quartz, silicon) and (c) flexible substrate (PEN)

4.2. Viability and selectivity of the detection scheme

To examine the viability of the detection scheme, the LSPR peak shifts of two experiments with and without insulin introduction were recorded and shown in Figs. 3a and 3b, respectively. Consideration of 1:1 binding ratio of insulin and their aptamer, $5 \mu\text{M}$ insulin and $1 \mu\text{M}$ aptamer was introduced in the experiments to eliminate the free aptamer (as described in 3.4). The LSPR peak shift of the nanodisks in this experiment was 50 nm (Fig. 3a) while the LSPR peak shift of the nanodisks in insulin absence experiment was 120 nm (Fig. 3b). The LSPR peak shift of the nanodisks in these experiments results from the changing in local refractive index at the surface of the nanodisks where insulin aptamer and gold nanoparticles were attached. No insulin was introduced, there were more DNA aptamers which are linkers attaching more gold nanoparticles to nanodisk surfaces. Consequently, the larger change in local refractive index was caused and the larger LSPR peak shifts were obtained. These recorded values proved that the “turn on” strategy detection worked successfully.

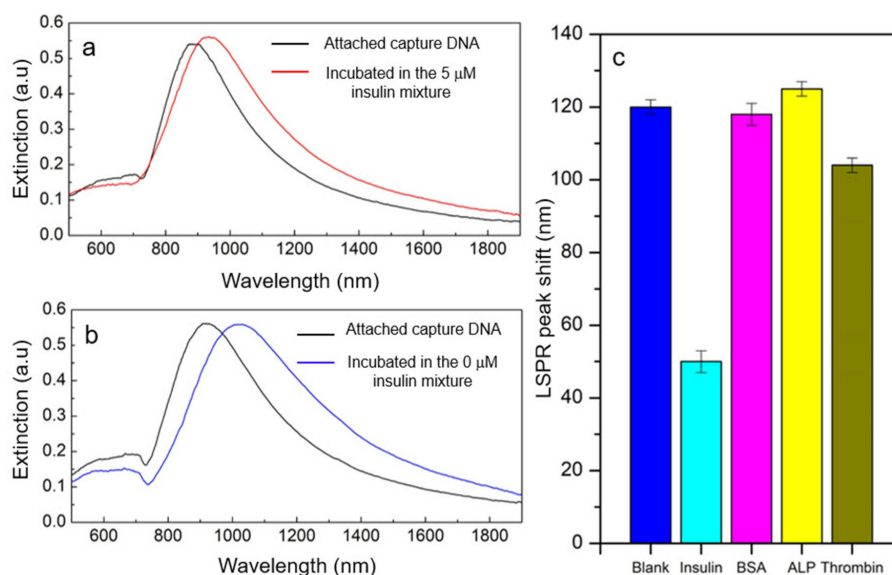


FIG. 3. LSPR peak shifts of viability and selectivity experiments with $1 \mu\text{M}$ of insulin aptamer DNA: a – in presence of $5 \mu\text{M}$ insulin, b – in absence of insulin (blank sample), c – in presence of $5 \mu\text{M}$ BSA, ALP and thrombin respectively

To validate the selectivity of the design, the same experiment was carried out with the $1 \mu\text{M}$ insulin aptamer and $5 \mu\text{M}$ of three different proteins: bovine serum albumin (BSA), and alkaline phosphatase (ALP) and thrombin. The recorded LSPR peak shifts of the nanodisks in these experiments were shown in Fig. 3c. The LSPR peak shifts of experiments with BSA, ALP and thrombin were 118 nm, 125 and 104 nm, respectively. These values are in the order of the peak shift of the blank sample (the sample without insulin) and distinctly higher than that of the sample with insulin. This means that the detection design exclusively “turn off” with insulin presence. These results obviously demonstrated the high selectivity of our insulin detection platform.

4.3. Signal enhancement by plasmonic interactions

Signal enhancement is the key to lower the limit of detection of molecules under consideration. The LSPR based sensing works on monitoring the LSPR peak shift according to the local refractive index change of the LSPR nanostructures. Without amplification agents, the DNA strands binding events on the LSPR nanostructure surface usually cause small changes in RI and results in low sensitivity of the detection [32, 34]. As mentioned, the gold nanoparticles in our detection played as signal enhanced agents by taking advantage of plasmonic interactions between gold/silver nanodisks and gold nanoparticles. The plasmonic interactions between them were verified by using the finite difference time domain (FDTD) simulation as shown in Figs. 4a and 4b. The simulated distance between the nanodisk and the gold nanoparticle is equal to the length of the linker insulin aptamer (the length of 32 bases strand is approximately 10 nm). As can be seen, with presence of the gold nanoparticle close to the nanodisk surface, the plasmon interaction between them makes the electromagnetic field of the nanodisk increases significantly. It should be emphasized that, during the sensing experiments there were many gold nanoparticles brought to the nanodisk surfaces as presented in the corresponding SEM image in Figs. 4c and 4d. In addition, the 2D gold/silver nanodisks were in a centimeter scale. Due to these factors, the collective resonance electromagnetic field of nanodisks in the sensing platform was extremely enhanced and resulting in an incredibly LSPR peak shifts that was caused by the binding of DNA to the nanodisk surfaces. In our “turn-on” insulin detection design, this enhancement strategy is greatly effective since the lesser insulin was introduced, the larger LSPR peak shift was created.

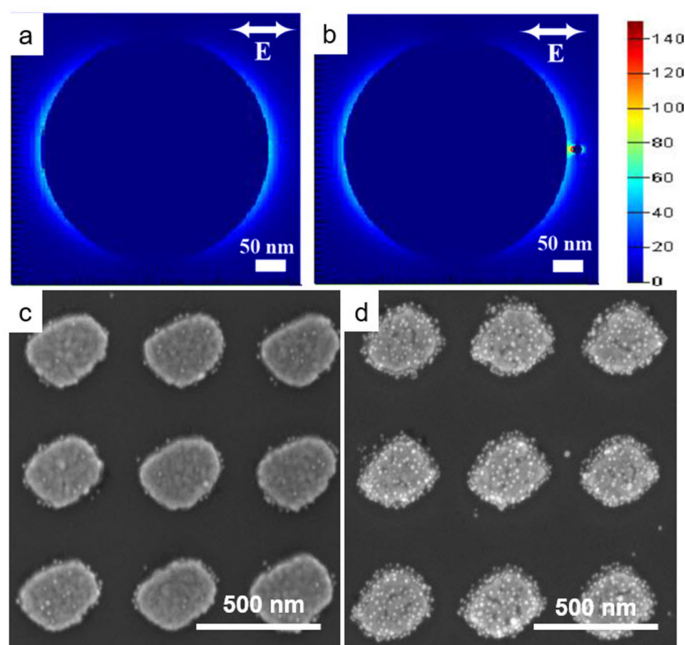


FIG. 4. Plasmonic interaction between gold nanoparticles and gold/silver nanodisks: (a) simulated electromagnetic field of one gold/silver nanodisk, (b) simulated electromagnetic field enhancement between one gold nanoparticle and one gold/silver nanodisk; attachment of gold nanoparticle to 2D gold/silver nanodisks (c) in the absence of insulin (blank sample) and (d) in the presence of $5 \mu\text{M}$ insulin

However, the unexpected of free DNA aptamer bindings were also enhanced. There were a number of nanoparticles bound on the nanodisk surfaces (Fig. 4c) and they caused a measurable LSPR peak shift of the system (Fig. 3a) in the experiment with insulin introduction. This evidence proposed that there was an amount of free insulin aptamer that did not bind to insulin in spite of the concentration of insulin ($5 \mu\text{M}$) is five times higher than that of their aptamer DNA ($1 \mu\text{M}$). These results may be caused by the dynamic range of the biological interaction between insulin and their aptamer [34]. Nevertheless, the affection of the inactive insulin aptamer binding was diminished in our “turn-on” detection scheme.

4.4. Sensitivity and specificity

The sensitivity of the insulin detection platform was demonstrated by a series of experiments at various concentrations from 10 pM to $50 \mu\text{M}$ of insulin in the presence of the same concentration of aptamer DNA ($1 \mu\text{M}$). The LSPR peak shifts of the system in these experiments are presented in Fig. 5a. Obviously, as the concentration of insulin decreases from $50 \mu\text{M}$ to 10 pM , the value of LSPR peak shift increases from 44 nm to 117 nm . The combination of the “turn-on” strategy with plasmonic enhancement over a centimeter scale of our system produces a distinctive shift (117 nm) of the LSPR peak with a small amount of insulin introduction (10 pM). To the best of our knowledge, such a large shift of the extinction spectrum peak has not been reported in literature of LSPR based insulin sensing, till date. We used the ICH

technique to calculate the limit of detection (LOD) of our sensing assay [35], $\text{LOD} = 3.3\sigma/s$ (σ – standard deviation of response, s – slope of the calibration curve). The data of the LSPR peak shifts in the insulin concentration range of 0 M to 500 pM were used to compute the LOD (the inset of Fig. 4). The calculated LOD of our insulin detection platform was 140 pM. The LOD of our sensing system is comparable to the concentration of free insulin in the blood, blood plasma or interstitial fluid that is in the picomolar range [11]. The result asserts strongly that our unoptimized system works on insulin detection with high sensitivity.

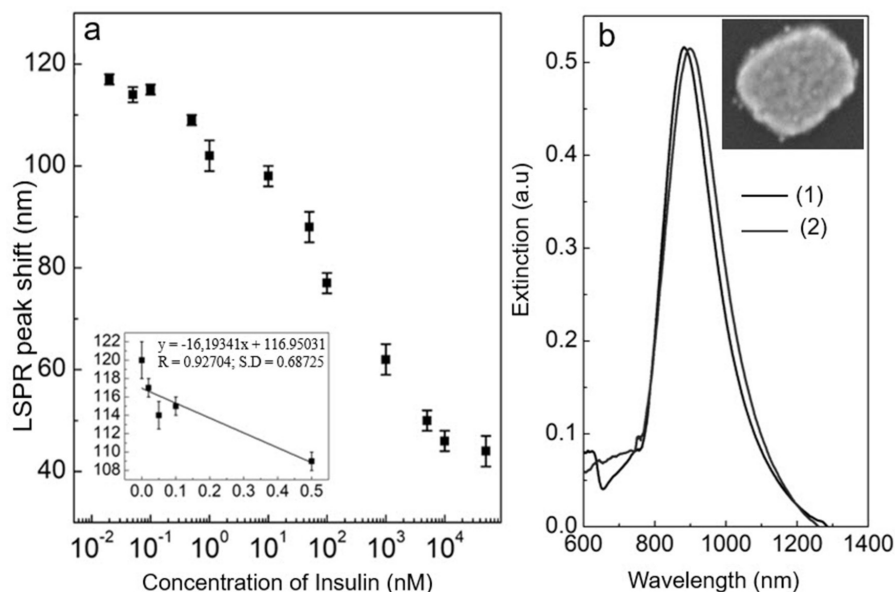


FIG. 5. Sensitivity and specificity experimental results: (a) LSPR peak shifts of 2D gold/silver nanodisks after the incubation with various concentrations of insulin, (b) LSPR peak shifts of 2D gold/silver nanodisks after the incubation with 5 μM insulin, DNA-captured gold nanoparticles, 1 μM adenosine aptamer DNA (1 – after attaching capture DNA, 2 – after the incubation)

The nonspecific binding experiments were carried out further to confirm the specificity of the sensing system. All biological components of the system were observed the nonspecific interaction to the nanodisks. Fig. 5b shows the LSPR peak shift of nanodisk after incubating with insulin, DNA-captured gold nanoparticles, adenosine aptamer (single DNA strands have the same base number as insulin aptamers but they form the G-quadruplex with adenosine not insulin). The nonspecific interactions of these components with the nanodisks only results in 15 nm red shift of the nanodisk LSPR peak. The SEM image inset also showed a couple of gold nanoparticles attached to the nanodisk surface after the nonspecific incubation. These data proved that the LSPR peak shifts in our sensing experiments were predominantly attributed to specific biological binding.

5. Conclusion

In summary, we reported a “turn-on” plasmon insulin detection platform by using LSPR structures combined with plasmonic amplification as optical transducers. The LSPR structures in this study were Au/Ag nanodisks of 320 nm diameter that were fabricated into centimeter scale 2D arrays on quartz substrates by laser interference lithography. The “turn on” detection strategy helped one to maximize the detecting optical signals at low concentrations of detecting insulin and to eliminate the nonspecific biological interactions. The plasmonic amplification is contributed by localized plasmonic interactions between a huge number of 15 nm gold nanoparticles with Au/Ag nanodisks. The combination of these factors led to the high sensitivity of our detection system that achieved the LOD of 140 pM that is comparable as picomolar range of insulin level in human body. The specificity of the system is assured by the distinct biological interaction of insulin and their DNA aptamers during the detection. The principles of our sensing platform can be applied for other DNA aptamer linked biological agents even small molecules. In addition, the large area of the fabricated LSPR nanostructures on all type of substrates in a short time may be an alternative approach for the lab-on-chip biological sensing.

References

- [1] Morris A. New test for diabetes insipidus. *Nature Reviews Endocrinology*, 2019, **15** (10), P. 564–565.
- [2] Mane K., Chaluvaraju K., Niranjan M., Zaranappa T., Manjuthaj T. Review of Insulin and its Analogues in Diabetes Mellitus. *J. of basic and clinical pharmacy*, 2012, **3**, P. 283–293.

- [3] Lian K., Feng H., Liu S., Wang K., Liu Q., Deng L., Wang G., Chen Y., Liu G. Insulin quantification towards early diagnosis of prediabetes/diabetes. *Biosensors and Bioelectronics*, 2022, **203**, 114029.
- [4] Warnken T., Huber K., Feige K. Comparison of three different methods for the quantification of equine insulin. *BMC Veterinary Research*, 2016, **12** (1), 196.
- [5] Manley S.E., Stratton I.M., Clark P.M., Luzio S.D. Comparison of 11 Human Insulin Assays: Implications for Clinical Investigation and Research. *Clinical Chemistry*, 2007, **53** (5), P. 922–932.
- [6] Tanaka T., Matsunaga T. Fully Automated Chemiluminescence Immunoassay of Insulin Using Antibody-Protein A/Bacterial Magnetic Particle Complexes. *Analytical Chemistry*, 2000, **72** (15), P. 3518–3522.
- [7] Ho J.A., Zeng S., Huang M., Kuo H. Development of liposomal immunosensor for the measurement of insulin with femtomole detection. *Analytica Chimica Acta*, 2006, **556** (1), P. 127–132.
- [8] Gillette M.A., Carr S.A. Quantitative analysis of peptides and proteins in biomedicine by targeted mass spectrometry. *Nature Methods*, 2013, **10** (1), P. 28–34.
- [9] Cho H., Kumar S., Yang D., Vaidyanathan S., Woo K., Garcia I., Shue H.J., Yoon Y., Ferreri K., Choo H. Surface-Enhanced Raman Spectroscopy-Based Label-Free Insulin Detection at Physiological Concentrations for Analysis of Islet Performance. *ACS Sensors*, 2018, **3** (1), P. 65–71.
- [10] Kimmel D.W., LeBlanc G., Meschievitz M.E., Cliffel D.E. Electrochemical Sensors and Biosensors. *Analytical Chemistry*, 2012, **84** (2), P. 685–707.
- [11] Soffe R., Nock V., Chase J.G. Towards Point-of-Care Insulin Detection. *ACS Sensors*, 2019, **4** (1), P. 3–19.
- [12] Mayer K.M., Hafner J.H. Localized Surface Plasmon Resonance Sensors. *Chemical Reviews*, 2011, **111** (6), P. 3828–3857.
- [13] Takeshima N., Sugawa K., Noguchi M., Tahara H., Jin S., Takase K., Otsuki J., Tamada K. Synthesis of Ag Nanoprisms with Precisely-tuned Localized Surface Plasmon Wavelengths by Sequential Irradiation of Light of Two Different Wavelengths. *Chemistry Letter*, 2020, **49** (3), P. 240–243.
- [14] Luo X., Zhu C., Saito M., Espulgar W.V., Dou X., Terada Y., Obara A., Uchiyama S., Tamiya E. Cauliflower-Like Nanostructured Localized Surface Plasmon Resonance Biosensor Chip for Cytokine Detection. *Bulletin of the Chemical Society of Japan*, 2020, **93** (9), P. 1121–1126.
- [15] Ortega M.A., Rodríguez-Comas J., Yavas O., Velasco-Mallorquí F., Balaguer-Trias J., Parra V., Novials A., Servitja J.M., Quidant R., Ramón-Azcón J. In Situ LSPR Sensing of Secreted Insulin in Organ-on-Chip. *Biosensors*, 2021, **11** (5), 138.
- [16] Hammond J.L., Bhalla N., Rafiee S.D., Estrela P. Localized Surface Plasmon Resonance as a Biosensing Platform for Developing Countries. *Biosensors*, 2014, **4** (2), P. 172–188.
- [17] Maphanga C., Manoto S., Ombinda-Lemboumba S., Ismail Y., Mthunzi-Kufa P. Localized surface plasmon resonance biosensing of Mycobacterium tuberculosis biomarker for TB diagnosis. *Sensing and Bio-Sensing Research*, 2023, **39**, 100545.
- [18] Bonyár A. Label-Free Nucleic Acid Biosensing Using Nanomaterial-Based Localized Surface Plasmon Resonance Imaging: A Review. *ACS Applied Nano Materials*, 2020, **3** (9), P. 8506–8521.
- [19] Nguyen T.T.V., Xie X., Xu J., Wu Y., Hong M., Liu X. Plasmonic bimetallic nanodisk arrays for DNA conformation sensing. *Nanoscale*, 2019, **11** (41), P. 19291–19296.
- [20] Szunerits S., Saada H., Pagneux Q., Boukherroub R. Plasmonic Approaches for the Detection of SARS-CoV-2 Viral Particles. *Biosensors*, 2022, **12** (7), 548.
- [21] Liu C.H., Hong M.H., Cheung H.W., Zhang F., Huang Z.Q., Tan L.S., Hor T.S. A. Bimetallic structure fabricated by laser interference lithography for tuning surface plasmon resonance. *Optics Express*, 2008, **16** (14), P. 10701–10709.
- [22] Xu L., Tan L.S., Hong M.H. Tuning of localized surface plasmon resonance of well-ordered Ag/Au bimetallic nanodot arrays by laser interference lithography and thermal annealing. *Applied Optics*, 2011, **50** (31), P. 74–79.
- [23] Nguyen T.T.V. Development of plasmonic nanostructures for biological sensing. Ph.D dissertation, National University of Singapore, 2013.
- [24] Tombelli S., Minunni M., Mascini M. Analytical applications of aptamers. *Biosensors and Bioelectronics*, 2005, **20** (12), P. 2424–2434.
- [25] Zhou J., Rossi J. Aptamers as targeted therapeutics: current potential and challenges. *Nature Reviews Drug Discovery*, 2017, **16** (3), P. 181–202.
- [26] Taghdisi S.M., Danesh N.M., Lavaee P., Sarreshtehdar Emrani A., Ramezani M., Abnous K. Aptamer Biosensor for Selective and Rapid Determination of Insulin. *Analytical Letters*, 2015, **48** (4), P. 672–681.
- [27] Connor A.C., Frederick K.A., Morgan E.J., McGown L.B. Insulin Capture by an Insulin-Linked Polymorphic Region G-Quadruplex DNA Oligonucleotide. *J. of the American Chemical Society*, 2006, **128** (15), P. 4986–4991.
- [28] Zhang X., Zhu S., Deng C., Zhang X. An aptamer based on-plate microarray for high-throughput insulin detection by MALDI-TOF MS. *Chemical Communications*, 2012, **48** (21), P. 2689–2691.
- [29] Malik R., Roy I. Stabilization of bovine insulin against agitation-induced aggregation using RNA aptamers. *Int. J. of Pharmaceutics*, 2013, **452** (1), P. 257–265.
- [30] Wu Y., Midinov B., White R.J. Electrochemical Aptamer-Based Sensor for Real-Time Monitoring of Insulin. *ACS Sensors*, 2019, **4** (2), P. 498–503.
- [31] Taib M., Tan L.L., Abd Karim N.H., Ta G.C., Heng L.Y., Khalid B. Reflectance aptasensor based on metal salphen label for rapid and facile determination of insulin. *Talanta*, 2020, **207**, 120321.
- [32] Willets K.A., Duyne R.P.V. Localized Surface Plasmon Resonance Spectroscopy and Sensing. *Annual Review of Physical Chemistry*, 2007, **58** (1), P. 267–297.
- [33] Grabar K.C., Freeman R.G., Hommer M.B., Natan M.J. Preparation and Characterization of Au Colloid Monolayers. *Analytical Chemistry*, 1995, **67** (4), P. 735–743.
- [34] Liu J., Cao Z., Lu Y. Functional Nucleic Acid Sensors. *Chemical Reviews*, 2009, **109** (5), P. 1948–1998.
- [35] Shrivastava A. Methods for the determination of limit of detection and limit of quantitation of the analytical methods. *Chronicles of Young Scientists*, 2011, **2**, P. 21–25.

Submitted 27 November 2023; revised 6 March 2024; accepted 10 March 2024

Information about the authors:

Thanh Thi Van Nguyen – School of Materials Science and Engineering, Hanoi University of Science and Technology, No.1 Dai Co Viet street, Hanoi 100000, Vietnam; ORCID 0009-0005-2040-2781; thanh.nguyenthivan@hust.edu.vn



NANOSYSTEMS:

PHYSICS, CHEMISTRY, MATHEMATICS

INFORMATION FOR AUTHORS

The journal publishes research articles and reviews, and also short scientific papers (letters) which are unpublished and have not been accepted for publication in other magazines. Articles should be submitted in English. All articles are reviewed, then if necessary come back to the author to completion.

The journal is indexed in Web of Science Core Collection (Emerging Sources Citation Index), Chemical Abstract Service of the American Chemical Society, Zentralblatt MATH and in Russian Scientific Citation Index.

Author should submit the following materials:

1. Article file in English, containing article title, the initials and the surname of the authors, Institute (University), postal address, the electronic address, the summary, keywords, MSC or PACS index, article text, the list of references.
2. Files with illustrations, files with tables.
3. The covering letter in English containing the article information (article name, MSC or PACS index, keywords, the summary, the literature) and about all authors (the surname, names, the full name of places of work, the mailing address with the postal code, contact phone number with a city code, the electronic address).
4. The expert judgement on possibility of publication of the article in open press (for authors from Russia).

Authors can submit a paper and the corresponding files to the following addresses: nanojournal.ifmo@gmail.com, popov1955@gmail.com.

Text requirements

Articles should be prepared with using of text editors MS Word or LaTeX (preferable). It is necessary to submit source file (LaTeX) and a pdf copy. In the name of files the English alphabet is used. The recommended size of short communications (letters) is 4-6 pages, research articles– 6-15 pages, reviews – 30 pages.

Recommendations for text in MS Word:

Formulas should be written using Math Type. Figures and tables with captions should be inserted in the text. Additionally, authors present separate files for all figures and Word files of tables.

Recommendations for text in LaTeX:

Please, use standard LaTeX without macros and additional style files. The list of references should be included in the main LaTeX file. Source LaTeX file of the paper with the corresponding pdf file and files of figures should be submitted.

References in the article text are given in square brackets. The list of references should be prepared in accordance with the following samples:

- [1] Surname N. *Book Title*. Nauka Publishing House, Saint Petersburg, 2000, 281 pp.
- [2] Surname N., Surname N. Paper title. *Journal Name*, 2010, **1** (5), P. 17-23.
- [3] Surname N., Surname N. Lecture title. In: Abstracts/Proceedings of the Conference, Place and Date, 2000, P. 17-23.
- [4] Surname N., Surname N. Paper title, 2000, URL: <http://books.ifmo.ru/ntv>.
- [5] Surname N., Surname N. Patent Name. Patent No. 11111, 2010, Bul. No. 33, 5 pp.
- [6] Surname N., Surname N. Thesis Title. Thesis for full doctor degree in math. and physics, Saint Petersburg, 2000, 105 pp.

Requirements to illustrations

Illustrations should be submitted as separate black-and-white files. Formats of files – jpeg, eps, tiff.



NANOSYSTEMS:

PHYSICS, CHEMISTRY, MATHEMATICS

Журнал зарегистрирован

Федеральной службой по надзору в сфере связи, информационных технологий и массовых коммуникаций

(свидетельство ПИ № ФС 77 - 49048 от 22.03.2012 г.)

ISSN 2220-8054

Учредитель: федеральное государственное автономное образовательное учреждение высшего образования

«Национальный исследовательский университет ИТМО»

Издатель: федеральное государственное автономное образовательное учреждение высшего образования

«Национальный исследовательский университет ИТМО»

Отпечатано в Учреждении «Университетские телекоммуникации»

Адрес: 197101, Санкт-Петербург, Кронверкский пр., 49

Подписка на журнал НФХМ

На второе полугодие 2024 года подписка осуществляется через

ОАО «АРЗИ», подписной индекс Э57385